

UVSOR

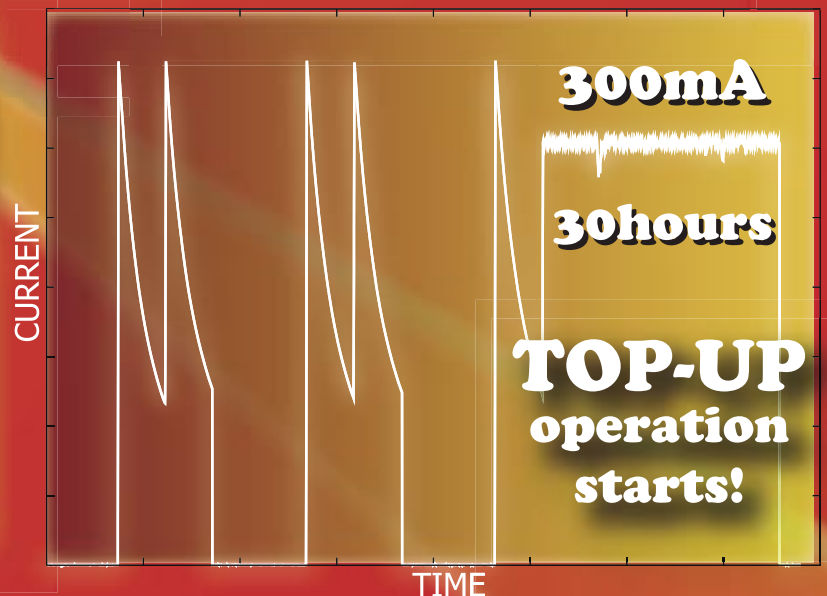
ISSN 0911-5730

UVSOR-37

June 2010

ACTIVITY REPORT 2009

UVSOR II
since 2003



UVSOR Facility
Institute for Molecular Science
National Institutes of Natural Sciences

Preface

This Activity Report covers the research activities carried out at the UVSOR facility in FY2009 (April 2009-March 2010). This is the seventh volume in the new series for the third decade of UVSOR, corresponding to the seventh year of the use of the low-emittance UVSOR-II storage ring. The ring is very stable in operation at the initial beam current of 350 mA for every 6-hour 0.75-GeV full-energy injection and the beam emittance of 27 nm-rad. The ring is in operation in the Top-up mode for 24 hours from Thursday's morning to Friday's morning. All the beam-lines have come to be ready for the Top-up mode until March 2010. In FY2010, the ring will be operated fully in the Top-up mode.



The UVSOR facility is exclusively responsible for the high-brilliant VUV light source as a low-energy third generation ring. There are four 4 m-long long straight sections and four 1.5 m-long short straight sections in the present UVSOR-II ring of 53 m in circumference. We already installed three long undulators at BL3U, BL5U and BL7U and one short undulator at BL6U. The fifth undulator beam-line BL1U will be constructed in FY2010, which will be dedicated to produce the coherent synchrotron radiation, under the Quantum Beam Technology Program of the Ministry of Education, Culture, Sports, Science and Technology (MEXT). Before starting the construction of BL1U, we will reconstruct and upgrade the present BL1A and BL1B at vacant dipole ports in 2010-2011.

In UVSOR, we have four research positions for accelerator physics (1 full prof., 1 assoc. prof., and 2 assist. profs.) and four research positions for photophysics and photochemistry (2 assoc. profs. and 2 assist. profs.). In the accelerator physics division, there was one vacancy for the associate professor. In the photochemistry division, Assist. Prof. Dr. Yasumasa Hikosaka has been promoted as an associate professor of Niigata University last September. Two young researchers have joined the photophysics and photochemistry divisions as assist. profs. this April.

Prof. Nobuhiro Kosugi, who has worked for the UVSOR facility as the Director for 16 years, has been promoted as Deputy Director-General of Institute for Molecular Science. We appreciate all his efforts in many years. I, Prof. Masahiro Katoh of the accelerator physics division, have been promoted as the new director of UVSOR.

We look forward to more exciting achievements in the coming years of UVSOR-II.

April, 2010

Masahiro Katoh
Director of UVSOR

Nobuhiro KOSUGI moves on

Professor Nobuhiro Kosugi, who led the UVSOR facility of the Institute for Molecular Science (IMS) from 1994 to 2010, resigned as Director of UVSOR. He has become the Deputy Director General of IMS. He is expected to continue to develop the promotion of molecular science. Professor Masahiro Katoh has undertaken the post of Director of UVSOR from 1 June 2010.

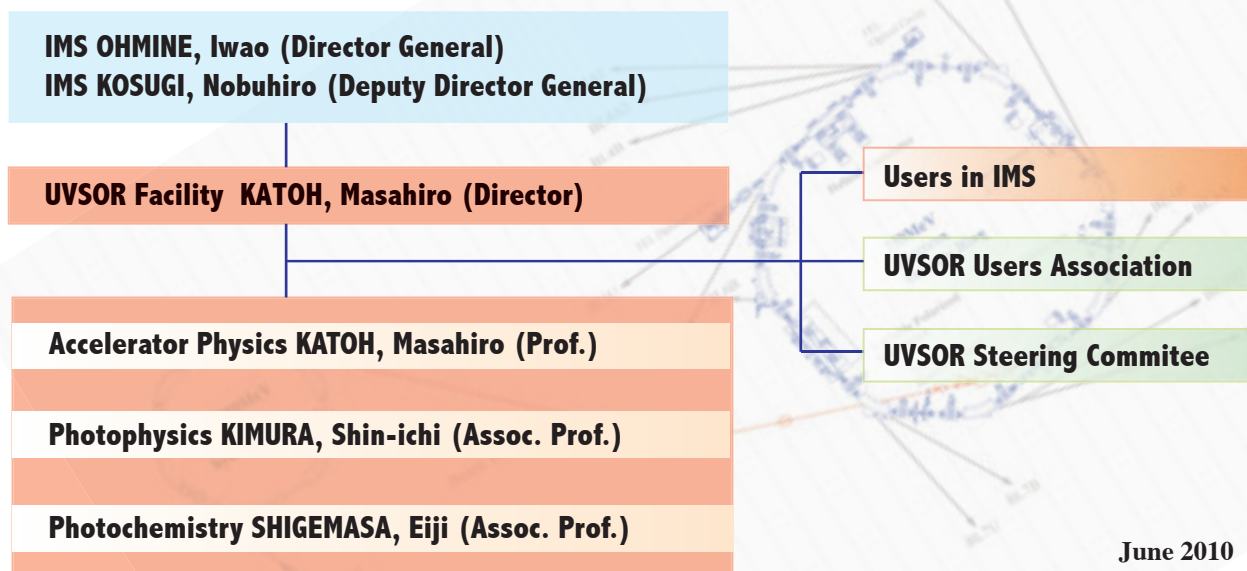


The JSSRR Young Scientist Award of the Japanese Society for Synchrotron Radiation Research Given to Dr. Hiroyuki YAMANE

Dr. Hiroyuki YAMANE, Assistant Professor working with Prof. Kosugi, won the JSSRR Young Scientist Award from the Japanese Society for Synchrotron Radiation Research in 2010, for his outstanding achievements on “High-precision experiments on the electronic structure of highly ordered organic thin films and interfaces”. Congratulations!



UVSOR Organization



UVSOR Staff

Director

KATO, Masahiro Professor mkato@ims.ac.jp

Light Source Division (Accelerator Physics)

KATO, Masahiro	Professor	mkato@ims.ac.jp
ADACHI, Masahiro	Assistant Professor	adachi@ims.ac.jp
ZEN, Heishun	Assistant Professor	zen@ims.ac.jp
YAMAZAKI, Jun-ichiro	Unit Chief Engineer	yamazaki@ims.ac.jp
HAYASHI, Kenji	Engineer	h-kenji@ims.ac.jp
TOKUSHI, Tetsuzyo	Supporting Engineer	tetsuzyo@ims.ac.jp

Beamline Division (Photophysics)

KIMURA, Shin-ichi	Associate Professor	kimura@ims.ac.jp	
MATSUNAMI, Masaharu	Assistant Professor	matunami@ims.ac.jp	(since Apr. 2010)
HASUMOTO, Masami	Unit Chief Engineer	hasumoto@ims.ac.jp	
SAKAI, Masahiro	Engineer	sakai@ims.ac.jp	
MIYAZAKI, Hidetoshi	IMS Fellow (PD)	hmiyazak@ims.ac.jp	
MORI, Tatsuya	Post-Doctoral Fellow	mori@ims.ac.jp	(since Apr. 2010)
TAKAHASHI, Toshiharu	Adjunct Associate Professor		(since Apr. 2010)
NISHI, Tatsuhiko	Guest Researcher	tnishi@ims.ac.jp	

Beamline Division (Photochemistry)

SHIGEMASA, Eiji	Associate Professor	sigemasa@ims.ac.jp	
HIKOSAKA, Yasumasa	Assistant Professor	hikosaka@ims.ac.jp	(until Aug. 2009)
IWAYAMA, Hiroshi	Assistant Professor	iwayama@ims.ac.jp	(since Apr. 2010)
HORIGOME, Toshio	Facility Chief Engineer	horigome@ims.ac.jp	
NAKAMURA, Eiken	Unit Chief Engineer	eiken@ims.ac.jp	
KONDO, Naonori	Engineer	nkondo@ims.ac.jp	
AMEMIYA, Kenta	Adjunct Associate Professor		(until Mar. 2010)

Secretary

HAGIWARA, Hisayo
MASUDA, Michiko

hagiwara@ims.ac.jp
masuda@ims.ac.jp

UVSOR Steering Committee

KOSUGI, Nobuhiro	UVSOR, IMS	Chair
KATO, Masahiro	UVSOR, IMS	
KIMURA, Shin-ichi	UVSOR, IMS	
SHIGEMASA, Eiji	UVSOR, IMS	
AMEMIYA, Kenta	KEK-PF(Adj. Assoc. Prof., IMS)	(until Mar. 2010)
TAKAHASHI, Toshiharu	Kyoto Univ. (Adj. Assoc. Prof., IMS)	(since Apr. 2010)
YOKOYAMA, Toshihiko	IMS	
OHMORI, Kenji	IMS	(until Mar. 2010)
NAKAMURA, Toshikazu	IMS	(until Mar. 2010)
MITSUKE, Koichiro	IMS	
OHSHIMA, Yasuhiro	IMS	(since Apr. 2010)
TADA, Mizuki	IMS	(since Apr. 2010)
TAKATA, Masaki	RIKEN/SPRING-8	(until Mar. 2010)
NAMATAME, Hirofumi	Hiroshima Univ.	(until Mar. 2010)
HONMA, Kenji	Univ. of Hyogo	(until Mar. 2010)
HINO, Shojun	Ehime Univ.	(until Mar. 2010)
FUKUI, Kazutoshi	Fukui Univ.	
MATSUDA, Iwao	Univ. of Tokyo	
YOSHIDA, Tomoko	Nagoya Univ.	
KINOSHITA, Toyohiko	JASRI	(since Apr. 2010)
KOBAYASHI, Yukinori	KEK-PF	(since Apr. 2010)
KONDOH, Hiroshi	Keio Univ.	(since Apr. 2010)
SHIMADA, Kenya	Hiroshima Univ.	(since Apr. 2010)

UVSOR Users Association

FUKUI, Kazutoshi	Chair, Fukui Univ.	(until Mar. 2010)
HINO, Shojun	Ehime Univ.	(until Mar. 2010)
GEJO, Tatsuo	Univ. of Hyogo	(until Mar. 2010)
NAKAGAWA, Kazumichi	Kobe Univ.	(until Mar. 2010)
YOSHIDA, Tomoko	Nagoya Univ.	(until Mar. 2010)
SODA, Kazuo	Chair, Nagoya Univ.	(since Apr. 2010)
FUKUI, Kazutoshi	Fukui Univ.	(since Apr. 2010)
NAKAGAWA, Kazumichi	Kobe Univ.	(since Apr. 2010)
YOSHIDA, Tomoko	Nagoya Univ.	(since Apr. 2010)
ITO, Takahiro	Nagoya Univ.	(since Apr. 2010)

Graduate Students

MIZUNO, Takafumi	Grad. Univ. Adv. Studies	tmizuno@ims.ac.jp	(until Mar. 2010)
IIZUKA, Takuya	Grad. Univ. Adv. Studies	takuizk@ims.ac.jp	
TANIKAWA, Takanori	Grad. Univ. Adv. Studies	tanikawa@ims.ac.jp	
NAGATANI, Atsumune	Nagoya Univ.		(until Sep. 2009)
FURUI, Yuta	Nagoya Univ.		(until Sep. 2009)
TAIRA, Yoshitaka	Nagoya Univ.		
MITANI, Hiroyuki	Shinshu Univ.		(until Mar. 2010)
HAJIRI, Tetsuya	Nagoya Univ.		
KIKUCHI, Yoshitaka	Nagoya Univ.		

Visiting Scientists

KWON, Yong-Seung	Sungkyunkwan Univ.	Aug. 2009, Feb. 2010
OH, Hyunjin	Masan College	Aug. 2009
SONG, Yun Young	Cheju Tourism College	Aug. 2009
JANG, Yu ran	Sungkyunkwan Univ.	Aug. - Sept. 2009
HONG, Jeong-Beom	Sungkyunkwan Univ.	Aug. - Sept. 2009, Feb. - Mar. 2010
KIM, Chul	Yonsei Univ.	Aug. 2009, Dec. 2009
SONG, Dongjoon	Yonsei Univ.	Aug. 2009
KIM, Chang Young	Yonsei Univ.	Aug. 2009, Oct. 2009
GUILLEMIN, Renand	LCPMR, Univ. Pierre et marie Curie	Oct. 2009
SIMON, Marc	LCPMR, Univ. Pierre et marie Curie	Oct. 2009
TALEB-IBRAHIMI, Amina	CNRS and SOLEIL SYNCHROTRON	Oct. 2009
GREBENNIKOV, Vladimir	Russian Academy of Science, Ural Division	Oct. 2009
PETACCIA, Luca	Elettra Sincrotrone Trieste	Oct. 2009
KUZNETSOVA, Tatyana	Russian Academy of Science, Ural Division	Oct. 2009
FENG, Donglai	Fudan Univ.	Oct. 2009
SZWAJ, Christophe	Univ. of Lill	Oct. - Dec. 2009
LABLANQUIE, Pascal	LCPMR, Univ. Pierre et marie Curie	Nov. 2009
LEPARQUIER, Marc	Univ. of Lill	Nov. 2009
BIELAWSKI, Serge	Univ. of Lill	Nov. 2009
PARK, Seung Ryong	Yonsei Univ.	Dec. 2009
JUNG, Wonsig	Yonsei Univ.	Dec. 2009
YOM, Han Woong	Yonsei Univ.	Feb. 2010

Light Sources in 2009

1. Status of UVSOR-II

In the fiscal year 2009, we have operated the UVSOR-II accelerators from April '09 to February '10. We had totally 37 weeks for the users operation, 35 weeks of which are in the multi-bunch mode, 2 weeks in the single-bunch mode. We had 6 weeks dedicated for machine studies. We have three month shut-down, starting from March '10 for a re-construction work on the storage ring and the beam transport line. We had 2 one week shut-down in May, August and September and 1 two week one around the New Years Day.

The monthly statistics of the operation time and the integrated beam current are shown in FIGURE 1. In these two years, the operation time per month has increased by approximately 20% on average. This is because of the extended operations for the top-up test runs as described later.

The weekly operation schedule is as follows. On Monday, from 0 am to 9 pm, the machine is operated for machine studies. From Tuesday to Friday, from 9am to 9pm, the machine is operated for users. The beam injection is made twice a day, at 9am and 3pm, with the filling beam current is 350 mA. On Thursday and Friday, the machine is operated in the top-up mode with the beam current, 300 mA. In 2009, we have been increasing the top-up operation time, step by step, as shown in FIGURE 2. In case of the single bunch mode, the machine is fully operated in the top-up mode with the beam current, 50 mA [1].

In this fiscal year, we had a few troubles on the injector. One is on the cooling water system of the linear accelerator. Others are on the pulse magnet power supplies. Fortunately, the users time could be secured by extending the operation time during the weeks.

2. Improvements

Top-up Operation

We have operated UVSOR-II in the top-up mode for users for one year and a half as shown in the previous section. So far, we have found several problems that

have to be solved. The most serious one is the instantaneous orbit movement at injection. Some beam-lines are located inside of the injection bump. Thus, the effect is inevitable. However, even in the other beam-lines, they observe the effect because of the leakage of the bump orbit. We have prepared a system to provide injection timing signal for the data acquisition system at the beam-lines to stop the data acquisition during the injection. It was successfully demonstrated in a few beam-lines to eliminate the effect of the injection on their data.

There are a few other practical problems. One is the stability of the injection efficiency. In particular, the drift of the injection efficiency from the linac to the booster synchrotron was significant. It was found that the origin of the drift mainly arises from the drift of the excitation voltage of the injection septum at the booster synchrotron. A drift of the RF power in the linac was also noticeable. Some feedback systems have been constructed by using digital oscilloscopes and PCs. The injection efficiency was drastically stabilized by using them [2].

Quantum Beam Technology Program

After the successes of the proof-of-principle experiments on the new light source technologies using lasers and a storage ring, we have started a new research project under Quantum Beam Technology Program of MEXT. This is a five year project started in 2008. In this program, we will reconstruct the beam transport line and move the injection point to produce another new 4 m long straight section in the ring. We will upgrade the laser system and install new undulators, which are dedicated to the coherent radiation production. We will also construct two new beam-lines which are also dedicated to applications of the coherent radiation in the THz and VUV ranges.

In FY2008 and FY2009, we have constructed an undulator, magnets and power supplies for new beam transport lines and new laser amplifiers. In March, 2010, we have started the reconstruction on the beam transport line and the storage ring.

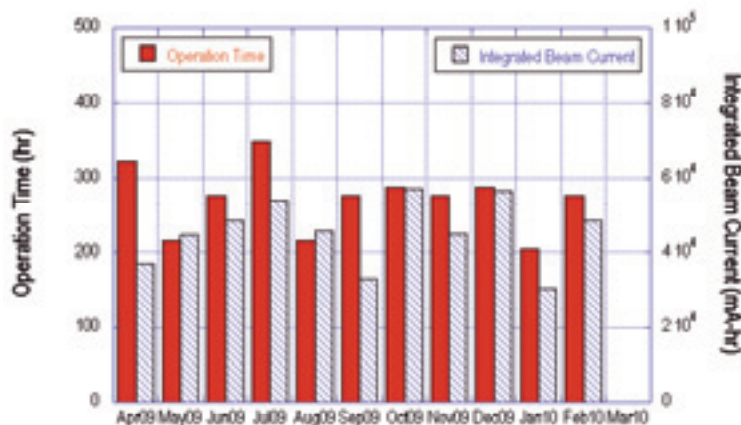


Fig. 1. Monthly statistics of the operation time (red bars) and of the integrated beam current (blue dashed bars).

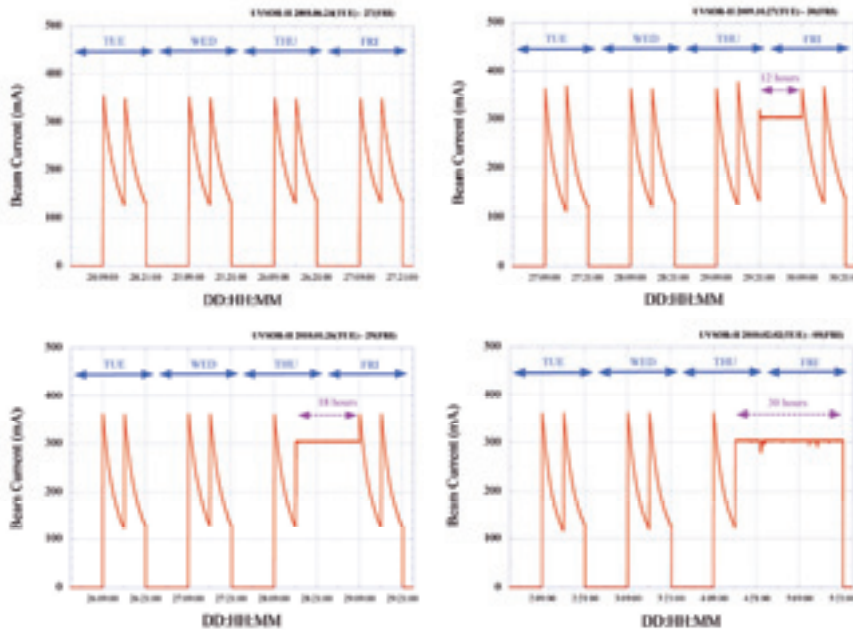


Fig. 2. Top-up Test Operation. Beam current histories in four days for users runs are shown. From 2008 to 2010, we have gradually increased the top-up operation time.

Accelerator Technologies

A single pass beam position monitor has been developed, which utilizes the existing BPM heads in the ring. The signals from the BPM heads are recorded by a digital oscilloscope and are analyzed off line [3]. It was successfully demonstrated that the injection bump orbit and the injection orbit could be measured. The beam orbit executing a betatron oscillation produced by the RFKO system was also successfully measured [4]. The result indicates that non-linear effect produced by the sextupole magnets strongly suppresses the amplitude of the betatron oscillation.

3. Researches and Developments

Free Electron Laser

The top-up injection is not only useful for the SR users experiments but also for the free electron laser (FEL) and other new light sources. In case of the FEL, since the ring is operated in single bunch mode, the beam lifetime is short. The rapid change in the beam current causes a rapid change in the FEL power, a part of which is due to the change in the gain and another part is due to the thermal deformation on the optical cavity mirror.

We have tried a FEL operation in the top-up mode [3]. It was found that the output power is quite stable. We carried out a users experiment in the top-up mode

and found that, since there is no interruption by the injection, the effective beam time for the FEL users increased much.

Coherent Harmonic Generation by using an External Laser

To get coherent radiation in the VUV range, which is hard to reach with the resonator type free electron laser, coherent harmonic generation (CHG) is under investigation. After the successful observations on the coherent 3rd harmonics of a Ti:Sa laser[4, 5], we prepared a spectrometer for the VUV range. By using this, we have succeeded in observing the CHG up to 9th harmonics [6]

[1] H. Zen *et al.*, in this report

[2] H. Zen *et al.*, in this report

[3] A. Nagatani *et al.*, in this report

[4] Y. Furui *et al.*, in this report

[3] H. Zen *et al.*, in this report

[4] M. Labat, C. Bruni, G. Lambert, M. Hosaka, M. Shimada, M. Katoh, A. Mochihashi, T. Takashima, T. Hara, M. E. Couprie, *Europhys. Lett.*, 81 (2008) 34004

[5] M. Labat, M. Hosaka, M. Shimada, M. Katoh, M. E. Couprie, *Phys. Rev. Lett.* 101, 164803 (2008)

[6] T. Tanikawa *et al.*, in this report

Masahiro KATOH (UVSOR Facility)

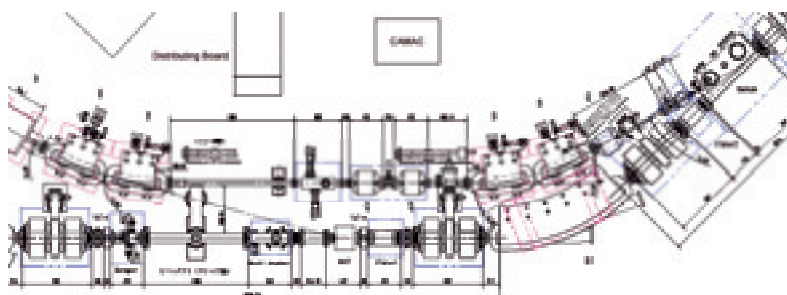


Fig. 3. New configuration of the beam transport line

UVSOR Accelerator Complex

Injection Linear Accelerator

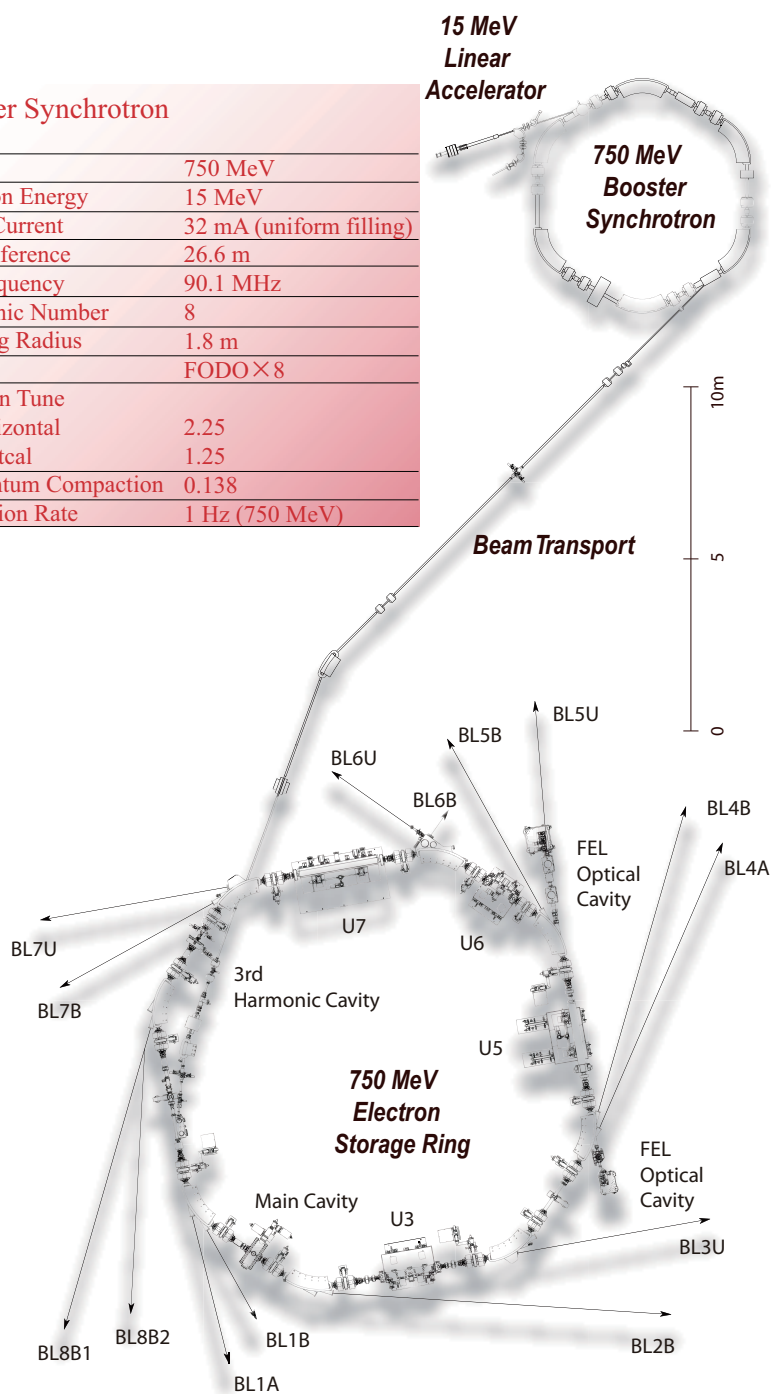
DC Gun	
Electron Source	EIMAC Y-646B
Applied Voltage	75 kV
Accelerator Tube	
Length	2.5 m
Frequency	2856 MHz
Structure	$2\pi/3$ Traveling Wave
Repetition Rate	2.6 Hz
Beam Energy	~15 MeV
Electron Beam Macro-pulse Duration	
Short Pulse Mode	~5 ns
Long Pulse Mode	~1.5 μ s
Beam Charge	
Short Pulse Mode	0.8 nC/Macro-pulse
Long Pulse Mode	130 nC/Macro-pulse

Booster Synchrotron

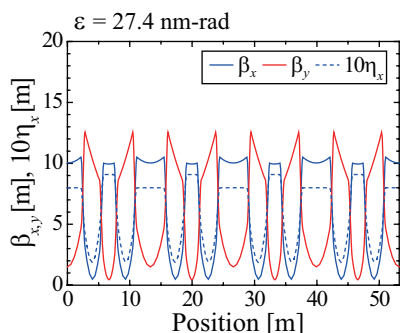
Energy	750 MeV
Injection Energy	15 MeV
Beam Current	32 mA (uniform filling)
Circumference	26.6 m
RF Frequency	90.1 MHz
Harmonic Number	8
Bending Radius	1.8 m
Lattice	FODO \times 8
Betatron Tune	
Horizontal	2.25
Vertical	1.25
Momentum Compaction	0.138
Repetition Rate	1 Hz (750 MeV)

UVSOR-II Storage Ring

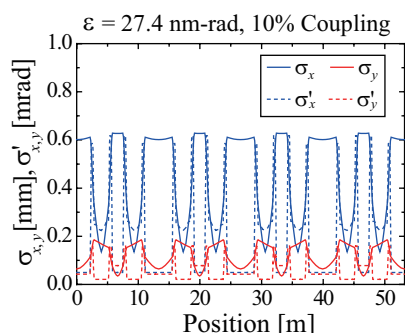
Energy	750 MeV
Injection Energy	750 MeV
Maximum Stored Current	500 mA (multi bunch) 100 mA (single bunch)
Normal Stored Current	300 mA (multi bunch) 50 mA (single bunch) (Top-up operation)
Natural Emittance	27.4 nm-rad
Circumference	53.2 m
RF Frequency	90.1 MHz
Harmonic Number	16
Bending Radius	2.2 m
Lattice	Extended DBA \times 4
Straight Section	(4 m \times 4) + (1.5 m \times 4)
RF Voltage	100 kV
Betatron Tune	
Horizontal	3.75
Vertical	3.20
Momentum Compaction	0.028
Natural Chromaticity	
Horizontal	-8.1
Vertical	-7.3
Energy Spread	4.2×10^{-4}
Natural Bunch Length	108 ps



Electron Beam Optics of UVSOR-II Storage Ring



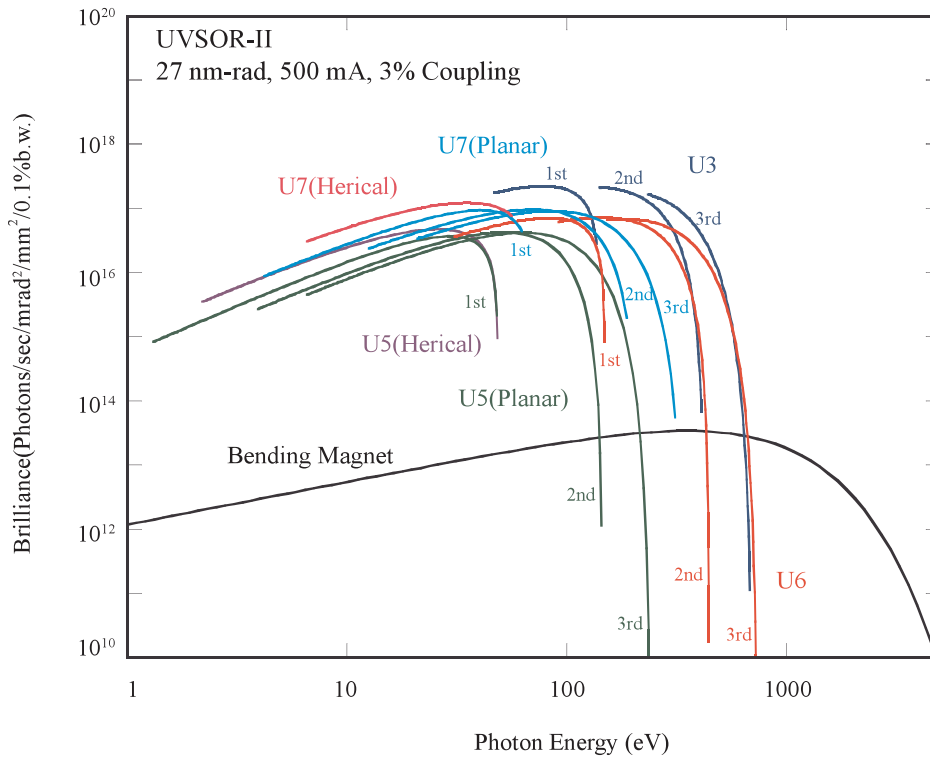
Horizontal / vertical betatron functions and dispersion function



Horizontal / vertical electron beam sizes and beam divergences

Insertion Devices

Brilliance of Radiation



Brilliance of radiation from the insertion devices (U3, U5, U6 and U7) and a bending magnet of UVSOR-II

U3 In-vacuum Undulator

Number of Periods	50
Period Length	38 mm
Pole Length	1.9 m
Pole Gap	15 - 40 mm
Deflection Parameter	2.00 - 0.24

U6 In-vacuum Undulator

Number of Periods	26
Period Length	36 mm
Pole Length	0.94 m
Pole Gap	15 - 40 mm
Deflection Parameter	1.78 - 0.19

U5 Herical Undulator / Optical Klystron

Number of Periods	21 / 9+9 (Opt. Kly.)
Period Length	110 mm
Pole Length	2.35 m
Pole Gap	30 - 150 mm
Deflection Parameter	4.6 - 0.07 (Helical) 8.5 - 0.15 (Linear)

U7 Apple-II Variable Polarization Undulator

Number of Periods	40
Period Length	76 mm
Pole Length	3.04 m
Pole Gap	24 - 200 mm
Deflection Parameter	5.4 (Max. Horizontal) 3.6 (Max. Vertical) 3.0 (Max. Helical)

Bending Magnets

Bending Radius	2.2 m
Critical Energy	425 eV

Beamlines in 2009

The UVSOR facility has become one of the highest brilliance extreme-ultraviolet radiation sources among synchrotron radiation facilities with electron energy less than 1 GeV, since the successful accomplishment of the upgrade project on the UVSOR storage ring (UVSOR-II project), in which the creation of four new straight sections and the achievement of much smaller emittance (27 nm-rad) were planned. Eight bending magnets and four insertion devices are available for utilizing synchrotron radiation at UVSOR. There is a total of fourteen operational beamlines in 2009, which are classified into two categories. Nine of them are so-called "Open beamlines", which are open to scientists of universities and research institutes belonging to the government, public organizations, private enterprises and those of foreign countries. The rest of the five beamlines are so-called "In-house beamlines", and are dedicated to the use of research groups within IMS.

The improvements and upgrades of the beamlines at UVSOR have been continuously discussed with users in a series of UVSOR workshops. Newly constructed (BL3U and BL7U) as well as the upgraded (BL5U and BL6B) beamlines synchronized with the UVSOR-II project have been routinely operated, and a number of outcome has emerged through the utilization of these beamlines. The in-vacuum type undulator U6, which has been relocated from the long straight section S7 to the short one S6, has 26 magnetic periods and the period length is 36 mm. The spectral region from 50 eV to 140 eV was covered with the first harmonic radiation. There was an inherent energy gap between the highest and lowest photon energies, covered by the first and third harmonics, respectively. The photon energy range from 30 to 500 eV can be covered by odd harmonics of U6 up to seventh without any energy gap. Then a new project for constructing the undulator beamline BL6U has been initiated.

The BL6U monochromator designed covers the photon energy ranging from 30 to 500 eV, with the resolving power higher than 10000 and the photon flux more than 10^{10} photons/sec. The practical construction of BL6U has begun from the summer shutdown in 2008, and the first light has been observed in December 2008. After the fine tuning of the monochromator, it has been confirmed that the photon energy ranging from 40 to 400 eV, with the resolving power higher than 5000 and the photon flux more than 10^{11} photons/sec, can be covered, when the storage ring is operated in the top-up mode.

Accordingly, BL4B will be allocated to an open beamline from fiscal year 2010. The experimental activities conducted at BL4A and BL8B1 were terminated in August 2009 and in February 2010, respectively. As a consequence, we have one soft X-ray station equipped with a double-crystal monochromator, seven extreme ultraviolet and soft X-ray stations with a grazing incidence monochromator, three vacuum ultraviolet stations with a normal incidence monochromator, one infrared (IR) station equipped with Fourier-Transform interferometers, as shown in the appended table (next page) for all available beamlines at UVSOR in 2010.

"Development and Application of Light Source Technology Based on Electron Storage Ring and Laser" proposed by the UVSOR machine group was accepted in 2008, as a research program in "Quantum Beam Technology Project" conducted by MEXT/JST. In connection, the straight section U1 will be used for generating coherent THz and VUV radiation, where two beamlines will be constructed. In response to this, BL1A and BL1B must be moved to vacant lots. Since spectroscopic research works on solids have been conducted very actively at these beamlines, it is essential that all the users' activities there should segue at new locations. Based upon the result of the discussion at the users' meetings, which were organized by the UVSOR User's Union, it was decided that BL1A will be moved to the location of the previous BL2A without any changes on the beamline components, and BL1B will be newly constructed at the place of the previous BL3B. A design study for the new beamline optics has been started. For the monochromator at BL3B, a 2.5-m off-plane Eagle type has been chosen. The practical movement and construction will start from the spring of 2011. Further discussion toward utilizing the available straight sections most effectively and formulating a basic plan on the beamline construction, will be continued.

All users are required to refer to the beamline manuals and the UVSOR guidebook (the latest revision in PDF format uploaded on the UVSOR web page in the summer of 2009), on the occasion of conducting the actual experimental procedures. Those wishing to use the open and in-house beamlines are recommended to contact the beamline master (see next page), respectively. For updated information of UVSOR, <http://www.uvsor.ims.ac.jp/>.

Eiji SHIGEMASA (UVSOR Facility)

Beamlines at UVSOR

Beam-line	Monochromator, Spectrometer	Energy Region (eV)		Experiments	Beamline master
1A	Double-Crystal		600 eV - 4 keV	Solid (Absorption)	N. Kondo nkondo@ims.ac.jp
1B	1m Seya-Namioka	2 eV - 30 eV		Solid (Reflection, Absorption)	M. Hasumoto hasumoto@ims.ac.jp
2B*	18m Spherical Grating (Dragon)	24 eV - 205 eV		Gas (Photoionization, Photodissociation)	K. Mitsuke mitsuke@ims.ac.jp
3U*	Varied-Line-Spacing Plane Grating (Monk-Gillieson)	60 eV - 800 eV		Gas, Liquid, Solid (Absorption, Photoemission, Photon Emission)	N. Kosugi kosugi@ims.ac.jp
4B*	Varied-Line-Spacing Plane Grating (Monk-Gillieson)	25 eV - 1 keV		Gas (Photoionization, Photodissociation) Solid (Photoemission)	E. Shigemasa sigemasa@ims.ac.jp
5U	Spherical Grating (SGM-TRAIN*)	5 eV - 250 eV		Solid (Photoemission)	M. Sakai sakai@ims.ac.jp
5B	Plane Grating	6 eV - 600 eV		Calibration Solid (Absorption)	M. Hasumoto hasumoto@ims.ac.jp
6U*	Variable-Included-Angle Varied-Line-Spacing Plane Grating	30 eV - 500 eV		Gas (Photoionization, Photodissociation) Solid (Photoemission)	E. Shigemasa sigemasa@ims.ac.jp
6B	Martin-Puplett FT-FIR Michelson FT-IR	0.1 meV - 2.5 eV		Solid (Reflection, Absorption)	S. Kimura kimura@ims.ac.jp
7U	10m Normal Incidence (Modified Wadsworth)	6 eV - 40 eV		Solid (Photoemission)	S. Kimura kimura@ims.ac.jp
7B	3m Normal Incidence	1.2 eV - 25 eV		Solid (Reflection, Absorption)	M. Hasumoto hasumoto@ims.ac.jp
8B	Plane Grating	1.9 eV - 150 eV		Solid (Photoemission)	T. Nishi nishi@ims.ac.jp
FEL	Free Electron Laser	1.6 eV - 6.2 eV			M. Katoh mkatoh@ims.ac.jp
CSR	Coherent Synchrotron Radiation	5 meV - 0.5 meV			M. Katoh mkatoh@ims.ac.jp

* In-House Beamline

* Spherical Grating Monochromator with Translating and Rotating Assembly Including Normal incidence mount

BL1A

Soft X-Ray Beamline for Photoabsorption Spectroscopy

BL1A is a soft X-ray beamline for photoabsorption spectroscopy. The beamline is equipped with a focusing premirror and a double crystal monochromator [1]. The monochromator serves soft X-rays in the energy region from 585 to 4000 eV by using several kinds of single crystals such as β -Al₂O₃, beryl, KTP (KTiOPO₄), quartz, InSb, and Ge. The throughput spectra measured by a Si photodiode (AXUV-100, IRD Inc.) are shown in Fig. 1. Typical energy resolution ($E/\Delta E$) of the monochromator is about 1500 for beryl and InSb. There are no experimental setups specific of this beamline, except for a small vacuum chamber equipped with an electron multiplier (EM) detector. Photoabsorption spectra for powdery samples are usually measured in a total electron yield mode, with the use of the EM detector.

[1] Hiraya et al, Rev. Sci. Instrum. **63** (1992) 1264.

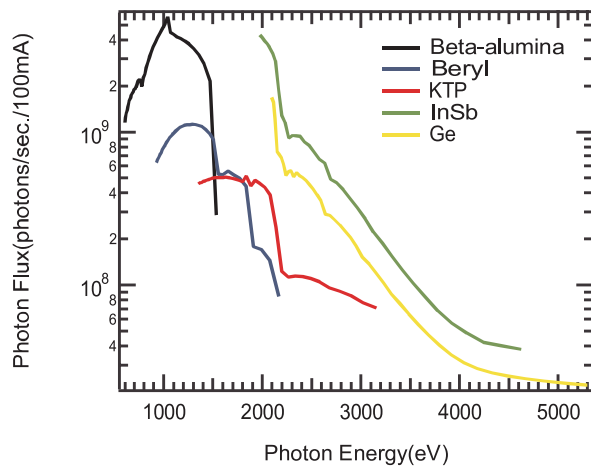


Fig. 1. Throughput spectra of the double crystal monochromator at BL1A.



Fig. 2. Side view of BL1A.

Beamline Specifications

Monochromator	Double crystal monochromator
Monochromator crystals: (2d value, energy range)	β -Al ₂ O ₃ (22.53 Å, 585-1609 eV), beryl (15.965 Å, 826-2271 eV), KTP (10.95 Å, 1205-3310 eV), quartz (8.512 Å, 1550-4000 eV), InSb (7.481 Å, 1764-4000 eV), Ge (6.532 Å, 2094-4000 eV)
Resolution	$E/\Delta E = 1500$ for beryl and InSb
Experiments	Photoabsorption spectroscopy

BL1B

Seya-Namioka Monochromator for General Purposes

BL1B has been constructed to perform various spectroscopic investigations such as absorption, reflectivity, and luminescence in condensed matters. This beamline consists of a pre-focusing mirror, a 1-m Seya-Namioka type monochromator, and post-focusing mirrors with different focal lengths. Three gratings of 600, 1200, and 2400 l/mm can cover the wavelength region ranging from 40 to 650 nm ($h\nu = 2 - 30$ eV). The post mirror with a longer focal length is usually used with an LiF window to separate the vacuum condition of the monochromator from a main experimental station, which make experiments for liquids and bio-specimens possible, while the other is mainly utilized for solid-state spectroscopy. The output flux from this monochromator is about 1010 photons/sec. around 200 nm with 0.1 mm slit openings. The spectral distributions for two gratings measured by a conventional photomultiplier are shown in Fig. 1. A second monochromator (Spex 270M) and a LN-cooled CCD detector (Princeton Inc.) are available for luminescence measurements, together with a liquid helium-flow type cryostat. To perform time-resolved experiments, a TAC system is also available.

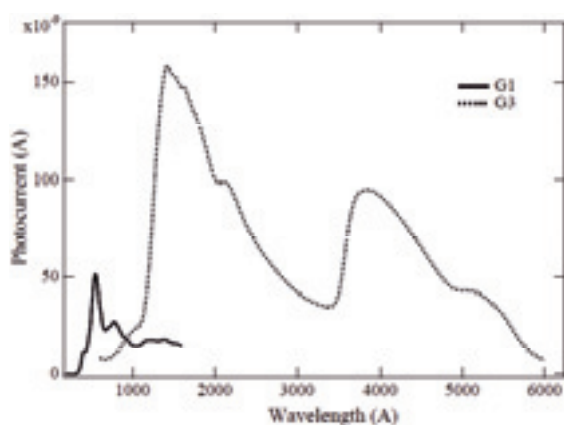


Fig. 1. Photocurrent at the sample position at BL1B.

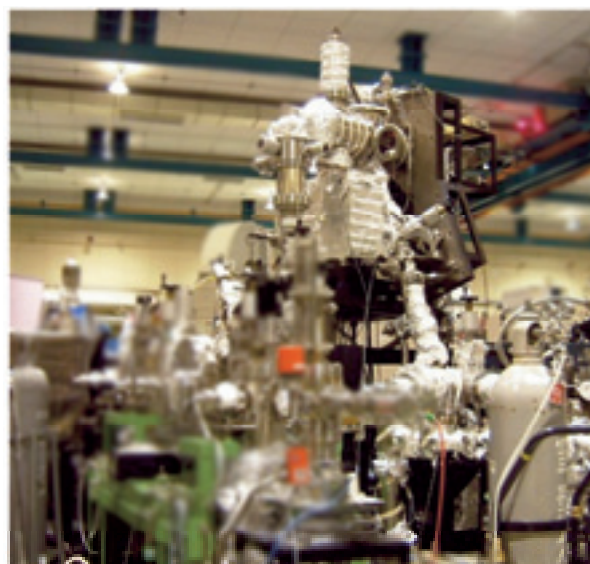


Fig. 2. Photo of BL1B..

Beamline Specifications

Monochromator	1-m Seya-Namioka type
Wavelength Range	40 to 600 nm (2-30 eV)
Resolution	$E/\Delta E \sim 1000$ at 100 nm (10 eV)
Experiments	Absorption, reflection, luminescence spectroscopy for solids

BL2B

Beamline for Gas Phase Photoionization and Reaction Dynamics

This beamline has been developed for the purpose of studying ionization, excitation and decay dynamics involving inner-valence electrons, $2p$ electrons of the third row atoms, and $4d$ electrons of the lanthanides. The monochromator is a spherical grating Dragon-type with 18-m focal length. High throughput (1×10^{10} photons s^{-1}) and high resolution ($E/\Delta E = 2000 - 8000$) are achieved simultaneously under the condition of the ring current of 100 mA [1]. The optical system consists of two prefocusing mirrors, an entrance slit, three spherical gratings (G1 - G3), two folding mirrors, a movable exit slit and a refocusing mirror [2]. The monochromator is designed to cover the energy range of 23 - 205 eV with the three gratings: G1 (2400 lines mm^{-1} , $R = 18$ m) at 80 - 205 eV; G2 (1200 lines mm^{-1} , $R = 18$ m) at 40 - 100 eV; G3 (2400 lines mm^{-1} , $R = 9.25$ m) at 23 - 50 eV. The percentage of the second-order light contamination at $h\nu = 45.6$ eV is 23 % for G2 or 7 % for G3.

We have been taking the yield curves of various fullerene ions [3]. Geometrical structures and electronic properties of fullerenes have attracted widespread attention because of their novel structures, novel reactivity, and novel catalytic behaviors as typical nanometer-size materials. However, spectroscopic information was very limited in the extreme UV region, owing to difficulties in acquiring enough amount of sample. This situation has been rapidly changed since the start of this century, because the techniques of syntheses, isolation, and purification have been advanced so rapidly that appreciable amount of fullerenes can be readily obtained.

[1] M. Ono, H. Yoshida, H. Hattori and K. Mitsuke, Nucl. Instrum. Meth. Phys. Res. A **467-468**, 577 (2001).

[2] H. Yoshida and K. Mitsuke, J. Synchrotron Radiation **5** (1998) 774.

[3] J. Kou, T. Mori, Y. Kubozono and K. Mitsuke, Phys. Chem. Chem. Phys. **7** (2005) 119.

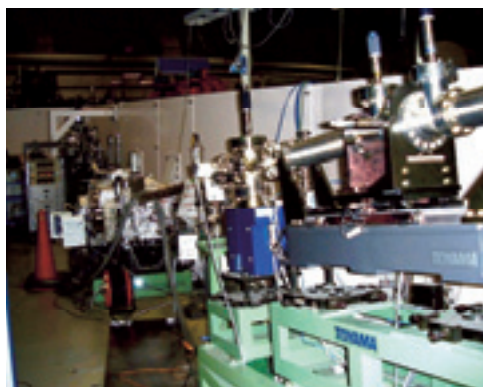


Fig. 1. 18-m spherical grating monochromator at BL2B.



Fig. 2. End station of BL2B for gas phase spectroscopy of refractory materials.

Beamline Specifications

Monochromator	18-m spherical grating Dragon-type
Wavelength Range	6 – 55 nm; 24-205 eV
Resolution	2000-8000 depending on the gratings
Experiments	Mass spectrom.; photoelectron spectrosc.; momentum imaging spectrosc.; e ⁻ -ion coincidence spectrosc.; fullerene beam source

BL3U

Varied-line-spacing Plane Grating Monochromator for Molecular Soft X-ray Spectroscopy

The beamline BL3U is equipped with an in-vacuum undulator composed of 50 periods of 3.8 cm period length. The emitted photons are monochromatized by the varied-line-spacing plane grating monochromator (VLS-PGM) designed for various spectroscopic investigations in the soft x-ray range including soft x-ray emission studies. Three holographically ruled laminar profile plane gratings are designed to cover the photon energy range from 60 eV to 800 eV. The beamline has two endstations, namely XES setup and Multi-purpose setup. The XES setup is used for soft x-ray emission spectroscopy. The beam is horizontally focused onto the sample position by plane-elliptical mirror, M2X. In the Multi-purpose setup, the beam is focused by the toroidal mirror M2. Between the sample position and M2, the differential pumping is placed.

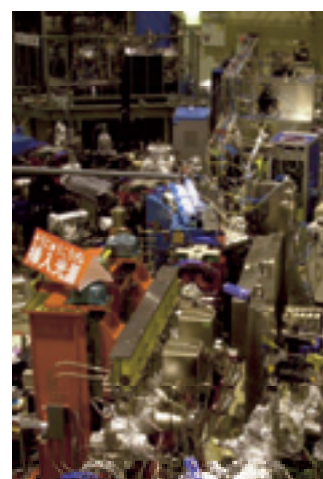
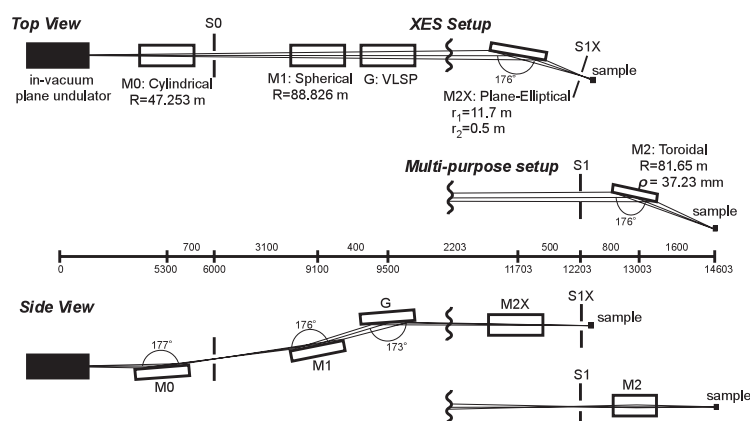


Fig. 1. Schematic layout (left) and the photography (right) of the BL3U. The distances along the beam from the center of the in-vacuum plane undulator are shown in mm. S1X and M2X can be replaced with the other exit slit S1 so that experiments can be carried out at either the XES or multi-purpose endstation. In the XES setup, the sample is placed at 5-10 mm downstream of S1X.

Beamline Specifications

Monochromator	Varied-line-spacing plane grating monochromator
Energy Range	60-800 eV
Resolution	$E/\Delta E > 10\,000$
Experiments	Soft X-ray spectroscopy (XPS, XES, XAS)
Beam Size (XES Endstation)	Gaussian shape Vertical 5-20 μm ; Horizontal 41 μm (FWHM)

BL4B

Varied-Line-Spacing Plane Grating Monochromator for Molecular Soft X-ray Spectroscopy

The beamline BL4B equipped with a varied-line-spacing plane grating monochromator (VLS-PGM) was constructed for various spectroscopic investigations in a gas phase and/or on solids in the soft X-ray range. Three holographically ruled laminar profile plane gratings with SiO₂ substrates are designed to cover the photon energy range from 25 eV to 800 eV. The gratings with the groove densities of 100, 267, and 800 1/mm cover the spectral ranges of 25-100, 60-300, and 200-1000 eV, respectively, and are interchangeable without breaking the vacuum. Fig. 1 shows the absolute photon flux for each grating measured by a Si photodiode (IRD Inc.), with the entrance- and exit-slit openings set at 50 and 50 μm , respectively. The maximum resolving power ($E/\Delta E$) achieved for each grating is more than 5000.

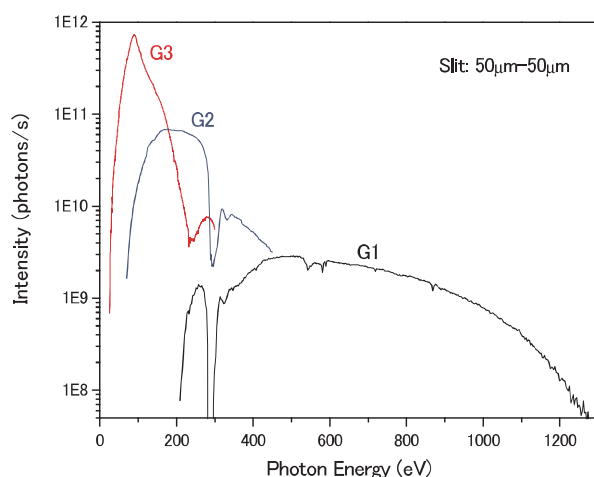


Fig. 1. Throughput from the VLS-PGM monochromator on BL4B.



Fig. 2. Photo of BL4B.

Beamline Specifications

Monochromator	Varied-line-spacing Plane Grating Monochromator
Energy range	25-1000 eV
Resolution	$E/\Delta E > 5000$ (at maximum)
Experiments	Soft X-ray spectroscopy (mainly, angle-resolved photoion spectroscopy for gaseous targets and photoelectron spectroscopy for gaseous and solid targets)

BL5U

Photoemission Spectroscopy of Solids and Surfaces

This beamline is designed for a high-resolution angle-resolved photoemission study on solids and surfaces with horizontal-linearly and circularly (CW, CCW) polarized synchrotron radiation from a helical undulator. The beamline consists of a Spherical Grating Monochromator with Translational and Rotational Assembly Including a Normal incidence mount (SGM-TRAIN), and a high-resolution angle-resolved photoemission spectrometer.

The SGM-TRAIN is an improved version of a constant-length SGM to aim the following points; (1) covering the wide energy range of 5-250 eV, (2) high energy resolving power, (3) use of linearly and circularly polarized undulator light, (4) reduction of higher order light, and (5) two driving modes (rotation and translation of gratings) by computer control. The second-order light is well suppressed by using laminar profile gratings and combinations of mirrors and gratings.

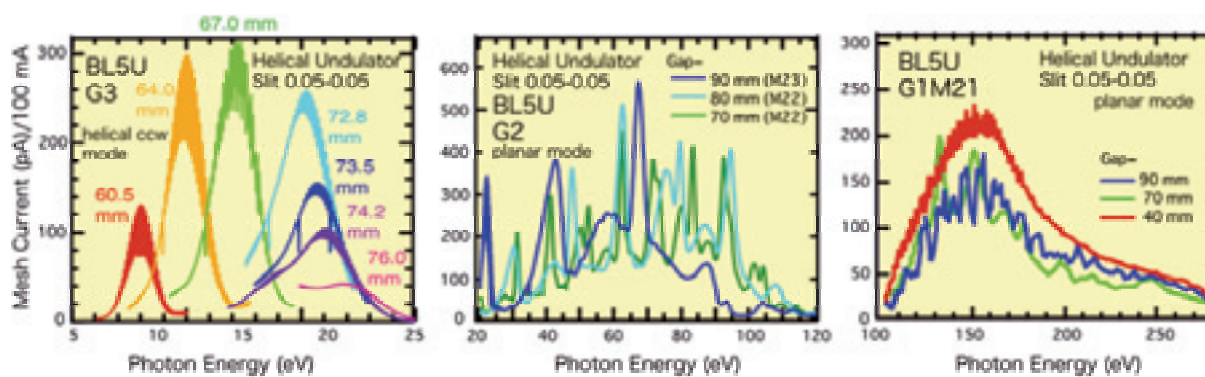


Fig. 1. Throughput spectra from the SGM-TRAIN monochromator at BL5U.

Beamline Specifications

Monochromator	SGM-TRAIN
Energy Range	5-250 eV
Resolution	$h\nu/\Delta E > 2,000$ for $< 40\mu\text{m}$ slits
Experiment	ARPES, AIPES, XAS
Flux	$< 10^{11}$ photons/s for $< 40\mu\text{m}$ slits (at the sample position)
Main Instruments	Hemispherical photoelectron analyzer (MBS-Toyama 'Peter' A-1), LEED of reverse type (OMICRON), Liq-He flow cryostat (5 – 400 K)

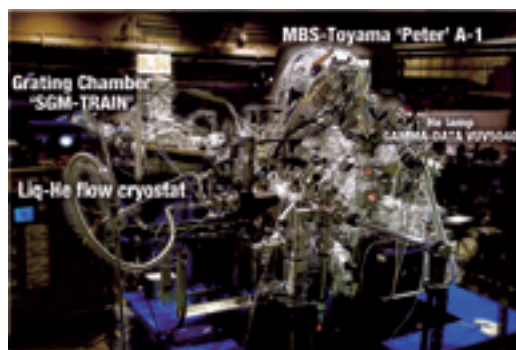


Fig. 2. High-resolution angle-resolved photoemission apparatus at BL5U.

BL5B

Calibration Apparatus for Optical Elements and Detectors

BL5B has been constructed to perform calibration measurements for optical elements and detectors. This beamline is composed of a plane grating monochromator (PGM) and three end stations in tandem. The most upstream station is used for calibration measurements of optical elements, the middle one for optical measurements for solids and the last for photo-stimulated desorption experiments. The experimental chamber at the most downstream station is sometimes changed to a chamber for photoemission spectroscopy. The calibration chamber shown in Fig. 2 is equipped with a goniometer for the characterization of optical elements, which has six-degree-of-freedom; X-Y translation of a sample, and interchange of samples and filters. These are driven by pulse motors in vacuum. Since the polarization of synchrotron radiation is essential for such measurements, the rotation axis can be made in either horizontal or vertical direction (s- or p-polarization).

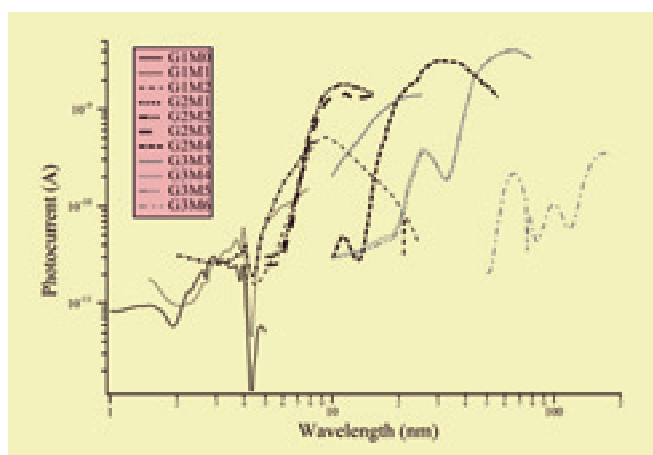


Fig. 1. Throughput spectra for possible combinations of gratings and mirrors at BL5B measured by a gold mesh.



Fig. 2. A side view of the experimental chamber for calibration measurements.

Beamline Specifications

Monochromator	Plane Grating Monochromator
Energy range	6-600 eV (2-200 nm)
Resolution	$E/\Delta E \sim 500$
Experiments	Calibration of optical elements, absorption of solids, photo-stimulated desorption from rare gas solids

BL6U

Variable-Included-Angle VLS-PGM for Molecular Soft X-ray Spectroscopy

The beamline BL6U equipped with a variable-included-angle Monk-Gillieson mounting monochromator with a varied-line-spacing plane grating was constructed for various spectroscopic investigations requiring high-brilliance Soft X-rays in a gas phase and/or on solids. By a combination of undulator radiation and the sophisticated monochromator design (entrance slit-less configuration and variable-included-angle mechanism), with using one single grating, the monochromator can cover the photon energy ranging from 30 to 500 eV, with the resolving power higher than 10000 and the photon flux more than 10^{10} photons/sec. Figure 1 shows an example of the monochromator throughput spectra measured by using a Si photodiode, with the exit-slit opening set at $30\ \mu\text{m}$, which corresponds to the theoretical resolving power of 10000 at 80 eV.

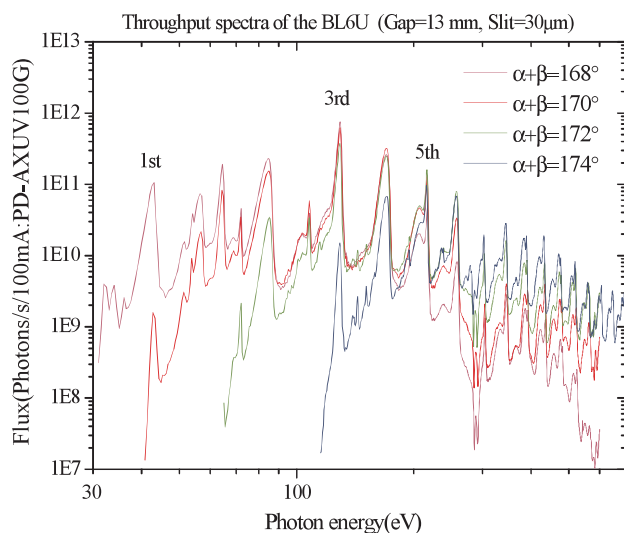


Fig. 1. Throughput spectra of the BL6U monochromator at various included angles.



Fig. 2. Photo of BL6U

Beamline Specifications

Monochromator	Variable-Included-Angle Varied-line-spacing Plane Grating Monochromator
Energy range	40-500 eV
Resolution	$E/\Delta E > 10000$ (at maximum)
Experiments	High-Resolution Soft X-ray spectroscopy (mainly, photoelectron spectroscopy for gaseous and solid targets)

BL6B (IR)

Infrared and Terahertz Spectroscopy of Solids

SR has a good performance (high brilliance and high flux) not only in the VUV and SX regions but also in the infrared (IR) and terahertz (THz) regions. BL6B covers in the IR and THz regions. The previous beamline BL6A1 that has been constructed in 1985 is the pioneer of the infrared SR research. The beamline was quitted at the end of FY2003 and a new IR/THz beamline, BL6B (IR), was constructed in FY2004. The front-end part including the bending duct #6 was replaced to a new one with higher acceptance angle ($215 \text{ (H)} \times 80 \text{ (V)} \text{ mrad}^2$) using a magic mirror as shown in Fig. 1 [1]. The brilliance and photon flux at the sample were highly improved.

The beamline is equipped with two interferometers, one is Michelson-type (Bruker Vertex 70v) and the other Martin-Puplett-type (JASCO FARIS-1), to cover the wide spectral region from 5 to 30,000 cm^{-1} ($h\nu = 0.6 \text{ meV} - 3.7 \text{ eV}$) as shown in Fig. 2. There are two end-stations; one is reflection/absorption spectroscopy for large samples (\sim several mm) and the other IR/THz microscopy for tiny samples (\sim several ten μm).

[1] S. Kimura, E. Nakamura, T. Nishi, Y. Sakurai, K. Hayashi, J. Yamazaki and M. Katoh, *Infrared Phys. Tech.* **49** (2006) 147.

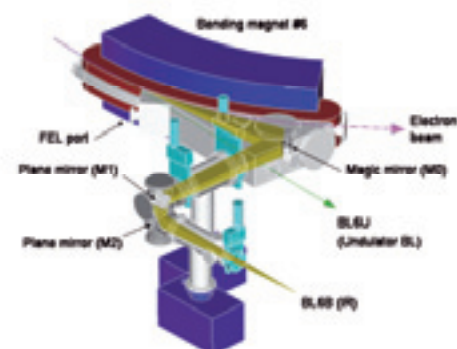


Fig. 1. The design of optics and front end of BL6B.

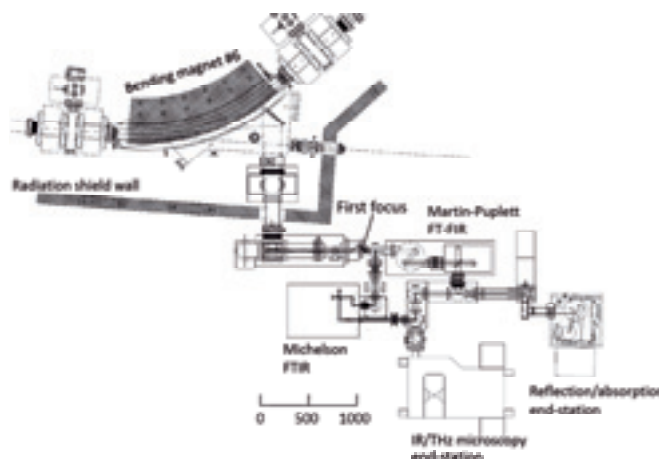


Fig. 2. Schematic figure of top view of BL6B.

Beamline Specifications

Interferometer	Michelson (Bruker Vertex 70v), Martin-Puplett (JASCO FARIS-1)
Wavenumber Range (Energy range)	5 – 30,000 cm^{-1} (0.6 meV – 3.7 eV)
Resolution in cm^{-1}	0.1 cm^{-1} for IFS66v 0.25 cm^{-1} for FARIS-1
Experiments	Reflectivity and transmission, microspectroscopy, and magneto-optics
Miscellaneous	User can bring their experimental system in this beamline

BL7U (SAMRAI)

Angle-Resolved Photoemission of Solids in the VUV Region

The beamline 7U, named Symmetry And Momentum Resolved electronic structure Analysis Instrument (SAMRAI) for functional materials, was constructed to provide the photon flux with high energy resolution and high flux mainly for high-resolution angle-resolved photoemission spectroscopy of solids. An APPLE-II-type variable polarization undulator is equipped for the light source. The undulator can make high intense VUV light with horizontal/vertical linear and right/left circular polarization. The undulator light is monochromatized by the modified Wadsworth-type monochromator with three gratings ($R = 10$ m; 1200, 2400 and 3600 lines/mm optimized at $h\nu = 10, 20,$ and 33 eV). The energy resolution of light ($h\nu/\Delta h\nu$) is more than 10^4 with the photon flux of more than $10^{11} - 10^{12}$ ph/s on samples in the whole energy region.

The beamline has a photoemission end-station which equips a 200-mm-radius hemispherical photoelectron analyzer (MB Scientific AB, A-1 analyzer) with a wide-angle electron lens and a liquid-helium-cooled cryostat with a 6-axes pulse motor control (A-VC Co. Ltd., i-GONIO). The main purpose is to determine the three-dimensional Fermi surface and electronic structure of solids at low temperatures and their temperature dependence to reveal the origin of the physical properties.

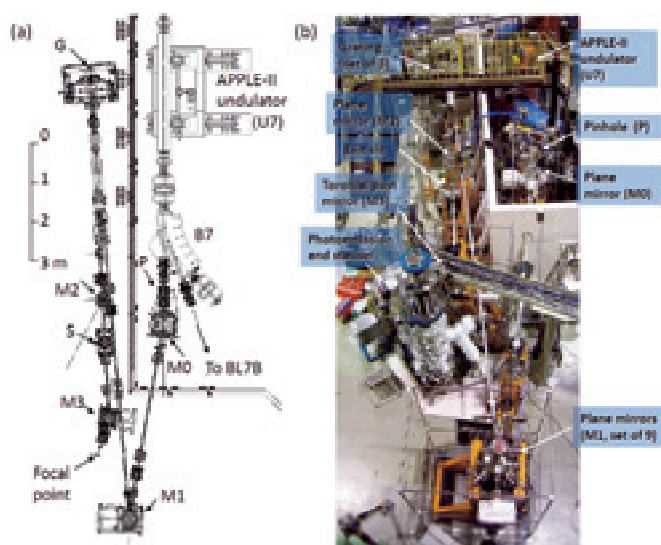


Fig. 1. Layout (a) and photograph (b) of the SAMRAI beamline consisting of the APPLE-II type undulator (U7), the modified Wadsworth type monochromator (M0 – S), and the high-resolution photoemission analyzer at the focal point. The monochromator, mainly has five optical components: two plane mirrors (M0 and M1) with water cooling, one set of three spherical gratings (G), an exit slit (S), and one toroidal refocusing mirror (M3). The spherical gratings with a radius of 10 m are located 22 m from the center of the undulator. There is no entrance slit. S is located 6.47 m from G. A second branch for a VUV microscope end station is planned to be constructed after the plane mirror (M2) located between G and S.

Beamline Specifications

Light source	APPLE-II type undulator ($\lambda_u = 76\text{mm}, N = 36$)
Monochromator	10-m Normal Incidence Monochromator (modified Wadsworth-type)
Photon energy range	6 ~ 40 eV ($\lambda = 30 \sim 200$ nm)
Resolution ($h\nu/\Delta h\nu$)	$1 \times 10^4 \sim 5 \times 10^4$
Photon flux on sample	$\geq 10^{12} - 10^{11}$ ph/s (depend on $h\nu$)
Beam size on sample	$200(\text{H}) \times 50(\text{V}) \mu\text{m}^2$
Experiments	Angle-resolved photoemission of solids (MB Scientific A-1 analyzer)

BL7B

3-m Normal Incidence Monochromator for Solid-State Spectroscopy

BL7B has been constructed to provide sufficiently high resolution for conventional solid-state spectroscopy, enough intensity for luminescence measurements, a wide wavelength coverage for Kramers-Kronig analyses, and the minimum deformation to the polarization characteristic of the incident synchrotron radiation. This beamline consists of a 3-m normal incidence monochromator which covers the vacuum ultraviolet, ultraviolet, visible and infrared, *i.e.* the wavelength region of 40 -1000 nm, with three gratings (1200, 600, and 300 l/mm). Two interchangeable refocusing mirrors provide two different focusing positions. For the mirror with the longer focal length, an LiF or a MgF₂ window valve can be installed in between the end valve of the beamline and the focusing position. Figure 1 shows absolute photon intensity for each grating with the entrance and exit slit openings of 0.5 mm. A silicon photodiode (AXUV-100, IRD Inc.) was utilized for measuring the photon intensity and the absolute photon flux was estimated, taking the quantum efficiency of the photodiode into account.

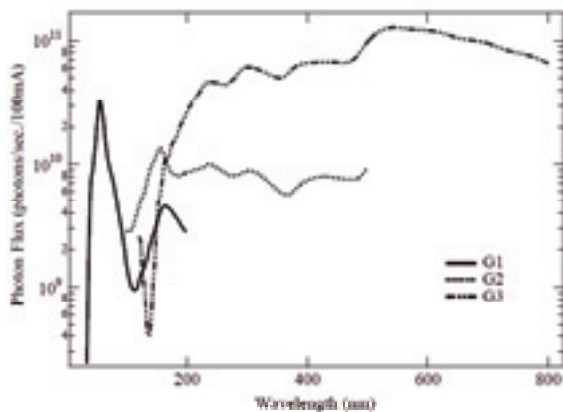


Fig. 1. Throughput spectra of BL7B measured by a silicon photodiode.



Fig. 2. Photo of BL7B.

Beamline Specifications

Monochromator	3-m Normal Incidence Monochromator
Wavelength Range	50 to 1000 nm (1.2 - 25 eV)
Resolution	$E/\Delta E = 4000 - 8000$ for 0.01 mm slits
Experiments	Absorption, reflection, fluorescence spectroscopy, mainly for solids

BL8B

Angle-Resolved Ultraviolet Photoelectron Spectrometer for Solids

BL8B is a beamline for angle-resolved ultraviolet photoemission spectroscopy (ARUPS) system which is designed for measuring various organic solids such as molecular crystals, organic semiconductors, and conducting polymers. This beamline consists of a plane-grating monochromator (PGM), a sample preparation chamber with a fast entry Load-Lock chamber, a measurement chamber with an accurate for temperature dependence (base pressure 1×10^{-10} Torr), a cleaning chamber (base pressure 1×10^{-10} Torr), and a sample evaporation chamber (base pressure 3×10^{-10} Torr). The cleaning chamber is equipped with a back-view LEED/AUGER, an ion gun for Ar^+ sputtering, and an infrared heating unit. The PGM consists of premirrors, a plane grating, focusing mirror, and a post-mirror, with an exit slit. It covers the wide range from 2 to 130 eV with exchanging two gratings (G1: 1200l/mm, G2: 450l/mm) and five cylindrical mirrors. The toroidal mirror focuses the divergent radiation onto the sample in the measurement chamber. The spot size of the zeroth-order visible light at the sample surface is about $1 \times 1 \text{ mm}^2$. Figure 1 shows the throughput spectra of PGM (slit=100 μm). The energy resolution at a slit width of 100 μm was found to be $E/\Delta E = 1000$ in the wavelength range from 2 to 130 eV. A hemi-spherical electron energy analyzer of 75 mm mean radius with an angular resolution less than 2° can be rotated around vertical and horizontal axes. The sample mounted on a manipulator can be also rotated around two axes.

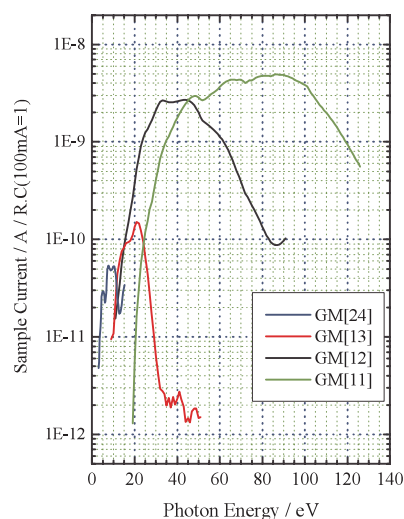


Fig. 1. Throughput spectra of plane-grating monochromator at BL8B2 (slit=100 μm).



Fig. 2. A photo of BL8B2.

Beamline Specifications

Monochromator	Plane-grating monochromator
Wavelength Range	9- 600 nm
Resolution	$E/\Delta E = 1000$
Experiments	Angle-resolved ultraviolet photoemission spectroscopy

FEL

Free Electron Laser

The free electron laser (FEL) at UVSOR-II is parasitically installed at BL5U. The FEL is equipped with a variably polarized optical klystron of 2.35 m long and an optical cavity of 13.3 m long. By using various multi-layer mirrors for the cavity, the FEL can provide coherent light in a wide wavelength range from 800 nm to 199 nm. The pulse width is typically several picoseconds. The repetition rate is about 11 MHz. The average output power depends on the wavelength but its typical value is several 100 mW. The output power higher than 1W was recorded at 230 nm and 570 nm. The FEL can be operated with the top-up injection mode. The users can use the FEL for several hours with quasi constant output power. The laser pulses are naturally synchronized with the synchrotron radiation pulses which are provided at other synchrotron radiation beam-lines. The laser beam can be transported to the beam lines by using a mirror system for pump and probe experiments if requested.

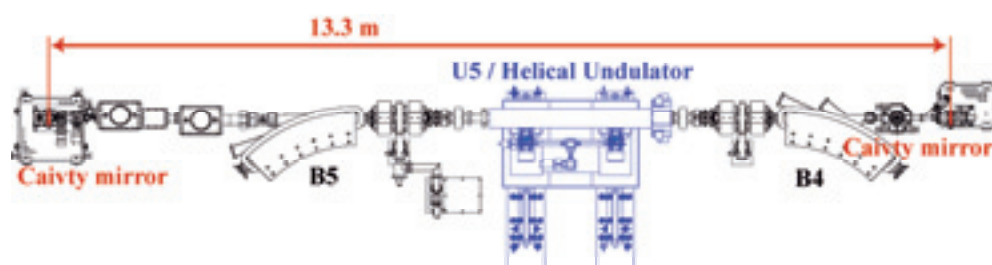


Fig. 1. The schematic of the 13.3-m long optical cavity.

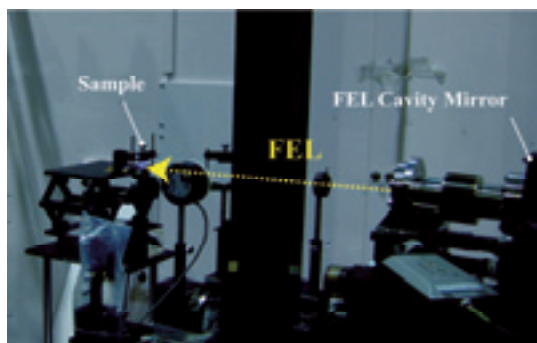


Fig. 2. Left and right circular polarized FEL is delivered to B4.

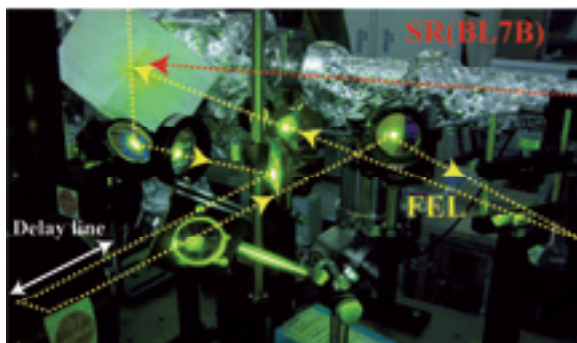


Fig. 3. The FEL is delivered to BL7B. The FEL is irradiated on a target simultaneously with the SR.

FEL Specifications

Wavelength	199-800 nm
Spectral Band Width	$\sim 10^{-4}$
Polarization	Circular / Linear
Pulse Rate	11.26 MHz
Max. Average Power	~ 1 W
Cavity Type	Fabry-Perot
Cavity Length	13.3 m
Cavity Mirror	HfO ₂ , Ta ₂ O ₅ , Al ₂ O ₃ multi-layer

Light Sources

Observation of Transverse-Longitudinal Coupling Effect at UVSOR-II

M. Shimada¹, M. Katoh^{2,3}, M. Adachi^{2,3}, T. Tanikawa³, S. Kimura^{2,3},
M. Hosaka⁴, N. Yamamoto⁴, Y. Takashima⁴ and T. Takahashi⁵

¹High Energy Accelerator Research Organization, KEK, Tsukuba 305-0801, Japan

²UVSOR Facility, Institute for Molecular Science, Okazaki 444-8585, Japan

³School of Physical Sciences, The Graduate University for Advanced Studies (SOKENDAI),
Okazaki 444-8585, Japan

⁴Graduate School for Engineering, Nagoya University, Nagoya 464-8603, Japan

⁵Research Reactor Institute, Kyoto University, Kumatori-cho 590-0494, Japan

Coherent synchrotron radiation (CSR) emits from the longitudinal dip-structure of radiation wavelength scale. We have demonstrated the measurements of CSR by the technique called ‘laser bunch slicing’ since 2005 [1] and succeeded in emission of the quasi-monochromatic CSR from the bending magnet using the amplitude-modulated laser pulse [2]. In this paper, the turn-by-turn CSR signal is observed by the Schottky diode detector for terahertz range with a time response of a few hundred pico-second [3]. The detector is prepared with three different frequency range. The UVSOR-II electron storage ring was operated with three electron beam optics, the normal optics, and the two low-alpha optics with different betatron tunes of 3.53 and 3.68. Since the tune is close to the half and third resonances, we refer to the latter two as low-alpha (1/2) and low-alpha (1/3) optics.

Figure 1 shows the CSR signals in two low-alpha optics. With the low alpha (1/2) optics, as shown in Fig.1 (a) - (c), the CSR is intense at every other turns. In the middle and high-frequency ranges, it is intense at the first and third arrivals. At the low-frequency range, it could be observed up to the 11th arrival. Although the CSR at the third and fifth arrivals is intense, that of the first arrival is weak.

In the low-alpha (1/2) optics, the betatron tune is close to a half integer. Thus, the intermittent CSR emission was expected to be related to the betatron motion. To confirm this, we tried the same experiment with the low-alpha (1/3) optics. Because of the limited beam time, CSR was observed only at the middle frequency range. The result is shown in Fig. 1 (d). The CSR is intense at every third arrival, the first and fourth. Weak CSR is also observed at the seventh arrival, despite the absence of CSR at the fifth and sixth.

For normal optics, although the results are not shown here, the CSR at the first arrival was detected by all three detectors.

We have observed the transverse-longitudinal coupling effect in laser bunch slicing by measuring the THz CSR turn by turn with ultra-fast diode detectors. The results were in good agreement with the numerical simulation based on linear beam dynamics theory.

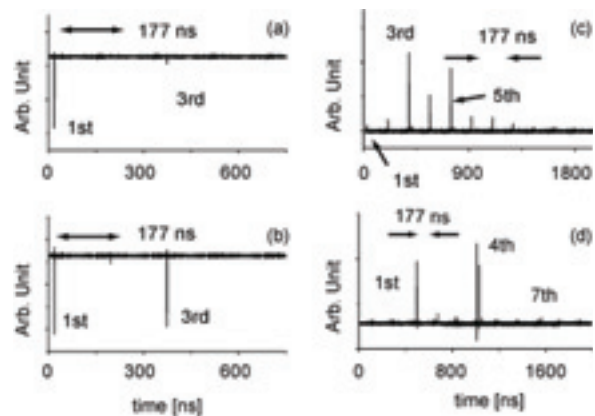


Fig. 1. CSR signals of three diode detectors at the low-alpha optics. Revolution time of the ring is 177 ns. (a), (b), and (c) are with the low-alpha (1/2) optics. Sensitivity ranges are (a) 11.0 - 16.6 cm^{-1} , (b) 7.3 - 11.0 cm^{-1} , and (c) 3.7 - 5.7 cm^{-1} . (d) is with low-alpha (1/3) optics. Sensitivity range is 7.3 - 11.0 cm^{-1} .

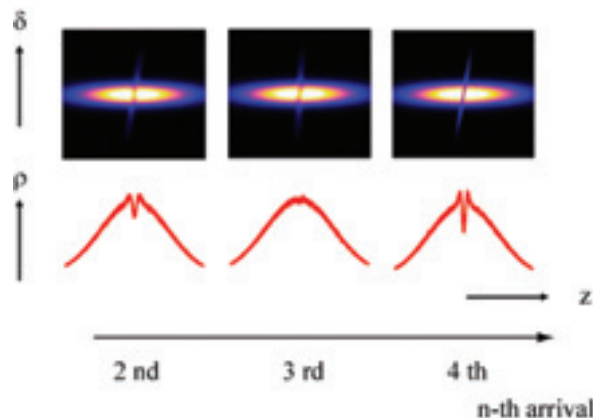


Fig. 2. An example of evolution of fragments and a dip structure in longitudinal phase space (upper) and its corresponding longitudinal density distribution (lower). The horizontal axis is an arrival order after the revolutions

[1] M. Shimada *et al.*, Jpn. J. Appl. Phys. **46** (2007) 7939.

[2] S. Bielawski *et al.*, Nat. Phys. **4** (2008) 390.

[3] M. Shimada *et al.* Phys. Rev. Lett. **103** (2009) 144802.

Measurement of Betatron Oscillation Amplitude Excited by RF Knockout at UVSOR-II

Y. Furui^{1,2}, M. Hosaka¹, N. Yamamoto¹, Y. Takashima¹, M. Adachi², H. Zen² and M. Katoh²
¹Graduate School of Engineering, Nagoya University, Nagoya, 464-8603 Japan
²UVSOR Facility, Institute for Molecular Science, Okazaki 444-8585 Japan

Abstract

In order to measure the betatron tune, we need to stimulate betatron oscillations. We measured betatron oscillation amplitudes stimulated by an RF knockout, by using a turn-by-turn beam position measuring technique. The results were compared with simulations. It was found that the non-linear effect of sextupole magnets produces a saturation effect on the betatron oscillation amplitude.

Experimental and Calculation

The electron beam circulating in the UVSOR-II storage ring was stimulated by the RF knockout system. The signals from a beam position monitor were processed by a high-speed digital oscilloscope (5GS/s). The beam position was measured turn by turn.

We simulated the betatron oscillation by transfer matrix calculation. This simulation includes the radiation damping, the kicks by the RF knockout, and the non-linear effect of sextupole magnets.

The kick angle of the RF knockout is based on the simulation using electromagnetic field analysis software, POISSON. Figure 1 shows the cross section of the RF knockout chamber at UVSOR-II and the magnetic field lines. In this case, magnetic field is generated for stimulating horizontal betatron oscillation.

The effect of sextupole magnets was included as using the following expression:

$$x'_{n+1} = x'_n + kx_n^2$$

where x_n is beam position at n-th turn, x'_n is beam angle at n-th turn, and k is a constant proportional to the sextupole field strengths which were determined to make the chromaticity zero.

Results and Discussion

Figure 2 shows simulated beam position at the beam position monitor turn by turn. After the betatron oscillation is excited very quickly within 7×10^4 turns, the amplitude is decreasing for the following 10^6 turns owing to the radiation damping and amplitude-dependent tune shift produced by sextupole magnets. Then the amplitude becomes constant. Figure 3 shows the measured and calculated horizontal betatron oscillation amplitude versus the electric power fed to the RF knockout. As the electric power is increasing, the amplitude is also increasing. However, the amplitude tends to saturate. We think

this is due to the non-linear effect of the sextupole magnetic fields. The measurement agrees well with the simulation results when the sextupole effect is included. This result indicates that it is essential to consider the non-linear effects of the sextupole magnets in the design of an RF knockout system.

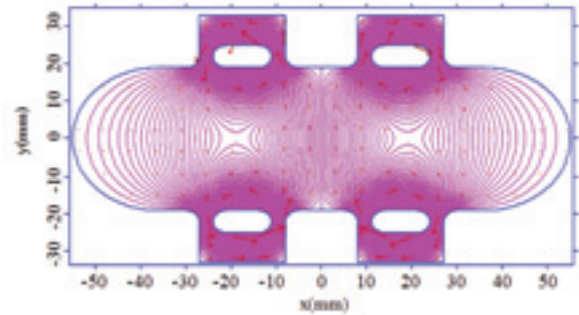


Fig. 1. Form of RF knockout chamber at UVSOR-II and magnetic field lines (magenta lines).

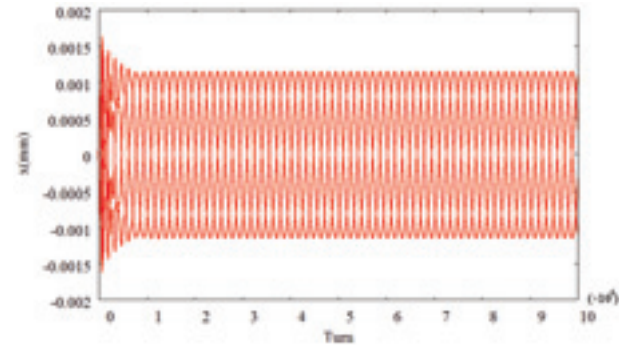


Fig. 2. Simulated horizontal beam position from center of BPM chamber every turn.

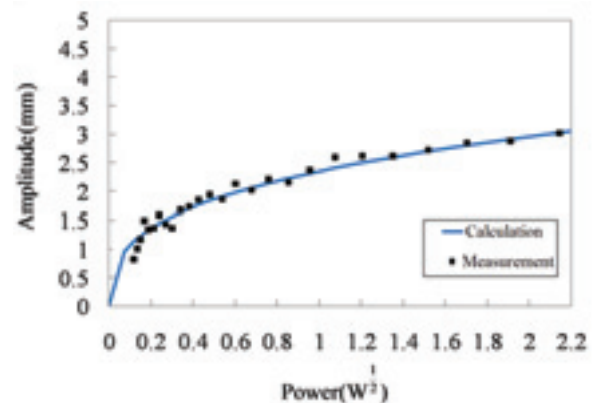


Fig. 3. Measured and calculated horizontal betatron oscillation amplitude to power.

Distribution of Injection Signal for Synchrotron Radiation Beam Lines

K. Hayashi, M. Katoh, M. Adachi, H. Zen and J. Yamazaki

UVSOR Facility, Institute for Molecular Science, Okazaki 444-8585, Japan

At UVSOR, so-called top-up operation was started in October 2008 [1]. The status of top-up operation at UVSOR is described elsewhere in this report. The test top-up operation has been held every Thursday night. It was revealed that user experiments were affected by beam injection at some beamlines. Especially, the effect was critical at BL6B, with FT-IR spectrometers.

Currently, the injection bump orbit is not closed in normal injection condition, because of the insufficiency of the current sources for the bump magnets. As consequence of bump leakage, large transverse oscillation of the beam occurs at all position of the storage ring.

Sufficient suppression of the oscillation is costly and need time. So we decided to distribute the signals that indicate whether beam injection is under way or not. Beamline users can neglect or stop acquiring data so as to get rid of the effect of beam injection. The signal is simple DC high/low (5V/0V) voltage, generated at the injection control system and distributed through a distribution board. The board is shown in Fig. 1.

At present, beam injection is held every minute, being continued at 1Hz until the beam current exceed the desired beam current, usually 300 mA for multi-bunch mode. We prepared for three types of signals: “short”, “long” and “long with prior notice”. They are described in Fig. 2. The “long” signal includes the whole period including all injection shots. The “Long with prior notice” signal is similar to “long” signal, but it goes high (+5V) several seconds before injection starts. On the other hand, the “short” signal rise up and go down at every shot, with controllable width.

The first application of the injection signal was done at BL3U [2]. The result is shown in Fig. 3. The spectrum has some spike without utilizing signals. The spikes on the spectrum disappear employing the “long” signal, stopping the data acquisition while beam injection is under way.

We have distributed the beam injection signal to desired beamlines. At BL6B, one of the FT-IR spectrometers has upgraded to utilize the beam injection signal [3]. The top-up operation is going to be the standard operation mode at UVSOR in FY2010.

[1] K Hayashi *et al.*, UVSOR Activity Report 2008 (2009) 35.

[2] M. Nagasaka, private communication.

[3] S. Kimura, private communication.

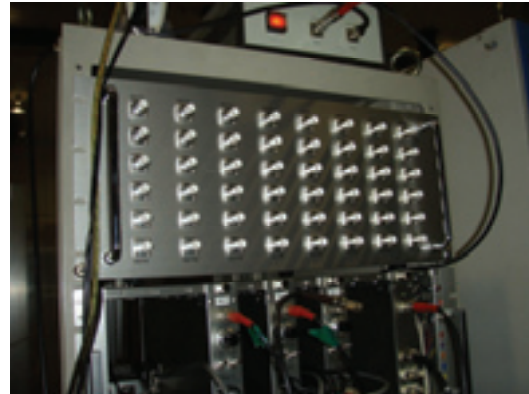


Fig. 1. Distribution board for injection signal.

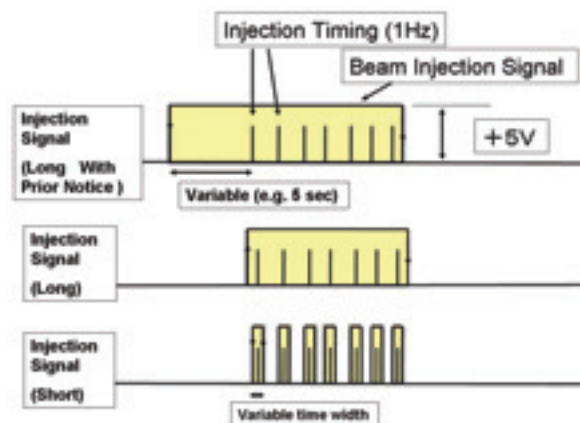


Fig. 2. Scheme of beam injection signals.

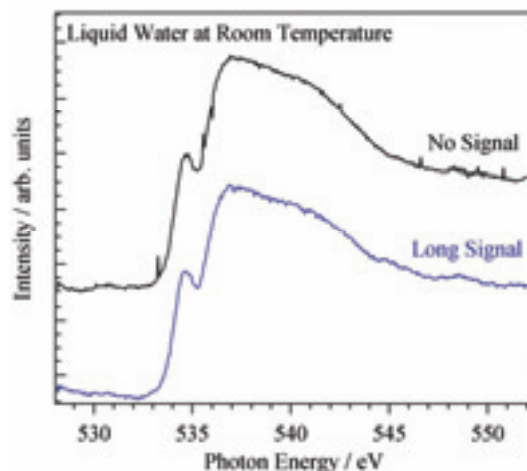


Fig. 3. Result of first application of beam injection signal (O K-edge X-ray absorption spectrum for liquid water).

Development of Turn-by-Turn BPM System at UVSOR-II

A. Nagatani¹, Y. Takashima¹, M. Hosaka¹, N. Yamamoto¹, K. Takami¹,
M. Katoh^{2,1}, M. Adachi², H. Zen² and K. Hayashi²

¹Graduate School of Engineering, Nagoya University, Chikusa-ku Nagoya 464-8603, Japan
²UVSOR Facility, Institute for Molecular Science, Okazaki 444-8585, Japan

Abstract

Recently, top up operation that keeps beam current constant began in the UVSOR storage ring. This operation temporally affects the beam orbit during beam injection. Therefore, a system that can measure the temporal orbit change was required to improve the operation. We have developed a TBT (Turn By Turn) BPM system and succeeded in measuring a bump orbit of a stored beam and an injection beam orbit by using this system for the first time at UVSOR-II.

TBT BPM system

The TBT BPM system consists of a high sampling rate digital oscilloscope (5 GHz/s), a high frequency amplifier and a waveform processing circuit between a BPM electrode and the oscilloscope. The direct signal from the electrode was found to be too fast to measure the signal peak voltage precisely under a limited sampling rate of the oscilloscope. Therefore we have developed a simple waveform processing circuit to make the pulse duration longer and broaden the signal peak. The diagram is shown in Fig. 1. We estimated the relative accuracy of the system via a repetitive measurement of a stable stored beam orbit. Figure 2 shows histograms of distribution of measured deviation from the averaged beam position. Standard deviations of 10 μm in horizontal and 50 μm in vertical have been obtained.

Measurements

We measured a bump orbit of the stored beam and an injection beam orbit using the TBT system. For the measurement, we used B1U BPM and set the oscilloscope low pass filter at 200 MHz.

Figure 3 shows the horizontal bump orbit measured using the system and a calculated one. The maximum value of the amplitude was 18 mm at the BPM. As shown in the figure, measured orbit agreed very well with the numerical result.

Figure 4 shows an injection beam orbit. The initial amplitude of the betatron oscillation was 20.1 mm. The oscillation was damped with a time scale of milliseconds. A vibration with a periodicity of about 20 kHz is accompanied with it.

Conclusion

We have developed a TBT BPM system which was composed of commercial products like the high frequency amplifier, the wave processing circuit and the digital oscilloscope. We confirmed the performance of this system. The measuring accuracy

of tens of microns in both horizontal and vertical direction is sufficient for TBT measurement. A bump orbit of a stored beam and an injected beam orbit were measured for the first time at UVSOR-II and the effectiveness of the system was demonstrated. The TBT system will be used for reducing the injection effect for user experiments.

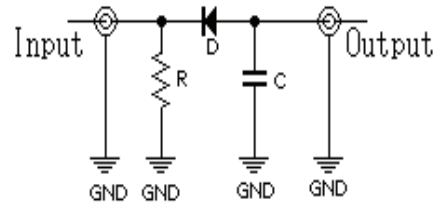


Fig. 1. Diagram of waveform processing circuit.

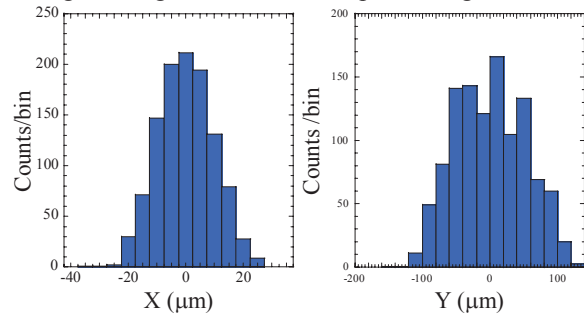


Fig. 2. Accuracy of this system (left shows horizontal right shows vertical).

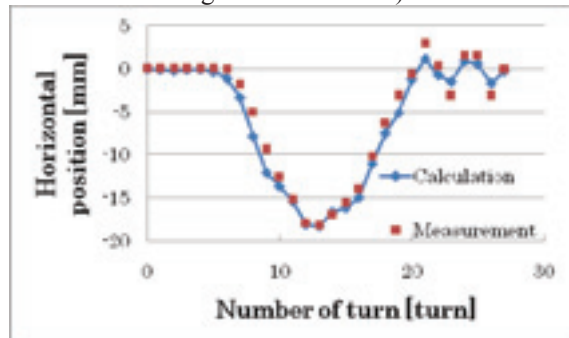


Fig. 3. Measured bump orbit compared with numerical one.

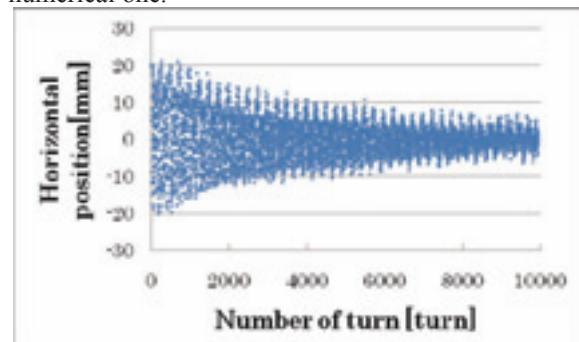


Fig. 4. Injection beam orbit measured by TBT system.

Stabilization of the Electric Septum of UVSOR-II Injector

H. Zen, K. Hayashi, J. Yamazaki, M. Adachi and M. Katoh
UVSOR Facility, Institute for Molecular Science, Okazaki 444-8585, Japan

Introduction

Top-up test runs was started in 2008. As the results of the test runs, the stored beam current was kept almost constant at 300 mA (see Fig. 1). The electron beam is injected for about 10 second every one minute with the repetition rate, 1 Hz. As shown in Fig. 1, sometimes stored beam current gets smaller than 300 mA even with top-up injection. The beam current reduction is due to reduction of injected beam charge caused by reduction of accelerated beam charge in the UVSOR-II injector. For keeping the constant beam current, operational condition of the injector should be stabilized. From long operational experience, we have recognized that the voltage fluctuation of the electric septum equipped in the injector is the most significant source of the fluctuation of the accelerated charge. In this fiscal year, we introduced a computer based control system to stabilize the septum voltage.

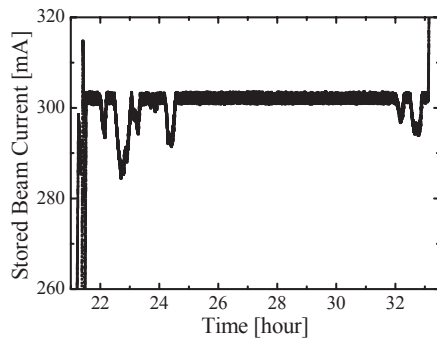


Fig. 1. Time trend of the stored beam current in the UVSOR-II storage ring.

Computer Based Stabilization System

Schematic drawing of the computer based stabilization loop is shown in Fig. 2. The pulsed voltage waveforms of the electric septum are measured by an oscilloscope and the waveform data are sent to the control PC. From the waveform and its time trend, the set value of a high voltage power supply for the septum is determined based on PID

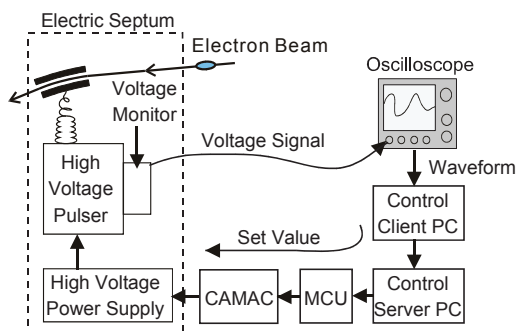


Fig. 2. Schematic drawing of the computer based stabilization loop.

algorithm by a control client PC. The PID determination of the set value is done by a program developed on LabView (shown in Fig. 3). The set value is sent to the power supply via a server PC, multi-control unit (MCU) and CAMAC modules.

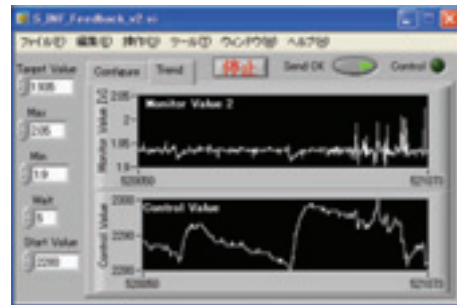


Fig. 3. The program for determining the set value of the electric septum used for the UVSOR-II injector.

Results

Demonstration experiment to check the effect of the developed system was carried out and the result is shown in Fig. 4. With the system, the septum voltage was kept constant and the accelerated charge in the injector is not so much fluctuated. While the stabilization system was turned off, the septum voltage gradually increased and the accelerated charge rapidly decreased. It was found that the stabilization system was really effective to compensate the fluctuation of septum voltage. The stabilization system is now usually used during user operation. And then we found another source of fluctuation, fluctuation of klystron output power which is used for driving a 15 MeV linac in the injector. The klystron fluctuation will be stabilized near future.

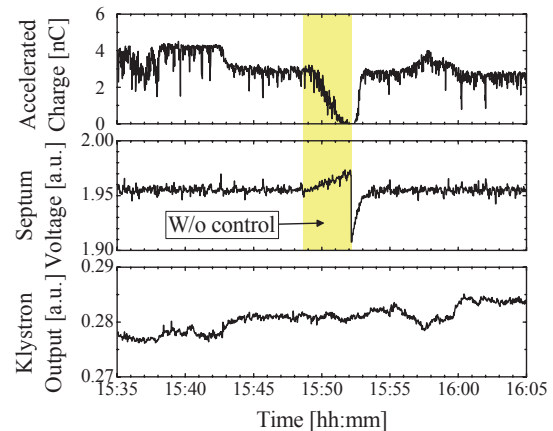


Fig. 4. Time trend of the accelerated charge in the UVSOR-II injector (top), peak voltage of the electric septum (middle) and output power for the accelerator tube (bottom) with and without the stabilization.

Single-Bunch Top-Up Operation and Single-bunch Injection at UVSOR-II

H. Zen, K. Hayashi, M. Adachi, J. Yamazaki and M. Katoh

UVSOR Facility, Institute for Molecular Science, Okazaki 444-8585, Japan

Introduction

The Single-Bunch (SB) top-up operation is strongly required at UVSOR-II, because of quite short beam lifetime with the operational mode. For the usual SB operation, we used to inject four bunches and undesired three bunches were eliminated by an RF Knock Out (RF-KO) [1]. With that injection scheme, electron loss in the storage ring is large and radiation is high. High radiation environment is not good for top-up operation. The best way to reduce the radiation is inject single electron bunch into the storage ring i.e. no bunch elimination in the storage ring. In fiscal year 2009, we achieved single-bunch injection and single-bunch top-up operation by only modifying electron gun and trigger system for the gun.

Single-Bunch Injection

A schematic drawing of the UVSOR-II injector is shown in the Fig. 1. For multi-bunch injection, electron bunch train with the energy of 15 MeV and the macro-pulse duration of 1.4 μ s is generated by the 70 keV DC Gun and Accelerator Tube. A part of bunch train is injected to the booster synchrotron and accelerated up to 750 MeV.

Since the frequency of the acceleration cavity of booster synchrotron is about 90 MHz, i.e. the bucket length is about 11 ns, single-bunch circulation and acceleration in the booster synchrotron could be accomplished if we could generate short pulse train (pulse duration of 5 ns) at the Linac. The DC Gun has already equipped a grid-pulsar for short pulse generation. The electron bunch waveform which is generated by the short pulse grid pulsar is shown in Fig. 2. We succeeded to generate 5 ns pulse trains.

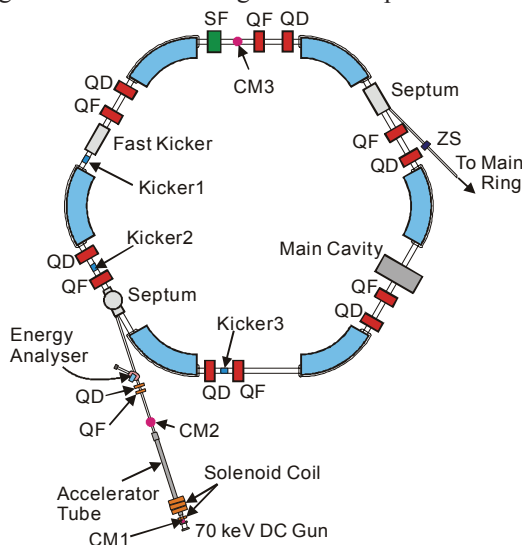


Fig. 1. Schematic drawing of UVSOR-II injector.

For stable injection of the electron to a certain bucket, firing timing of the gun is generated from 90 MHz RF signal and 1 Hz trigger signal. Test injection and purity measurement was done. The result is shown in Fig. 3. It was confirmed that the bunch purity more than 500 was achieved by only the single-bunch injection.

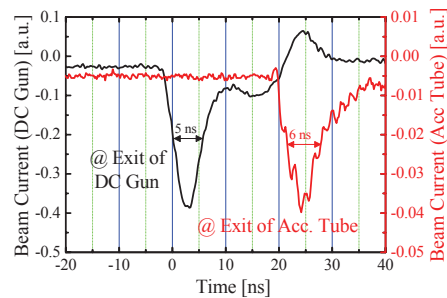


Fig. 2. Short bunch train generated by the Linac.

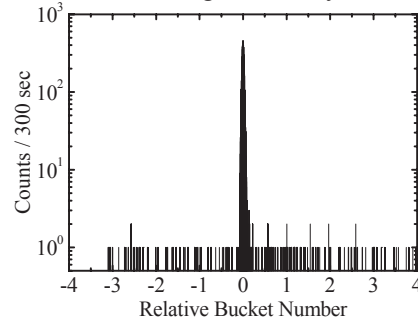


Fig. 3. Result of test injection.

Single-Bunch Top-up Operation

Single-bunch top-up operation was done during single-bunch user operation. The beam current was kept at 53 mA for 12 hours as shown in Fig. 4. Single bunch users were really satisfied with constant and high beam current.

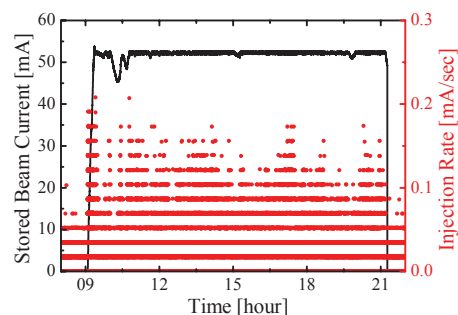


Fig. 4. Time trend of the stored beam current and injection rate during the single-bunch top-up operation in 16 Sep. 2009.

[1] A. Mochihashi *et al.*, UVSOR Activity Report **30** (2003) 39.

Upgrade of the Ti:sapphire Laser System at UVSOR-II

M. Adachi^{1,2}, H. Zen^{1,2}, K. Hayashi^{1,2}, J. Yamazaki^{1,2}, T. Tanikawa², Y. Taira^{1,3}
and M. Katoh^{1,2,3}

¹UVSOR Facility, Institute for Molecular Science, Okazaki 444-8585, Japan

²School of Physical Sciences, the Graduate University for Advanced Studies (SOKENDAI),
Okazaki 444-8585, Japan

³Graduated School of Engineering, Nagoya University, Nagoya 464-8603, Japan

UVSOR-II is equipped with the Ti:sapphire laser system which delivers intense laser pulses into the storage ring and to beamlines in synchronized with the RF frequency of the ring, and is utilized in user experiments and light source developments such as coherent synchrotron radiation (CSR) in THz region [1,2] and coherent harmonic generation (CHG) in VUV region [3].

CSR and CHG are coherent light sources obtained from the electron bunch at the bending and undulator magnets in the ring. Though the synchrotron radiation, in usual, obtained at the storage ring are incoherent in the wavelength region shorter than the electron bunch length, around 30 nm at UVSOR-II, such coherent radiations are obtained from the electron bunch by using the electron-laser interaction in the magnetic field of the undulator U5. In the previous studies, we have succeeded to generate broadband and monochromatic THz-CSR [1,2] and VUV-CHG [3].

The five-year plan supported by Quantum Beam Technology program of JST and MEXT has been started from FY2008, in which we aim to the user application using these coherent lights. For the user application, we plan to upgrade characteristics of the light sources. One of them is enhancement of the radiation power, which will be accomplished by enhancing the laser energy. We have installed a 10-Hz 50-mJ/pulse laser amplifier at FY2008 and a 1-kHz 10-mJ/pulse laser amplifier at FY2009.

Figure 1 shows a schematic drawing of the laser system. Their specifications are summarized in Table 1. The laser system consists of the oscillator Mira-900/COHERENT, the regenerative amplifier Legend-HE/COHERENT, the multi-pass amplifier Hidra-50/COHERENT, the multi-pass amplifier Legend-Cryo/COHERENT and is equipped with a Michelson interferometer (MIF) which provides envelope modulation with an arbitrary frequency to a uncompressed laser pulse to generate monochromatic CSR [1]. The modulation frequency is changed by an optical delay length of a splitted laser pulse inside the MIF [1], and a pulse compressor which compressed the stretched laser pulse from 130 fs (minimum) to tens of ps. In usual, these intense laser pulses are transported by using several mirrors (laser travels in air). Recently, we have installed an optical fiber which realizes stable transportation of the oscillator laser pulses from oscillator MIRA to the beamlines

BL6B and is utilized as the probe pulse in the THz-CSR field measurement experiment [4].

In the near future, we will generate high power CHG and CSR by using these upgraded laser pulses.

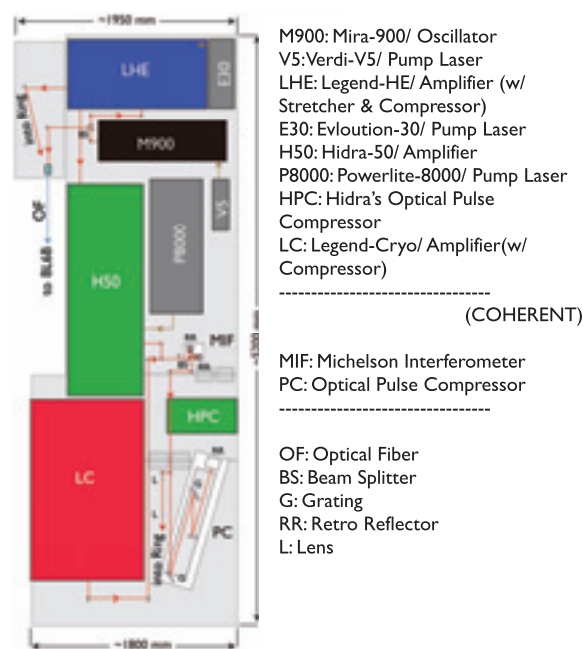


Fig. 1. A schematic drawing of the Ti:sapphire laser system.

Table 1. Specifications of the laser system. [5]

	Legend	Hidra	Legend -Cryo
Repetition Rate	1 kHz	10 Hz	1 kHz
Max. Pulse Energy	2.5 mJ	50 mJ	10 mJ
Center Wavelength	800 nm	800 nm	800 nm
Min. Pulse Duration	130 fs	130 fs	130 fs

[1] S. Bielawski *et al.*, Nature Physics **4** (2009) 390.

[2] M. Shimada *et al.*, Jpn. J. Appl. Phys. **46** (2007) 7939.

[3] T. Tanikawa *et al.*, in this report.

[4] I. Katayama *et al.*, in this report.

[5] <http://www.coherent.co.jp>

Feasibility Study of Ultra-Short Gamma Ray Pulse Generation by Laser Compton Scattering in an Electron Storage Ring

Y. Taira^{1,2}, M. Adachi^{2,3}, H. Zen^{2,3}, T. Tanikawa³, M. Hosaka¹, Y. Takashima¹, N. Yamamoto¹, K. Soda¹ and M. Katoh^{2,3,1}

¹Graduate School of Engineering, Nagoya University, Nagoya 464-8603, Japan

²UVSOR Facility, Institute for Molecular Science, Okazaki 444-8585, Japan

³School of Physical Sciences, The Graduate University for Advanced Studies, Okazaki 444-8585, Japan

The collision of laser photons with free relativistic electrons results in laser Compton scattered (LCS [1]) gamma rays. The scattered gamma rays are intense, quasi-monochromatic, tunable in energy, narrow in angular spread, and highly polarized. They are useful for applications such as nuclear physics, generation of polarized positrons, nondestructive inspection, and electron beam diagnosis. We aim to generate ultra-short gamma ray pulses with sub-picosecond width through laser Compton scattering technology, and explore the applications. The size of an electron bunch circulating in a storage ring is a few centimeters in the longitudinal direction, a few hundreds of microns in the horizontal direction, and a few tens of microns in the vertical direction. Therefore, the ultra-short gamma ray pulses may be generated by injecting femtosecond laser pulses from the perpendicular direction into the electron beams, because the interaction time between the electron beams and the laser will be shortened.

We carried out the head-on collision experiment because it was much easier to realize the collision between the laser and the electron bunch. For the 90-degree collision, it is necessary to adjust the timing in the picosecond range. An existing optical port for FEL at was used for the head-on collision experiment. The laser and detector system used in this experiment can be applied to the 90-degree collision experiment. The pulse width, the pulse energy, and frequency of the laser were 55 fs (rms), 2.0 mJ, and 1 kHz, respectively. The laser was 10 mm in diameter, which made aligning the laser beam and the electron beam easy. The power of the laser at the collision point was estimated at 0.25 W from the attenuation at the mirrors. The LCS gamma rays are detected by a NaI scintillator. In front of the detector, a collimator is placed to restrict the angular acceptance. The collimator is a lead block 10 cm thick with a hole 5 mm in diameter. For energy calibration of the detector, ¹³⁷Cs and ⁶⁰Co are used. A gate signal synchronized with the laser injection is sent to the MCA. The noise from bremsstrahlung gamma rays is reduced to 1/20. By adjusting the laser timing, the laser and electron can be collided at an arbitrary place in the straight section. We set the collision point 7.6 m from the detector. The beam current was around 1 mA, much lower than the normal operating condition, to avoid

pile-up in the detector. The maximum energy and intensity of the LCS gamma rays under the experimental conditions are 13.1 MeV and 460 photons s⁻¹ mA⁻¹, respectively.

Figure 1 shows the measured spectra. We compared the measured and calculated gamma ray spectra. The response of the scintillator detector was calculated by the EGS5 code [2]. Curves in Fig. 1 show the calculated spectra. The measured spectral shapes agree well with the calculation when the intensity of the calculated spectra is multiplied by 0.73, while the spectral shape measured with the collimator does not agree well with the calculation. This disagreement is presumably due to the misalignment of the collimator. If the collimator is assumed to be shifted by 1.7 mm in the horizontal direction, the measured spectrum agrees well with the calculation.

In the near future, we will carry out a 90-degree collision experiment using another view port for vertical injection.

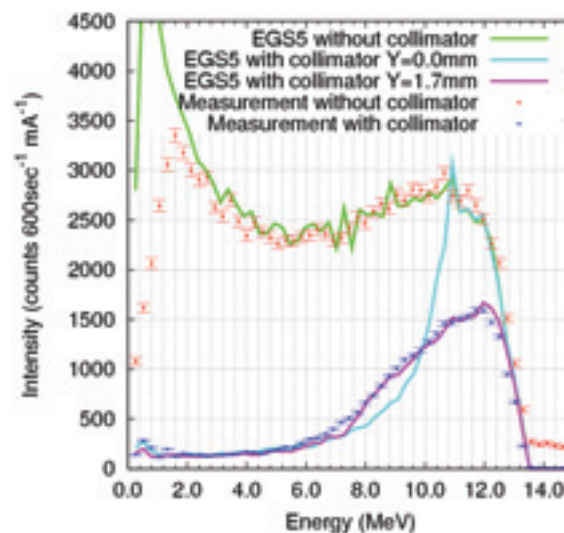


Fig. 1. Measured spectra of the LCS gamma rays. Red points are measured without collimator; blue ones are with collimator. Error bars are 1σ of statistical error.

[1] J. Stepanek, Nucl. Instr. and Meth. A **412** (1998) 174.

[2] H. Hirayama *et al.*, SLAC-R-730 (2005).

Top-Up Operation of the UVSOR-II Free Electron Laser

H. Zen¹, M. Adachi¹, T. Tanikawa^{1,3}, N. Yamamoto², J. Yamazaki¹, M. Hosaka²,
Y. Takashima² and M. Katoh¹

¹UVSOR Facility, Institute for Molecular Science, Okazaki 444-8585, Japan

²Graduate School of Engineering, Nagoya University, Nagoya 464-8603, Japan

³The Graduate University for Advanced Studies, Okazaki 444-8585, Japan

Introduction

At the UVSOR-II, a free electron laser (FEL) has been developed. The FEL has various good features such as intense, monochromatic, short pulse duration, variable polarization and wavelength tunability. However, the long term stability of the FEL is really poor because of the time varying nature of stored electron beam current. There are two main effects of the time varying beam current. One is the variation of heat load on the resonator mirror and resulting deformation of the mirror. This effect is quite rapid as shown in Fig. 1. To compensate the deformation, frequent mirror adjustments are required for maintaining the laser power. The other is the variation of the laser gain. As shown in Fig. 2, the laser power gradually decreased as the beam current decreased.

Keeping the stored beam current by top-up operation of the storage ring is a solution for those problems. In this fiscal year, we demonstrated FEL lasing during top-up operation of the storage ring.

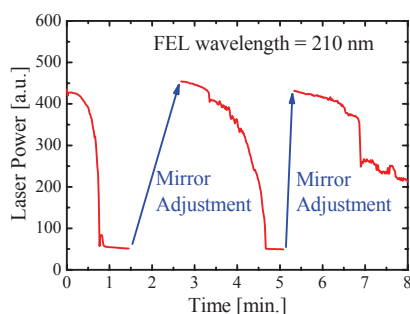


Fig. 1. Laser power decrease due to rapid heat load variation on the resonant cavity.

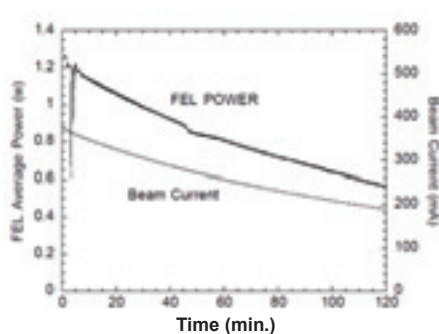


Fig. 2. Laser power decrease due to FEL gain decrease caused by beam current decrease [1].

Demonstration of FEL Top-Up Operation

The FEL lasing during top-up operation was demonstrated. The main operational parameters are listed in Table 1. As the result of top-up operation, we succeeded in keeping the stored beam current and FEL power as shown in Fig. 3. The FEL power was kept around 110 mW more than one and half hour.

During this FEL top-up demonstration, VUV irradiation experiments were carried out by user group of Yokohama National University.

Table 1. Main operational parameters

Electron Beam	Beam Energy	750 MeV
	Beam Current	130 mA/2-bunch
	Emittance	27 nm-rad
	Energy Spread	4.2×10^{-4}
	Bunch Length	108 ps
Optical Klystron	Period Length	110 mm
	Num. of Period	9 + 9
	Num. of Disp.	95
	Polarization	Helical
	Gap	43.9 mm
FEL	Cavity Length	~13.3 m
	Pulse Rate	11.26 MHz
	Wavelength	215 nm

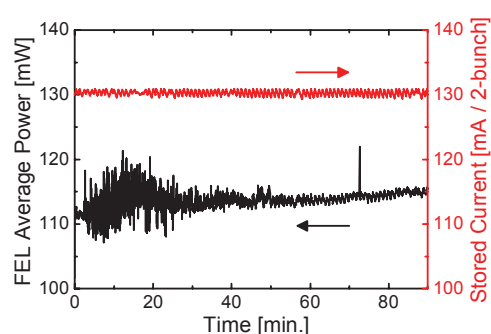


Fig. 3. Time trend of the FEL average power and stored beam current during a FEL top-up operation.

[1] M. Hosaka *et al.*, UVSOR Activity Report **29** (2002) 45.

Coherent Harmonic Generation in VUV Region at UVSOR-II

T. Tanikawa¹, M. Adachi^{1,2}, H. Zen^{1,2}, M. Hosaka³, N. Yamamoto³, J. Yamazaki², Y. Taira³
and M. Katoh^{1,2}

¹The Graduate University for Advanced Studies, Okazaki 444-8585, Japan

²UVSOR Facility, Institute for Molecular Science, Okazaki 444-8585, Japan

³Graduate School of Engineering, Nagoya University, Nagoya 464-8603, Japan

Introduction

At the UVSOR-II, electron storage ring, coherent light source developments based on laser seeding techniques are in progress. In the previous results, generation of deep ultra-violet (UV) coherent harmonic (CH) with variable polarization by using a femto-second laser and an optical klystron (OK) has been demonstrated^[1,2].

Based on the successful results, the coherent harmonic generation (CHG) in a shorter wavelength region has been aimed. For the purpose to measure it, a vacuum ultra-violet (VUV) spectrometer has been constructed. In this experiment, the spectra of CH in VUV region have been successfully observed^[3].

Design and Construction of VUV Spectral Measurement System

At the UVSOR-II, the spectral measurement of CHG has been performed by utilizing a spectrometer for visible and deep UV light (C5904, Hamamatsu Photonics). In order to measure VUV CH, the new VUV spectral measurement system has been constructed.

Figure 1 illustrates configuration of the new one, which is directly connected to the storage ring at downstream of OK. The VUV spectrometer covers the wavelength range of 50-300 nm limited by a concave replica grating (2400 grooves/mm, Pt coated, 4.5 of F number). It is Seya-Namioka configuration of 64 degree of input-output angle and compatible with an ultra-high vacuum environment. An electron multiplier tube is used as the photo detector, whose wavelength range is below 200 nm.

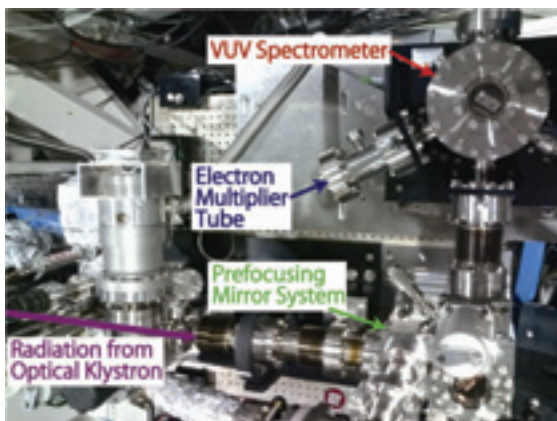


Fig. 1. Photo of VUV spectral measurement system.

Experimental Parameters

Table 1 shows parameters of the electron beam, the OK and Ti: Sapphire laser in this experiment.

Table 1. Experimental parameters.

Electron Beam	Beam Energy	600 MeV
	Beam Current	20 mA/1-bunch
	Emittance	18 nm-rad
	Energy Spread	3.4×10^{-4}
	Bunch Length	114 ps
Optical Klystron	Period Length	110 mm
	Number of Periods	9 + 9
	Number of Dispersion	45
Ti: Sapphire Laser	Central Wavelength	801 nm
	Pulse Energy	2.05 mJ
	Pulse Duration	1.3 ps

Experimental Results

The CHG up to 9th order (89 nm) has been observed. In Fig. 2 the spectrum of the 5th harmonic of SE (Spontaneous Emission) and CH are shown. The data clearly demonstrate a bandwidth of CH becomes much narrower than that of SE.

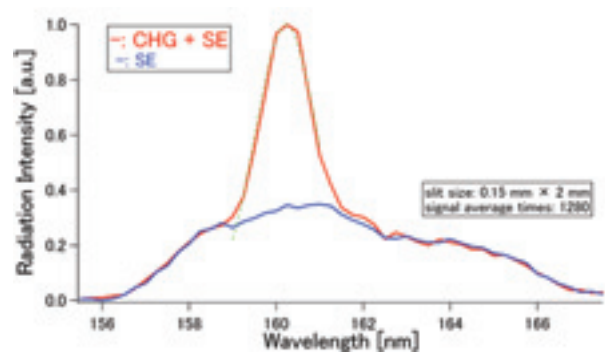


Fig. 2. Spectra of SE (blue line) and CH (red line) at the 5th harmonic.

[1] M. Labat, *et.al.*, The European Physical Journal D, 44, Number1 (2007) 187-200.

[2] M. Labat, *et.al.*, Proceedings of FEL 08, Korea, 2008.

[3] T. Tanikawa, *et.al.*, Proceedings of FEL 09, England, 2009.

Electric Field Detection of Coherent Synchrotron Radiation

I. Katayama¹, H. Shimosato², M. Bito², K. Furusawa², M. Adachi^{3,4}, M. Shimada⁵, H. Zen^{3,4}, S. Kimura^{3,4}, N. Yamamoto⁶, M. Hosaka⁶, M. Katoh^{3,4} and M. Ashida^{2,7}

¹Interdisciplinary Research Center, Yokohama National Univ., Yokohama 240-8501, Japan

²Graduate School of Engineering Science, Osaka University, Toyonaka 560-8531, Japan

³UVSOR Facility, Institute of Molecular Science, Okazaki 444-8585, Japan

⁴Graduate Universities for Advanced Studies (SOKENDAI), Okazaki 444-8585, Japan

⁵High Energy Accelerator Research Organization (KEK), Tsukuba 305-0801, Japan

⁶Graduate School of Engineering, Nagoya University, Nagoya 464-8603, Japan

⁷PRESTO JST, Tokyo 102-0075, Japan

Coherent terahertz synchrotron radiation (CSR) is a very promising light source for nonlinear terahertz spectroscopy because it may potentially have ultrahigh power and it can be combined with the normal synchrotron radiation. We recently demonstrated generation of CSR by applying the laser bunch slicing technique [1], which is first invented for X-ray generation. However the detection of the electric field of CSR from laser bunch slicing has not been realized until now because the laser and the measurement port are far separated (20 m in the case of UVSOR). In this work, we show that the use of the seed oscillator for probe and 24 m optical fiber for delivering it to the measurement port are useful and robust techniques to observe the electric field of the CSR. These techniques can be applied to the far-infrared spectroscopy using CSR and non-destructive characterization of the electron bunches with longitudinal density modulations [2].

Figure 1 shows the setup for the CSR measurement. Probe pulse for terahertz detection is divided from the seed oscillator and is coupled to the large mode-area photonic-crystal optical fiber that delivers the pulses to the detection port. Positive chirping due to the long fiber is compensated by a compressor. The pulse duration after the compressor is about 180 fs. The probe goes through the optical stage with a long delay-line and is focused on the electro-optic crystal (ZnTe). The polarization rotation due to the CSR electric field is detected with electro-optic sampling method.

The rest of the seed oscillator is amplified and is sent to the storage ring. The laser pulse interacts with the electron bunch at the undulator. The spacial and temporal overlaps are confirmed by monitoring the undulator radiation and the laser at the monitor station. As the result of the laser-electron interaction, a part of the electron bunch is strongly energy-modulated and a dip is created on the bunch as it passes through two bending magnets.

The inset of Fig. 1 shows the detected electric field of the CSR waveform. This waveform can be obtained repeatedly, that means the CSR is very stable and is not from the chaotic CSR. The oscillation of the terahertz

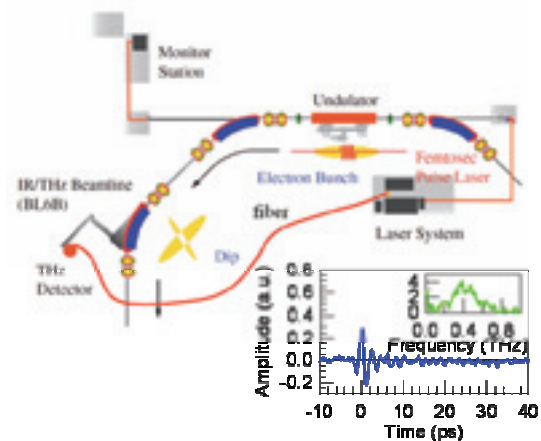


Fig. 1. Experimental setup for the electron bunch slicing. Whole laser setup is synchronized with the RF frequency. We used the seed oscillator for probing the electric field of coherent synchrotron radiation.

field is detected with the period of 2.5 ps. In the inset of Fig. 1 we also show the Fourier transformation that indicates the peak frequency is about 0.4 THz. This spectrum is in good agreement with the FTFIR measurement of the same radiation at the same port as is reported in the reference [1,3].

In summary, we have demonstrated that the CSR generated with the laser bunch slicing technique has a phase-locked waveform. The use of the electro-optic sampling method and the 24 m long fiber enables us to realize a robust technique for electric field detection even if the distance between the laser and the detection port is far. The use of seed oscillator for probe also has strong advantage since we can choose the nearest pulse to the CSR for detection within the 11 ns range (90 MHz). Therefore, the technique we used in this study is promising for detecting the electric field of novel coherent synchrotron radiations.

[1] M. Shimada *et al.*, Jpn. J. Appl. Phys. **46** (2007) 7939-7944.

[2] S. Bielawski *et al.*, Nat. Phys. **4** (2008) 390-393.

[3] M. Shimada *et al.*, Phys. Rev. Lett. **103** (2009) 144802.

Trajectory Simulations of C_{58}^+ from C_{60} in the VMI Spectrometer

B. P. Kafle¹, Md. S. I. Prodhan¹, H. Katayanagi^{1,2} and K. Mitsuke^{1,2}

¹Dept. Photo-Molec. Sci., Inst. Molec. Sci., Okazaki 444-8585, Japan

²Graduate Univ. Adv. Studies (SOKENDAI), Okazaki 444-8585, Japan

The performance of the mass-selective velocity map imaging (VMI) spectrometer has been studied by the computer simulation of the ion trajectories, by taking an example of C_{58}^+ from C_{60} .

The geometry of the VMI spectrometer is given in [1] and is essentially the same as that in [2]. The lens system contains three square electrodes, *viz.* repeller, ion extractor and tube entrance, all of which have the sides of 50 mm and the internal diameters of 20 mm. The central holes of the latter two electrodes have no mesh. Such open-hole structures have enabled us to bend the equipotential surfaces simply by manipulating the ion-extractor voltage and to achieve the excellent focusing of the PSD image.

We performed ion trajectory simulations utilizing the SIMION 3D software [3] to optimize the dimensions of the electrodes. Here, dissociative ionization of C_{60} was considered to take place within a region of rectangular parallelepiped $\Delta x \Delta y \Delta z = 1 \times 3 \times 1 \text{ mm}^3$. The y -direction was assigned to the passage of SR, so that it ranges from -1.5 to $+1.5 \text{ mm}$. The eight corners and center of the ionization region were chosen for the starting points of the ion flights. From each point 171 trajectories were generated in the range of the elevation angle θ from -90° to $+90^\circ$ at intervals of 22.5° and in the range of the azimuth angle ϕ from 0° to $+180^\circ$ at intervals of 10° (see [2]).

Application of the pulse voltages to the repeller and mass gate (V_R and V_G , respectively) has been realized by means of a “user program” of SIMION [3]. The base line values of all the pulse voltages were 0 V. The amplitude and duration of V_R were 300 V and 7 μs , respectively. At the same time a pulse voltage with the amplitude of 214 V was applied to the ion extractor. Such applications permit the ions produced during the past 13 μs to be guided into the drift tube. To filter C_{58}^+ ions we set the timing of V_G at 44.5 μs later than that of V_R . At the mass gate the spread of the TOF of C_{58}^+ was estimated to be 0.65 μs which arises from the finite volume of the ionization region and distribution of the kinetic energy of the fragment ions. Thus, the amplitude and duration of V_G were set to 120 V and 1 μs , respectively. A continuous voltage of 320 V was applied to the retarding grid of the ion reflector.

Most of the simulated trajectories of C_{58}^+ were found to go beyond the retarding grid and reach the PSD, whereas the trajectories of C_{60}^+ and C_{56}^+ were reflected completely. This observation may provide evidence for exclusive imaging detection of C_{58}^+ without interference from the neighboring ions, C_{60}^+ and C_{56}^+ , with the same kinetic energies.

Figure 1 shows the simulated velocity map images of C_{58}^+ ions on the PSD at the kinetic energies of 0.1 eV (\circ) and 0.11 eV (\blacksquare). It should be noted that these images result from momentum distributions of the ions in the laboratory system. We took into account the ion trajectories generated in the elevation and azimuth angle ranges of 0° to $+90^\circ$ and 0° to $+180^\circ$, respectively, which cover only one quarter of the full 3D trajectories over the 4π solid angle. The trajectories with a given elevation angle form a horizontal stripe, and the envelope of all the stripes makes an arc, which clearly demonstrates that scattering distribution in spherical symmetry can be successfully projected on an image plane. It is likely that C_{58}^+ fragment ions with kinetic energy difference of 0.01 eV are almost separable. Comparison between the simulations with and without the mass gate and ion reflector confirmed that the images are not distorted in the presence of these devices.

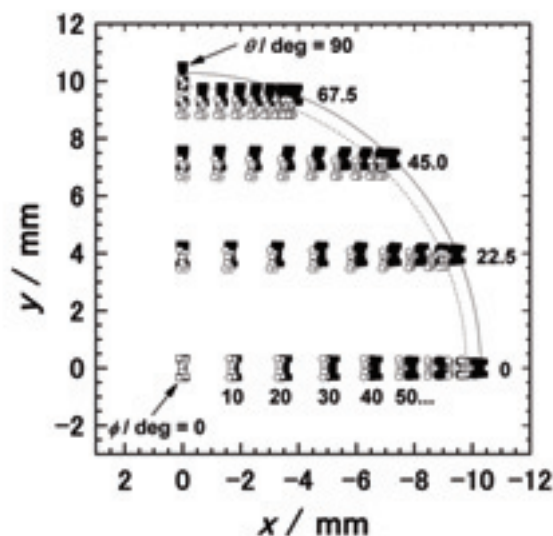


Fig. 1. Simulated 2D images of the 3D velocity distribution of C_{58}^+ from C_{60} projected on the PSD. The initial kinetic energies of C_{58}^+ were set to 0.1 (\circ) and 0.11 eV (\blacksquare).

[1] H. Katayanagi, B. P. Kafle, C. Huang, Md. S. I. Prodhan, H. Yagi and K. Mitsuke, in the Proceed. of Pure and Applied Chemistry International Conference 2010 (PACCON2010), Thailand, PTC-PO-45.

[2] B. P. Kafle, H. Katayanagi, K. Mitsuke, AIP Conf. Proc. **879** (2007) 1809.

[3] D. A. Dahl, SIMION 3D ver. 7.0, Boise Idaho, Scientific Instrument Services Inc., 2000.

Performance of a High-Precision Transmission Grating with 5555-lines/mm Groove Density for High-Resolution Soft X-Ray Emission Spectroscopy

H. Yamane¹, T. Hatsui² and N. Kosugi¹

¹ Institute for Molecular Science, Okazaki 444-8585, Japan

²XFEL Project Head Office, RIKEN & JST-PREST, Hyogo 679-5148, Japan

The X-ray emission spectroscopy (XES) measures X-rays emitted as a photon-in/photon-out process of the inner-shell excitation. The XES technique combined with the synchrotron radiation is a powerful method to investigate element-specific excitations and occupied partial density of states of gases, liquids, and solids under various conditions. However, a serious problem in the conventional XES using a grazing-incidence spectrometer based on the Rowland circle mount is a rather low quantum efficiency, arising from various factors, *e.g.*, (i) the low emission probability of $\sim 0.1\%$ at the emission point, (ii) the number of focusing elements for emitted X-rays (horizontal direction only), and (iii) the low acceptance angle and low quantum efficiency at charge-coupling devices (CCD) detector with the grazing-incidence geometry in the soft X-ray region. Moreover, these factors significantly sacrifice the energy resolution. Such problems are in general solved by the use of high brilliant X-ray beam of over 10^{12} – 10^{13} photons/s. In this case, however, one has to take care of radiation damage, in particular for soft materials such as organic and biomolecular systems.

In order to overcome the above problems, recently, we have developed a new type of soft X-ray emission spectrometer using a transmission grating (TG) at BL3U of the UVSOR facility [1]. The spectrometer adopts a novel optical design with a Wolter type I premirror, a free-standing TG, and a back-illuminated CCD, which enables high efficiency (~ 1 spectrum/h at 10^{11} photons/s) and high energy resolution. A self-standing TG made of silicon carbide (SiC) with the groove density of 6250 lines/mm (160 nm periods) has been evaluated as a prototype TG by NTT-AT N. However, as confirmed from the scanning electron microscopy (SEM) image, shown in Fig. 1(a), there is a distortion of the slit structure due to the resolution limit in the present electron-beam lithography method during the fabrication of TG.

In FY2009, the new TG, which is focused on the stability and accuracy of the slit structure as shown in Fig. 1(b), has been fabricated. In the new TG, the SiC thickness is about 500 nm, the groove density is 5555 lines/mm (180 nm periods), and the size of the slit is 108 nm at the surface side and 64 nm at the backside as shown in Fig. 1(c). The flatness of the TG surface is identically deflected as confirmed by a ZYGO method (not shown).

Figure 2 shows a test XES spectrum for a Si(111) wafer, measured at an incident photon energy $h\nu_{in} = 100$ eV with $\Delta E_{in} = 28.5$ meV. We have preliminary

observed a very sharp elastic peak in the Si L α resonant XES spectrum with the full-width at half-maximum of about $\Delta E_{out} = 35$ meV, *i.e.*, $E/\Delta E_{out} \sim 3000$, although the alignment of the new TG optics has not yet completed as suggested by the tail structure in the elastic peak, which should be fixed by the further alignment.

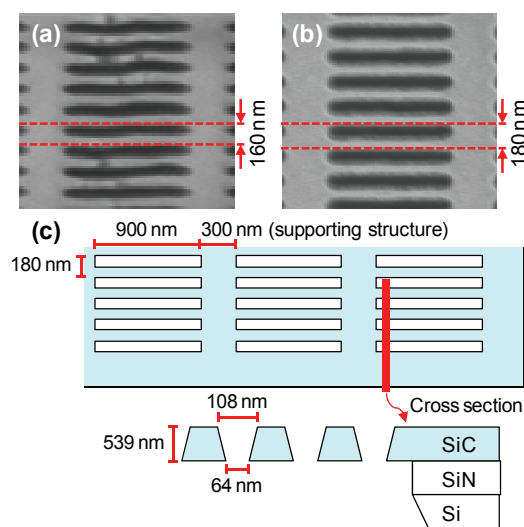


Fig. 1. SEM image for the prototype TG (a) and new TG (b) with the groove density of 6250 lines/mm (160 nm period) and 5555 lines/mm (180 nm period), respectively. (c) Basic structure of the new TG.

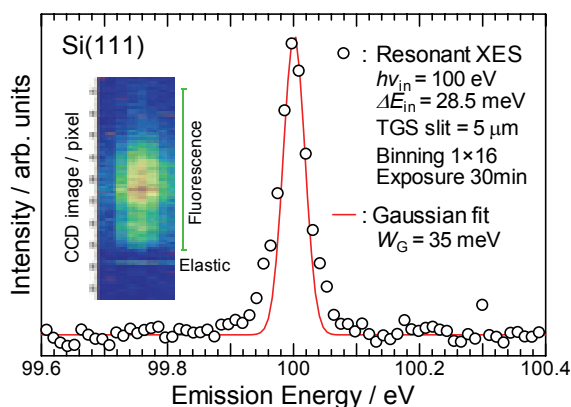


Fig. 2. Si L α resonant XES spectrum ($h\nu_{in} = 100$ eV) for the Si(111) wafer obtained by using new TG with the best fit curve using the Gaussian function with the linewidth of 35 meV.

[1] T. Hatsui *et al.*, J. Electron Spectrosc. Relat. Phenom. **144-147** (2005) 1059.

Quantum Detection Efficiency of CsI-Coated Microchannel Plates Measured by Using Pure-Calibrated EUV Beam

G. Murakami, G. Ogawa, K. Yoshioka, H. Watanabe and I. Yoshikawa
*Department of Earth and Planetary Science, Graduate School of Science,
 The University of Tokyo, Tokyo 113-0033, Japan*

Introduction

We study to optically observe the Earth's plasmasphere, which is filled with cold plasmas (mainly H⁺, He⁺, O⁺ and electrons). The He⁺ and O⁺ ions have resonance scattering emission lines in the extreme ultraviolet (EUV) region, at 30.4 nm (HeII) and 83.4 nm (OII) respectively. The intensity of each emission is proportional to column density of each scattered particle under the assumption of the optically thin condition.

Microchannel plate (MCP) detection systems have been widely used in a variety of laboratory and space applications to detect EUV radiations. EUVI (Extremity Ultra-Violet Imager) for the ISS-IMAP mission (Ionosphere, Mesosphere, upper Atmosphere and Plasmasphere mapping onboard the International Space Station) is under development. The instruments consist of band-pass filters and MCP detectors. The top MCP surface is covered with cesium iodide (CsI) photocathode in order to enhance the quantum detection efficiencies (QDEs).

It is very important to get the absolute efficiency of the instrument in order to grasp the plasma density properly. In this experiment, we measure the QDE of the MCPs which we use as a standard detector in our laboratory and evaluate the effect of CsI on the QDE.

Measurement and Result

We install an Al/Mg/Al (744Å/3958Å/747Å) filter and an Sn (1730Å) filter on the entrance of the SOR beam to eliminate the multi-order lines from 30.4nm and 58.4 nm lines, respectively. At first, we investigate the purity of each line through the entrance filter. We judge the purity from the consistency between the wavelength characteristics of an Al/Mg/Al sample filter for the continuous lines at UVSOR and those for the particular lines at the EUV facilities of Institute of Space and Astronautical Science (ISAS). The latter is measured for the emission lines of the helium gas with the discharge light source. Fig. 1 shows the transmittances of the sample filter measured at UVSOR and at ISAS. The Al/Mg/Al filter and the Sn filter are used as the entrance filter at UVSOR for 30.4 nm (Fig. 1a) and 58.4 nm (Fig. 1b), respectively. It is clear that both transmittances of the filter are consistent at 30.4 nm and 58.4 nm. We interpret from the result that the pure 30.4nm and 58.4 nm lines can be introduced through each entrance filter by using PGM35.

With the available pure lines, then we measure the QDEs of the MCP detector. The half area of the top MCP is covered with CsI and the other area is bare

(without CsI). The QDEs are calculated by the rate of the MCPs count to the electron yield of the photo diode which is absolutely calibrated. Table 1 shows the result of the measurement. It shows that the QDE of CsI is higher than that of bare MCP by 1.2 at 30.4 nm and 1.5 at 58.4 nm respectively.

For the next step, in addition to the 30.4nm and 58.4 nm lines, we plan to measure the QDE at the 83.4 nm line. Then the purity of 83.4 nm line is essential, and must be investigated for the next machine time.

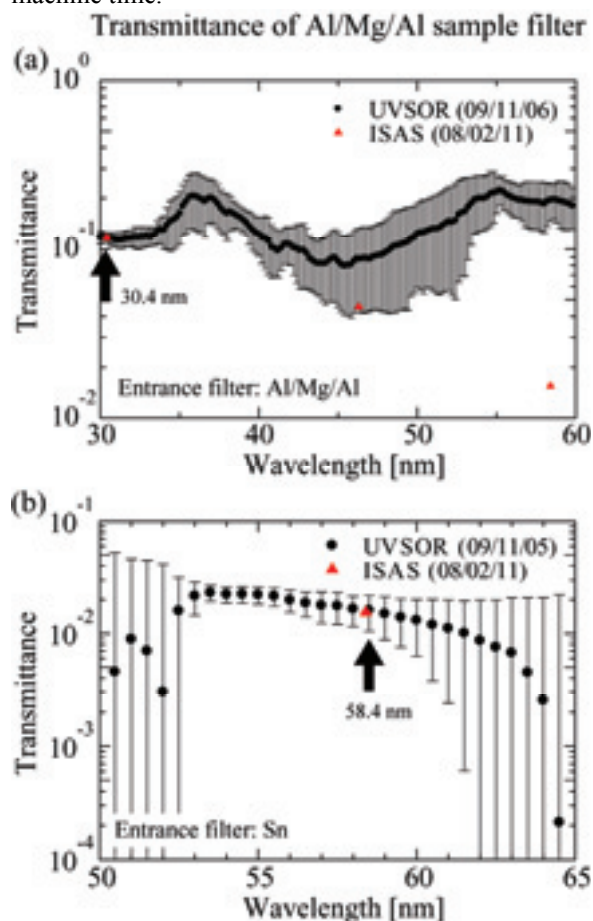


Fig. 1. The transmittances of the Al/Mg/Al sample filter measured at UVSOR and at ISAS. The Al/Mg/Al filter and the Sn filter are used as the entrance filter at UVSOR for (a) 30.4 nm and (b) 58.4 nm, respectively.

Table 1. QDEs of the MCP detector

	30.4 nm	58.4 nm
Bare	$3.45 \pm 0.06\%$	$13.04 \pm 1.71\%$
CsI	$4.13 \pm 0.07\%$	$19.41 \pm 2.24\%$

Construction of a New Experimental Setup with a High-Resolution Electron Spectrometer for Gas Phase Spectroscopy on BL6U

E. Shigemasa, E. Nakamura, N. Kondo and T. Horigome

UVSOR Facility, Institute for Molecular Science, Okazaki 444-8585, Japan

A new project for constructing the undulator beamline BL6U has been started since 2007. We have decided to choose the entrance slit-less configuration for the monochromator, as a result of the successful installation of such a configuration to BL7U. In order to cover a wide photon energy region (30-500 eV) with one single grating, a variable-included-angle Monk-Gillieson mounting has been selected. The practical construction of BL6U has begun from the summer shutdown in 2008. The first light through the monochromator has been observed in December 2008 and then precise tunings of the monochromator have been continued. It has been confirmed through its performance tests that the monochromator designed can cover the photon energy ranging from 40 to 400 eV with the resolving power higher than 5000 and the photon flux more than 10^{11} photons/sec, when the storage ring is operated in the top-up mode.

Parallel to the construction program of BL6U, the installation of a new electron spectrometer for gas phase spectroscopy has been planned. It is well known that high-resolution electron spectroscopy is a powerful tool to investigate electronic structures of atoms and molecules, especially when high-resolution electron spectra and their polarization dependences are measured as a function of photon energy in high-resolution mode. The ability of this two dimensional (2D) electron spectroscopy has been demonstrated in our recent work at SPring-8 [1], where a special attention is paid for detecting slow electrons following core excitations. In order to apply high-resolution 2D electron spectroscopy to the investigation of the L-shell excitations of the second row elements, a new experimental setup for BL6U has been designed and constructed. As a high performance hemispherical electron energy analyzer, MBS-A1, developed by the MB Scientific AB company, has been selected.

Figure 1 shows a photograph of the experimental setup, which is roughly composed of a vacuum chamber, a rotational mechanism, an MBS-A1 analyzer, a gas cell, and a double layer mu-metal screen. The analyzer is rotatable around the photon beam axis. The vacuum chamber and the rotational mechanism have been designed at UVSOR, and fabricated by TOYAMA Co., Ltd. The other components of the experimental setup have been designed by MBS, and all the components related to MBS have been transported and assembled at UVSOR in August 2009.

In order to check the performance of the analyzer,

autoionizing electrons from atoms and molecules have been measured, since their peak widths are determined by the lifetimes, which are independent on the photon energy resolution. One example of the spectra obtained is given in Fig. 2, which corresponds to the autoionization peaks from Ar^{+*} populated by the recapture of the 2p photoelectron from Ar due to the near threshold ionization. The narrowest peak width observed is about 4 meV (FWHM) including the Doppler broadening of ~ 2.9 meV, which indicates the high performance of the present experimental setup. The development of software to realize 2D electron spectroscopy is in preparation.

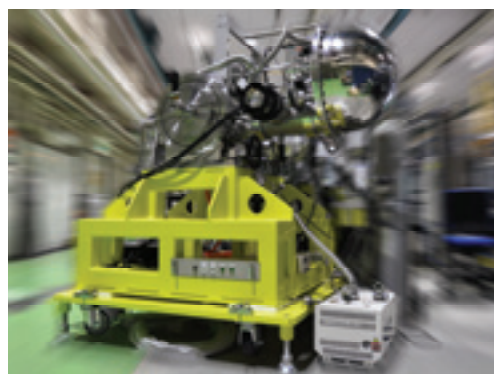


Fig. 1. Photograph of a new experimental setup for gas phase electron spectroscopy at BL6U.

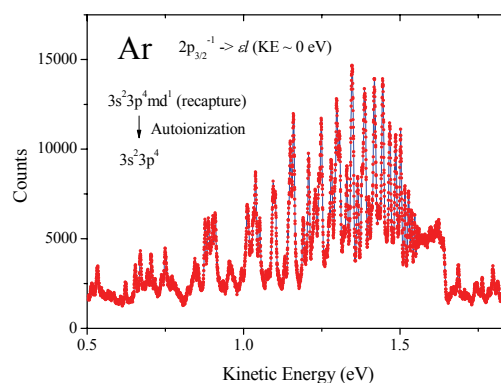


Fig. 2. Autoionization spectrum following the 2p photoionization of Ar.

[1] T. Kaneyasu, Y. Hikosaka, P. Lablanquie, F. Penet, L. Andric, G. Gamblin, J.H.D. Eland, Y. Tamenori, T. Matsushita and E. Shigemasa, *Phys. Rev. Lett.* **101** (2008) 183003.

Development of a High-Resolution Angle-Resolved UV/SX Photoemission Spectroscopy System for Solid Surface Study at BL6U

H. Yamane¹, T. Horigome¹, S. H. Kang², M. Nagasaka¹, H. W. Yeom² and N. Kosugi¹
¹Institute for Molecular Science, Okazaki 444-8585, Japan
²CAWL, Yonsei University, Seoul 120-749, Korea

Recently, a new undulator beamline BL6U, which covers the photon energy ($h\nu$) of 40–600 eV with the resolution power ($E/\Delta E$) of 10^4 at 10^{11} – 10^{12} photons/s, has been constructed. Beside the development of a gaseous high-resolution photoemission spectroscopy system at BL6U [1], we have developed a high-resolution angle-resolved photoemission spectroscopy (ARPES) system for solid and surface study.

Our ARPES system consists of an analysis chamber, sample preparation chamber, and load-lock chamber. In the analysis chamber, we have installed a (i) high-resolution angle/spatially-resolved electron analyzer (A1ER-SES200), (ii) liquid-helium (LHe) flow cryostat (Janis ST-400 UHV) with a compact 5-axes manipulation system, and (iii) low-energy electron diffraction optics with a micro-channel plate (OCI MCP-LEED). The MCP-LEED optics realizes the significantly reduced sample current ($\mu\text{A} \rightarrow \text{nA} \sim \text{pA}$), and thereby, one can apply the LEED technique to soft materials such as organic thin films without the radiation damage by electrons. Thus, the combination of (i)–(iii) allows the high-precision ARPES and photoelectron diffraction (PED) experiments.

The A1ER-SES200 system (MBS A1 combined with the SCIENTA SES-200 hemispherical electron analyzer) gives a very sharp Xe $5p_{3/2}$ peak with the full-width at half-maximum of 4.6 meV at the pass energy (E_p) of 5 eV can be achieved (cf. 3.8 meV at $E_p = 1$ eV). In the angle-resolved mode, the electron acceptance angle (θ) is ± 6 – 7° .

For the precise ARPES and PED experiments, we have designed and constructed the compact LHe 5-axes manipulator (Fig. 2). An azimuthal rotation (ϕ) is controlled by the motorized worm-&-wheel and bevel gears, which have allowance for the small backlash and the small thermal expansion between room and LHe temperature. The LHe temperature is transferred from the cryostat to samples via the copper braids. At the present diameter of the copper braids, the maximum ϕ rotation is about $\pm 50^\circ$, and the lowest temperature at the sample position is about 20–25 K. At this low temperature, the total energy resolution (ΔE_{tot}), which includes the broadening factors from the analyzer, incident photon beam, and temperature, is obtained to 9.9 meV at $h\nu = 43.2$ eV and $E_p = 5$ eV for the common use, as confirmed from the ARPES spectrum for the Fermi edge of an evaporated polycrystalline Au film (Fig. 3).

The scheduled ARPES/PED experiments at BL6U are organic semiconductor films and interfaces, and

adatoms (or small molecules) on metal surfaces.

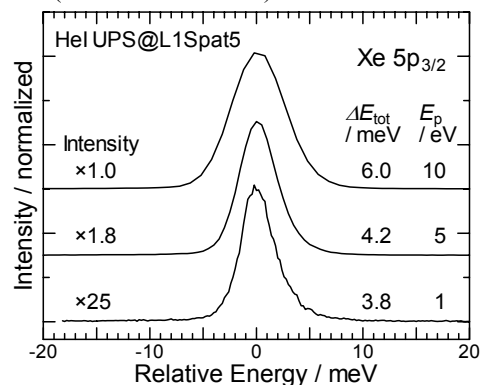


Fig. 1. Xe $5p_{3/2}$ peak obtained by using a Gammatdata VUV5000 He lamp and the A1ER-SES200 system at $E_p = 1, 5,$ and 10 eV.

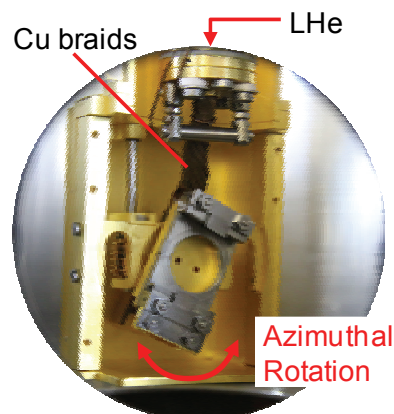


Fig. 2. Photo of the LHe 5-axes manipulator without a front radiation shield and a sample-mounting puck.

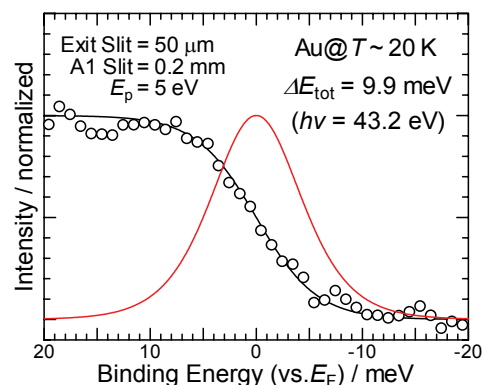


Fig. 3. Fermi edge of Au film measured at $E_p = 5$ eV, $h\nu = 43.2$ eV, and $T \sim 20$ K.

[1] E. Shigemasa *et al.*, UVSOR Activity Report 37 (2010) a separate page in this volume.

Measurement of Grating Reflectivity and Ghost Image Created by MgF₂ Plate

R. Ishikawa^{1,2}, D. Fujimura^{1,3}, K. Ueda^{1,2}, H. Watanabe⁴, T. Bando¹, T. Kobiki¹,
N. Narukage¹, H. Hara¹, R. Kano¹ and S. Tsuneta¹

¹*Hinode Science Center, National Astronomical Observatory of Japan, Mitaka 181-8588, Japan*

²*Department of Astronomy, University of Tokyo, Bunkyo-ku 113-0033, Japan*

³*Department of Earth & Planetary Science, University of Tokyo, Bunkyo-ku, 113-0033, Japan*

⁴*Kwasan and Hida Observatories, Kyoto University, Yamashina-ku 607-8417, Japan*

We are developing instruments for Chromospheric Lyman-Alpha SpectroPolarimeter (CLASP), which will be on board NASA sounding rocket. With this rocket experiment, we will explore the magnetism of solar outer atmosphere (chromosphere and transition region) with the Hanle effect in the Ly-alpha line at 121.6 nm.

Measurement of grating reflectivity at 121.6 nm

The estimation of the grating reflectivity is critical for the development of CLASP spectrograph, since the high throughput is required to achieve the high polarization sensitivity of 0.1 – 0.3%. However, we did not have any information about the grating reflectivity at 121.6 nm. Hence we planned to actually measure the reflectivity of an existing grating by ourselves as a reference.

We borrowed the Toroidal Varied Line Space (TVLS) grating from NASA MSFC for the measurement. The groove number and the applied coating (Al/MgF₂) of this TVLS grating are the same as what we plan to develop. Fig. 1 shows the test setup for our measurement. We set the incident angle to 12° which is consistent with the designed one for CLASP, and measured the reflectivity at 121.6 nm for the vertical (aligned to rulings) and the horizontal (wavelength dispersion) polarization. We had already developed a beam cleaner using UV radiation at BL7B, and were able to make perfect linear polarization light in vertical and horizontal direction combined with MgF₂ waveplate. Though this grating is not optimized for Ly-alpha line, we found that its reflectivity was 17.5% and 14.4% in horizontal and vertical polarization, respectively, and there was no significant difference in the reflectivity between two polarizations. These values are higher than what we expected before. On the basis of the conservative estimation of CLASP throughput with these values, we confirmed that our instrument achieves the high polarization sensitivity of 0.1-0.3%. We note that the CLASP gratings will be optimized for Ly-alpha, and we will obtain higher throughput.

Measurement of ghost image

The polarization beam splitter in CLASP is made of MgF₂ plate, and the reflection from its back surface creates a ghost image. This issue also should be kept

in mind for the CLASP spectrograph design. Using CCD, we took images of a main beam and a ghost image produced by MgF₂ plate with the thickness of 0.5 mm at 121.6 nm. The CCD was located around the focus position of BL7B. It was found that the intensity ratio of the ghost to the main beam was 25%, and the difference in the positions imaged on the CCD was 2.2 mm (Fig. 2). This information will be helpful for our design of CLASP.

Finally, we briefly report the properties of the beams at BL7B with G2 grating which we noticed in our measurement. (1) The beam size became larger in vertical direction with widening slit width of G2 grating from 10 μm to 500 μm. (2) The 121.6 nm beam in the 1st order was imaged on our CCD, i.e., around the focus position of BL7B, 0.8 mm and 10 mm away in horizontal and vertical direction, respectively, from the 0th order beam, when the slit width was 10 μm.

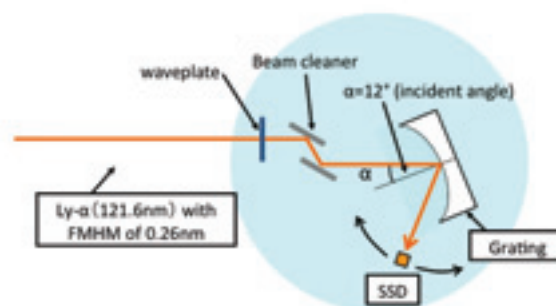


Fig 1. Setup of grating reflectivity measurement for the vertical polarization.



Fig. 2. Main beam and ghost image induced by MgF₂ plate with the thickness of 0.5 mm at 121.6 nm with the slit width of 300 μm.

Development of MgF₂ Waveplate and Polarization Analyzer

H. Watanabe¹, N. Narukage², D. Fujimura², K. Ueda², R. Ishikawa², T. Kobiki² and T. Bando²

¹*Kwasan and Hida observatories, Kyoto University, Kyoto 607-8417, Japan*

²*National Astronomical Observatory of Japan, Mitaka 181-8588, Japan*

We developed a half waveplate and a polarization analyzer made of MgF₂ for Lyman-alpha line (121.6 nm) by means of UV radiation at BL7B with the G2 grating. This is the basic experiment for “Chromospheric Lyman-Alpha Spectro-Polarimeter (CLASP)” rocket, which is planned to be launched in 2013. CLASP rocket will measure the weak vector magnetic field in the solar chromosphere using Lyman-alpha wavelength. As the magnetic field in the solar chromosphere is very weak, the signal is dominated by linear polarizations from the Hanle effect [1]. Our method is to measure the linear polarization by taking the spectra of two orthogonal polarization states simultaneously with a rotating half waveplate and two polarization analyzers (one of the analyzers works as a beam splitter).

MgF₂ is a transparent crystal for UV wavelength above 110 nm, and has birefringency with one slow axis (n_e : extraordinary refractive index) and two fast axes (n_o : ordinary refractive index). In order to evaluate the performance of MgF₂ polarization analyzer, we measured the reflection/transmission (R-T) ratio as a function of the incident angle for both p-polarized (the electric vector parallel to the optical surface) and s-polarized (electric vector perpendicular to the optical surface) light. The reflected beam at Brewster's angle is almost purely polarized consisting of s-polarized component, and thus is useful as a polarization analyzer. By fitting the R-T ratios shown in Fig. 2, we found that the *the Brewster's angle of MgF₂ is 59°*, and *121.6 nm beam at BL7B is 89% linearly polarized in the horizontal direction*. The reflection ratio at Brewster's angle is 29.4% for s-polarized and 0.30% for p-polarized component.

As the retardation measurement needs highly linearly polarized light source, we set a beam cleaner at the entrance of the chamber. The beam cleaner is made of one Aluminum plate and one MgF₂ plate both located at incident angle of 60° (~Brewster's angle for MgF₂), and makes perfect linear polarization light in horizontal direction (see Fig. 2).

The half waveplate for Lyman-alpha is also made of MgF₂ by stacking two plates whose slow axes are perpendicular to each other and whose thicknesses slightly differ from each other. The retardation of a waveplate is proportional to the product of the thickness difference and $(n_e - n_o)$. For developing a half waveplate, the accurate value of $(n_e - n_o)$ is necessary. There are few early works which measured $(n_e - n_o)$ [2]. We measured the retardation of three kinds of waveplates with thickness differences of 7.03 μm , 8.46 μm , and 14.04 μm . *We deduced the*

value of $(n_e - n_o)$ is 0.0035 +/- 0.00018 at 121.6 and the thickness difference for a Lyman-alpha half waveplate is 17.18 μm . We are developing the half waveplate for Lyman-alpha line using this result. On the basis of R-T ratio and retardation measurements, we can derive the optical constants of MgF₂ at 121.6 nm as $n_o = 1.63$, $k = 1.0 \times 10^{-6}$. We are going to submit these results to the Journal of the Optical Society of America in 2010 (the title will be “Optical Constant of MgF₂ Plate at Lyman-Alpha Wavelength for CLASP Experiment”).

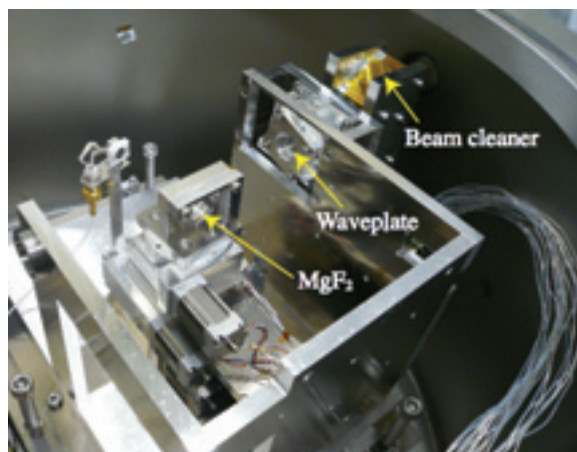


Fig. 1. Photo of our measurement system. The position of the waveplate and MgF₂ plate are controlled by the stepping motors.

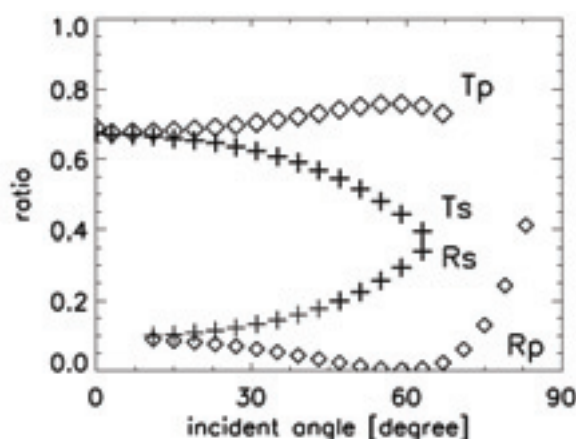


Fig. 2. Result of reflection/transmission ratio measurement.

[1] J. Trujillo Bueno and A. Asensio Ramos, *Astrophysical Journal* **655** (2007) 642.

[2] P. Laporte *et al.*, *J. Opt. Soc. Am.* **8** (1983) 1477.

Oscillator Strength Sum Rule of Sulfur K-edge NEXAFS Spectra of Sulfur-Containing Amino Acids

Y. Izumi, M. Tanabe, K. Sugiki and K. Nakagawa

Graduate School of Human Development and Environment, Kobe University, Kobe 657-8501, Japan

Absolute values of optical absorption cross section $\sigma(h\nu)$ as a function of photon energy $h\nu$ over the wide range, is a fundamental and important data for molecular science. Synchrotron radiation is very powerful as a continuum light source to measure $\sigma(h\nu)$ within the wide energy range. Here we report our experimental result to measure the $\sigma(h\nu)$ spectra with the focus at the near edge X-ray absorption fine structure NEXAFS for the sulfur K-edge region.

The reason why we measured the sulfur K-edge NEXAFS spectra is that sulfur is the heaviest atom within amino acid molecules [1, 2] which have been found in many meteorites and thus are believed to be formed in space in prior to the emergence of the first life. Our objective to measure the sulfur K-edge NEXAFS spectra is to study the role of sulfur atoms in the chemical evolution.

Methionine (Met) and cystin (Cys) were purchased from Wako Chemical company. Putting amino acid powder between 7.5 μm polyimide films, we pressed and prepared pellet samples of which thickness were about 5 to 30 μm . NEXAFS spectra measurement were carried out at the beamline 1A by the transmittance mode with the double crystal monochromator equipped with InSb crystals. Analyzing the transmitted X-ray intensities $I_0(h\nu)$ for polyimide films and $I(h\nu)$ for the amino acids and polyimide, we determined relative values of absorption cross section. Assuming that absolute values of cross section around 2460 eV and 2560 eV should be equal to the sum of atomic absorption cross sections [3] of each constituent atom making the amino acid molecule, we determine the absolute values of $\sigma(h\nu)$. Obtained results are shown in Fig. 1.

After detailed analyses of the NEXAFS spectra shown in Fig. 1 using the DV- $X\alpha$ calculation, we found that our spectra could not resolve the chemical shift components of S-S bond and S-C bond, probably due to relatively worth resolution energy ($\Delta h\nu = 1.5$ eV) of the measurement system with the InSb crystals. More detailed spectra with the higher resolution energy ($\Delta h\nu = 0.5$ eV) were reported by Risberg et al.[2] with the Si crystals.

In spite of the worth resolution energy, we examined our spectra in terms of the oscillator strength sum rule in which integrated oscillator strength n_0 should be equal to the number n_e of electrons responsible to the optical transition within the subjected energy region. By the integration of

$\sigma(h\nu)$ from 2460 eV to 2590 eV, we obtained n_0 to be 0.25 for Cyt. This value is reasonable to the report by Reynaud et al. [4] for H_2S , SO_2 and SF_6 , n_0 values of which molecules are 0.13, because $n_0 = 4$ of Cyt is twice of $n_0 = 2$ of H_2S , SO_2 and SF_6 . The integration of $\sigma(h\nu)$ from 2460 eV to 2800 eV gave 0.3 for Met. This value was also reasonable with comparison to 0.31 for H_2S , SO_2 , and SF_6 reported by Reynaud et al. [4].

We concluded that sulfur atom plays an important role in chemical evolution in space because x-ray photons can be absorbed with higher efficiency by the sulfur containing amino acids than those without sulfur atoms. This effect may be compared to the effect of antenna to absorb the electromagnetic waves with higher efficiency.

This work was done by the joint study program of UVSOR 20-804 and 21-506.

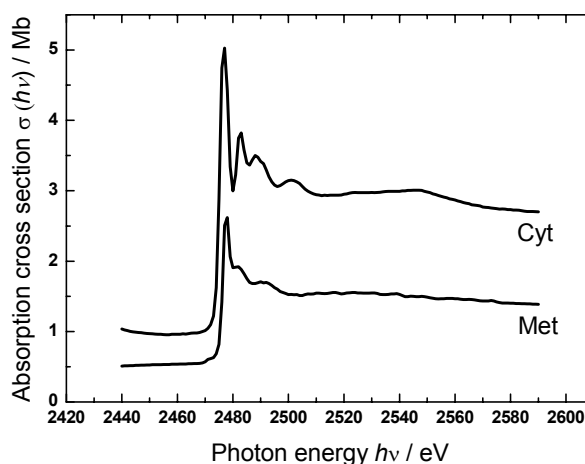


Fig. 1. Absolute values of absorption cross sections of cystin (Cyt) nad Methionine (Met).

- [1] J. Siritapetawee and W. Pattanasiriwisawa, J. Synshrotron Rad. **15** (2008) 158-161.
- [2] E. D. Risberg *et al.*, The Royal Society of Chemistry 2009 Dalton Trans. (2009) 3542-3558.
- [3] B. L. Henke *et al.*, Atomic Data and Nuclear Data Tables **54-2** (1993) 181-342.
- [4] C. Reynaud *et al.*, J. Phys. B: At Mol. Opt. Phys. **29** (1996) 5403-5419.

Exclusive Detection of Photofragments from C₆₀ with a Potential-Switch Mass Selector

H. Katayanagi^{1,2}, Md. S. I. Prodhani¹, B. P. Kafle¹, C. Huang¹ and K. Mitsuke^{1,2}

¹Dept. of Photo-Molecular Science, Institute for Molecular Science, Okazaki 444-8585, Japan

²Graduate University for Advanced Studies (SOKENDAI), Okazaki 444-8585, Japan

We have developed a potential-switch mass selector (PMS) incorporated into the apparatus of velocity map imaging for the photofragmentation of fullerenes. The performance of the PMS was tested by time-of-flight (TOF) mass spectrometry of the photofragments from C₆₀. A peak of C₅₄²⁺ was exclusively detected with a sufficient mass resolution.

The structure of our photofragment mass spectrometer used in the present experiment is almost identical to that described elsewhere [1, 2]. The fullerene (C₆₀) sample was loaded in a cylindrical quartz cell and heated up to around 700-800 K in vacuum. The C₆₀ vapor sublimated from the cell passed through two apertures and reached the ionization region, and irradiated with the monochromatized synchrotron radiation. Ions produced at the ionization region were extracted by a Wiley-McLaren type electrode assembly, which consists of the ion repeller, extractor and entrance plate of an ion drift tube. The ions were pushed out by a pulse voltage (75 V, 4.5 μs, 1.1 kHz) applied to the repeller and projected on to a Z-stack MCP of 27 mm in diameter. The MCP was located 375 mm away from the ionization region. The ion drift tube was kept at -340 V and the extractor at 1 V.

The PMS is composed of a mass gate and an ion reflector. They were installed in the end of the ion drift tube. Their dimensions and positions were optimized by ion trajectory simulation [1, 3]. Thin meshes were attached to the both ends of the mass gate in order to avoid the distortion of the equipotential surfaces due to a fringe effect. The ion reflector consists of a triplet of disk electrodes that have central holes covered with fine meshes. The second disk electrode named "retarding grid" was placed 5 mm apart from the first and third disk electrodes that were kept at -340 V. These two electrodes made the equipotential surfaces flat and parallel inside the ion reflector.

The retarding grid was biased to 80 V. Eventually all the ions were forced back there and cannot enter the MCP. We then applied a pulse voltage changing from -340 to $V_G = 100$ V to the mass gate by a home made pulse generator. Instantaneously the potential energies of the ions were elevated the ions of interest were made to pass through the retarding grid and reach the MCP, if we had adjusted the application timing of V_G to their arrival time into the mass gate. For the control experiment we applied DC voltages of -340 and 0 V to the mass gate and retarding grid, respectively. This combination resulted in no mass discrimination and allowed all the ions to go beyond

the ion reflector.

Figure 1(a) shows TOF mass spectrum of the photofragments in the control experiment. All the parent and fragment ions reached the detector. The presence of PMS has no essential effect on the mass resolution. Figure 1(b) shows the TOF spectrum of doubly charged ions which were selected with PMS. A pulse voltage applied to the mass gate was at 24 μs after the repeller pulse and 3 μs in width. The parent and fragment ions were selected without any distortion. With applying the shorter pulse voltage of 0.7 μs, we succeeded in selecting the C₅₄²⁺ peak without any distortion and contamination from neighboring peaks. The selected C₅₄²⁺ peak is shown in Fig. 1(c).

From the present result we can expect that the mass selective imaging experiment can be conducted using the PMS with replacement of the MCP by a position sensitive detector.

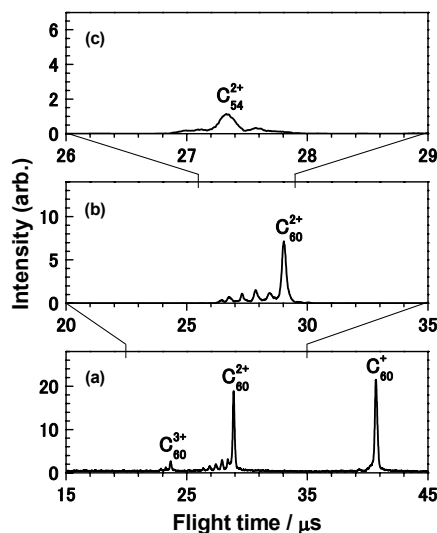


Fig. 1. TOF spectra of C₆₀ at $h\nu = 90$ eV. (a) The control experiment; (b) and (c) the discrimination of all species in doubly charged states and C₅₄²⁺, respectively.

[1] H. Katayanagi *et al.*, in the proceedings of Pure and Applied Chemistry International Conference 2010 (PACCON2010), Thailand, PTC-P0-45.

[2] Md. S. I. Prodhani *et al.*, Chem. Phys. Lett. **469** (2009) 19.

[3] B. P. Kafle, H. Katayanagi and K. Mitsuke, AIP Conf. Proc. **879** (2007) 1809.

Development of a TEPICO Technique for Determination of Excess Energy Partitioning in Dissociative Photoionization

H. Katayanagi^{1,2}, Md. S. I. Prodhani¹, B. P. Kafle¹, C. Huang¹ and K. Mitsuke^{1,2}

¹Dept. of Photo-Molecular Science, Institute for Molecular Science, Okazaki 444-8585, Japan

²Graduate University for Advanced Studies (SOKENDAI), Okazaki 444-8585, Japan

We have observed ion yield spectra of photofragments produced by the dissociative photoionization of fullerenes. Maximum internal energies of parent ions were estimated from appearance photon energies of the fragments. The obtained maximum internal energies agreed well with those calculated on the basis of the RRKM theory [1]. So far in our discussion kinetic energies of photoelectrons were assumed to be zero. In order to remove this crude assumption a coincidence technique was developed. In this technique photofragments are detected in coincidence only with the electrons with zero-kinetic-energy or threshold photoelectrons.

In the beginning we observed the threshold ion yield spectra of He at the first ionization energy by means of the threshold photoelectron photoion coincidence technique (TEPICO) developed in the present study. We then evaluated the feasibility of this technique to experimentally elucidate the photodissociation mechanism of fullerenes.

The helium gas was introduced to a vacuum chamber through a 1/4" tube. Helium atoms were ionized with the monochromatized synchrotron radiation at an ionization region between an ion repeller (R) and ion extractor (E) electrodes. The electrode R also acts as the entrance to an electron detector. The photoelectrons were detected by a chevron MCP. In order to select the threshold electrons we made use of the "dark gaps" in the temporal profile of a bunch structure of UVSOR. There is a 20-40 ns dark gap in every 176 ns. No ionization takes place during the dark gap. While the threshold electrons remain at the ionization region during the dark gap, high-energy electrons escape immediately. Only the threshold electron signals were detected by application of a pulse voltage (-3 V, 30 ns) to the electrode E at the timing of the dark gap. This synchronization of the pulse voltage with the dark gap was achieved with a "pick-up" signal (5.68 MHz) supplied from the UVSOR. The pick-up signal was frequency-divided by 8-10 in order to fit it to the maximum triggering rate of the apparatus.

Electron TOF spectra were measured with respect to the pick-up signal. A peak of threshold electrons was observed. The threshold electron signal was used to trigger a pulse voltage (75 V, 4.5 μ s) applied to the electrode R. The ions produced simultaneously with threshold electrons are thus extracted and projected on to a Z-stack MCP.

Figure 1 shows threshold photoelectron spectra of

He. A peak was clearly observed at 24.6 eV which agreed well with the first ionization potential of He. The resolution was found to be *ca.* 50 meV from the full-width at half-maximum of the peak. An ion yield curve of He obtained by the TEPICO method is shown in Fig. 2. A peak of 20 meV in width was clearly observed at 24.6 eV.

We succeeded in obtaining the TEPICO spectra of He. The present resolution of 20 meV was found to be sufficient to discuss the energy-partitioning mechanism on a basis of the transient-state theory. However, we have not yet succeeded in obtaining TEPICO spectra of other samples than He. This is due to low collection efficiency of the threshold electron in the present method since the electrons are collected only when the pulse voltage is applied during the dark gap. It is insufficient to discriminate small number of threshold electrons from large amount of energetic electrons. This is the case with most of samples except He. We will fabricate the electron detector that has a higher efficiency to collect threshold electrons.

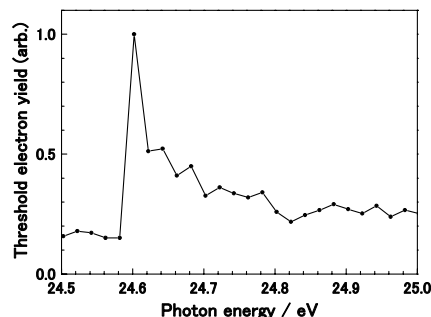


Fig. 1. Threshold photoelectron spectrum of He.

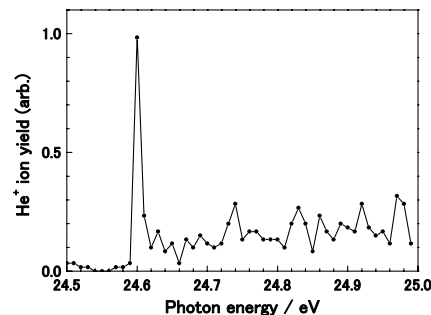


Fig. 2. Ion yield curve of He obtained by TEPICO.

[1] J. Kou *et al.*, Phys. Chem. Chem. Phys. 7 (2005) 119.

Small Kr-Xe Mixed Clusters Studied by X-Ray Photoelectron Spectroscopy

M. Nagasaka¹, N. Kosugi¹ and E. Rühl²

¹*Institute for Molecular Science, Myodaiji, Okazaki 444-8585, Japan*

²*Physikalische Chemie, Freie Universität Berlin, Takustr. 3, D-14195 Berlin, Germany*

Heterogeneous clusters mixed with different atoms show richer behavior than single atomic clusters. The structures of small mixed clusters have been investigated by theoretical simulations such as Monte Carlo method [1], and these results suggest that the structures are dependent on competition of several factors, such as atomic radii, surface energies, and interaction energies between different atoms. But there exist few experiments to study the structures of small mixed clusters. Recently, we have measured X-ray photoelectron spectroscopy (XPS) of the Kr₃₀ clusters, and observed different binding energy shifts dependent on the surface site [2]. These shifts are derived from the induced polarization of surrounding atoms on the photoionization, and reflect the local environments. In this work, we have studied the structure of small Kr-Xe mixed clusters with different compositions by using XPS.

The experiments were performed at BL3U. The Kr-Xe mixed clusters were formed by the supersonic expansion of the primary gas mixtures with the Xe 1 – 5 % regions. The average compositions of the mixed clusters were estimated to be the Xe₅Kr₂₇, Xe₁₁Kr₂₆, Xe₁₅Kr₂₂, and Xe₂₂Kr₁₄ at the 1, 2, 3, and 5 % Xe conditions, respectively.

Figure 1 shows the Xe 4d_{5/2} XPS spectra at different compositions. All the sites in the Xe₅Kr₂₇ clusters show smaller binding energy shifts than those in the Xe₃₀ clusters. Because the polarizability of Kr is smaller than that of Xe, the smaller shifts mean that the Xe atoms contact with the Kr atoms. The peak intensities of bulk sites are close to those of edge sites in the Xe₅Kr₂₇ clusters. These results suggest that the small Xe₅ core is embedded on the surface of the Kr clusters in the Xe₅Kr₂₇ clusters.

In the Xe₁₁Kr₂₆ clusters, the edge and bulk sites are slightly shifted to the lower binding energies from the Xe₅Kr₂₇ clusters. By calculating the binding energy shifts considering the induced polarization, we found that the two Xe cores exist on the surface of the Kr clusters. The single component cluster below the size of 200 shows icosahedron structures, where the surface is not closed packed structures [3]. The space in the Kr surface is filled by the Xe cores, and the Kr clusters show the denser structures. As a result, the Xe cores move to the outer parts of the Kr clusters, and the peak intensities of the edge sites are increased compared to those of the bulk sites. In the Xe₁₅Kr₂₂ clusters, the Xe cores are growing up on the surface of the Kr clusters and merged with each other because the Kr clusters have no space for the formation of the additional Xe cores.

In the Xe₂₂Kr₁₄ clusters, the binding energies of the edge and bulk sites are shifted to the lower binding energy. These results indicate that the separated layer between the large Xe and Kr clusters are formed in the Xe₂₂Kr₁₄ clusters.

In conclusion, we have revealed the structures of the small Kr-Xe mixed clusters, in which the structures are changed dynamically with the different mixing ratios. We also confirmed that these structures are consistent with the theoretical results [1].

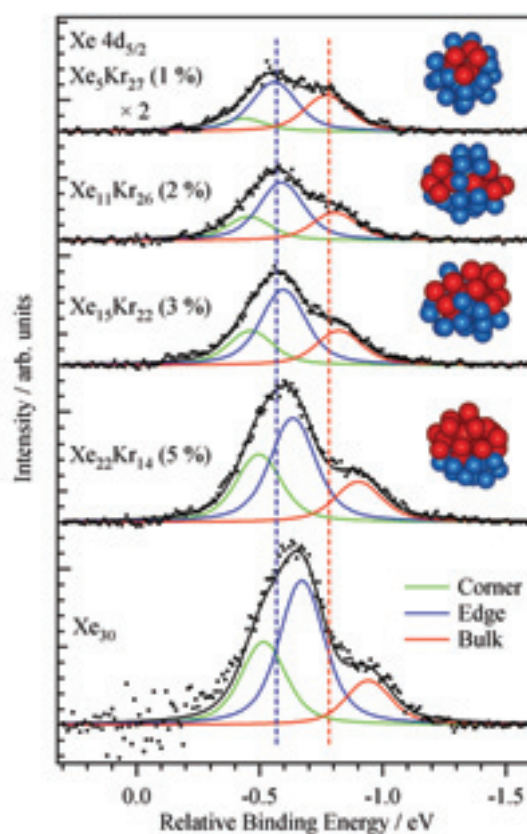


Fig. 1. The Xe 4d_{5/2} XPS spectra for the mixed clusters with different compositions, where the average size is shown. The atomic signal was subtracted, and the binding energy of the Xe atom was set to be zero. The proposed models are also shown, in which the blue and red spheres represent the Kr and Xe atoms, respectively. The sizes of the model structures are set to be 35.

[1] F. Calvo and E. Yurtsever, *Phys. Rev. B* **70** (2004) 045423.

[2] T. Hatsui *et al.*, *J. Chem. Phys.* **123** (2005) 154304.

[3] S. Kakar *et al.*, *Phys. Rev. Lett.* **78** (1997) 1675.

Development of Liquid Cell with Different Thickness for Soft X-Ray Absorption Spectroscopy of Aqueous Solutions in Transmission Mode

M. Nagasaka¹, T. Hatsui², T. Horigome¹ and N. Kosugi¹

¹*Institute for Molecular Science, Myodaiji, Okazaki 444-8585, Japan*

²*XFEL Project Head Office, RIKEN, Sayo-cho, Hyogo 679-5148, Japan*

X-ray absorption spectroscopy (XAS) is a powerful method to investigate local electronic and geometric structures around core-excited atoms. But the chemically important inner shells such as C, N, and O K-edges are difficult to apply XAS in transmission mode because of the short attenuation length of soft X-rays. XAS is mainly applied in the vacuum condition by collecting secondary ions, electrons, and fluorescence following the inner-shell excitations. Recently, O K-edge XAS spectra of liquid water were measured with the yields of the secondary processes [1]. There exist several debates in the interpretation of the liquid water. In order to settle the discussion, the transmission measurement is very important. Näslund *et al.* successfully measured XAS in transmission mode [2]. In the present study, we have developed a thickness controllable liquid cell for the O K-edge XAS of aqueous solutions in transmission mode [3].

Figure 1(a) shows a diagram of our liquid flow cell. There are four regions I, II, III, and IV, separated by 100 nm-thick SiN_x membranes (NTT-AT N Co.). The region I is connected to BL3U in a vacuum condition. The regions II and IV are in an atmospheric condition of helium gas, where the pressure is controllable. The pressure difference between the regions I and II is quite large. The SiN_x membranes with the sizes of 200 × 200 μm² are settled in this border. Soft X-rays in the region I pass through the region II and the liquid layer in the region III, and reach a photodiode detector in the region IV. In order to transmit soft X-rays at the O K-edges, the thickness of the liquid layer should be below 1 μm. The gap in the region III is formed by sandwiching two SiN_x membranes with the sizes of 2 × 2 mm². As shown in Fig. 1(b), the two 20 μm-thick Teflon sheets are put as a spacer and pressed with the sealed O-rings. The fresh liquid is supplied with a tubing pump system during changing the photon energy, and suspended automatically at the absorption measurement of the destination photon energy. The XAS spectrum was obtained as $\ln(I_0/I)$, in which the currents I_0 for the blank cell and I for the sample cell. The contributions of the high order X-rays were removed in this spectrum.

Figure 2 shows the transmission O K-edge XAS for liquid water at room temperature by changing the He backpressure (0 to 10 kPa) in the regions II and IV. As a result, the thickness is ranged from 700 nm to 200 nm. The three characteristic features are obtained as the pre-edge peak (~535.5 eV), the main-edge (~537 eV), and the post-edge maximum (~540 eV). The ratio of pre-edge to main-edge becomes 0.49.

These results are consistent with the previous transmission results (0.4) [2].

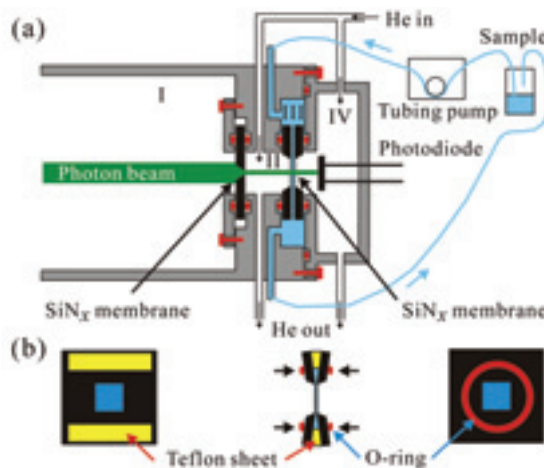


Fig. 1. (a) A schematic liquid flow cell for the soft X-ray transmission measurements. (b) The details of the thin liquid layer in the region III.

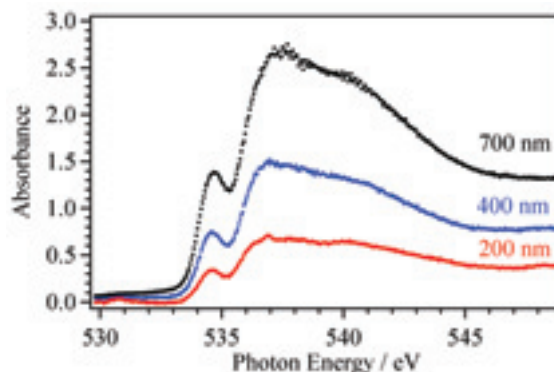


Fig. 2. O K-edge X-ray absorption spectrum of the liquid water with the thickness from 700 nm to 200 nm by controlling the He backpressures.

- [1] Ph. Wernet *et al.*, *Science* **304** (2004) 995.
 [2] L.-Å. Näslund *et al.*, *J. Phys. Chem. B* **109** (2005) 13835.
 [3] M. Nagasaka *et al.*, *J. Electron Spectrosc. Relat. Phenom.* **177** (2010) 130.

Doppler Effect in Fragment Autoionization Following Core-to-Valence Excitation of O₂

R. Guillemin¹, M. Simon¹ and E. Shigemasa²

¹LCPMR, Université Pierre et Marie Curie, 75231 Paris Cedex 05, France

²UVSOR Facility, Institute for Molecular Science, Okazaki 444-8585, Japan

The Doppler effect is known to occur when the source and observer are in motion relative to each other, leading to an apparent change in the observed frequency of the propagating wave. This effect has a wide variety of applications in many fields, relating to the sensing of movement. In the research field of molecular physics, the sensing of nuclear motion has long been an important issue. Gel'mukhanov and co-workers predicted in 1997 [1] that the nuclear motion in 'ultrafast dissociation' following molecular core-level photoexcitation can be probed by the Doppler effect in emitted Auger electron. Ultrafast dissociation is a process in which the molecular dissociation at the core-excited state precedes the Auger decay and then an atomic fragment emits an Auger electron [2]. The atomic Auger electron can possess the opposite Doppler shift depending on the direction approaching the detector or moving away from it.

The electronic Doppler effect on ultrafast dissociation was experimentally evidenced for the first time at the core-to-valence excitation in O₂ [3]. Recently, the electronic Doppler effect after the core-to-Rydberg excitations in N₂ has been revealed [4]. In the present work, similar experiments for observing slow electron emissions from atomic fragments have been conducted for the core-to-valence excitation of O₂.

The experiment was performed on the soft X-ray beamline BL6U at UVSOR. The radiation from an undulator was monochromatized by a variable included angle varied line-spacing plane grazing monochromator. The photon energy resolution $E/\Delta E$ was set to 2000. The monochromatized radiation was introduced into a cell with sample gases. Kinetic energies of the emitted electrons were measured by a hemispherical electron energy analyzer (MBS-A1) placed at a right angle with respect to the photon beam direction. The degree of the linear polarization of the incident light was essentially 100%, and the direction of the electric vector was set to be parallel to the axis of the electrostatic lens of the analyzer. The kinetic energy resolution of the analyzer was set to 25 meV for autoionizing slow electrons, and 60 meV for atomic Auger electrons.

Figure 1 shows the blowup of the atomic Auger line following the ultrafast dissociation [3] in the resonant Auger spectrum obtained at 539.43 eV, where the lower σ^* resonance without overlapping with any Rydberg state lies. The atomic Auger line

clearly demonstrates the Doppler splitting. Figure 2 displays an autoionizing slow electron spectrum measured at the same photon energy. All the peaks observed are assignable to the autoionization of O* into O⁺, which exhibit double peak structures due to the Doppler effect. The kinetic energy releases estimated from the Doppler splittings seen in Fig. 1 and 2 are nearly the same. This means that the ultrafast dissociation following the σ^* excitation produces two excited oxygen atoms: one is core excited and the other excited in the valence shell. The detailed data analysis is now in progress.

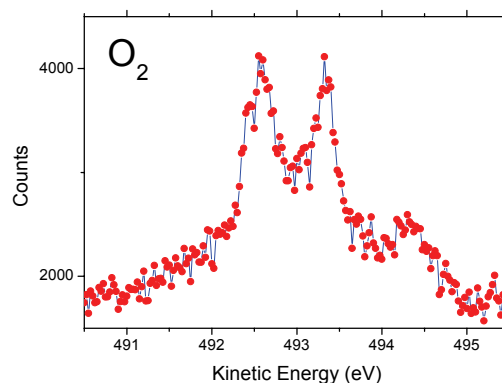


Fig. 1. Doppler profile of atomic Auger line measured at the lower σ^* resonance position of O₂.

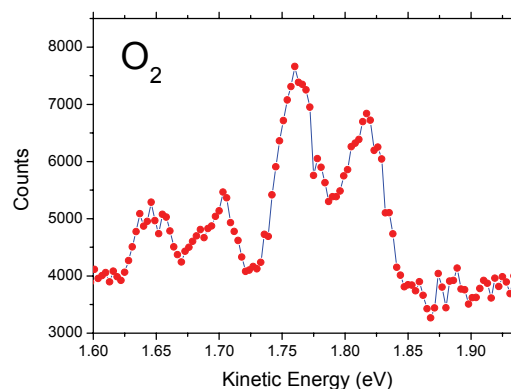


Fig. 2. Doppler profile of atomic autoionization line measured at the lower σ^* resonance position of O₂.

[1] F. Gel'mukhanov, H. Ågren and P. Salek, Phys. Rev. A **57** (1998) 2511.

[2] P. Morin and I. Nenner, Phys. Rev. Lett. **56** (1986) 1913.

[3] O. Björneholm *et al.*, Phys. Rev. Lett. **84** (2000) 2826.

[4] E. Shigemasa *et al.*, submitted to New J. Phys.

High Resolution Electron Spectroscopic Study on Cascade Double Auger Processes After Ar 2p Photoionization

P. Lablanquie¹ and E. Shigemasa²

¹LCPMR, Université Pierre et Marie Curie, 75231 Paris Cedex 05, France

²UVSOR Facility, Institute for Molecular Science, Okazaki 444-8585, Japan

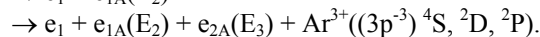
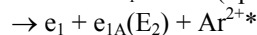
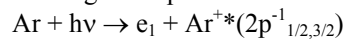
An inner shell vacancy created by photoionization decays either via emission of radiation (fluorescence) or electron emission (Auger decay). The Auger decay is generally more favorable for L-shells, which can occur with emission of one electron (single Auger decay) or of a few electron (multiple Auger decay). The probability of multiple Auger decay is usually lower than that of single Auger decay, but can be high enough to allow experimental observations. Thanks to the recent progress in coincidence measurements, the path toward a deeper understanding of double Auger (DA) decays, where the filling of the inner shell vacancy by an outer electron causes the ejection of two electrons, has been opened [1]. This process can be divided into two categories: the direct double Auger decay (DDA) when the two electrons are emitted simultaneously, and cascade double Auger decay (CDA) when the electron emission occurs in two sequential steps.

More recently, coincidence measurements based on the utilization of magnetic bottle time of flight electron spectrometers have opened the possibility to obtain the complete state selected triple photoionization (TPI) continua over a wide range of kinetic energies [2]. The application of this method to the multi-electron decays of the Ar 2p shell [3] reveals that the position and shapes of the photoelectron lines related to the DA decay differ for the DDA and CDA processes [4]. Moreover, the peak profiles assigned to the DA processes are strongly distorted by post collision interaction (PCI) effects [4]. Post-collision interaction (PCI) is an exchange of energy between charged particles, usually electrons, emitted in single events. PCI in single Auger decay following inner shell photoionization is well investigated both experimentally and theoretically. However, PCI in the DA processes has been much less studied so far.

In order to obtain the detailed spectroscopic information on the Ar²⁺ states involved in the CDA decay, high resolution electron spectroscopy has been applied to the study of the decay processes following the 2p photoionization of Ar. High resolution electron spectra were obtained on BL6U at UVSOR, by using a high performance hemispherical electron energy analyzer MBS-A1, developed by the MB Scientific AB company. The experimental setup is equipped with a gas cell, and reaches a theoretical 1.3 meV (FWHM) resolution when operated with a pass energy of 2 eV and a slit opening of 0.2 mm.

As an example, a high resolution electron spectrum

for the strongest second-step Auger electron in the following CDA process is shown in Fig. 1:



The spectrum of Fig. 1 was measured at the photon energy of 270 eV, in order to minimize the PCI distortion of the peaks. During the course of the experiments, slow drift of the peak positions occurred with time, which was minimized by short scans of less than a few minutes. The main peak at 2.19 eV corresponds to the second Auger electron emitted in the CDA path, associated with the Ar^{2+*} state of 86.31 eV (A1) binding energy, which decays towards the Ar³⁺(3p⁻³ 4S) final state [3]. The shoulder on the high energy side of the peak is attributed to the contribution of a weak CDA path mediated by an Ar²⁺ intermediate state different from A1. Through the analysis of the peak width in a series of similar measurements, it is found that a lifetime broadening of the corresponding intermediate state is 3.7 ± 0.4 meV, taking into account the theoretical resolution of 1.3 meV for the analyzer and the Doppler contribution of 2.9 meV.

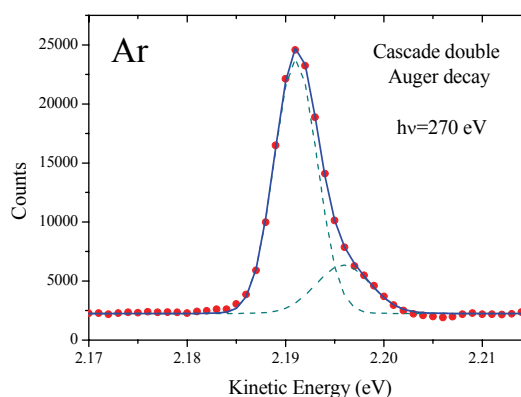


Fig. 1. Cascade double Auger electron spectrum measured with the MBS-A1 analyzer at the photon energy of 270 eV.

[1] F. Penent *et al.*, Phys. Rev. Lett. **95** (2005) 083002.

[2] Y. Hikosaka *et al.*, Phys. Rev. Lett. **102** (2009) 013002.

[3] P. Lablanquie *et al.*, J. Electron Spectrosc. Relat. Phenom. **156-158** (2007) 51.

[4] S. A. Sheinerman *et al.*, submitted to J. Phys. B.

BL5U

Temperature-Dependent Angle-Resolved Photoemission Spectra of EuO Ultrathin Films

H. Miyazaki¹, H. Mitani^{2, 1}, T. Hajiri³, T. Ito³ and S. Kimura^{1, 4}

¹UVSOR Facility, Institute for Molecular Science, Okazaki 444-8585, Japan

²Graduate School of Engineering, Shinshu University, Nagano 380-8553, Japan

³Graduate School of Engineering, Nagoya University, Nagoya 464-8603, Japan

⁴School of Physical Sciences, The Graduate University for Advanced Studies, Okazaki 444-8585, Japan

Europium monoxide (EuO) is a ferromagnetic semiconductor with the Curie temperature (T_C) at around 70 K [1, 2]. The magnetic moment originates from the half-filled $4f$ shell of the Eu^{2+} ion with a spin-only magnetic moment of $S = 7/2$. Recently, we reported that the origin of the magnetic properties of EuO is caused by the hybridizations of the Eu $4f$ –O $2p$ and Eu $4f$ – $5d$ [3–5]. Next step is to investigate the electronic and magnetic structure of thin films of a few nanometers, which is the thickness of spin filter tunnel barriers [3]. Three dimensional angle-resolved photoemission spectroscopy (3D-ARPES) using synchrotron radiation is the most powerful technique to directly determine the electronic band structure. Using this technique we observed the change of the electronic structure across T_C .

Single-crystalline EuO ultrathin films with a thickness of about 2 nm were fabricated by a molecular beam epitaxy (MBE) method. Epitaxial growth of the single-crystalline EuO ultrathin films with the 1×1 EuO (100) patterns was confirmed by a low energy electron diffraction (LEED) method. By an *in-situ* magneto-optical Kerr rotation measurement, was about 40 K that is lower temperature than that of the bulk material. The magnetic properties and 3D-ARPES measurements were performed at the beam line 5U of UVSOR-II combined with the MBE system. The EuO ultrathin films were prepared in the growth chamber and were transferred to a 3D-ARPES chamber under UHV condition. The total energy and momentum resolutions for the ARPES measurement were set 123 meV and 0.020 \AA^{-1} at the Γ point and 45 meV and 0.014 \AA^{-1} at the X point, respectively.

Figure 1 (a) and (b) show the energy distribution curves (EDCs) of Eu $4f$ states for EuO (100) thin films with a thickness of 100 nm and 2 nm near the Γ and X points, respectively. The band width of Eu $4f$ states of the 2 nm thickness sample become narrower compare to those of the 100 nm sample. Across the ferromagnetic phase transition, the EDC with 2 nm thickness shifts to the lower binding energy side only X point. The energy shifts of Eu $4f$ states with 100 and 2 nm thickness samples are 0.3 and 0.16 eV, respectively. This result indicates that the hybridization intensity between the Eu $4f$ and other states become weaker with decreasing thickness. This is consistent with the decreasing T_C .

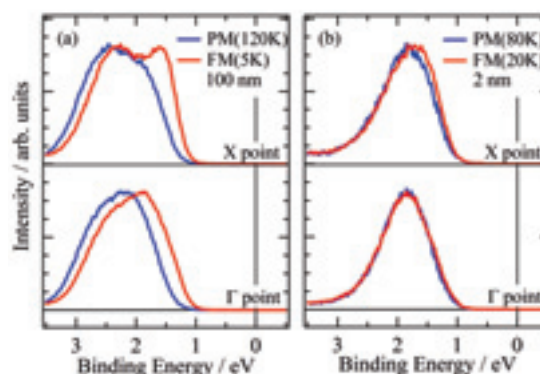


Fig. 1. Temperature-dependent energy distribution curves (EDCs) of Eu $4f$ states with a thickness of 100 nm (a) and 2 nm (b) at the Γ and X point.

- [1] N. Tsuda *et al.*, *Electronic Conduction in Oxides* (Springers College) (1976).
- [2] A. Mauger *et al.*, *J. Phys. (paris)* **39** (1978) 1125.
- [3] H. Miyazaki *et al.*, *Physica B* **403** (2008) 917.
- [4] H. Miyazaki *et al.*, *Jpn. J. Appl. Phys.* **48** (2009) 055504.
- [5] H. Miyazaki *et al.*, *Phys. Rev. Lett.* **102** (2009) 227203.
- [6] M. Müller *et al.*, *J. Appl. Phys.* **105** (2009) 07C917.

XAFS Study on the Surface Structures of the Positive Electrodes for High Power-Type Li-ion Battery Cells

M. Shikano¹, H. Kobayashi¹, H. Hori¹ and Y. Saito²

¹Research Institute for Ubiquitous Energy Devices, AIST, Ikeda, Osaka 563-8577, Japan

²Energy Technology Research Institute, AIST, Tsukuba, Ibaraki 305-8568, Japan

Introduction

Li-ion batteries are an important device because they have a higher energy density than any other type of batteries. Therefore, they are a key component for next generation vehicle such as hybrid electric vehicle (HEV), plug-in HEV (PHEV) and electric vehicle (EV). For these applications, high specific power, long calendar life and safety are very important requirements. In our previous work, degradation mechanism of Li-ion batteries has been studied by various analyzing techniques in synchrotron facilities. We concluded that the major factor of power fade was degradation of positive electrode surface [1-4]. For the degradation control of the oxide surface, we considered coating method by mechanochemical process. The coating material may protect the surface condition of positive electrode from degradation mechanism. In order to determine the coating effect, we performed X-ray absorption fine structure (XAFS) analysis of $\text{LiNi}_{1/3}\text{Mn}_{1/3}\text{Co}_{1/3}\text{O}_2$ (NMC)-based powder and obtain information on their surfaces.

Experimental

NMC was mixed with ZrO_2 (20:1 in weight), and mixture was introduced Nobilta (Type: NOB-MINI, Hosokawa Micron) to treat the surface of NMC for five minutes. Morphology of powders was observed by scanning electron microscopy (SEM). 18650-type cylindrical lithium-ion cells were manufactured using mixture of NMC, acetylene black and poly vinylidene fluoride (PVDF) as positive electrode. XAFS spectra of these powders were measured at UVSOR BL1A for Ni *L*-edge, BL4B for O *K*-edge and BL8B1 for Li *K*-edge. All measurements were performed with Total Electron Yield (TEY) technique at room temperature.

Results

According to SEM observation, submicron-sized ZrO_2 powder dispersed on the surface of NMC after Nobilta treatment. ZrO_2 powders are not dense on the surface of NMC. Morphology of powders of NMC was kept during mechanochemical process.

Obtained O *K*-edge XANES spectra of the powders are shown in Fig. 1. Peaks at 523 and 526 eV of NMC spectrum are concerned with oxygen in layered rock-salt structure and cubic structure respectively [1]. On the other hand, in case of ZrO_2 coated NMC, the peak at 523 eV seems to be enhanced by oxygen of ZrO_2 . A peak of Li_2CO_3 was not observed neither O *K*-edge XANES spectra of NMC and ZrO_2 coated NMC.

After cycle tests, degraded Li-ion cells were disassembled in order to obtain electrode materials. According to O 1s spectra of X-ray photoelectron spectroscopy (XPS), amount of Li_2CO_3 on the surfaces of positive electrodes increased after the tests similar with using $\text{LiNi}_{0.80}\text{Co}_{0.05}\text{Al}_{0.05}\text{O}_2$ positive electrodes [1]. Because XAFS measurement is unsuitable for quantitative analysis of Li_2CO_3 , comparison between XANES and XPS spectra is needed. To determine ZrO_2 -coating effect, detailed structural analysis will be studied using Ni *L*-edge spectra and so on.

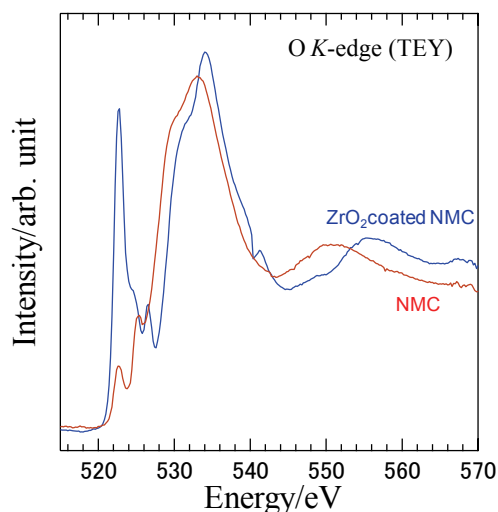


Fig. 1. O *K*-edge XANES spectra of $\text{Li}(\text{Ni}_{1/3}\text{Mn}_{1/3}\text{Co}_{1/3})\text{O}_2$ (NMC). Blue line shows ZrO_2 coated NMC.

[1] H. Kobayashi, M. Shikano, S. Koike, H. Sakaebe and K. Tatsumi, *J. Power Sources* **174** (2007) 380.

[2] M. Shikano, H. Kobayashi, S. Koike, H. Sakaebe, E. Ikenaga, K. Kobayashi and K. Tatsumi, *J. Power Sources* **174** (2007) 795.

[3] M. Rahman and Y. Saito, *J. Power Sources* **174** (2007) 889.

[4] Y. Saito and M. Rahman, *J. Power Sources* **174** (2007) 877.

Photoionization Threshold of Pyrene and Perylene on the Surface of 1-Butyl-3-Methylimidazolium Tetrafluoroborate/Water Mixture

T. Ishioka, N. Inoue, N. Fujii, K. Nishimura and A. Harata

Department of Molecular and Material Science, Kyushu University, Kasuga 816-8580, Japan

Photoionization threshold of polycyclic aromatic molecules has been measured on the surface of the mixture of 1-butyl-3-methylimidazolium tetrafluoroborate and water. The threshold energy of perylene monotonously decreased with the content of water while the value of pyrene had a minimum value around 50%. This result suggests the solvation structure of pyrene at the surface is largely different from those of perylene.

Introduction

Ionic liquids have attracted much attention due to its unique characteristics such as low melting point, high conductivity, negligible vapor pressure, and designable solubility to other solvents. Their special dielectric properties has been applied to enhance photosensitized reactions.[1]

Interfacial properties of ionic liquids also attract large interest because interface structures play a crucial role in transport kinetics and they are related directly to the applications of ionic liquids such as solvent extraction and rechargeable batteries. Interfacial characteristics of ionic liquids have been studied theoretically and experimentally by various groups. Their common conclusion on air/ionic liquid structure is that cations are present at the surface with long alkyl chains directed to the air. This conclusion implies surface molecules suffer different dielectric environment from those in bulk solutions.

The dielectric environment is directly related to the solvation conditions of solute molecules. However, it is difficult to know solvation conditions experimentally at the liquid surfaces. Photoionization is one of such methods to inform dielectric conditions at the surface because the threshold energy is lowered by the polarization energy.

In this report, photoionization thresholds of two aromatic molecules, pyrene and perylene, were measured at the surface of the mixture of 1-butyl-3-methylimidazolium tetrafluoroborate (BMIM-BF₄) and water. The water content was varied from 0-100% and the solvation characteristics were discussed.

Experimental

The monochromated synchrotron light (4-8 eV) was emitted from the chamber to the He-purged cell through an MgF₂ window. The emitted light was reflected on an Al mirror and vertically irradiated on the solution surface through a Cu-mesh electrode. The electrode was set above the liquid surface and high voltage (400 V) was applied to the electrode. The photocurrent was measured by a picoammeter.

Solution samples were prepared by spreading dilute hexane solution of pyrene or perylene on the surface of the mixture of BMIM-BF₄ and water.

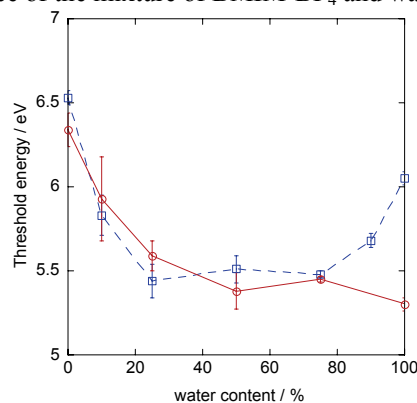


Fig. 1. Photoionization threshold energy of aromatic molecules on the surface of 1-butyl-3-methyl-imidazolium/water mixture. Solid line: perylene. Broken line: pyrene. The threshold value was derived from the mathematical fitting of $I = C(E - E_{th})^{2.5}$. I : photocurrent, C : constant, E : Photon energy.

Results and Discussion

Photoionization threshold energy (E_{th}) on the solution surface can be explained by

$$E_{th} = IP + P^+ \quad (1)$$

where IP is ionization potential in vacuum and P^+ is the polarization energy. IP s of pyrene and perylene are 7.43 eV and 6.96 eV, respectively. From Fig.1 measured photoionization threshold shows 0.9-1.9 eV lower value than each IP , indicating P^+ values. P^+ is the function of surrounding solvent properties such as dielectric constant and coordination numbers. In the case of perylene, the photoionization threshold decreases by increasing the water content showing large solvation energy by surrounding water molecule. In the case of pyrene, the threshold energy once decreases in the same manner as perylene but again increases when water content reaches above 90%. In the previous report [2], pyrene is not solvated at any content of ethylammonium nitrate. These results suggest that the solvation of pyrene is more sensitive to the structure of the surface and solvation become possible only when the dielectric condition is appropriate for pyrene. Further discussion is now in progress including molecular dynamics studies.

[1] N. Inoue, T. Ishioka and A. Harata, Chem. Lett. **38** (2009) 358.

[2] T. Ishioka, N. Inoue and A. Harata, UVSOR Activity Report **36** (2009) 58.

Exciting Phenomena of Matrix in Inorganic Phosphor

M. Ohta

Department of Material Science and Technology, Faculty of Engineering, Niigata University, Ikarashi 950-2181, Japan

It was known that rare earth ions dosed for oral administration to mouse and rat are transferred to blood vessel through the ileum and deposited its teeth and bone, which mainly consists of hydroxyapatite ($\text{Ca}_{10}(\text{PO}_4)_6(\text{OH})_2$) [1, 2]. Recently, rare earth is also useful as a contrast medium for magnetic resonance imaging, restriction enzyme, biocatalyst, and so on in fields of biochemistry, physiology, medicine, etc. However, the behavior of rare earth in the living body system remains an open question until now. We have found that Eu ion substituted Ba ion in Eu doped $\text{Ba}_{10}(\text{PO}_4)_6\text{Cl}_2$ phosphor, which matrix is apatite structure [3]. The Sm ion, Eu ion, Gd ion or Yb ion are also found to substitute easily for calcium ions in hydroxyapatite which is soaked in SmCl_3 , EuCl_3 , GdCl_3 or YbCl_3 aqueous solution, and to play on emission center.

In this study, hydroxyapatite matrix were prepared by soaking in deionized water in order to be compatible with rare earth ion doped hydroxyapatite.

Their characteristics were investigated by photoluminescent property of hydroxyapatite matrix excited by ultraviolet synchrotron orbital radiation light.

Hydroxyapatite matrix were prepared as follows: hydroxyapatite was soaked in deionized water. After

72 hr, hydroxyapatite matrix was separated from deionized water by filtration and then dried by using with infrared ray (unfired sample). The fired sample was prepared by firing the unfired sample at 1,373 K in air.

The photoluminescent property of each sample excited by ultraviolet synchrotron orbital radiation light (BL-1B) was observed by using with a multi-channel analyzer.

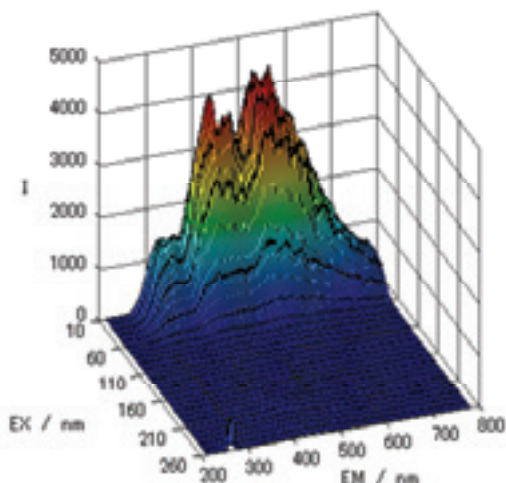
Figure 1 shows photoluminescence spectra of hydroxyapatite matrix samples excited by BL-1B. The photoluminescence spectra of both unfired and fired samples have wide length peak from 250 to 800 nm. These emission peak intensities decreased with the wave length from 10 to 100 nm of excitation wave length. This phenomenon is thought to be due to the multi-electron excitation.

[1] S. Hirano, K. T. Suzuki, *Environ. Health Perspect.* **104** (Supplement 1) (1996) 85.

[2] K. Kostial, B. Kargacin, M. Lendeka, *Int. J. Radiat. Biol. Relat. Stud. Phys. Chem. Med.* **51** (1987) 139.

[3] M. Sato, T. Tanaka, M. Ohta, *J. Electrochem. Soc.* **141** (1994) 1851.

Unfired



Fired

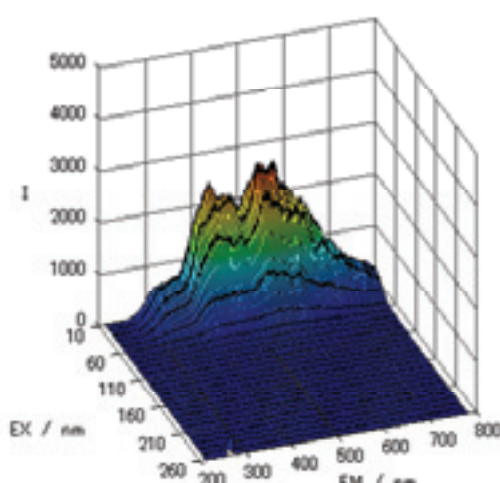


Fig. 1. Photoluminescent spectra of hydroxyapatite matrix excited by ultraviolet synchrotron orbital radiation light.

Field Effect on the Electronic States of Oligothiophene Thin Films Studied by Fluorescence-Yield X-Ray Absorption Spectroscopy

H. S. Kato¹, H. Yamane², N. Kosugi², M. Kawai^{1,3}

¹RIKEN (The Institute of Physical and Chemical Research), Wako 351-0198, Japan

²Institute for Molecular Science, Okazaki 444-8585, Japan

³Department of Advanced Materials Science, University of Tokyo, Kashiwa 277-8501, Japan

Introduction

In order to extend new functionality of electronic devices, the molecular devices have recently been investigated with great efforts. The organic field effect transistor (OFET) is a typical molecular device that controls electric conductivity by injection of carriers into the organic thin film under the applied electric field. Since the organic materials consist of molecular units having their own molecular orbitals, it is not clear that the energy diagram of OFET is exactly the same as that of inorganic semiconductors, i.e., band bending at the interface in the semiconductor side. Therefore, the direct observation of electronic states in the organic thin films under operative conditions has been required.

In this study, we aim to elucidate the electronic state of organic thin films in OFET under the electric field. The fluorescence-yield X-ray absorption spectroscopy (FY-XAS) should be a promising method for detection of inner electronic states of organic devices, because the fluorescent X-rays have a long penetration depth of about 100 nm in most of materials even for the soft X-ray region. In addition, X-rays are not disturbed by applied electric fields, and have different characteristics from the emitted electrons. Thus, we have attempted to utilize FY-XAS for investigation of inner electronic states of OFETs.

Experimental

To investigate the electronic states of OFET, α,ω -dihexylsexithiophene (DH6T) thin films on the SiO₂-covered Si substrates were fabricated at RIKEN. It is known that DH6T FET shows as *p*-type-like I-V property. The fabricated DH6T films were covered homogeneously with a thin Au electrode (25 nm thick). By the incident angle dependence of XAS spectra, we confirmed that the orientation of molecules in the DH6T thin film is not change significantly even after the Au electrode deposition.

The FY-XAS measurements were performed at the BL3U beamline of the UVSOR facility in IMS. The samples were set in a BL3U end-station through a sample-entry system. The fluorescence intensities were measured using a retarding field detector consisting of the MCP system.

Results and Discussion

Figure 1(a) shows the gate bias dependence of the C K-edge FY-XAS spectra of the DH6T films (17 nm thick), in which the spectra at the bias of 0 V and -90 V are plotted. The bias voltage was applied with a

square wave (7 Hz) synchronized to the veto signals to the two fluorescence signal counters for each of the bias conditions, which enabled reliability of the difference spectrum. Figure 1(b) shows the spectral change at the biases from 0 V to -90 V, in which the sharp peaks at the photon energies around 285 eV on the original spectra are absent, while the broader components at 288 and 291 eV appears in the difference spectrum. In Fig. 1(b), the spectral change of a DH6T-lacked sample at the same bias conditions is also shown, and no meaningful spectral changes are confirmed. These results clearly show that the observed spectral change is caused by an electronic state modification in the DH6T thin films under the applied bias. From the bias dependence of the FY-XAS spectra, the spectral change is considered as a result of distorted molecular orbitals by the applied electric field.

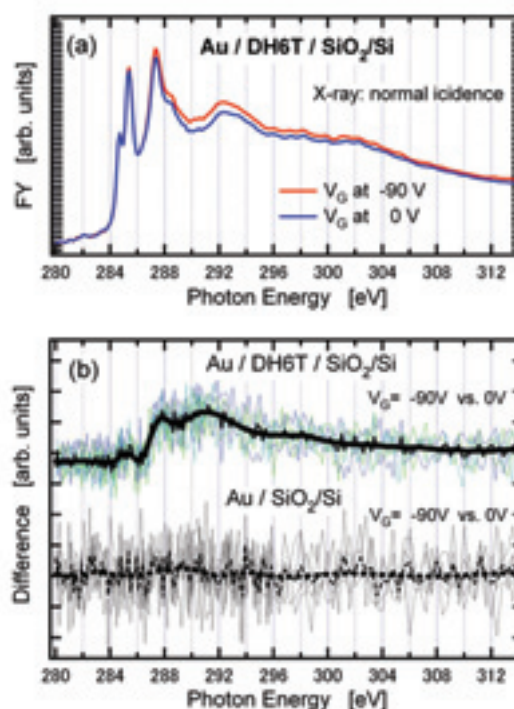


Fig. 1. Bias dependence of the C K-edge fluorescence-yield XAS spectra of the Au-covered DH6T films (17 nm thick) measured at normal incidence geometry: (a) the spectra at the biases of 0 V and -90 V, (b) spectral changes at the biases from 0 V to -90 V (solid lines) as compared with that of a DH6T-lacked sample (broken lines).

Temperature-Dependent Magnetic Circular Dichroism Spectra of Ferromagnetic Semiconducting EuO Thin Films

H. Miyazaki¹, H. Mitani^{2,1}, T. Hajiri³, T. Ito³, Y. Takagi^{4,5}, T. Nakagawa^{4,5}, Y. Yamamoto⁴
T. Yokoyama^{4,5} and S. Kimura^{1,5}

¹*UVSOR Facility, Institute for Molecular Science, Okazaki 444-8585, Japan*

²*Graduate School of Engineering, Shinshu University, Nagano 380-8553, Japan*

³*Graduate School of Engineering, Nagoya University, Nagoya 464-8603, Japan*

⁴*Department of Materials Molecular Science, Institute for Molecular Science, Okazaki 444-8585, Japan*

⁵*School of Physical Sciences, The Graduate University for Advanced Studies, Okazaki 444-8585, Japan*

Europium monoxide (EuO) is a ferromagnetic semiconductor with the Curie temperature (T_C) at around 70 K [1, 2]. In the electron doping case by Eu excess or substitution of Eu^{2+} by Gd^{3+} or La^{3+} ion, T_C increases up to 200 K and the electrical resistivity drops twelve-order of magnitude below T_C originating in a metal-insulator transition (MIT) [2-4]. To reveal the origin of these physical properties of EuO, it is important to clarify the relation of the electronic structure to the magnetic property. Soft X-ray Magnetic Circular Dichroism (XMCD) is a powerful technique to determine a magnetic configuration of electronic structure. Using this technique we observed the electronic structure of the Eu 4f states under a magnetic field.

Single-crystalline EuO thin films with a thickness of about 50 nm were fabricated by a molecular beam epitaxy (MBE) method. Epitaxial growth of single-crystalline EuO thin films with the 1×1 EuO (100) patterns was confirmed with low energy electron diffraction (LEED) and reflection high energy electron diffraction (RHEED) methods. T_C measured with a Superconducting QUantum Interference Device (SQUID) magnetometer was 71 K [5]. *In situ* Eu M -edge X-ray adsorption spectra (XAS) and XMCD measurements were performed using a total electron yield mode at the bending magnet beamline 4B of UVSOR-II combined with the MBE system. The EuO thin films were prepared in the growth chamber and were transferred to a superconducting magnet chamber under UHV condition.

Figure 1 shows the temperature-dependent Eu M_5 XMCD spectra of an EuO (100) thin film recorded at the magnetic field H of ± 1 T. The magnetic field was applied perpendicular to the sample surface. The XMCD spectrum, which is obtained by the subtraction of the XAS spectrum of $H = -1$ T from that of 1 T, is in good agreement with previously results and theoretical spectrum for a Eu^{2+} ion with $L = 0$ and $S = 7/2$ [6, 7]. The inset of Fig.1 shows the temperature dependence of the integration of the MCD spectrum and the magnetization curve measured by SQUID. The MCD signals are in good agreement with the magnetization curve.

To summarize, we succeeded to measure temperature dependent XMCD spectra of single-crystalline EuO (100) thin films. The method is a good probe to investigate the electronic structure of each element. The detailed analysis and further study on the magnetic electronic structure of EuO thin films are in progress.

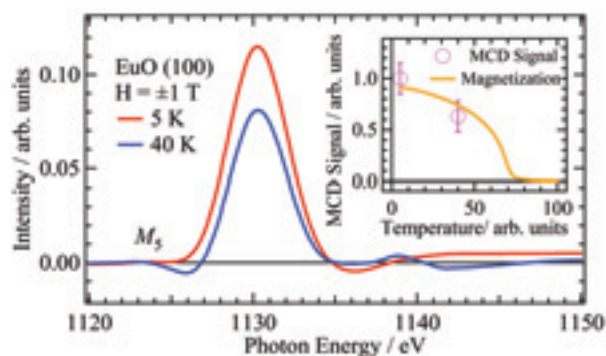


Fig. 1. Temperature-dependent Eu M_5 XMCD spectra of EuO thin films recorded at ± 1 T. The inset shows the temperature dependence of the integration of the MCD spectrum and the magnetization curve.

- [1] N. Tsuda *et al.*, *Electronic Conduction in Oxides* (Springers College) (1976).
- [2] A. Mauger *et al.*, *J. Phys. (paris)* **39** (1978) 1125.
- [3] Y. Shapira, S. Foner and T. B. Reed, *Phys. Rev. B* **8** (1973) 2299 ; **8** (1973) 2316.
- [4] H. Miyazaki *et al.*, *Appl. Phys. Lett.* (2010) *in press*.
- [5] H. Miyazaki *et al.*, *Jpn. J. Appl. Phys.* **48** (2009) 055504.
- [6] J. Holroyd *et al.*, *J. Appl. Phys.* **95** (2004) 6571.
- [7] J. B. Goedkoop *et al.*, *Phys. Rev. B* **37** (1988) 2086.

Magnetism of Mn and Fe Ultrathin Films on Bi(0001)

T. Nakagawa, Y. Takagi, I. Yamamoto and T. Yokoyama

Department of Material Molecular Science, Institute for Molecular Science, Okazaki
444-8585, Japan

Elements with large atomic number have strong spin orbit coupling (SOC). Their compounds are used as magnetic materials since they show large magnetic anisotropy due to SOC. Bi is the largest atom with stable isotopes and one of the Bi-Mn compounds is well known as a magnetic material, which shows large uniaxial anisotropy derived from SOC by Bi and exhibits a perpendicular magnetization and a large magneto-optical constant. Since the large SOC of Bi is a good candidate to give strong anisotropy magnetic properties, we have studied the magnetic properties of Mn and Fe on Bi(0001) surface using x-ray magnetic circular dichroism (XMCD).

XMCD experiments were carried out at BL4B, which delivers circular polarized light. The end station was an ultrahigh vacuum chamber equipped with a superconductive magnet (5 T) and a low temperature insertion of 5 K [1]. Fe and Mn were deposited onto a Bi(0001) crystal, which was cleaned by Ar ion sputtering and annealing. After the deposition at 300 K, the samples were annealed up to 400 K to obtain good surface ordering, as judged by low energy electron diffraction (shown in Fig.1). The Mn and Fe coverages were 0.5 ML (1ML = $1.11 \times 10^{19} \text{ m}^{-2}$), determined from a calibration of the evaporators. The Mn/Bi(0001) and Fe/Bi(0001) exhibits similar diffraction patterns ($n \times 1$) structure, $n = 3$ and 4).

Figure 1 shows an XMCD spectrum for Mn/Bi(0001) at $T_s = 5 \text{ K}$ and $H = 5 \text{ T}$. The x-ray absorption spectra (XAS) taken at $H = \pm 5 \text{ T}$ are almost identical, resulting in no magnetic signal. Thus the Mn/Bi(0001) is not ferromagnetic even at 5 K.

Figure 2 shows XMCD result for Fe/Bi(0001) at $T_s = 5 \text{ K}$ and $H = \pm 5 \text{ T}$. Figure 2(a) shows magnetization curves for the photon incidence angle of 55° (GI) and 0° (NI) from the surface normal. The magnetization in the case of GI is almost saturated at $H = 2.5 \text{ T}$, while the sample with the magnetic field normal to the surface is not magnetically saturated even at $H = 5 \text{ T}$. Therefore the magnetization easy axis is within the film plane. The evaluated effective spin magnetic moment (m_s^{eff}) and orbital magnetic moment (m_{orb}) for Fe are $1.40 \mu_B$ and $0.11 \mu_B$, respectively. Its spin magnetic moment is much smaller than that for bulk Fe ($2.2 \mu_B$). The reduced magnetic moment could be due to the alloying of Fe with Bi. The ratio between the spin and orbital magnetic moments ($m_{\text{orb}}/m_s^{\text{eff}}$) is 0.08, larger than that for bulk Fe. The obtained anisotropy constant is $\sim 100 \mu\text{eV}/\text{atom}$.

In conclusion, the Mn(0.5 ML)/Bi(0001) surface

does not show ferromagnetism even at $T_s = 5 \text{ K}$ in contrast to the MnBi alloy. This is probably ascribed to different crystalline structures. The Fe(0.5 ML)/Bi(0001) is ferromagnetic and shows an in-plane magnetization easy axis and its anisotropy constant is $100 \mu\text{eV}/\text{atom}$.

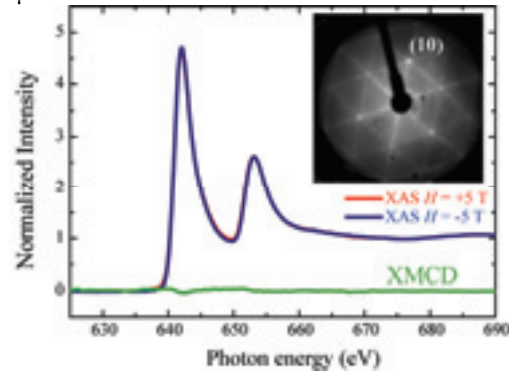


Fig. 1. XAS and XMCD spectra at Mn L edges for Mn(0.5 ML)/Bi(0001) surface. The inset shows a corresponding diffraction pattern.

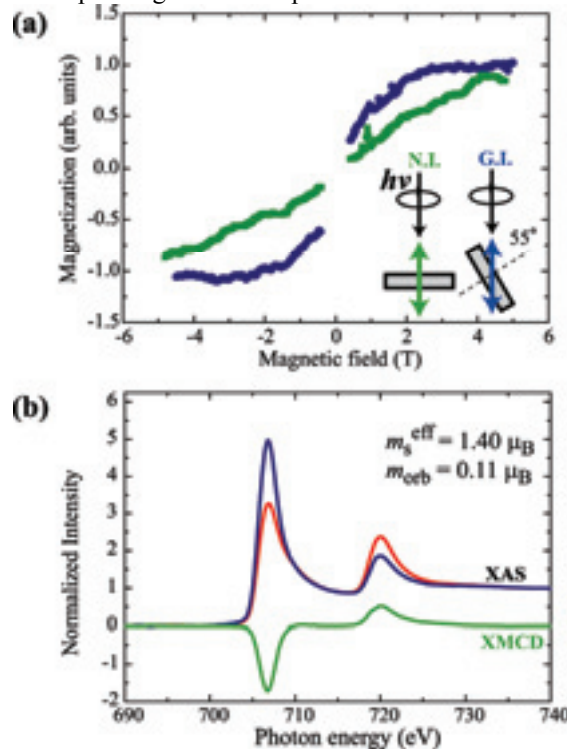


Fig. 2. (a) Magnetization curves taken at Fe L_3 edge on Fe(0.5 ML)/Bi(0001) for the normal incidence (N.I.) and grazing incidence (G.I.) (b) XAS and XMCD spectra at Fe L edges at $H = 5 \text{ T}$.

[1] T. Nakagawa, Y. Takagi, Y. Matsumoto and T. Yokoyama, Jpn. J. Appl. Phys. **47** (2008) 2132.

Oscillatory Magnetic Anisotropy in Fe/Ag(116)

M. Przybylski¹, F. Yildiz¹, U. Bauer¹, Y. Takagi², I. Yamamoto², T. Nakagawa²
and T. Yokoyama²

¹Max-Planck-Institut für Mikrostrukturphysik, Weinberg 2, 06120 Halle, Germany

²Institute for Molecular Science, Okazaki 444-8585, Japan

Magnetic thin films deposited on vicinal single crystal surfaces are well known to exhibit double loop hysteresis along the magnetically hard axis within the surface plane, in which the separation between the two loops is called a shift field H_s . Very recently, Li *et al.* [1] discovered a very interesting phenomenon in Fe/Ag(1 1 10), whereby the shift field measured along the \perp step direction (hard axis within the film plane) shows an oscillatory structure as a function of Fe thickness at 5 K, while room temperature measurements give a monotonic increase with Fe thickness. The oscillation period is ~ 5.7 ML, which might correspond to the quantum well state. The finding should be ascribed to the oscillatory change in magnetocrystalline or magnetoelastic anisotropies. In this work, we have investigated magnetic anisotropy of Fe/Ag(116) from the view point of microscopic magnetic orbital magnetic moments by recording angle dependent Fe L-edge x-ray magnetic circular dichroism (XMCD). The reason for the replacement of the substrate from Ag(1 1 10) to Ag(116) is for possible enhancement of the oscillation amplitude.

An Ag(116) single crystal was cleaned by repeated cycles of Ar⁺ sputtering and annealing, and the surface cleanliness and order were verified by LEED/AES and x-ray absorption spectroscopy. The LEED pattern exhibits very beautiful double spots typical to vicinal surfaces. Fe was deposited on clean Ag(116) at room temperature to provide wedge-shaped or flat films.

In situ Fe L-edge XMCD spectra were recorded with a total electron yield mode from a sample drain current. The magnetic field applied with a JANIS UHV superconducting magnet [2] was ± 5 or ± 0 T, and the sample temperature was 5.0 K. Angle dependence was examined to derive components of magnetic moments along \perp surface, \parallel step, and \perp step (\parallel surface). The magnetization along any direction was confirmed to be well saturated at ± 5 T.

Figure 1 shows the angle dependent XMCD spectra of 7.2 and 7.4 ML Fe/Ag(116) at remanence magnetization. By analyzing the angle dependence, the remanence magnetization vectors can be obtained, which are depicted in the figure. At 7.4 ML the remanence magnetization is parallel to the step, while at 7.2 ML it is almost perpendicular to the surface. An abrupt spin reorientation transition is confirmed around 7.3 ML.

The orbital magnetic moments m_{orb} were evaluated

by using the well established XMCD sum rule. The m_{orb} values along \parallel surface and \parallel step shows gradual monotonic decrease as the Fe thickness. On the contrary, those along \perp step (\parallel surface) exhibits two sharp minima around 5 and 11 ML. The magnetic anisotropy within the surface plane is maximized at 5 and 11 ML. The period of ~ 6 ML agrees well with the previous value [1]. Note that in the previous experiments using magneto-optical Kerr effect measurements, thinner ranges below ~ 10 ML Fe were not investigated due to the spin reorientation transition to perpendicular magnetization as in Fig. 1. In this work, the presence of the oscillatory behavior is newly confirmed even in thinner Fe films exhibiting perpendicular magnetization.

Conclusively, the oscillatory behavior of the shift field is ascribed to the periodic change of the orbital magnetic moment along the \perp step (\parallel surface) direction.

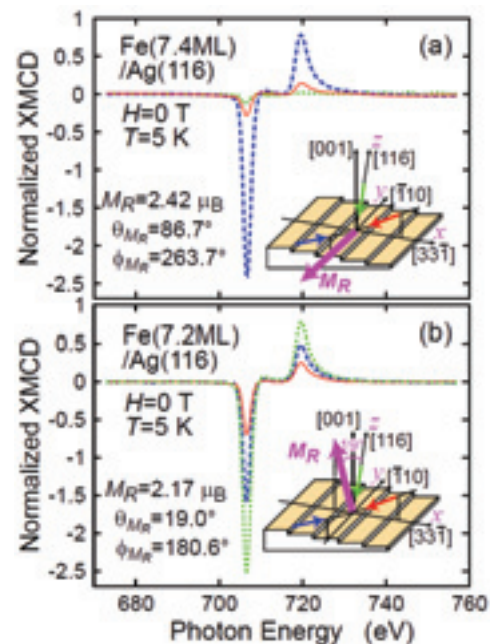


Fig. 1. Fe L-edge XMCD spectra of (a) 7.4 ML and (b) 7.2 ML Fe/Ag(116) at $T=5.0$ K and $H=0$ T. Determined remanence magnetizations are depicted in insets.

[1] J. Li, M. Przybylski, F. Yildiz, X. D. Ma and Y. Z. Wu, Phys. Rev. Lett. **102** (2009) 207206.

[2] T. Nakagawa, Y. Takagi, Y. Matsumoto and T. Yokoyama, Jpn. J. Appl. Phys. **47** (2008) 2132.

Magnetic Films Formed on the Si Substrates with Passivation Layers

Y. Takagi^{1,2}, K. Isami², I. Yamamoto¹, T. Nakagawa^{1,2} and T. Yokoyama^{1,2}

¹Institute for Molecular Science, Okazaki 444-8585, Japan

²The Graduate University for Advanced Studies, Okazaki 444-8585, Japan

We report on a study of magnetic films formed on the Si substrate by means of X-ray magnetic circular dichroism (XMCD) at BL4B, equipped with a superconducting magnet system.

The sample preparation and XMCD measurement were carried out in a UHV chamber. A Si(111) wafer was degassed in the UHV chamber over 5 h and was flashed at 1200 °C. After these cleaning procedures, the Si(111) surface exhibits a 7×7 reconstruction. We used Si(111)- $\sqrt{3}\times\sqrt{3}$ Ag and silicon nitride (SiN) surfaces as passivation layers. The former was prepared by depositing silver of 1 monolayer (ML) on the Si(111)- 7×7 substrate at 450 °C. The latter was obtained by exposing to low energy (200 eV) N^+ bombardment with pressure (2×10^{-6} Torr) at room temperature (RT) for 20 min and subsequently flashing at 1200 °C. The ordering and cleanness of the surfaces were checked by low energy electron diffraction and Auger electron spectroscopy. Pure iron (99.99%) was evaporated from an electron-beam evaporator. In this report, we define a unity monolayer as atomic concentration of Fe of 7.83×10^{14} atoms/cm², which corresponds to the Si atomic density of the Si(111)- 1×1 surface.

Figure 1 gives XMCD spectra of Fe L_{III,II}-edge measured under the magnetic field of ± 5 T at a sample temperature of 5 K. The magnetization of the Fe film on Si(111)- $\sqrt{3}\times\sqrt{3}$ Ag is stronger than that on Si(111)- 7×7 substrate. Regarding bulk iron silicide, the magnetic moment decreases with increasing the composition ratio of Si to Fe and becomes almost zero when the stoichiometry of Fe:Si is 1:1. The XMCD results indicate that the films contain the Fe-rich silicide and the $\sqrt{3}\times\sqrt{3}$ Ag layer on Si(111) suppresses the reactivity of the substrate with Fe. On the other hand, the spin magnetic moment of the Fe film on SiN obtained by XMCD is $2.17\mu_B$, which is almost the same as the bulk Fe of $2.2\mu_B$. The passivation effect of SiN is stronger than that of the $\sqrt{3}\times\sqrt{3}$ Ag layer and the reaction between Fe and Si is quenched almost completely.

To investigate the passivation effect to annealing, we have measured the XMCD spectra for the Fe films grown on the substrates held at 200 °C (Fig. 2). For the film on $\sqrt{3}\times\sqrt{3}$ Ag layer, the magnetization is quite small because the silicidation is enhanced with increasing growth temperature. On the other hand, the decrease in the magnetization on SiN is much smaller than that on $\sqrt{3}\times\sqrt{3}$ Ag. The passivation effect of SiN is more effective than that of $\sqrt{3}\times\sqrt{3}$ Ag in the heating deposition at elevated temperature.

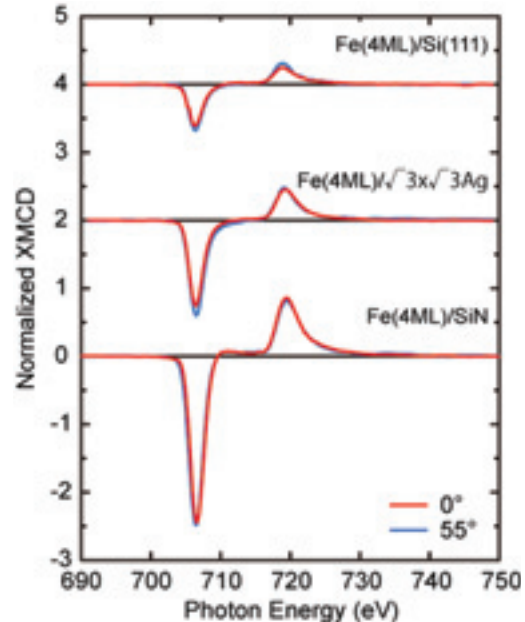


Fig. 1. Fe L_{III,II}-edge XMCD spectra of 4ML Fe film deposited on Si(111)- 7×7 , Si(111)- $\sqrt{3}\times\sqrt{3}$ Ag, SiN substrates at RT, taken at $T=5$ K and $H=\pm 5$ T, with x-ray incident angles $\theta=0^\circ$ (red line) and $\theta=55^\circ$ (blue line).

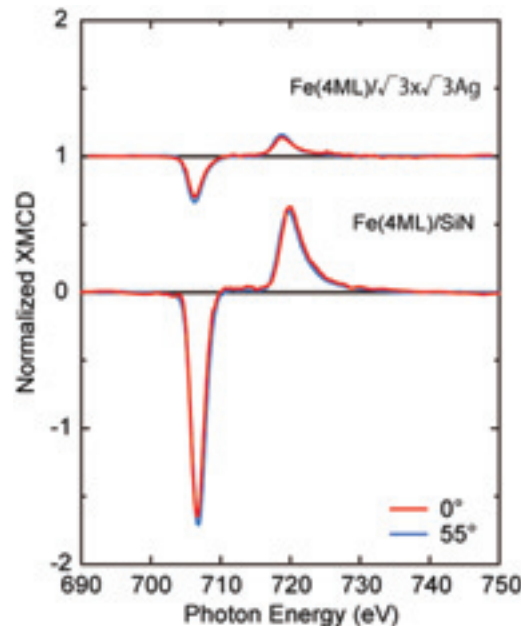


Fig. 2. Fe L_{III,II}-edge XMCD spectra of 4ML Fe films deposited on Si(111)- $\sqrt{3}\times\sqrt{3}$ Ag and SiN at 200 °C, taken at $T=5$ K and $H=\pm 5$ T, with x-ray incident angles $\theta=0^\circ$ (red line) and $\theta=55^\circ$ (blue line).

Magnetic Property of Manganese Phthalocyanine on Ferromagnetic Thin Films Studied by XMCD

I. Yamamoto¹, K. Eguchi², T. Nakagawa^{1,2}, Y. Takagi^{1,2} and T. Yokoyama^{1,2}

¹Department of Molecular Structure, Institute for Molecular Science, Okazaki 444-8585, Japan

²School of Physical Science, The Graduate University for Advanced Studies (SOKENDAI), Okazaki 444-8585, Japan

To realize molecular spintronic devices, it is important to understand the magnetic coupling between molecules and magnetic metal surfaces as well as the magnetization of organic materials. Metal phthalocyanines (Pc's) have attracted much interest due to their characteristic electronic, optical and magnetic properties. Manganese phthalocyanine (MnPc) is one of the interesting molecules because only β -phase MnPc is known as a ferromagnet among undoped Pc's [1]. Isolated MnPc in Ar matrix has an orbital degenerate ground state, which leads to large orbital magnetic moments [2]. Moreover, the epitaxial MnPc film grown on H-Si(111) has a large perpendicular magnetic anisotropy [3]. In this study, we have investigated magnetic properties of MnPc thin films on ferromagnetic metal films.

Co films were prepared on a clean Cu(001) substrate by the e-beam evaporation method at room temperature (RT). Purified MnPc was deposited at RT by sublimation. The Co L - and Mn L -edge XMCD measurements were done using a system (JANIS: 7THM-ST-UHV) with a superconducting magnet and a liq. He cryostat. The XMCD spectra were recorded with reversal of the magnetic field. The XMCD measurements were done at 5 K.

Figure 1 shows magnetization curves for MnPc/Co(3 ML)/Cu(001) recorded with the Co L_3 intensity. By depositing MnPc monolayer, the anisotropic magnetic field H_a decreases from 6.2 to 3.2 T, implying that the MnPc-Co interface favors perpendicular magnetization, though the magnetization easy axis is still in-plane. The effective magnetic anisotropy energy K^{eff} were obtained as -230 and -70 $\mu\text{eV}/\text{atom}$ for the bare Co (3 ML) and the MnPc (1 ML) covered films, respectively.

The Mn L -edge XMCD spectra for various MnPc thickness on Co(3 ML)/Cu(001) measured at incident angle $\theta_i=55^\circ$ from the surface normal and at 5 K are shown in Fig. 2. For the monolayer MnPc film, the Mn L -edge XMCD displays the same sign as the Co L -edge XMCD. The Mn L_3 XMCD intensity at 0.3 T is about 80 % of the saturation value, which coincides with the magnetization curves recorded with the Co L_3 intensity. Thus the magnetization behavior of the Mn atom in phthalocyanine is the same as that of the ferromagnetic Co film. These results suggest that the presence of a ferromagnetic exchange coupling between Mn and Co. Above 2 ML, however, the Mn

L_3 XMCD intensity at 0.3 T is not consistent with Co L_3 intensity, and the magnetization behavior of the Mn atom is paramagnetic. In addition, the Mn L_2 XMCD sign is same negative as the Mn L_3 , indicating an intrinsic large orbital magnetic moment of MnPc. Therefore substantial interaction is present at the MnPc-Co interface, resulting in the ferromagnetic exchange coupling between MnPc and Co.

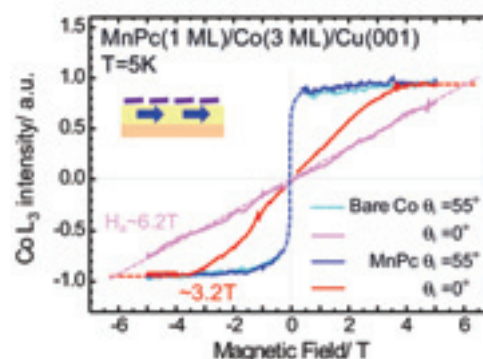


Fig. 1. Magnetization curves for bare Co (3 ML) and MnPc(1 ML) covered films at 5 K with $\theta=0^\circ$ (surface normal) and 55° .

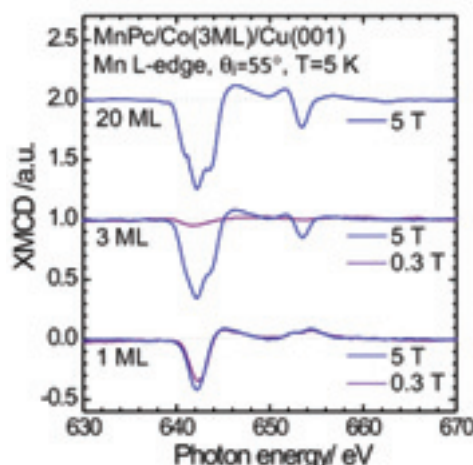


Fig. 2. Mn L -edge XMCD spectra for various MnPc thickness on Co(3 ML)/Cu(001) measured at incident angle $\theta_i=55^\circ$ from the surface normal and at 5 K.

[1] H. Miyoshi *et al.*, Bull. Chem. Soc. Jpn. **46** (1973) 2724.

[2] B. E. Williamson *et al.*, J. Am. Chem. Soc. **114** (1992) 2412.

[3] H. Yamada *et al.*, J. Chem. Phys. **108** (1998) 10256.

A Topological Metal at the Surface of an Ultrathin BiSb Alloy Film

T. Hirahara¹, Y. Sakamoto¹, Y. Saisyu¹, H. Miyazaki², S. Kimura²,
T. Okuda^{3,4}, I. Matsuda⁴, S. Murakami⁵ and S. Hasegawa¹

¹Department of Physics, University of Tokyo, Tokyo 113-0033, Japan

²UVSOR Facility, Institute for Molecular Science, Okazaki 444-8585, Japan

³Hiroshima Synchrotron Radiation Center, Hiroshima University,
Higashi-Hiroshima 739-0046, Japan

⁴Synchrotron Radiation Laboratory, ISSP University of Tokyo, Kashiwa 277-8581, Japan

⁵Department of Physics, Tokyo Institute of Technology, Tokyo 152-8551, Japan

Recently there has been growing interest in *topological insulators* or the *quantum spin Hall (QSH) phase*, which are insulating materials with bulk band gaps but have metallic edge states that are formed topologically and robust against any non-magnetic impurity [1]. In a three-dimensional material, the two-dimensional surface states correspond to the edge states (topological metal) and their intriguing nature in terms of electronic and spin structures have been experimentally observed in bulk $\text{Bi}_{1-x}\text{Sb}_x$ single crystals [2-4]. However, if we want to investigate the transport properties of these topological metals, high purity samples as well as very low temperature will be needed because of the contribution from bulk states or impurity effects. In a recent report, it was also shown that an intriguing coupling between the surface and bulk states will occur [5] for the single crystal BiSb. A simple solution to this bothersome problem is to prepare a topological metal on an ultrathin film, in which the surface-to-bulk ratio is drastically increased.

Therefore in the present study, we have investigated if there is a method to make an ultrathin $\text{Bi}_{1-x}\text{Sb}_x$ film on a semiconductor substrate. From reflection high-energy electron diffraction observation, it was found that single crystal $\text{Bi}_{1-x}\text{Sb}_x$ films ($0 \leq x < 0.32$) as thin as ~ 30 Å can be prepared on Si(111)-7x7. The core level spectra of Bi *5d* and Sb *4d* showed that the stoichiometry of ratio of Bi and Sb is fairly homogeneous over the whole sample. Figure 1 represents the Fermi surface of 40 Å thick $\text{Bi}_{0.92}\text{Sb}_{0.08}$ (a) and $\text{Bi}_{0.84}\text{Sb}_{0.16}$ (b) films mapped by angle-resolved photoemission spectroscopy. The basic features of the electronic structure of these surface states were shown to be the same as those found on bulk surfaces, meaning that topological metals can be prepared at the surface of an ultrathin film. Finally, the transport properties of such films were characterized by *in situ* monolithic micro four-point probes [6]. The temperature dependence of the resistivity for the $x=0.1$ samples was insulating when the film thickness was 240 Å. However, it became metallic as the thickness was reduced down to 30 Å, indicating surface-state dominant electrical conduction for the thinnest films. Therefore by investigating the properties of these ultrathin BiSb alloy films, it can be expected that we can verify the

intriguing topological nature of the edge states.

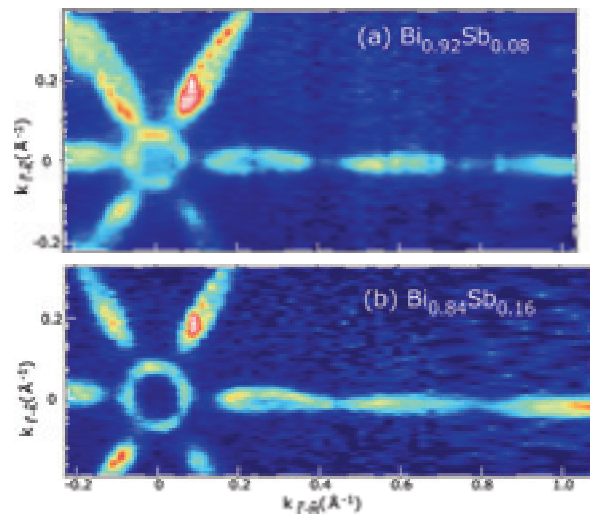


Fig. 1. The Fermi surface mapped by ARPES at 10 K for 40 Å thick $\text{Bi}_{0.92}\text{Sb}_{0.08}$ (a) and $\text{Bi}_{0.84}\text{Sb}_{0.16}$ (b) films, respectively. A circularly polarized light was used at the photon energy of 28 eV.

- [1] L. Fu and C. L. Kane, Phys. Rev. B **76** (2007) 045302.
- [2] D. Hsieh, D. Qian, L. Wray, Y. Xia, Y. S. Hor, R. J. Cava and M. Z. Hasan, Nature **452** (2008) 970.
- [3] D. Hsieh, Y. Xia, L. Wray, D. Qian, A. Pal, J. H. Dil, J. Osterwalder, F. Meier, G. Bihlmayer, C. L. Kane, Y. S. Hor, R. J. Cava and M. Z. Hasan, Science **323** (2009) 919.
- [4] A. Nishide, A. A. Taskin, Y. Takeichi, T. Okuda, A. Kakizaki, T. Hirahara, K. Nakatsuji, F. Komori, Y. Ando and I. Matsuda, Phys. Rev. B. **81** (2010) 041309(R).
- [5] A. A. Taskin and Y. Ando, Phys. Rev. B **80** (2009) 085303.
- [6] T. Tanikawa, I. Matsuda, R. Hobara and S. Hasegawa, e-Journal of Surface Science and Nanotechnology, **1** (2003) 50.

NEXAFS Study on the Synchrotron Radiation Effect on the Local Structure of Highly-Hydrogenated Diamond-Like Carbon Film

K. Kanda and S. Matsui

Laboratory of Advanced Science and Technology for Industry, University of Hyogo, Kamigori, Hyogo, 678-1205 Japan

DLC films are generally known to be etched by the exposure to the synchrotron radiation (SR) in the soft x-ray region under oxygen gas atmosphere, while they are not etched in the absence of oxygen gas.¹⁾ Recently, the irradiation of soft x-ray against highly-hydrogenated DLC (H-DLC) films in the vacuum are reported to bring about the departure of hydrogen and increase in the film density, hardness and refractive index.²⁾ In the present study, we investigated the SR effect on the highly-hydrogenated DLC film in the vacuum. Highly-hydrogenated DLC thin films were deposited on Si wafer with 200 nm thickness by amplitude-modulated RF plasma-CVD method. The irradiation of SR against DLC films was carried out at BL-6 of NewSUBARU.³⁾ The SR at the BL-6 sample stage had a continuous spectrum from IR to soft X-ray, which was lower than 1 keV.

The hydrogen content in the DLC film was determined with the combination of ERDA/RBS techniques. It decreases exponentially with a soft X-ray exposure dose in the high-hydrogenated DLC film. Thus, the departure of the hydrogen was observed from high-hydrogenated DLC films, while was not observed from the low-hydrogenated DLC film by soft X-ray irradiation.

The measurement of NEXAFS spectra was performed at BL8B1 of UVSOR. X-ray beam in the desired energy range was extracted using monochromator equipped with a 540 lines/mm laminar grating which had a 15 m radius. The carbon K edge absorption NEXAFS spectra were measured in the energy range of 275–320 eV. The energy resolution of x-ray beam was estimated to be ≈ 0.5 eV in full width at half maximum with slit width of 20 μm . The reading of monochromator was calibrated against the pre-edge resonance corresponding to the carbon $1s \rightarrow \pi^*$ transition appeared at 285.3 eV in the NEXAFS spectrum of graphite. The detection of electrons coming from the sample was performed in the total electron yield mode. The intensity of incident x-ray was measured by detecting the photocurrent from a gold film. The NEXAFS spectrum was given by the ratio of the photocurrent from the sample to that from the gold film.

Observed NEXAFS spectra are shown in Fig. 1. In the NEXAFS spectrum of as-deposited highly-hydrogenated DLC film, three peaks (orange arrow) were observed in the 283–308 eV. These peaks were not observed in the NEXAFS spectra of typical DLC films. In addition, these peaks were disappeared after the SR irradiation of 3600 mA·h. Therefore,

these peaks can be regarded to generate from the storage of hydrogen, which was departed by the SR exposure.

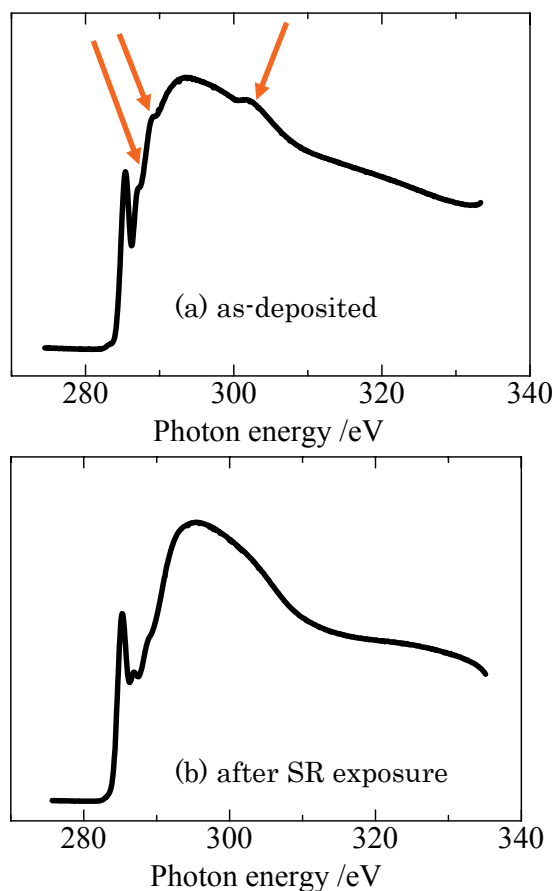


Fig. 1. C K-edge NEXAFS spectra of high-hydrogenated DLC films: (a) as-deposited, and (b) after SR exposure of 3600 mA·h.

[1] H. Kyuragi and T. Urisu, *Appl. Phys. Lett.* **50** (1987) 1254.

[2] H. Matsuura, S. Okubo, K. Oda and T. Ushiro, *SEI Technical Review* **171** (2007) 39 (Japanese).

[3] K. Kanda, T. Ideta, Y. Haruyama, H. Ishigaki and S. Matsui, *Jpn. J. Appl. Phys.* **42** (2003) 3983.

Electronic Structure and Molecular Orientation of Picene Film

D. Ikeda¹, S. Hosoumi², R. Tateishi¹, T. Nishi^{2,3}, S. Nagamatsu³, N. Ueno^{1,2} and S. Kera^{1,2,3}

¹ Faculty of Engineering, Chiba University, Chiba 263-8522, Japan

² Graduate School of Advanced Integration Science, Chiba University, Chiba 263-8522, Japan

³ Institute for Molecular Science, Okazaki 444-8585, Japan

Picene has a larger band gap (3.3eV) than polyacene compounds such as pentacene (1.8eV) which has been widely researching as an organic device material. Recently picene has a paid attention to as a new candidate for organic device material because of high mobility (3cm²/Vs) and superconductivity (Tc~20K) with K doping [1].

In this study, we measured the electronic structure of picene film prepared on highly oriented pyrolytic graphite (HOPG) by angle-resolved ultraviolet photoelectron spectroscopy (ARUPS). ARUPS has been known as a powerful technique to obtain crucial information on electronic band structure for various kinds of materials. Moreover, for organic thin films, information on the geometrical structure of the thin films can be discussed in accordance with a quantitative analysis of the ARUPS intensity using photoelectron scattering theory [2].

Experimental

A cleaved HOPG (ZYA grade) is used as the inert substrate. The sample molecule was degassed under UHV, and the films are prepared on a clean substrate kept at 295K under the deposition rate of ~0.6nm/min. The experimental geometry is shown in Fig. 1 (b). The dependences of ARUPS on photoelectron emission angle (θ) were analyzed using multiple-scattering theory combined with molecular orbital (MST/MO) calculation [2]. We have calculated the θ pattern from a free molecule itself.

Results and Discussion

Figure 1 (c) shows the UPS of picene thick film (ca.10nm) on HOPG at photon energy ($h\nu$) of 28eV and $\theta=30^\circ$. We found six peaks A-F at the valence top region and they are represented well by the calculation for a free molecule, indicating the intermolecular interaction is very small in this film. These bands are all assigned to π MOs from the θ dependence (Fig. 2 (a)). The ionization energy of picene film is found to be 6.1eV.

The θ dependence of peak A (HOMO) in polar plot is shown in Fig.2 (b). Intensities of each peak are analyzed for the deconvoluted spectra where the contribution of HOPG substrate was subtracted because the thin film takes to form an island structure. The θ dependences of other peaks B-F are similar to that of HOMO, though they are categorized into two groups in the detailed pattern (not shown).

For the HOMO, the observed intensity gives the maximum at around 40° . The calculated intensities are evaluated for the molecular tilt angles β , which is inclined angle from the long-molecular axis, and γ , which is angle from the short axis (see the Fig. 1 (b)).

Azimuthal angle is integrated due to the polycrystalline sample. Among them, the $\gamma=\pm 5^\circ$ configuration gives the best agreement with the observed θ pattern. We found that most molecules are nearly flat to the substrates in the thin film phase.

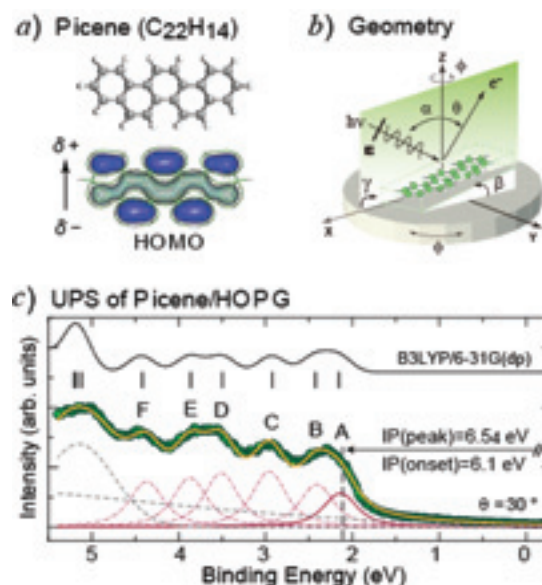


Fig. 1. a) Chemical structure and HOMO pattern of picene. b) Computation and experimental geometry for the MST/MO method. c) UPS of picene (10nm) film. The spectrum is convoluted with Voigt function. The calculated density-of-state and energy position of the molecular levels are also shown.

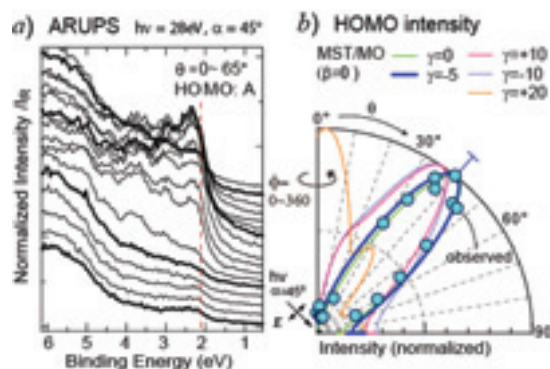


Fig. 2. a) θ dependence of ARUPS of picene film on HOPG. b) Observed and calculated θ patterns of the HOMO (peak A). The MST/MO results of the dependence on the molecular inclination angle of γ are shown for $\beta=0^\circ$.

[1] R. Mitsuhashi *et al*, Nature **464** (2010) 76.

[2] S. Nagamatsu *et al*, e-J. Surf. Sci. Nano, **3** (2005) 461.

Effects of Local Electrostatic Potential of Polar Molecule on Electronic Structure: ClGa-Phthalocyanine

H. Machida¹, S. Hosoumi¹, R. Tateishi¹, T. Nishi^{1,2}, S. Nagamatsu², T. Hosokai³, N. Ueno¹ and S. Kera^{1,2}

¹ Graduate School of Advanced Integration Science, Chiba University, Chiba 263-8522, Japan

² Institute for Molecular Science, Okazaki 444-8585, Japan

³ Institut für Angewandte Physik, Universität Tübingen, Germany

We investigated the electronic structure of chlorogallium phthalocyanine (ClGaPc) films on graphite. The electronic structure is significantly different between monolayer (ML) and bilayer (BL) at the HOMO band region especially. The effect of the local electrostatic potential of molecular permanent dipole on the interface electronic structure is an important subject to clarify the mechanism of the energy-level alignment. Angle-resolved ultraviolet photoelectron spectroscopy (ARUPS) measurements using synchrotron light source were conducted on ClGaPc/graphite system to reveal the effects of local and nonlocal electric field on the energy levels as well as the work function of the molecular film.

Experimental

The purified molecules were evaporated onto the graphite (HOPG) substrate kept at 295 K. The monolayer thickness was confirmed by the work function of the annealed monolayer film. The photoemission angle (θ) dependence was measured for HOMO band and Ga 3d band regions.

Results and Discussion

Figure 1 (a) shows the HeI UPS for the ML and BL of ClGaPc on HOPG at the HOMO band region. The spectra were fitted using Voigt function in accordance with hole-vibration(phonon) interaction [1]. For the ML film, the sharp asymmetric band A is assigned to the HOMO state with vibronic coupling. Unknown features at both sides of main band A are found (labeled as *). For the BL film, where the molecules are facing each other to compensate the permanent dipole, the HOMO is observed as two prominent bands (A' and B) with energy separation of 0.23eV. Band A' is related to photoemission from the underlying 1st layer, in which molecules are lying flat with Cl-atom protruding to vacuum side. Band B might be related to the 2nd layer, where molecules are oriented reversely as confirmed by the work function change and metastable atom electron spectroscopy [2]. Furthermore, θ dependences of band A and bands A' and B are shown in Figs. 1 (b) and (c), respectively. The observed intensities give the maximum at around 55° for every band as seen in other Pcs, indicating the same distribution of π MO as the origin of UPS bands.

To reveal the contribution of final-state screening of photohole on the UPS, which depends on the distance between the hole position and the image plane, we measured the Ga 3d state at $h\nu=80\text{eV}$ (Fig. 2 (a)). The Ga 3d-band shape is nearly the same

between ML and BL. θ dependences of Ga 3d peak for ML and BL show also no significant difference (Fig. 2 (b)), indicating the energy shift by the image potential is not the origin of the HOMO split.

The HOMO is delocalized over the Pc macrocycle, hence its orbital population may be affected by the electric field underneath. The results indicate that it is necessary to consider both the impacts of potential gradient by the local molecular dipole and the spontaneous polarization effect for a well-ordered staggered bilayer system.

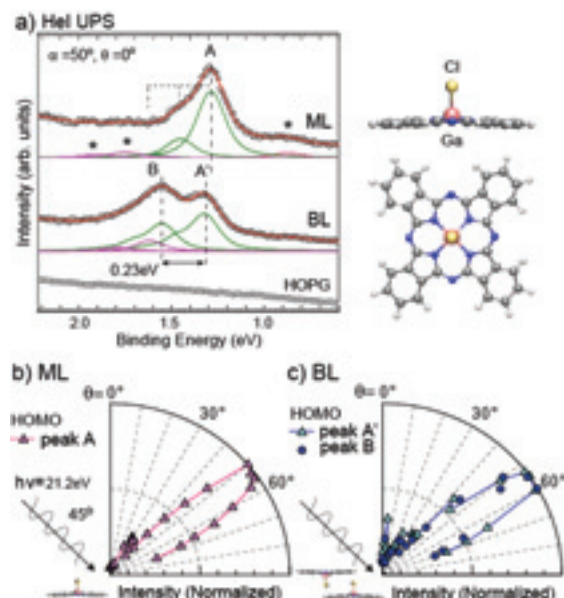


Fig. 1. (a) High-resolution UPS (HeI) of ClGaPc ML and BL on HOPG. (b) θ pattern of the HOMO for the ML and (c) for the BL.

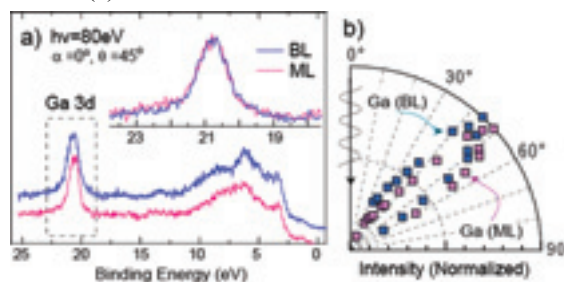


Fig. 2. (a) ARUPS at $h\nu=80\text{eV}$. Inset shows Ga band region. (b) θ pattern of the Ga3d for ML and BL.

[1] S. Kera *et al*, Prog. Surf. Sci. **84** (2009) 135.

[2] S. Kera *et al*, Surf. Sci. **566-568** (2004) 571.

Molecular Orientation at Organic-Organic Heterojunction Interfaces by ARUPS

K. K.Okudaira, K. Ito, N. Ueno

Association of Graduate Schools of Science and Technology, Chiba University, Inage-ku, Chiba 263-8522, Japan

Introduction

Organic field-effect transistors (OFETs) are of current interest due to their unique characteristics compared with those of conventional inorganic semiconductors. Because of the large size, anisotropy, and relatively weak van der Waals interaction of organic molecules, their growth is far more complex than that of inorganic materials. Studies on organic-inorganic heterojunction have revealed that the equilibrium structure is dependent on a delicate balance of various noncovalent weak interactions. Comparatively, the scenario of the rarely studied organic-organic interface (OOI) is much less understood. The investigation of structure of OOI may give information on the mechanism of the film growth at the OOI.

In this report we observed angle-resolved ultraviolet photoelectron spectroscopy (ARUPS) of pentacene (Pn) on organic thin film such as copper phthalocyanine (CuPc) and pentacene on HOPG to clarify the molecular orientation of OOI.

Experimental

ARUPS measurements were performed at the beam line BL8B2 of the UVSOR storage ring at the Institute for Molecular Science. The take-off angle (θ) dependencies of photoelectron spectra were measured at incident angle of photon (α) = 45° with the photon energy ($h\nu$) of 40 eV. CuPc thin film (1.6 nm) was first deposited on HOPG. An additional organic layer of pentacene was subsequently evaporated to a final thickness of 4.0 nm (Pn(4.0nm)/CuPc(1.6nm)/HOPG).

Results and Discussion

Figures 1 (a) and (b) show the take-off angle (θ) dependencies of ARUPS spectra of Pn(2.0nm)/HOPG and Pn(4.0nm)/CuPc(1.6nm)/HOPG, respectively. The peak located at binding energy of about 1 eV corresponds to the localized π state (HOMO). In Fig.2 the θ dependences of Pn(2.0nm)/HOPG have a sharp maxima at $\theta = 30^\circ$. These θ dependences are similar to those of CuPc on HOPG.[1] From these comparisons, it is found that Pn molecules lie flat on HOPG substrate. On the other hand, the θ dependences of Pn(4.0nm)/CuPc(1.6nm)/HOPG show broad distribution and have a maximum at $\theta = 60^\circ$, which is higher than that of Pn(2.0nm)/HOPG. We determined the orientation of pendant groups of polystyrene by the analysis of θ dependences of

ARUPS spectra.[2] These results indicate that Pn molecules on CuPc thin film show a tilt orientation. To determine the molecular orientation quantitatively, it needs to compare the observed θ dependencies with the calculated ones.

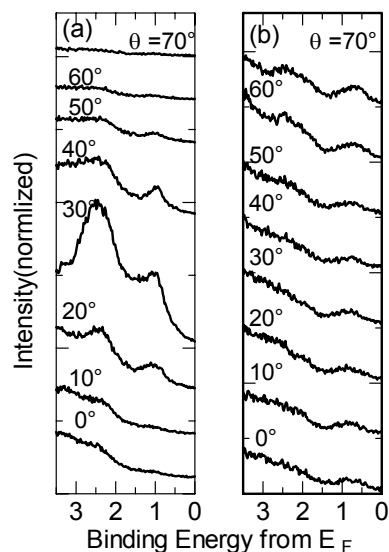


Fig.1. Take-off angle (θ) dependence of ARUPS of Pn(2.0nm)/HOPG (a), Pn(4.0nm)/CuPc(1.6nm)/HOPG (b), respectively.

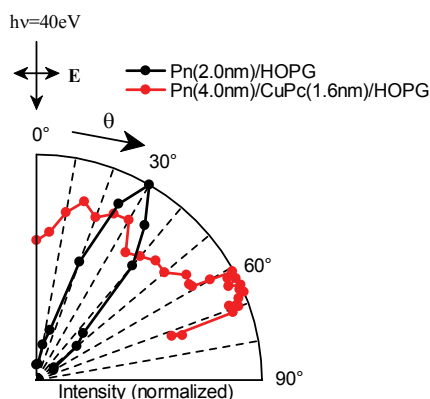


Fig.2. Take-off angle (θ) dependences of photoelectron intensities of HOMO peak for Pn(2.0nm)/HOPG (●) and Pn(4.0nm)/CuPc(1.6nm)/HOPG (●).

[1] K. K. Okudaira *et al.*, J. Appl. Phys **85** (1999) 6453.

[2] N. Ueno *et al.* Jpn. J. Appl. Phys. **37** (1998) 4979.

Effect of Insertion of a Thin Li-Phthalocyanine Layer at Indium Tin Oxide/Zn-Phthalocyanine Interface on Energy Level Alignment

S. Tanaka, T. Hanada and I. Hiromitsu

Department of Material Science, Interdisciplinary Faculty of Science and Engineering,
Shimane University, Matsue 690-8504, Japan

Introduction

The properties of metal-electrode/organic semiconductor interfaces affect the functionality and performance of organic semiconductor devices. An insertion of a thin layer in the metal-electrode/organic interfaces is a well known technique to improve the performance of organic semiconductor devices. [1] As an example of an interesting insertion effect on device performance, we recently observed that the power conversion efficiency of a Zn-phthalocyanine (ZnPc) /C₆₀ heterojunction organic photovoltaic (OPV) cell is improved with the insertion of a Li-phthalocyanine (LiPc) film to the indium tin oxide (ITO)/ ZnPc interface. The molecular structure of LiPc is shown in Fig. 1. It is known that the electronic structure of the ITO/organic interface is intimately related to the charge transfer properties of the ITO/organic layer. [2] Hence, in this study, we investigate the electronic structures of ITO/ZnPc and ITO/LiPc/ZnPc interfaces using photoelectron spectroscopy.

Experiment

The photoelectron measurements were carried out with photon energy of 40 eV. The incidence angle of light and the observed angle of the photoelectron were 45° and normal emission, respectively. The commercial ITO (supplied by Geomatec) substrate was cleaned with ultrasonication in organic solvents. LiPc was synthesized by electrochemical oxidation of dilithium phthalocyanine (Li₂Pc) following the synthesis procedure described in literature. [3] ZnPc was purchased from Kanto chem. co. LiPc and ZnPc were purified by vacuum sublimation. LiPc and ZnPc were deposited step by step at room temperature.

Results and Discussion

Figure 2 shows photoelectron spectra of LiPc and ZnPc incrementally deposited on the ITO substrate. The abscissa is the kinetic energy of the photoelectron. The Fermi level position of the ITO substrate was observed at 35.9 eV. The solid bars indicate the peak position of the highest occupied molecular orbital (HOMO) of LiPc and ZnPc at each sample thickness. The HOMO peak of LiPc was observed at 34.5 eV in 0.5 nm LiPc thickness. The HOMO peak of LiPc was settled at 34.7 eV with increasing the thickness of LiPc. The HOMO peak of ZnPc on the LiPc layer showed a 0.3 eV shift towards lower kinetic energy, indicating band bending in ZnPc due to the formation of an hole accumulation layer. The hole accumulation layer was not observed in the

thickness dependence of photoelectron spectrum of ZnPc at the ITO/ZnPc interface (not shown). In the OPV cell, ZnPc works as the path of the hole transport from the exciton dissociation interface. The present results indicate that the improvement of the power conversion efficiency is related to the band bending in the ZnPc layer caused by the insertion of the LiPc layer.

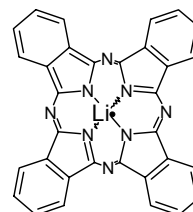


Fig. 1. Molecular structure of LiPc.

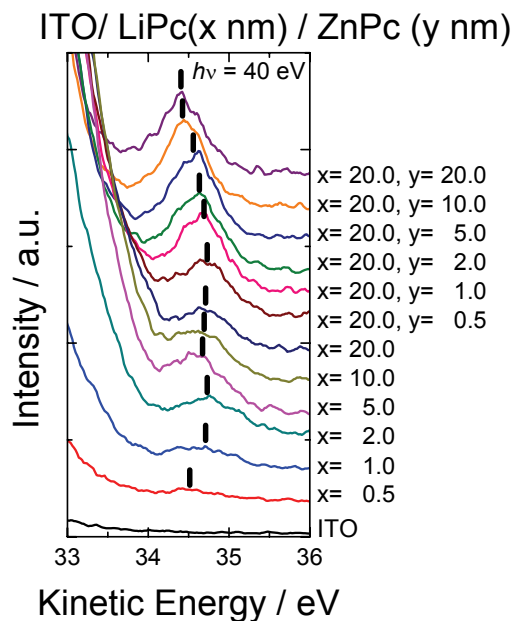


Fig. 2. Photoelectron spectra of LiPc and ZnPc incrementally deposited on the ITO substrate. The LiPc thickness and ZnPc thickness are indicated by the x and y in the right column, respectively.

[1] S. Tanaka *et al.*, *Thin Solid Films* **516** (2008) 1006.

[2] N. R. Armstrong *et al.*, *Thin Solid Films* **445** (2003) 342.

[3] P. Turek *et al.*, *Chem. Phys. Lett.* **134** (1987) 471.

Interface Electronic Structure of Co-Phthalocyanine/Cu(111)

R. Tateishi¹, S. Hosoumi¹, H. Machida¹, T. Nishi^{1,2}, S. Nagamatsu², N. Ueno¹ and S. Kera^{1,2}
¹Graduate School of Advanced Integration Science, Chiba University, Chiba 263-8522, Japan
²Institute for Molecular Science, Okazaki 444-8585, Japan

The interface electronic structure formed at an organic/electrode interface is of fundamental importance to understand mechanisms of charge injection and transfer phenomena in organic thin film devices, since they usually appear in the band gap region of the organic material. In general, however, it is very difficult to understand the mechanism of interface-states formation due to complicated and non-well-defined interface structure both in energetically and structurally. We studied on the valence electronic structure of cobalt-phthalocyanine (CoPc) thin films prepared on Cu(111) by using angle-resolved ultraviolet photoelectron spectroscopy (ARUPS).

Experimental

ARUPS spectra were measured at photon incidence angle $\alpha=45^\circ$, $h\nu=18$ and 40eV and $T=295\text{K}$. The purified molecules were evaporated onto the Cu(111) substrate at 295K . The coverage/thickness of the monolayer was confirmed by the work function of the densely-packed monolayer film. The high-resolution spectra were recorded by using HeI light source.

Results and Discussion

Figure 1 (a) shows the thickness-dependent ARUPS of CoPc (0.2nm; sub-monolayer(0.88ML) and 4.5nm) on Cu(111) obtained at $h\nu=40\text{eV}$. For the thicker film, the band A is ascribed to $2p$ (π) MO and B is from $3d$ - π hybridized MO of CoPc, respectively. For the thinner film, we found three interface states I1-I3. The energies of bands I2 and I3 are slightly higher ($\delta\sim 0.05\text{eV}$ and 0.18eV) than that for the CoPc/Ag(111), respectively. A modified Shockley-surface state (SS) is also observed at around $\theta=0^\circ$.

The intensity map for the ARUPS along the ΓM direction of CoPc(0.2nm)/Cu(111) is shown in Fig. 1 (b). No clear energy-band dispersion is found for valence states of CoPc film. The photoelectron angular distribution (PAD) of bands I2 and I3 are accidentally similar each other at $h\nu=40\text{eV}$, where each curve has a maximum at $\sim 34^\circ$. On the other hand, we found similarities of the PADs between CoPc/Cu(111) and CoPc/Ag(111). By considering the systematic changes in the electronic structure for various transition-metal Pcs, band I2 is ascribed to the $3d$ -related MO and I3 is from the $2p$ -related MO. Band I1 might be described to an adsorption-induced gap state. The re-ordering and modification of MOs is keys to understand the formation mechanism of the interface states.

Figure 2 shows the evolution of SS of Cu(111) with increasing the coverage of CoPc. The peak energy at Γ point shifts to lower energy side with increasing the coverage (see a guided curve). The characteristics of

the modified SS are that (i) the SS at uncovered region disappears for subML films and (ii) the electron mass (m^*) tends to be heavier with increasing the coverage. This tendency clearly differs from the case of rare gases adsorption. The SS at the bare surface region survives and m^* of the modified SS does not changed so much for Xe/Cu(111) [1].

A peculiar interaction between organic molecule and metal as well as a film growth process should take part in. The study to obtain the detailed structural information on lattice constant by LEED as well as adsorption distance by XSW that depends on the coverage is in progress.

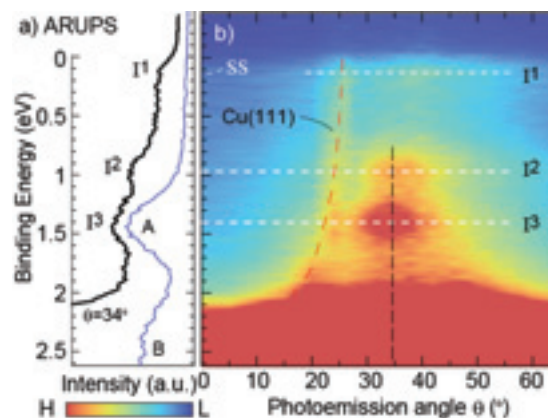


Fig. 1. a) Thickness-dependent ARUPS of CoPc/Cu(111), subML(black) and thick film(blue). b) Intensity map for the θ dependence of ARUPS at the subML. The band dispersion of the Cu(111) is overlapping (see a dashed curve).

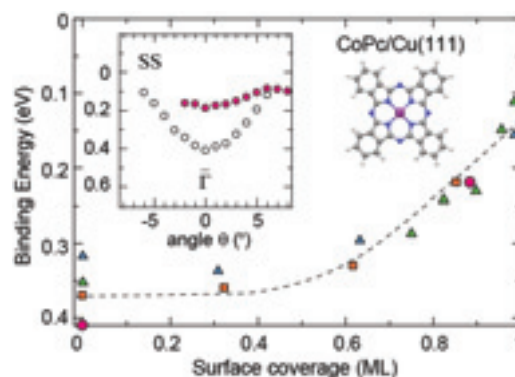


Fig. 2. Thickness dependence of the SS peak position (Γ point). Results of three different experiments by HeI UPS are compared. Inset shows ARUPS of clean Cu(111) (open circles) and CoPc(0.88ML)/Cu(111) (filled circles) taken at $h\nu=18\text{eV}$.

[1] F. Forster *et.al.*, J. Phys. Chem. B **108** (2004) 14692.

BL7U

ARPES Studies of Quasi-Particle Dynamics in Topological Insulators

S. R. Park¹, W. S. Jung¹, G. R. Han¹, Y. K. Kim¹, Ch. Kim¹, D. J. Song¹, Y. Y. Koh¹, C. Kim¹, S. Kimura², K. D. Lee³, N. Hur³, J. Y. Kim⁴, B. K. Cho⁴, J. H. Kim⁵, Y. S. Kwon⁵, J. H. Han⁵

¹*Institute of Physics and Applied Physics, Yonsei University, Seoul, Korea*

²*UVSOR Facility, Institute for Molecular Science, Okazaki 444-8585, Japan*

³*Department of Physics, Inha University, Incheon, Korea*

⁴*Department of Materials Science & Engineering, GIST, Gwangju, Korea*

⁵*Department of Physics, Sungkyunkwan University, Suwon, Korea*

Topological insulators (TIs) are a new class of materials which always have metallic surface states. These metallic surface states are protected by the time reversal symmetry and have their spins locked into the momentum. The latter fact brings about suppression of back scattering and quasi-particles are expected to have a longer life time. An experimental verification of this fact is essential to understand the novel properties of the metallic states, and therefore we have performed temperature and photon energy dependent angle resolved photoemission (ARPES) experiments on various TIs.

Bi_2Se_3 , Bi_2Te_3 and Sb single crystals were grown by flux and Bridgman methods. Samples were cleaved in situ and ARPES measurements were performed at the beam line 7U [1][2]. Samples were sometimes left in the vacuum for a few days to age the surface.

Figure 1(a) shows ARPES data from a freshly cleaved surface of Bi_2Se_3 taken with 8 eV photons. At 8 eV, the photoemission matrix element for the bulk states is suppressed that the bulk signal is very weak (intensity at the Γ point near the Fermi energy). The cone shape and fast dispersing band is the surface metallic states. The surface band reaches the Γ point near the 0.3 eV binding energy. This point is called the Dirac point. After exposing the surface to a relatively poor vacuum for 4 days ages the surface, ARPES data was retaken and is shown in figure 1(b). Note that the Dirac point has shifted to a higher binding energy side by about 0.1 eV. This is due to the electron doping effect by the adsorbed atoms and molecules on the surface.

Suppression of the bulk ARPES states allows us to perform reliable self energy analysis on the data. The imaginary parts of the self energies from the data are plotted in figure 2(a). In the data, it is noted that $\text{Im}\Sigma$ initially increases but then decreases near the bulk band bottom energy (dashed lines). This is true for both fresh and aged surfaces and thus strongly indicates that the kinks are related to the bulk states. The scattering of the quasi-particles in the metallic surface states can be analyzed in terms of electron-electron, electron-phonon and impurity scatterings. The analysis results in figure 2(b) show that the quasi-particles in the surface states mostly decay to the bulk states but not to other surface states.

Even though the above results provide us valuable information, we still do not have the intrinsic properties because the quasi-particle dynamics is dominated by the coupling to the bulk states. To overcome this, we performed ARPES on higher quality TIs, e.g., Bi_2Te_3 shown in figure 1(a). The result plotted in figure 2(a) along with the result from Sb show that the scattering rate is more or less binding energy independent. This constant term is attributed to the contribution from uneven surfaces, thus an extrinsic effect. These results strongly suggest that the intrinsic life time of the quasi-particles in surface states is extremely long. This is an important property for TIs as the candidate materials for the future spintronic applications.

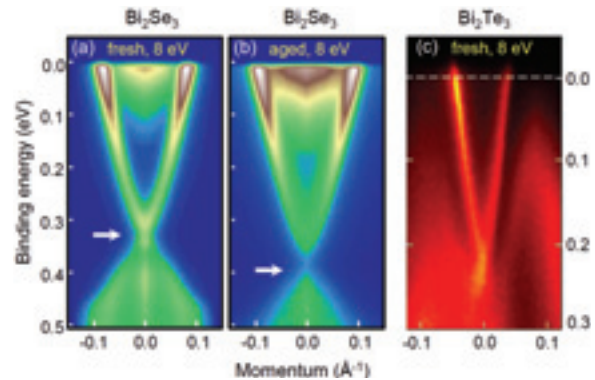


Fig. 1. ARPES data near the Γ point from TIs under various conditions. Bi_2Se_3 data from (a) fresh and (b) aged surfaces. (c) Data from fresh Bi_2Te_3 surface.

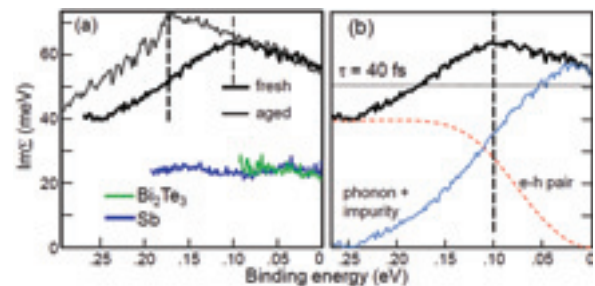


Fig. 2. (a) Imaginary parts of the self energy from various TIs. (b) Contributions from various scattering channels.

[1] S. R. Park *et al.*, Phys. Rev. B **81** (2010) 041405.

[2] S. R. Park *et al.*, in preparation.

Characterization of Calcium in Huntite by an XAFS Method

T. Kurisaki¹, D. Tanaka¹, S. Kokubu¹ and H. Wakita^{1,2}

¹*Department of Chemistry, Faculty of Science, Fukuoka University, Jonan-ku, Fukuoka 814-0180, Japan*

²*Advanced Materials Institute, Fukuoka University, Jonan-ku, Fukuoka 814-0180, Japan*

A huntite was called ‘a hanto-ishi’ and was used as a pigment of the white in ancient Egypt. This mineral chemical formula is expressed in $\text{CaMg}_3(\text{CO}_3)_2$. The huntite has very few reports about locality, and it is a rare mineral. However, this mineral is used abundantly in ancient Egypt. It is not apparent why the huntite which is a rare mineral was used as a pigment of the white. It is reported that the huntite is produced in Nagasaki. For various light element compounds, we have studied the electronic structure by X-ray absorption spectroscopy [1]. These results suggested that there is a correlation between XANES spectra and the local structures.

In this work, we performed the XANES spectra measurement about various calcium salts and minerals such as huntite and dolomite. The obtained experimental XANES spectra are analyzed using the calculated theoretical spectra from DV-X α calculations. The X-ray absorption spectra were measured at BL1A of the UVSOR in the Institute of Molecular Science, Okazaki [4]. The ring energy of the UVSOR storage ring was 750MeV and the stored current was 110-230 mA. P K-edge absorption spectra were recorded in the regions of 2125-2270eV by use of two InSb crystals. The absorption was monitored by the total electron yield using a photomultiplier. The samples were spread into the carbon tape on the first photodiode made of CuBe of the photomultiplier. Figure 1 shows the observed Ca K-edge XANES spectra for the Huntite and Dolomite. The Ca-K XANES spectra of Huntite and Dolomite show different peak profiles. This result shows that the calcium in these minerals has different electronic states. We are going to try to calculate the spectra by DV-X α molecular orbital calculations. The calculated XANES spectra and the observed XANES spectra of the Huntite and the Dolomite are shown in Fig. 2. The observed XANES spectra and the calculated XANES spectra showed good agreement. The peaks A and B are estimated to the electron transition (mainly Ca 1s to unoccupied mixed orbital consisting of O 3d, O 3p, O 3s and O 4s).

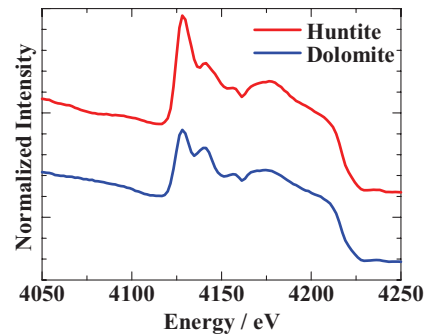


Fig. 1. Observed Ca K-edge XANES spectra of Huntite and Dolomite.

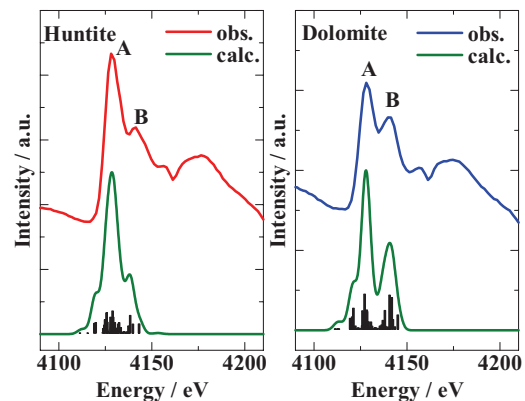


Fig. 2. The comparison of observed XANES spectra with calculated XANES spectra for Ca K-edge.

[1] T. Kurisaki, S. Matsuo, I. Toth and H. Wakita, *Anal. Sci.* **24** (2008) 1385.

[2] S. Murata, T. Matsukawa, S. Naoè, T. Horigome, O. Matsudo and M. Watatabe, *Rev. Sci. Instrum.* **63** (1992) 1309.

Excitonic Structures of PbMoO₄ and PbWO₄ Crystals

M. Fujita¹, M. Itoh², H. Mitani², Sangeeta³ and M. Tyagi³

¹Japan Coast Guard Academy, Kure 737-8512, Japan

²Dept. of Electrical and Electronic Engineering, Shinshu University, Nagano 380-8553, Japan

³Crystal Technology Laboratory, Bhabha Atomic Research Center, Mumbai 400 085, India

Metal tungstates and molybdates are widely used for scintillation detectors. Therefore information on the exciton states is deeply desired to understand the de-excitation processes after high-energy electronic excitation in these materials. PbWO₄ and PbMoO₄ crystallize in the scheelite structure. We found that PbWO₄ exhibits a pronounced exciton band with distinct dichroism, and proposed that the exciton transition is explained in terms of the cationic Pb 6s → 6p excitation [1]. In the present study, reflectivity spectra of PbMoO₄ crystals are measured in order to get more detailed information on the excitonic structures in Pb compounds.

Figure 1 shows reflectivity spectra of PbMoO₄ up to 20 eV measured with the light polarized parallel to the *a*-axis (**E**//*a*) and *c*-axis (**E**//*c*). Remarkable dichroism is seen in the region below 6 eV. In Fig. 2 are presented the imaginary-part ϵ_2 spectra of the dielectric function calculated from the spectra in Fig. 1 using a Kramers-Kronig analysis. The lowest exciton band 1 for **E**//*a* has two peaks *a*₁ and *a*₂. On the other hand, the spectrum for **E**//*c* exhibits a weak plateau in this region. The ϵ_2 spectra of PbWO₄ [1] are also shown in Fig. 2 for the sake of comparison. Common features are observed between the structures in PbMoO₄ and PbWO₄; i. e. the lowest band 1 shows doublet structure for **E**//*a* and the band 2 is observed for **E**//*c*.

Theoretical calculation of the electronic structure of PbMoO₄ (PbWO₄) by the DV-*X* α method indicates that the valence band and the conduction band are mainly composed of O 2p and Mo 4d (W 5d) states, respectively, and the Pb state contributes appreciably to the top of the valence band and the bottom of the conduction band [2]. Similarity of the optical spectra in Fig. 2 suggests that the exciton transition of PbMoO₄ is also attributed to the cationic excitation as in the case of PbWO₄. In the scheelite structure, a Pb²⁺ ion is at the site of S₄ symmetry surrounded by eight O²⁻ ions. The Pb 6p state splits into the $\Gamma_{3,4}$ level and the Γ_2 level due to the uniaxial crystal-field along the *c*-axis. The band 1 observed for **E**//*a* and the band 2 for **E**//*c* are ascribed to the transitions from the top of the valence band of the Γ_1 level to the $\Gamma_{3,4}$ level and the Γ_2 level, respectively. The splitting of the peaks *a*₁ and *a*₂ of the band 1 originates from the spin-orbit splitting of the Pb 6p state.

On the other hand, some differences are also observed between the spectra of both materials. The intensity of the peak *a*₁ is stronger than that of *a*₂ in

PbWO₄, and vice versa in PbMoO₄. In PbWO₄, peaks *c*₁ and *c*₂ are observed clearly, while no appreciable structure is seen on the weak plateau in the 3.4–4.0 eV region for **E**//*c* in PbMoO₄. According to the theoretical calculation [2], the magnitudes of the contribution of Pb state to the top of the valence band and the bottom of the conduction band of PbMoO₄ are about 0.7 times as small as those of PbWO₄. It is supposed that the difference in magnitudes of the contribution of Pb state is responsible for the different features of the exciton band of PbMoO₄ and PbWO₄ [3].

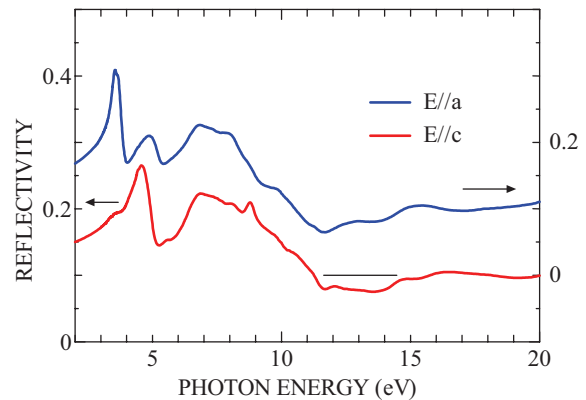


Fig. 1. Reflectivity spectra of PbMoO₄ at 6 K for **E**//*a* and **E**//*c*.

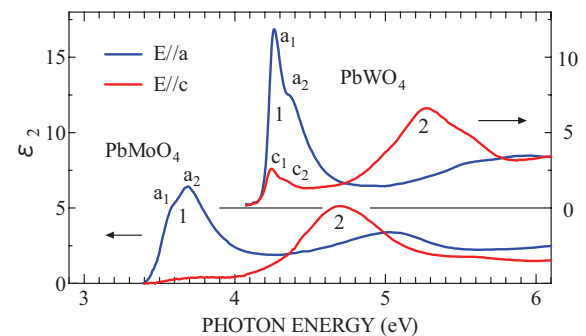


Fig. 2. Imaginary part of the dielectric function of PbMoO₄ and PbWO₄ for **E**//*a* and **E**//*c* in the region below 6 eV.

[1] M. Fujita *et al.*, Phys. Rev. B **65** (2002) 195105.

[2] M. Itoh *et al.*, J. Phys. Soc. Jpn. **75** (2006) 084705.

[3] M. Fujita *et al.*, Phys. Status Solidi B **247** (2010) 405.

Identification of Cr³⁺ Impurity in LaAlO₃ by Photoluminescence

E. Hirata and Y. Ohki

Dept. Electrical Engineering and Bioscience, Waseda University, Shinjuku 169-8555, Japan

Lanthanum aluminate (LaAlO₃) has been attracting much attention as a promising candidate for a gate insulator in advanced metal-oxide-semiconductor devices. By analyzing photoluminescence (PL) properties of LaAlO₃, we have been examining presence of localized states in the band gap, which may induce leakage current.

Experimental

The samples examined are LaAlO₃ (100) single crystals grown by the Czochralski method and LaAlO₃ thin films prepared by a spin-coating method. The films were annealed in oxygen at designated temperatures between 600 and 1000 °C. Using synchrotron radiation under multibunch operation at the BL1B line of UVSOR Facility as a photon source, PL spectra were measured at 10 K. Crystallization of thin films were confirmed by in-plane X-ray diffraction (XRD) measurements.

Results and Discussion

Figure 1(a) shows PL spectra induced by 6.4-eV photons, obtained at 10 K for the crystal and the films deposited and annealed on Si monocrystal substrates. The films annealed at 600 and 700 °C have no PL peaks, while those annealed at 800, 900, and 1000 °C and the crystal sample have three sharp PL peaks at about 1.60, 1.64, and 1.68 eV. Figure 1(b) shows PL spectra similarly obtained for the films deposited on CaF₂ monocrystal substrates. When the films were annealed at 800 °C or higher, three PL peaks appear similarly to the films on the Si substrates, but at much higher energies, namely at 1.86, 2.00, and 2.14 eV.

The XRD patterns shown in Fig. 2 indicate that the films annealed at 800 °C or higher are polycrystalline, while those annealed at 600 and 700 °C are amorphous. Comparison of XRD spectra between the two annealed polycrystalline films on the Si and CaF₂ substrates indicates that the lattice constant is smaller if substrate is CaF₂.

It is known that the luminescence due to Cr³⁺ in Al₂O₃ appears only when the sample is crystalline [1]. This is due to energy state splitting of *d* orbitals in Cr³⁺ by the crystal field [2]. Furthermore, the PL spectral shapes observed in the single crystal samples and polycrystalline films on the Si substrate in the present study and those of R lines of Cr³⁺ in LaAlO₃ are similar [3]. Therefore, there is a possibility that the present LaAlO₃ samples contain Cr³⁺ ions as an impurity. Since the energy state of Cr³⁺ ions is significantly influenced by the crystal field [2], the difference in PL peak energy among the samples deposited on different substrates should be due to the lattice distortion.

The authors bought the single crystals and

chemicals for making thin films from different companies. Furthermore, it is known that Al₂O₃ often contains Cr³⁺ ions as an impurity [1,4]. Therefore, there is a high possibility that the raw material or ore of Al contains chromium as an impurity. Detection of Cr³⁺ ions by inductively coupled plasma optical emission spectrometry (ICP-OES) failed, indicating that the Cr³⁺ content in the present samples is below 1 ppm.

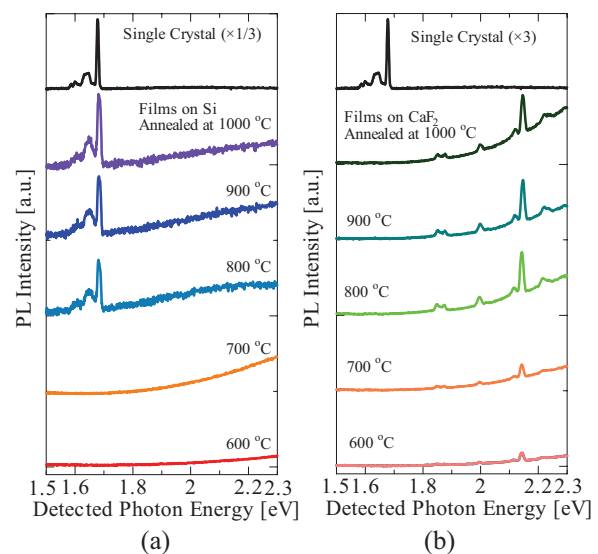


Fig. 1. Comparison of PL spectra induced by 6.4-eV photons, obtained at 10 K in film samples deposited on Si substrates (a) and on CaF₂ ones (b). The PL spectrum obtained in the crystal sample is also shown in each figure (a, b).

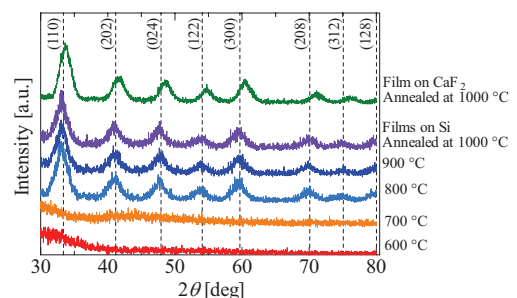


Fig. 2. In-plane XRD patterns of LaAlO₃ film samples.

- [1] J. Kakoš *et al.*, *J. Sol-Gel Sci. Technol.* **21** (2001) 167.
- [2] S. Xia *et al.*, *Phys. Rev. B* **35** (1987) 7671.
- [3] J. Heber *et al.*, *Z. Phys.* **246** (1971) 261.
- [4] T.-P. Lee *et al.*, *J. Vac. Sci. Technol. B* **22** (2004) 2295.

Photoluminescence from a Bundle of Single-Walled Carbon Nanotubes

M. Itoh, T. Kajitani and H. Mitani

Department of Electrical and Electronic Engineering, Shinshu University, Nagano 380-8553, Japan

The observation of photoluminescence (PL) from single-walled carbon nanotubes (SWNTs) underlines their enormous and promising potential for photonic and optoelectronic applications. The PL is ascribed to the radiative decay of free excitons (FEs).

In practical growth condition, about one-third of all possible SWNTs exhibit metallic properties and the remaining two-third act as semiconductors. Therefore, there is a broad consensus [1, 2] that, if one wants to observe the PL from SWNTs, a semiconducting SWNT should be spatially isolated, because the bundling leads to rapid energy transfer to metallic SWNTs where the FEs decay nonradiatively. This consensus, however, neglects an inviting possibility that the FEs can emit PL before the energy transfer takes place, because they have finite lifetimes. In the present study, we have examined whether this possibility is ruled out or not.

Experiment

HiPco-grown SWNTs (CNI; USA) were dispersed in ethanol with the help of a homogenizer. By spraying the nanotube suspension onto a freshly cleaved BaF₂ crystal, homogeneous SWNT film with a thickness of about 10⁻⁵ cm was prepared. PL was observed by an Acton SpectraPro300i monochromator equipped with a liquid-nitrogen cooled ICCD camera. This detection system has suitable sensitivity in the wavelength range $\lambda_m = 200\text{--}1000$ nm, with a spectral resolution of 10 nm. The excitation wavelength λ_{ex} was changed in 2 nm steps with a resolution of 0.5 nm, and for each step the emission spectrum was integrated over 300 sec. Although as-made and aged films were examined, no clear difference was found between both results. Morphological information of the new film was obtained by using a digital microscope VHX-1000 (Keyence).

Results and Discussion

Figure 1 shows a microscope image ($\times 5000$) of the as-made film investigated in this study. From the figure, it is obvious that our sample consists of a bundle of well-dispersed SWNTs.

In Fig. 2 is presented the contour plot of the three-dimensional emission-excitation spectrum of our SWNTs measured at a temperature $T = 5$ K. An emission band peaking at $\lambda_m \approx 950$ nm is clearly observed. This emission is excited in the range of $\lambda_{ex} > 590$ nm. Judging from these spectral characteristics, we likely attribute the 950 nm emission peak to the radiative recombination of FEs in STWNs with (8, 3)

chiral index [1, 2]. Of course, only a small part of FEs could decay in semiconducting SWNTs by emitting PL. From the present observation, however, it is supposed that the coherent length of energy transfer is not so long as one has predicted so far.

The emission intensity of the 950 nm peak was nearly temperature-independent in the range $T = 5\text{--}300$ K, which suggests that the coherent length is not so sensitive to the temperature.

The authors would like to thank Mr. Y. Aihara of Keyence Co. for his help in the observation of microscope images of our sample. This work was supported by the CLUSTER (the second stage) of the Ministry of Education of Japan.

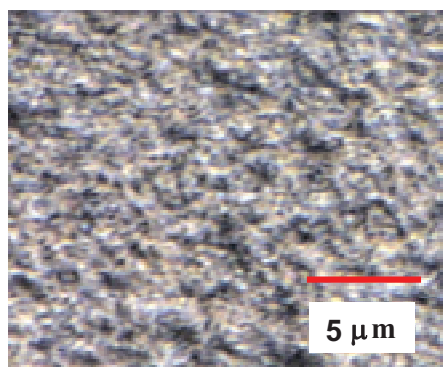


Fig. 1. Microscope image ($\times 5000$) of an as-made SWNT film investigated in the present study.

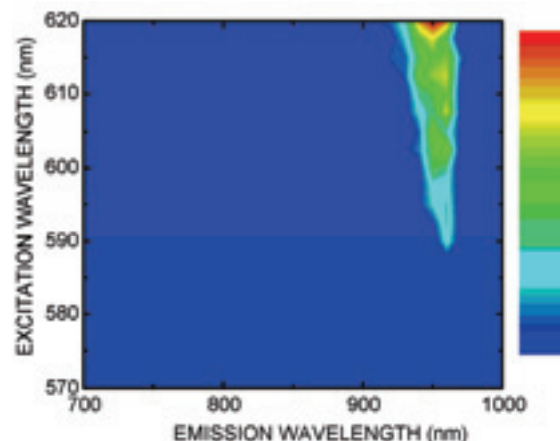


Fig. 2. Contour plot of the three-dimensional emission-excitation spectrum of a bundle of SWNTs dispersed on a BaF₂ substrate measured at $T = 5$ K.

[1] S. M. Bachilo, *et al.*, *Science* **298** (2002) 2361.

[2] P. H. Tan, *et al.*, *Phys. Rev. Lett.* **99** (2007) 137402.

Optical Study of the Insulator-Metal Transition in $R_{2-x}\text{Sr}_x\text{NiO}_4$

M. Uchida¹, J. Fujioka², Y. Kaneko², Y. Onose^{1,2} and Y. Tokura^{1,2,3}

¹*Department of Applied Physics, University of Tokyo, Tokyo 113-8656, Japan*

²*Multiferroics Project, ERATO, Japan Science and Technology Agency (JST), Tokyo 113-8656, Japan*

³*Cross-Correlated Materials Research Group (CMRG), ASI, RIKEN, Wako, Saitama 351-0198, Japan*

Insulator-metal transition in strongly correlated electron systems has attracted great attention in the field of condensed matter physics [1]. It results in the reconstruction of the electronic structure on a large energy scale of several eV accompanying the changes of charge/spin/orbital states. Optical spectroscopy is one of the most powerful probes for investigating the change of high-energy electronic states systematically and provides the essential information for understanding the multi-degree-of-freedom coupled phenomena.

During this beam time, we measured the in-plane reflectivity spectra for layered perovskite nickelates $R_{2-x}\text{Sr}_x\text{NiO}_4$ (R : rare earth element) in an energy region between 4 and 42 eV at room temperature using the beam line BL1B. We obtained the optical conductivity spectra by the Kramers-Kronig analysis of the measured spectra connected to the lower-energy ones. $R_{2-x}\text{Sr}_x\text{NiO}_4$ is a typical two-dimensional insulator-metal transition system. While diagonal-stripe charge-spin ordering and checkerboard charge ordering are discerned around $x \sim 1/3$ and $x \sim 1/2$, respectively, the insulator-metal transition occurs at $x \sim 1$ accompanying the melting of the charge ordered state [2, 3].

First, we discuss the overall features of the high-energy electronic states. Figure 1 shows the optical conductivity of $\text{Nd}_{2-x}\text{Sr}_x\text{NiO}_4$ ($x=1.0$) in the energy range 0-35 eV at room temperature. It is noted that several peaks are observed in the spectrum. Previous optical study reported similar spectra for other layered perovskites $\text{La}_{2-x}\text{Sr}_x\text{MO}_4$ ($M = \text{Cr, Mn, Fe, and Co, } x=1.0$). The authors could successfully assign the origin of the peaks based on the systematic M -dependent energy shift [4]. Comparing our data

with them, three peaks above 10 eV (A, B, and C) can be assigned to $\text{Nd}4p \rightarrow \text{Nd}5d$, $\text{Sr}4p \rightarrow \text{Sr}4d$, and $\text{O}2s \rightarrow \text{Ni}3d$ excitations, respectively. We also assign two peaks D and E to the transitions from the $\text{O}2p$ band to some higher-lying conduction bands. The broad peak indicated by the solid triangle is remnant of the charge transfer (CT) gap excitation. The small CT gap compared with the other layered perovskites implies the instability of the insulator-metal transition for $M=\text{Ni}$ (except the superconducting transition for $M=\text{Cu}$).

Next, we focus on the doping variation of the electronic structure in the course of the insulator-metal transition. In Fig. 2, we show the low-energy optical conductivity spectra of $\text{Nd}_{2-x}\text{Sr}_x\text{NiO}_4$ ($x=0.5-1.3$) at 10K. The magnitude of the gap rapidly decreases with hole doping from $x=0.5$, reflecting the melting of the checkerboard-type charge order. While the gap is almost closed around $x=1.0$, a conspicuous peak structure is observed around 0.2 eV, indicating the incoherent transport caused by the strong charge correlation. In the higher doping range ($x=1.3$), the peak shifts to the lower energy and is merged to Drude response. Thus, we show in terms of optical spectra that the checkerboard type charge correlation dominates the charge dynamics near the insulator-metal transition in this system.

- [1] M. Imada *et al.*, Rev. Mod. Phys. **70** (1998) 1039.
 [2] S. Shinomori *et al.*, J. Phys. Soc. Jpn. **71** (2002) 705.
 [3] K. Ishizaka *et al.*, Phys. Rev. B **67** (2003) 184418.
 [4] Y. Moritomo *et al.*, J. Phys. Soc. Jpn. **64** (1995) 4117.

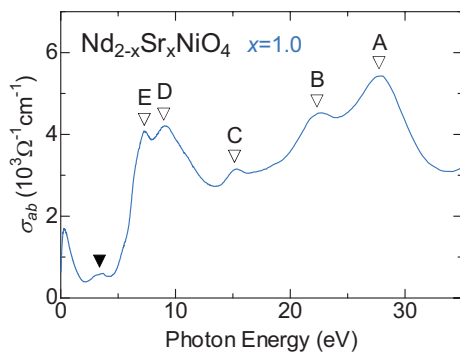


Fig. 1. Optical conductivity spectrum of $\text{Nd}_{2-x}\text{Sr}_x\text{NiO}_4$ ($x=1.0$) over wide energy region at room temperature.

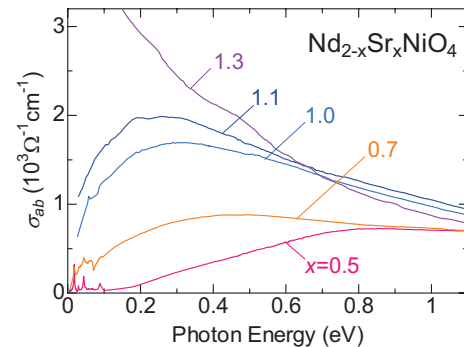


Fig. 2. Doping variation of the in-plane optical conductivity of $\text{Nd}_{2-x}\text{Sr}_x\text{NiO}_4$ ($x=0.5-1.3$) at the lowest temperature, 10K.

Soft X-Ray Spectroscopy of DNA Duplexes

H. Yamane¹, W. Hua², H. S. Kato³, T. Hatsui⁴, M. Kawai^{3,5}, Y. Luo², H. Ågren² and N. Kosugi¹
¹ Institute for Molecular Science, Okazaki 444-8585, Japan

² Dept of Theoretical Chemistry, Royal Institute of Technology, S-106 91 Stockholm, Sweden

³ The Institute of Physical and Chemical Research (RIKEN), Wako 351-0198, Japan

⁴ XFEL Project Head Office, RIKEN & JST-PREST, Hyogo 679-5148, Japan

⁵ Dept of Advanced Materials Science, University of Tokyo, Kashiwa 277-8501, Japan

Introduction

The electronic structure and its properties in DNA polymers have received great attention for possible molecular nanoelectronics since the discovery of the double helix structure of DNA. In the present work, we have undertaken experimental and theoretical study of soft X-ray spectroscopies for DNA base pairs, that is, fluorescence yield X-ray absorption (FY-XAS) and X-ray emission (XES) spectroscopies applied to poly(dA)-poly(dT) (AT) and poly(dG)-poly(dC) (GC) DNA duplexes. We have found that the stacking of pairs has very little influence on the spectra. The X-ray spectra of a DNA composed by mixed Watson-Crick base pairs are well reproduced by linear combinations of base pairs involved, and the amine and imine nitrogens show noticeable differences as building blocks in the FY-XAS and XES spectra [1].

Experiment

We prepared thick films of AT- and GC-DNA. These duplexes were diluted with deionized water (17.8 MΩ·cm) to a concentration of 1.25 mg/ml. The solutions were casted on the SiO₂/p-Si(111) substrates. The film thickness is about 100–200 nm. These samples are almost the same as those measured at the previous resonant photoemission experiments [2].

The FY-XAS and XES experiments were performed at BL3U. The FY-XAS spectra were measured by the highly efficient fluorescence-yield method using an MCP assembly with the center hole (F2223-21SH, Hamamatsu Photonics K.K.). The XES spectra were measured using a transmission-grating spectrometer. All measurements were performed at 300 K. In order to avoid the radiation damage of the sample during the measurements, the X-ray beam spot on the sample was continuously moved by scanning the sample.

Results and Discussion

Figure 1 shows a set of the N K-edge FY-XAS spectrum and the excitation energy ($h\nu$) dependence of the N K α XES spectra for the AT-DNA film. One finds in the XES spectra that the spectral difference between the imine ($-N=$) and amine ($-NH-$) groups can be distinguished; the resonance photoabsorption for the imine nitrogens appears at $h\nu = 399.4$ eV, while that for the amine nitrogens appears at a higher $h\nu = 401.6$ eV. At the imine site, the resonant XES spectrum has two prominent features; one shoulder at $h\nu = 390$ eV and one peak at $h\nu = 393$ eV. At the amine site, in contrast, the peak structure appears at

different photon energy ($h\nu = 394$ eV) with weak intensity as compared to that appears at the imine site. From the theoretical calculation [1], we found that the effect of stacking between pairs is of little consequence for the experimental XES spectra and that these with a good approximation can be represented just by one of its constituting base pairs with the hydrogen-bonding interaction.

Furthermore, one can find that the elastic peak in the XES spectra shows an asymmetric lineshape with a low-energy tail structure. The intensity of this tail structure depends on $h\nu$; in particular at the imine site, the tail structure is more intense. This tail structure may originate from the recombination emission [3] due to the fast motion of hydrogen bonded protons between the pairs, which depends on the degree of localization of the excited state. The observation of the tail structure indicates that the excited π^* state at the imine site is strongly localized, which agrees well with the scenario of a charge hopping transport in DNA duplexes proposed by the previous resonant photoemission work [2].

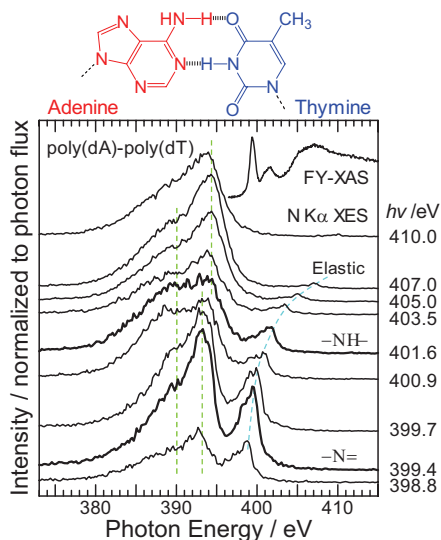


Fig. 1. Set of the N K-edge FY-XAS spectrum and the N K α XES spectra for the AT-DNA film. The molecular structure of adenine and thymine, included in the AT-DNA, at the configuration of the hydrogen-bonding interaction are also shown.

[1] W. Hua *et al.*, J. Phys. Chem. C, submitted.

[2] H.S. Kato *et al.*, Phys. Rev. Lett. **93** (2004) 086403.

[3] Y. Ma *et al.*, Phys. Rev. Lett. **71** (1993) 3725.

Local Intermolecular Interaction in α -Crystalline Films of Zinc-Phthalocyanine Studied by Soft X-Ray Emission Spectroscopy

H. Yamane¹, T. Hatsui² and N. Kosugi¹

¹ Institute for Molecular Science, Okazaki 444-8585, Japan

²XFEL Project Head Office, RIKEN & JST-PREST, Hyogo 679-5148, Japan

Introduction

The photon-in/photon-out technique of X-ray emission spectroscopy (XES) measures X-rays emitted as a resonant Raman scattering or decay process of the inner-shell excitation, which gives information about element-specific excitations and occupied partial density of states (pDOS) of unionized and ionized materials. This technique has no restriction about samples and its atmospheres, and moreover, it is known as bulk sensitive methods (typically, hundreds of nm for soft X-rays).

In this work, we investigated the local electronic structure of Zn-phthalocyanine (ZnPc), which is one of the promising materials for organic photovoltaics. In order to study the local intermolecular interaction in ZnPc solids, we prepared the crystalline and amorphous films of ZnPc. We found a distinct crystalline structure dependence in the resonant XES (RXES) spectra, which can be originated from the site-specific intermolecular interaction.

Experiment

The ZnPc sample was prepared by the vacuum evaporation onto the naturally oxidized *p*-Si(111) surface. The deposition amounts of 400 nm and deposition rate of 1 nm/min were measured with a quartz crystal microbalance. The crystalline ZnPc film was obtained at the substrate temperature during the deposition of 340 K, while the amorphous ZnPc film was obtained at 84 K. The crystallinity of these ZnPc films at the room temperature of 300 K was confirmed by X-ray absorption spectroscopy (XAS) and by X-ray diffraction (XRD).

The XES measurements were performed by using a transmission grating spectrometer at BL3U of the UVSOR facility [1]. The incident soft X-ray beam was focused to 40 μm (horizontal) \times 20 μm (vertical) at the sample position. All XES measurements were performed at 300 K. For the XES spectra, we need a small photon spot size and long accumulation times of 60–90 min per 1 spectrum. Even in the photon flux of 10^{11} photons/sec range, the XES spectra of ZnPc films show the evidence for the radiation damage within 10–15 min X-ray irradiation. In order to avoid the radiation damage, the X-ray irradiated spot was continuously moved by scanning the sample at the rate of 20 $\mu\text{m}/\text{min}$ during the measurements.

Results and Discussion

Judging from the XRD and XAS results (not shown), the ZnPc molecules, deposited at the 340 K

substrate temperature, form an ordered α -crystalline structure where the molecular plane is tilted of about 70° with respect to the substrate surface, while the molecules deposited at 84 K form an amorphous structure.

The normal XES spectra, which reflect the occupied pDOS, do not show the clear difference between the crystalline and amorphous film (not shown). On the other hand, as shown in Fig. 1, the distinct crystalline structure dependence was observed in the RXES spectra. The elastic peak in the C $K\alpha$ RXES shows a symmetric lineshape for both the crystalline and amorphous films, but the elastic peak in the N $K\alpha$ RXES shows an asymmetric lineshape for the crystalline film, while the amorphous film gives the symmetric elastic peak, which is the indication of the presence of the Raman active intermolecular interaction at the N site in the crystalline film. As the origin of the asymmetric elastic peak, the vibronic excitation that accompanies direct recombination emission [2] can be considered. In this context, the broad peak around 0–1 eV in the recombination emission suggests the higher degree of localized character of the π^* states as compared to the case of graphite [2] and DNA molecules [3].

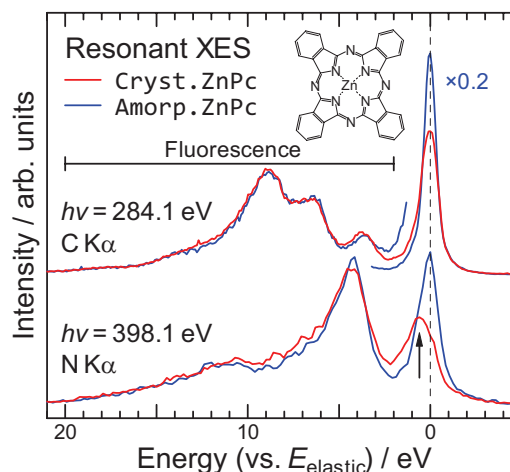


Fig. 1. The C $K\alpha$ and N $K\alpha$ resonant XES spectra of crystalline and amorphous films of ZnPc. The C $K\alpha$ and N $K\alpha$ excitation energies $h\nu$ were set to the first C K and N K resonance peaks in XAS.

- [1] T. Hatsui *et al.*, J. Electron Spectrosc. Relat. Phenom. **144-147** (2005) 1059.
- [2] Y. Ma *et al.*, Phys. Rev. Lett. **71** (1993) 3725.
- [3] H. Yamane *et al.*, a separate page in this volume.

Dilute Multi Ferroic Semiconductor GaCrN-II

S. Emura¹, H. Tambo¹, K. Higashi¹ and K. Fukui²

¹ISIR, Osaka University, Ibaraki 567-0047, Japan

²Faculty of Engineering, University of Fukui, Fukui 910-8507, Japan

Semiconductor systems with a wurtzite structure carrying a small amount of transition metals sometimes show the various physical properties. GaN:Cr is one of those. This substance exhibits magnetism and ferro-electrics. Therefore, we can expect to observe the anisotropic phenomena. The specimens studied here are single crystals in the thin layer form on a MgO and an Al₂O₃ substrate. On the MgO substrate, the crystal constructs the cubic structure (zinc-blende structure) and grows with a wurtzite structure on the Al₂O₃ substrate.

Figure 1 exhibits the incident angle dependence of the absorption spectra of the crystal with the wurtzite structure and CrN with rock salt structure for the reference in VUV region observed at BL4B at UVSOR. At zero angles, the electric field of incident photon is vertical to the crystal c-axis of GaN:Cr. The absorption band around 28 nm (44.3 eV), which is tentatively assigned to the transition from 3p of the Cr atom to the s-like conduction band of matrix because of the wide half width, strongly depends on the direction of the electric polarization of the incident photon. In the parallel electric field to the c-axis, the band vanishes, indicating anisotropy along the c-axis. As the XAFS analysis of these specimens predicts the spontaneous elastic deformation (quasi Jahn – Teller effect) involving the local electric polarization, this finding is an evidence of the ordering of the deformation and consequent electric polarization.

Figure 2 present the linear dichroism spectra for the cubic GaN:Cr in X-ray energy region. Here, the intensity of the spectra is normalized at the end (6030 eV) of the spectra shown in the figure. A clear doublet peak in the pre-edge region, which is assigned to the transition from 1s to 3d, and splits owing to the ligand field, can be found. The lower peak of the doublet exhibits the explicit linear dichroism. The observation indicates the ordering of the deformation in the cubic GaN:Cr also. In conclusion, the both hexagonal and cubic GaN:Cr crystals show the Jahn – Teller deformation around the Cr ions and the deformation is in ordering.

The detailed VUV and X-ray excitation spectra are observed. The strong angular dependence of the peak around 28 nm and linear dichroism at 5988 eV are found. This observation of the dichroism in GaN:Cr with the cubic structure indicates that the CrN₄ tetrahedron in the local coordination at the Cr ion suffers deformation. The Cr ions may shift slightly from the lattice center. it is apparent from the figures that the local spontaneous electric polarization is

induced around the doped Cr ion. Here, it should be noticed that there are four nearly equivalent legs because the original site symmetry is nearly T_d, and we cannot distinguish these four legs from the XAFS analysis. The parallel shifts may randomly be distributed in the matrix or ordered along some direction of the matrix.

The GaN:Cr is one of the dilute magnetic semiconductors. From our observation, it behave as a ferro-electric and elastic material. The coupling among those may lead to substances of a new category in multi-ferroic research field.

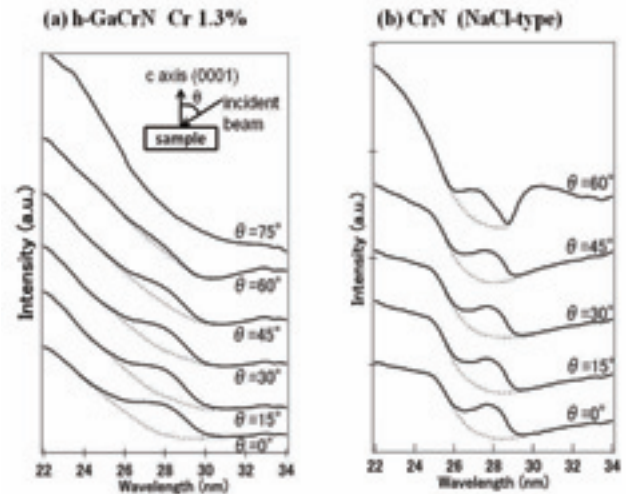


Fig. 1. Angular dependence of the absorption spectra.

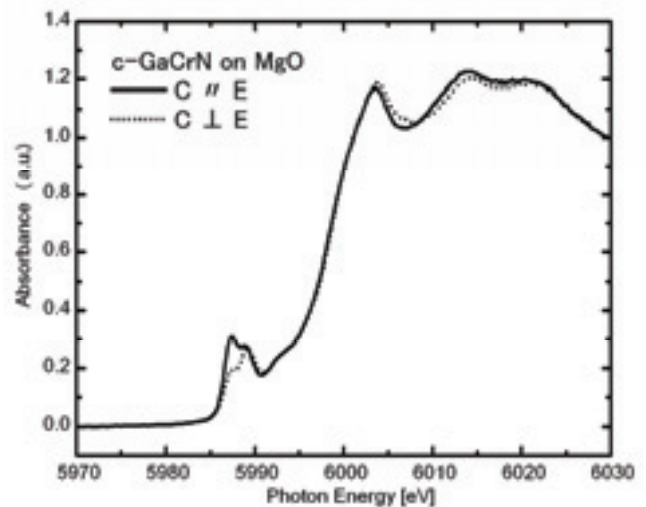


Fig. 2. Linear dichroism spectra in X-ray energy region.

Charge State Analysis of Mn Ions in $\text{Pr}_{1-x}\text{Ca}_x\text{MnO}_{3-\delta}$ by Mn-L_{2,3} XANES Spectra

H. Kanamori, T. Yoshioka and T. Yamamoto

Faculty of Science and Engineering, Waseda University, Shinjuku 169-8555, Japan

$\text{Pr}_{1-x}\text{Ca}_x\text{MnO}_{3-\delta}$ has been extensively studied, because it has unique electronic and magnetic properties such as colossal magnetoresistance and metal-insulator transition [1]. In order to understand such properties, it is essential to know the charge state, i.e., valence, of Mn ions in these materials. There are two scenarios to compensate the system; i) valence of Mn ions control the system, i.e., from Mn^{3+} to Mn^{4+} , ii) oxygen vacancy is created, when Ca is incorporated into PrMnO_3 . However, these mechanisms have not yet been understood. Then we have performed the charge state analysis of Mn ions in $\text{Pr}_{1-x}\text{Ca}_x\text{MnO}_{3-\delta}$ by the Mn-L_{2,3} X-ray absorption near-edge structure (XANES) measurements.

$\text{Pr}_{1-x}\text{Ca}_x\text{MnO}_{3-\delta}$ samples are synthesized by the conventional solid-state reaction method. Mn-L_{2,3} XANES spectra were observed at BL4B in UVSOR by the total electron yield (TEY) method. The incident beam was monochromatized with a grating (800 lines/mm) double crystal monochromator.

Prior to XANES analysis, all the samples were characterized by the X-ray diffraction (XRD). $\text{Pr}_{1-x}\text{Ca}_x\text{MnO}_{3-\delta}$ crystallizes perovskite structure at ambient condition. No extra peaks can be found in the observed XRD patterns except for those of the perovskite structured $\text{Pr}_{1-x}\text{Ca}_x\text{MnO}_{3-\delta}$.

Observed Mn-L₃ XANES spectra of the samples here synthesized are shown in Fig. 1. Valences of Mn ions in PrMnO_3 and CaMnO_3 are 3+ and 4+, respectively, when it is assumed that there is no oxygen vacancy in these materials. Spectral profiles of Mn-L₃ XANES spectra of these two materials show significant difference. Those of $\text{Pr}_{1-x}\text{Ca}_x\text{MnO}_{3-\delta}$ with $x=0.3, 0.4, 0.5$ changes from the shape of Mn^{3+} to Mn^{4+} as increment of Ca concentration. These experimental results suggest that valence of Mn ions in $\text{Pr}_{1-x}\text{Ca}_x\text{MnO}_{3-\delta}$ changes continuously as increment of Ca concentration.

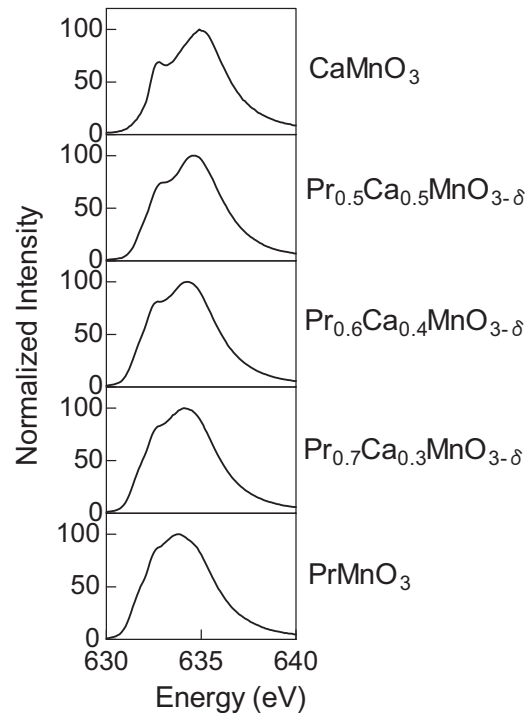


Fig. 1. Observed Mn-L₃ XANES spectra of $\text{Pr}_{1-x}\text{Ca}_x\text{MnO}_{3-\delta}$.

[1] Y. Tokura and N. Nagaosa, *Science* **288** (2000) 462.

Three-Dimensional Angle-Resolved Photoemission Study on EuFe_2As_2

T. Hajiri¹, R. Niwa², S. Murakami², H. Miyazaki³, J. B. Hong⁴, Y. R. Jang⁴, S. Kimura^{3,5},
Y. S. Kwon⁴ and T. Ito^{1,6}

¹Graduated School of Engineering, Nagoya University, Nagoya 464-8603, Japan

²School of Engineering, Nagoya University, Nagoya 464-8603, Japan

³UVSOR Facility, Institute for Molecular Science, Okazaki 444-8585, Japan

⁴Department of Physics, Sungkyukwan University, Suwon 440-749, Korea

⁵School of Physical Sciences, the Graduate University for Advanced Studies (SOKENDAI),
Okazaki 444-8585, Japan

⁶Nagoya University Synchrotron Radiation Research Center, Nagoya University, Nagoya
464-8603, Japan

Iron pnictides superconductor discovered recently has been intensively studied both from experiment and theory, however an essential mechanism of its anomalous superconductivity has not been clarified yet. To understand the mechanism of superconductivity, the superconducting gap information, i.e., the origin of superconducting pairing, is one of the most important issues.

To clarify the fundamental electronic structure of Iron pnictides, especially of '122' series, we have performed angle-resolved photoemission spectroscopy (ARPES) on EuFe_2As_2 in the heavily underdoped regime where the spin density wave (SDW) formation at $T_{\text{SDW}}=190$ K as well as an antiferromagnetic transition at $T_{\text{N}}=20$ K has been expected [2].

Figure 1 (a) and (b) shows momentum distribution curves (MDC) at $E_{\text{F}}\pm 50$ meV together with the experimental band structure along ΓX and ZR , respectively, obtained by plotting the second-derivative intensity of ARPES spectra of EuFe_2As_2 at 30 K. We have found two and one hole-like FS's around Γ and Z points, respectively, while the band structure calculation on the '122' series BaFe_2As_2 expects one and two hole-like FS's around the Γ and Z points [3] in against to the present ARPES result.

Furthermore, from the inter-plane FS along k_z -direction (Fig. 2) obtained by utilizing the photon energy dependent ARPES on the same sample EuFe_2As_2 at 30K, we found that the hole-like FS observed around the Γ point has been separated to the two hole-like FS as approaching to the Z point together with the reduction of FS sizes. This suggests that a single hole-like FS pocket around Γ point originating from the combination of two hole-like FS degenerating within our experimental momentum resolution ($\Delta\theta\sim 0.17^\circ\sim\Delta k\sim 0.011\text{ \AA}^{-1}$ at $h\nu=38$ eV).

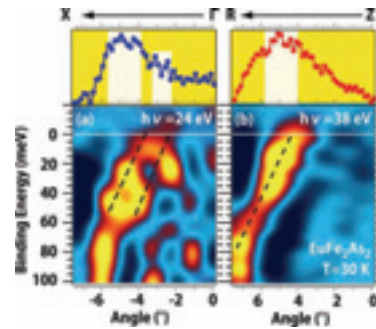


Fig. 1. Band structure along ΓX (a) and ZR (b) axis obtained by plotting the second-derivative intensity of ARPES spectra of EuFe_2As_2 with $h\nu=24$ eV (a) and 38 eV (b), respectively, at $T=30$ K. Upper panel shows MDC spectrum at $E_{\text{F}}\pm 50$ meV.

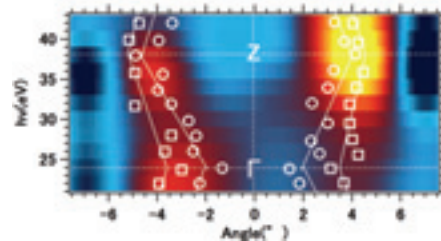


Fig. 2. Fermi surface image on ΓXRZ plane of EuFe_2As_2 . Open circles and squares are the peak positions of MDC spectra at E_{F} . Thin lines are guide for the eyes.

[1] Y. Kamihara *et al.*, J. Am. Chem. Soc. **130** (2008) 3296.

[2] H. S. Jeevan *et al.*, Phys. Rev. B **78** (2008) 020503(R).

[3] Walid MALAEB *et al.*, arXiv: **0906** (2009) 1846v1.

Ce 4d-4f Resonant Angle-Resolved Photoemission Studies on Quantum Criticality in Heavy-Fermion Ce112 Systems

H. J. Im¹, H. Miyazaki², T. Ito³, S. Kimura^{2,4}, K. E. Lee⁵ and Y. S. Kwon⁵

¹*Department of Advanced Physics, Hirosaki University, Hirosaki 036-8561, Japan*

²*UVSOR Facility, Institute for Molecular Science, Okazaki 444-8585, Japan*

³*Graduate School of Engineering, Nagoya University, Nagoya 464-8603, Japan*

⁴*School of Physical Sciences, The Graduate University for Advanced Studies, Okazaki 444-8585, Japan*

⁵*Department of Physics, Sungkyunkwan University, Suwon 440-746, Korea*

We have performed Ce 4d-4f resonant angle-resolved photoemission spectroscopy (rARPES) on CeNiGe₂ and CeNi_{0.7}Co_{0.3}Ge₂, whose ground states are antiferromagnetism (AFM) and quantum critical point (QCP), respectively, in the beamline BL5U of UVSOR. In this weakly hybridized regime, Ce 4f-electrons are considered to be highly localized due to the large repulsive Coulomb interaction between f-electrons and the weak hybridization strength between f- and conduction electrons. In addition, the localized character of f-electrons has been a key point to understand QCP. Therefore, the systematic investigation of Ce 4f-character in weakly hybridized regime is inevitable.

Figure (a) shows the high-resolution on-rARPES spectral image of CeNiGe₂. In order to investigate the momentum-dependence of Kondo resonance (KR) peaks near the Fermi level (E_F), the spectra (energy distribution curves, EDCs) are normalized to the intensity of Ce 4f^{7/2} peak around -0.3 eV: it is well known that the intensity ratio of Ce 4f^{5/2} peak (the tail of KR peak) to Ce 4f^{7/2} peak empirically represents the strength of Kondo coupling in angle-integrated photoemission (AIPES) spectra. Near E_F , the momentum-dependence of Ce 4f^{5/2} state is clearly observed. Besides the above Ce 4f-bands, there is another linearly dispersive band from -0.6 eV to E_F with weak intensity. This band is composed of non-f states and corresponds to conduction band. We find that the intensity of KR peak is largely enhanced where the conduction band crosses E_F as in CeCoGe_{0.8}Si_{1.2}, whose ground state is non-magnetism due to large hybridization strength [1]. Such behaviors are also observed in CeNi_{0.7}Co_{0.3}Ge₂ (not shown here). As a result, we conclude that the character of f-electrons is itinerant across QCP in agreement with the results of AIPES studies of CeNi_{1-x}Co_xGe₂ [2].

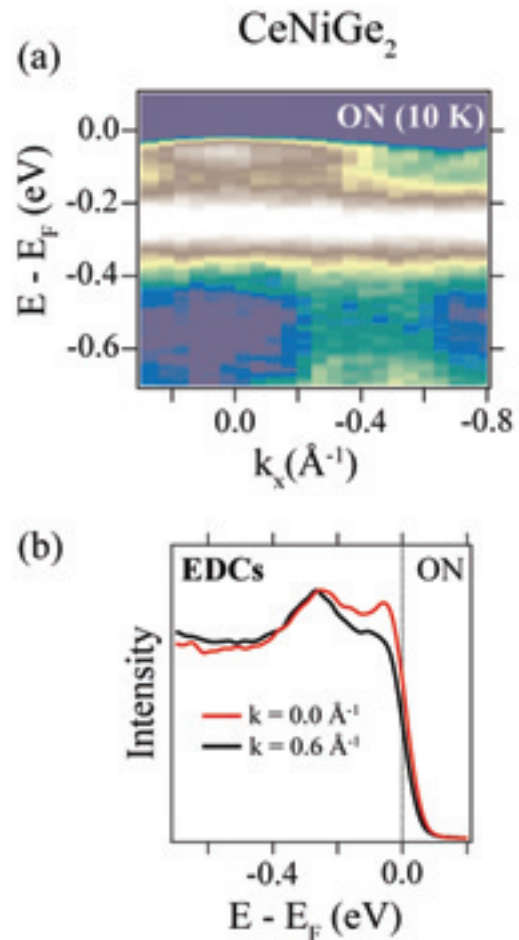


Fig. (a) Ce 4d-4f on-rARPES image of CeNiGe₂ ($h\nu = 122 \text{ eV}$, $T = 10 \text{ K}$). (b) The energy distribution curves at $k = 0 \text{ \AA}^{-1}$ (red line) and $k = 0.6 \text{ \AA}^{-1}$ (black line).

[1] H. J. Im *et al.*, Phys. Rev. Lett. **100** (2008) 176402.

[2] H. J. Im *et al.*, Phys. Rev. B **72** (2005) 220405.

Temperature-Dependent Photoemission Spectra of Alkanethiolate-Passivated Au Nanoparticles

M. Imamura, T. Fujino, S. Fujimasa and H. Yasuda

Department of Mechanical Engineering, Kobe University, Kobe 657-8501, Japan

Metallic nanoparticles attract much attention due to their characteristic properties such as Coulomb blockade, nonlinear optical response, and catalytic activity. In order to elucidate their detailed intriguing properties and to develop the future devices, it is indispensable to understand the electronic structures. In this work, we have carried out the synchrotron-radiation photoemission study of dodecanethiolate-passivated Au nanoparticles supported on the HOPG substrate at various temperatures.

The synthesis procedure of DT-passivated Au nanoparticle is described elsewhere [1]. The synchrotron photoemission study was carried out with the incident photon energy of 190 eV at BL-5U of UVSOR facility.

Figure 1 shows the synchrotron-radiation photoemission spectra of DT-passivated Au nanoparticles with the mean diameter of 2.5 nm in the vicinity of Fermi-level measured at room temperature, 160, and 100 K. The leading edges of the spectra in the vicinity of Fermi-level of all the Au nanoparticles at various temperatures moved away from Fermi-level. Furthermore, the photoemission intensities of the leading edges decrease with decreasing the measurement temperature, and change to the background intensity of HOPG. In our previous work, we have reported that the photoemission spectra in the vicinity of Fermi level of DT-passivated Ag nanoparticles show the deviation from the metallic Fermi-edge, and concluded that these spectra reflect the final-state effect [1, 2]. We have explained the experimental spectra using a theoretical model that takes into account the influence of the photohole remaining on the nanoparticle during the photoemission process and the nanoparticle-substrate interaction. The shift of Fermi edge in the present photoemission spectrum measured at room temperature is well explained by the same picture. Since the final-state effects do not depend on the measurement temperature, the temperature dependence of present photoemission spectra is considered to originate from the change of intrinsic electronic structure of Au nanoparticles. Kubo criterion predicted that the discrete energy states are exhibited when the mean energy-level spacing near Fermi-energy exceeds the characteristic thermal

energy. In the present case, Au nanoparticles at room temperature remain bulk-like electronic structure, since the energy level spacing is narrower than the thermal broadening. With decreasing temperature, the mean energy-level spacing of Au nanoparticles exceeds the characteristic thermal energy. Consequently, Au nanoparticles is expected to have discrete electronic structures. The discrete and low densities of states of Au nanoparticle will lead to decrease the photoemission intensities. From these results it is concluded that the temperature-dependent photoemission spectra in the vicinity of Fermi-level is attributed to temperature-dependent metal-insulator transition that is theoretically predicted.

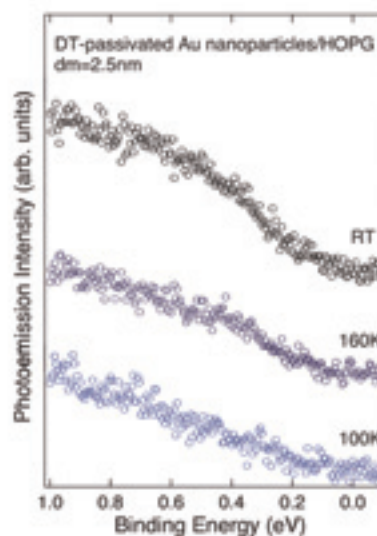


Fig. 1. Synchrotron-radiation photoemission spectra of DT-passivated Au nanoparticles supported on the HOPG substrates in the vicinity of Fermi-level measured with the photon energy of 190 eV at room temperature, 160K, and 100K.

- [1] A. Tanaka, Y. Takeda, M. Imamura and S. Sato, *Appl. Surf. Sci.* **237** (2004) 537-542.
 [2] M. Imamura and A. Tanaka, *Phys. Rev. B* **73** (2006) 125409-1-125409-5.

BL5U **Detection of Spin-Filtered Surface-States of a Topological Insulator by Polarization Dependent Angle-Resolved Photoemission Spectroscopy**

A. Nishide, F. Nakamura and I. Matsuda

Institute for Solid State Physics, University of Tokyo, Kashiwa 277-8581, Japan

The quantum spin Hall (QSH) effect, which makes it possible to produce topologically protected spin currents without magnet, has now attracted interests of researchers in condensed matter physics. Recently, photoemission spectroscopy (PES) studies [1] have mapped band dispersion curves of the surface states of the semiconductor alloy, $\text{Bi}_{1-x}\text{Sb}_x$ ($x \sim 0.1$), and high-resolution spin-resolved PES measurements [2] have determined their spin orientations between the two time-reversal invariant momenta. These experimental results have clearly indicated a trace of the predicted topological band structure, giving direct evidence of the topological insulator. These previous works have also demonstrated that PES is the most powerful tool for such researches. On the other hand, it has been known that, during the PE process, photoexcitation of electrons with different spin orientations depend on circular polarizations of incident light [3]. Thus, we conducted polarization dependent angle-resolved PES measurements to obtain direct evidence of spin-filtered surface-states of the QSH phase. The experiment was performed at UVSOR BL-5U with the Apple-II type undulator, generating right and left helical light. As shown in Fig., we observed clear variations of photoemission intensity with the circular polarizations. Moreover, we succeeded in detecting two surface-state bands [2], Σ_2 and Σ_1' , of the three-dimensional QSH phase at the \bar{M} point, Fig.(b), confirming the non-trivial topological nature of $\text{Bi}_{1-x}\text{Sb}_x$ ($x=0.15$).

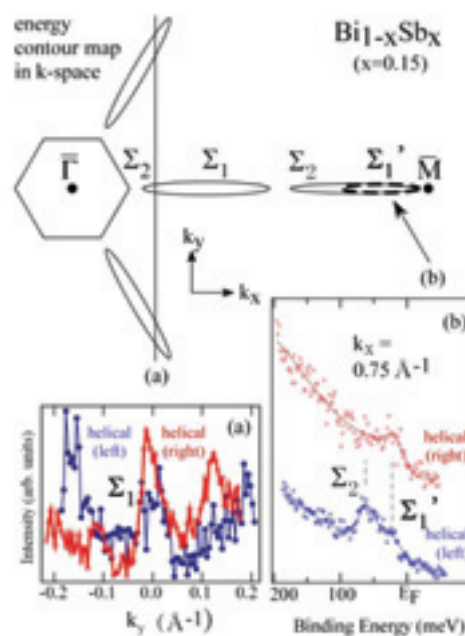


Fig. Schematic drawing of the energy contour map of $\text{Bi}_{1-x}\text{Sb}_x$ ($x=0.15$) around Fermi level with a series of (a,b) experimental photoemission spectra taken at 20K.

Acknowledgements

Alexey A. Taskin and Yoichi Ando in Osaka University are gratefully acknowledged for sample crystals and valuable comments

[1] D. Hsieh *et al.*, Nature **452** (2008) 970.
 [2] A. Nishide *et al.*, Phys. Rev. B **81** (2010) 041309 (R).
 [3] M. Mulazzi *et al.*, Phys. Rev. B **74** (2006) 035118.

Resonance Photoemission Study of Pseudo-One Dimensional Cobalt Oxide $\text{Ba}_3\text{Co}_2\text{O}_6(\text{CO}_3)_{0.7}$

K. Soda¹, M. Kikuchi², H. Miyazaki^{1,3}, M. Inukai^{1,4}, M. Kato¹, S. Yagi¹,
K. Iwasaki^{1,5} and T. Matsui^{1,6}

¹Graduate School of Engineering, Nagoya University, Nagoya 464-8603, Japan

²School of Engineering, Nagoya University, Nagoya 464-8603, Japan

³UVSOR Facility, Institute for Molecular Science, Okazaki 444-8585, Japan

⁴Venture Business Laboratory, Nagoya University, Nagoya 464-8603, Japan

⁵Toyota Boshoku Coporation, Kariya 448-8651, Japan

⁶EcoTopia Science Institute, Nagoya University, Nagoya 464-8603, Japan

Recently it has been found that a pseudo-one dimensional $\text{Ba}_3\text{Co}_2\text{O}_6(\text{CO}_3)_{0.7}$ shows a fairly large thermoelectric power factor of $0.9 \text{ mWm}^{-1}\text{K}^{-2}$ at 300 K with the thermoelectric power of about $+120 \mu\text{V K}^{-1}$ and metallic behavior of its electric conductivity above 300 K [1]. In order to understand its physical properties, we have investigated its valence-band electronic structure by photoelectron spectroscopy.

Photoelectron measurements were carried out with use of single-crystalline specimens prepared in size of $5 \times 0.5 \times 0.5 \text{ mm}^3$ by a flux method [1]. A Pt wire was attached to one end of the specimen to avoid the charging up at low temperatures, and the clean surface was obtained by *in situ* fracturing another end of the specimen in perpendicular to the *c* axis.

Figure 1 shows typical valence-band photoelectron spectra recorded at 20 K with the excitation photon energies $h\nu$ of 60 and 75 eV and their difference spectrum. Each spectrum is normalized with the integrated intensity and subtracted the background by an iteration method [2]. Observed features A to C are ascribed to the hybridized bands of the Co *3d* and O *2p* states, and the Co *3p-3d* resonance photoemission shows the relatively large Co *3d* contribution to the features A and B, as seen in the difference spectrum. The other features D, E, F, G and H are assigned to the CO_3 -derived states, the surface components, Ba *5p* spin-orbit doublets and O *2s* state, respectively.

Figure 2 shows temperature dependence of the valence-band spectra near the Fermi level E_F together with reference Au spectra. $\text{Ba}_3\text{Co}_2\text{O}_6(\text{CO}_3)_{0.7}$ reveals large reduction in intensity towards E_F but clear finite intensity at E_F , which suggests the electron doping into the low-spin $\text{Co}^{4+}(t_{2g}^5 3d^6)$ bands and the positive thermoelectric power of 81 or $141 \mu\text{V K}^{-1}$ at high temperatures for the Co^{4+} concentration *x* of 0.7 [3]. Although a 1/8-power-law dependence of the intensity on the binding energy E_B might be expected in one-dimensional fermion system [4], the anomalous exponents from 0.5 at 20 K to 0.8 at 200 K are obtained for $E_B = 0.01\sim 0.1 \text{ eV}$, which suggests the larger short-range interaction at the lower temperature. A small hump at $E_B \sim 0.02 \text{ eV}$ observed at $T = 20 \text{ K}$ might also indicate the opening of a

pseudogap or a magnetic ordering, which may cause the recently observed reduction in the electric conductivity at low temperatures [5].

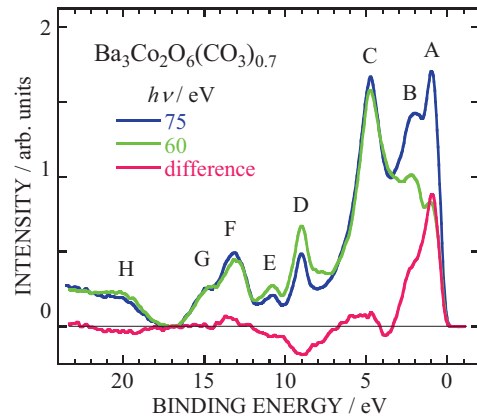


Fig.1. Valence-band spectra and difference spectrum of $\text{Ba}_3\text{Co}_2\text{O}_6(\text{CO}_3)_{0.7}$.

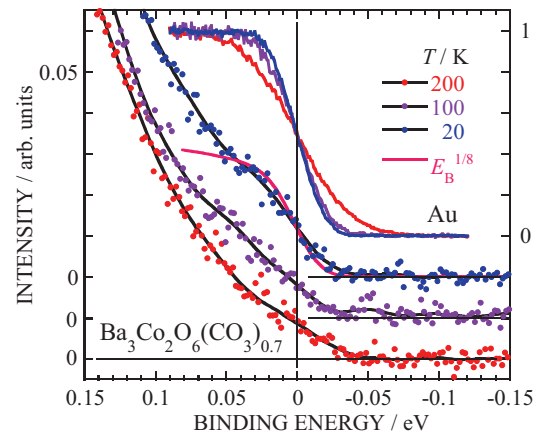


Fig.2. Temperature dependence of valence-band spectra near the Fermi level of $\text{Ba}_3\text{Co}_2\text{O}_6(\text{CO}_3)_{0.7}$.

[1] T. Yamamoto *et al.*, Proc. Int. Symp. on EcoTopia Science 2007, p.145.

[2] K. Soda *et al.*, J. Phys. Soc. Jpn. **60** (1991) 3059.

[3] W. Koshibae *et al.*, Phys. Rev. B **62** (2000) 6869.

[4] J. Voit, Pep. Prog. Phys. **57** (1994) 977.

[5] K. Iwasaki, *private communication*.

Terahertz Spectroscopy of Doped Superionic Conductors

T. Awano

Department of Electronic Engineering, Tohoku Gakuin University, Tagajo 985-8537, Japan

RbA_4X_5 (A=Ag or Cu, X=halogen) crystal has high ionic conductivity as liquid even at room temperature. Silver (copper) ions move fast in conductive channels which are composed of silver (copper) sites surrounded by iodide tetrahedra. Sixteen ions in a unit cell are able to occupy 56 such sites. These available sites for the conducting ion are not enough to avoid Coulomb repulsion by each other. This suggests that collective movement of conducting ions should occur. Such correlative motion should be enhanced largely by doping excess conduction ions. In this study, terahertz spectra of excess silver (copper) doped RbA_4X_5 and silver (copper) vacancy doped one were investigated to study such effect by the collective motion.

Excess silver was doped by evaporation of silver film on the crystal and diffusion by heating. Vacancy of silver was introduced by iodine vapor addition at room temperature.

Figure 1 shows reflectivity spectra of $\text{RbAg}_4\text{I}_5:\text{Ag}$ and $\text{RbAg}_4\text{I}_5:\text{I}_2$. The latter corresponds to introducing silver vacancy. Figures 2 and 3 show dielectric constants obtained by Kramers-Kronig analysis. The dielectric constants decreased by silver addition and increased by iodine addition in the spectral region below 20cm^{-1} . This spectral region corresponds to "attempt mode" which is a movement of a silver ion going out from surrounding iodide tetrahedral cage. Therefore spectral change of this region seems to concern dynamics of the ion conduction strongly.

In the study of Raman scattering spectra of doped RbAg_4I_5 , drastic spectral changes were reported previously^{1, 2}. The scattering intensity in terahertz region (under 50cm^{-1}) increased by silver addition and decreased by iodine addition. Moreover fine structures at low temperature disappeared in the case of iodine addition².

The FIR results of this study are contrary to those of the Raman spectroscopic study. The intensity change of low wave number region was exactly reverse between them. The fine structure did not disappear in the FIR spectra. These differences between them seem to be due to difference of optical process between FIR and Raman spectroscopy.

[1] S. Bredikhin, T. Hattori and M. Ishigame, *Solid State Ionics* **67** (1994) 311.

[2] S. Bredikhin, N. Kovaleva, T. Hattori and M. Ishigame, *Solid State Ionics* **74** (1994) 149.

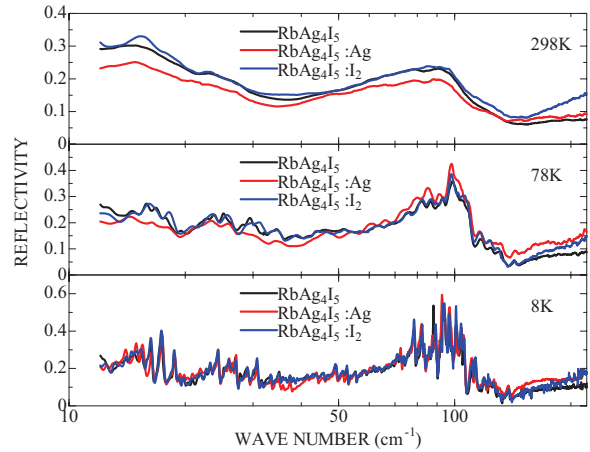


Fig. 1. Reflectivity spectra of doped- RbAg_4I_5 .

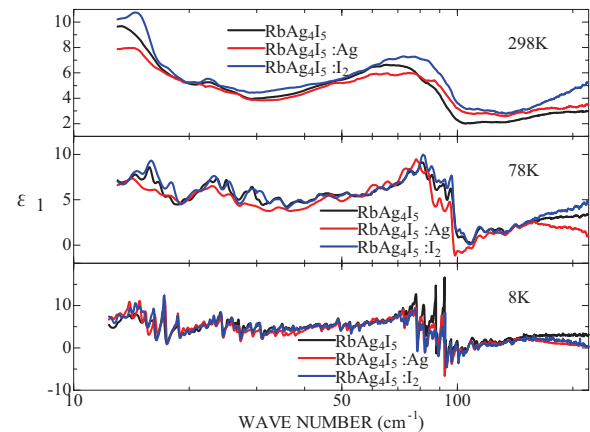


Fig. 2. Real part of dielectric constant of doped- RbAg_4I_5 .

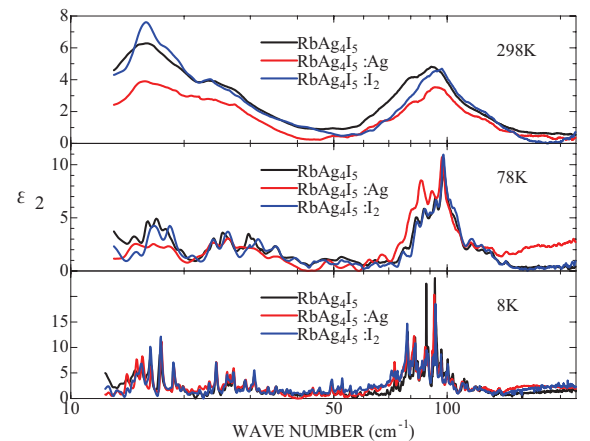


Fig. 3. Imaginary part of dielectric constant of doped- RbAg_4I_5 .

Evolution of c - f Hybridization State of CeIn_3

T. Iizuka¹, T. Mizuno¹, C. I. Lee², Y. S. Kwon², S. Kimura^{3,1}

¹*School of Physical Sciences, The Graduate University for Advanced Studies (SOKENDAI), Okazaki 444-8585, Japan*

²*Department of Physics, Sungkyunkwan University, Suwon 440-746, Korea*

³*UVSOR Facility, Institute for Molecular Science, Okazaki 444-8585, Japan*

Introduction

“Heavy fermion” attracts attention because of their various physical properties, which originate from the hybridization between the localized $4f$ and conduction electrons, namely c - f hybridization [1]. According to the periodic Anderson model (PAM), which theoretically describes the change of electronic structure with the c - f hybridization, the bonding and antibonding bands due to the c - f hybridization are created. The size of the energy gap increases with increasing c - f hybridization intensity.

The purpose of this study is to investigate the evolution of the c - f hybridization state. The hybridization intensity can be controlled by applying pressure. The target material of this study, CeIn_3 , which has a localized $4f$ -electron, is the antiferromagnetic (AFM) ground state (the Néel temperature $T_N \sim 10$ K). With applying pressure, T_N is monotonically suppressed and is disappeared at $P_C = 2.6$ GPa. Then a superconducting phase appears. In addition, from a NQR measurement on CeIn_3 under pressure, there is T^* -line which divides the local regime ($T^* > T$) and the itinerant regime ($T^* < T$), at around 2 GPa in the nonmagnetic state [2]. Therefore this material is suitable to investigate the evolution of the c - f hybridization state by applying pressure.

Experimental

The single phase CeIn_3 was synthesized by an arc-melting method under argon atmosphere, and then was annealed at 600 °C for three weeks inside an evacuated quartz tube. The THz reflection spectroscopy under pressure was performed at the THz micro-spectroscopy end station of BL6B, UVSOR-II. A diamond anvil cell was employed to produce high pressure. KBr was used as a pressure medium and gold as a reference. The pressure was calibrated by a ruby fluorescence method.

Results and Discussion

We obtained pressure-dependent reflectivity spectra [$R(\omega, P)$] of CeIn_3 at 5.6 K in the pressure region from 0.2 to 2.7 GPa as shown in Fig. 1a. At the lowest pressure ($P = 0.2$ GPa), the spectrum intensity monotonically decreases with increasing photon energy indicating the normal metallic character. At 0.9 GPa in the AFM phase, a peak appears at around

17meV. The peak corresponds to the optical transition between the bonding and antibonding state of the c - f hybridization state. The peak shifts to higher photon energy side with increasing pressure. The peak shift is consistent with the increase of the c - f hybridization intensity behavior predicted by PAM.

The c - f hybridization state is evolved not only in the nonmagnetic state but also in the AFM state. This result supports the spin-fluctuation (SDW) model [1, 3], which has a phase boundary dividing the local/itinerant regime in the AFM phase.

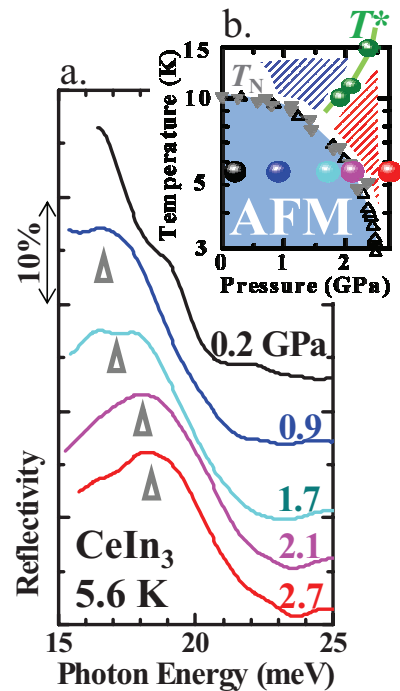


Fig. 1. (a) Pressure-dependent reflectivity spectra [$R(\omega, P)$] of CeIn_3 at 5.6 K. Triangles suggest peak positions. (b) Temperature-pressure phase diagram previously obtained from a NQR measurement ($T_{\text{Néel}}$ and T^*) [2]. T^* divide local (blue mesh) and itinerant (red mesh) regime. The solid circles indicate the positions where the optical spectra were taken.

[1] P. Gegenwart *et al.*, Nat. Phys. 4 (2008) 186.

[2] S. Kawasaki *et al.*, J. Phys. Soc. Jpn. 73 (2004) 1647.

[3] S. Watanabe and K. Miyake, J. Phys. Soc. Jpn. 79 (2010) 033707.

Magneto-Plasma Reflection Study of Superconducting InN

T. Inushima¹, T. Iizuka², S. Kimura^{2,3} and K. Fukui⁴

¹Department of Electronics, Tokai University, Hiratsuka 259-1292, Japan

²School of Physical Sciences, The Graduate University for Advanced Studies (SOKENDAI), Okazaki 444-8585, Japan

³UVSOR Facility, Institute for Molecular Science, Okazaki 444-8585 Japan

⁴Department of Electrical and Electronics Engineering, University of Fukui, Fukui, 910-8507, Japan

Among the III-nitride semiconductors, InN is a key material for optical and high temperature device applications. Since it was reported that InN had a small band gap energy (0.64 eV) and a superconducting character [1], it has become a big issue to determine the electron effective mass. Hence we measured the electron effective mass of superconducting InN from the reflection spectra with the cyclotron resonance.

The InN film (GS1949) investigated here was grown by the Cornell University group and had a carrier density of $\sim 4.5 \times 10^{17} \text{ cm}^{-3}$ and a mobility of $\sim 2000 \text{ cm}^2(\text{Vs})^{-1}$. The sample showed Meissner effect below 1.8 K. It was set in an Oxford spectromag 6T and the reflectivity was measured from 50 to 660 cm^{-1} at 6 K by Jasco FTIR610 at Faraday configuration. The optical resolution was 0.5 cm^{-1} .

Figure 1 shows the reflectivity spectrum at 6 K. It is analyzed using the following dielectric function (n_i),

$$n_i^2(\omega) = \epsilon_\infty \left(1 - \frac{\omega_p^2}{\omega(\omega \pm \omega_c + i\gamma)} + \frac{(\omega_{LO}^2 - \omega_{TO}^2)}{\omega_{TO}^2 - \omega^2 - i\Gamma\omega} \right),$$

$$\omega_c = \frac{eB}{m^*}, \quad (1)$$

where ω_p and ω_c are plasma and cyclotron frequencies, respectively. Reflectivity R is calculated using the following equation,

$$\frac{E_{or}}{E_{oi}} = \frac{(n_1 - n_2)(n_1 + n_0)e^{ikn_1d} + (n_2 + n_1)(n_0 - n_1)e^{-ikn_1d}}{(n_2 - n_1)(n_1 - n_0)e^{ikn_1d} + (n_2 + n_1)(n_0 + n_1)e^{-ikn_1d}},$$

$$R = \left| \frac{E_{or}}{E_{oi}} \right|^2, \quad (2)$$

where d ($\sim 5 \mu\text{m}$) is the film thickness, n_0 and n_2 are the refractive indices of air and sapphire, respectively.

Figure 2 shows the change of the reflectivity ($\Delta R(B) = R(B) - R(0)$) caused by the magnetic field. In this experiment, unpolarized light was used. Hence, when there is a plasma oscillation, $\Delta R(B)$ has a peak near ω_p . The two peaks ($\sim 230 \text{ cm}^{-1}$ and 100 cm^{-1}) in the spectrum indicate that there are two plasma oscillations in the sample investigated. Therefore we add another plasma oscillation in the dielectric function as follows,

$$n_i^2(\omega) = \epsilon_\infty \left(1 - \frac{\omega_{p1}^2}{\omega(\omega \pm \omega_c + i\gamma_1)} - \frac{\omega_{p2}^2}{\omega(\omega \pm \omega_c + i\gamma_2)} + \frac{(\omega_{LO}^2 - \omega_{TO}^2)}{\omega_{TO}^2 - \omega^2 - i\Gamma\omega} \right), \quad \omega_c = \frac{eB}{m^*}. \quad (3)$$

Here we assume that InN has a spherical Fermi sur-

face and a unique effective mass m^* . The best fittings are obtained when $m^* = 0.08 m_0$, $\omega_{p1} = 0.016 \text{ eV}$ with $\gamma_1 = 15 \text{ meV}$ and $\omega_{p2} = 0.028 \text{ eV}$ with $\gamma_2 = 3.3 \text{ meV}$. This result indicates that the conduction band of superconducting InN has at least two electrons with different mobilities. This will explain many of the controversial problems reported for InN[2].

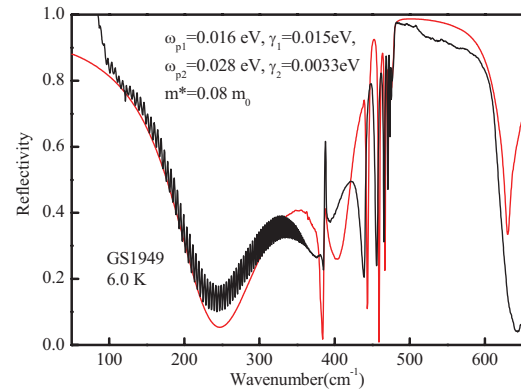


Fig. 1. Reflectivity spectrum of GS1949 at 6 K at zero magnetic field. Fitting is done using Eqs. (2) and (3) with parameters given in the figure.

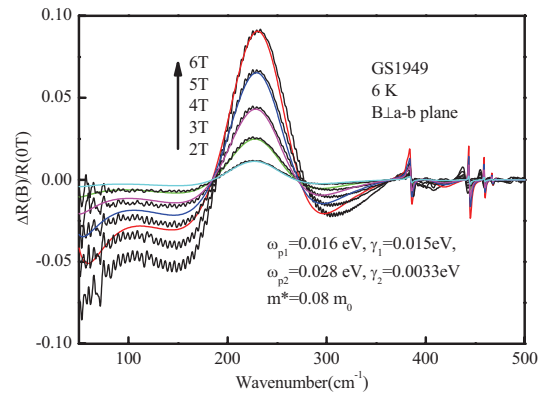


Fig. 2. Change of the reflectivity $\Delta R(B)$ as a function of the applied magnetic field at 6K. Fittings are done using Eqs. (2) and (3) with parameters given in the figure.

[1] T. Inushima *et al.*, J. Crystal Growth **227-228** (2001) 481.

[2] C. H. Swartz *et al.*, J. Crystal Growth **269** (2004) 29.

Optical Study of Metal-Insulator Change in LiV_2O_4 under High Pressure

A. Irizawa¹, T. Iizuka² and S. Kimura^{2,3}

¹Graduate School of Science and Technology, Kobe University, Kobe 657-8501, Japan

²School of Physical Sciences, The Graduate University for Advanced Studies (SOKENDAI), Okazaki 444-8585, Japan

³UVSOR Facility, Institute for Molecular Science, Okazaki 444-8585, Japan

Introduction

The optical study under multi-extreme condition such as high-pressure and low-temperature is one of the most attractive techniques for the investigation of electronic states of solids. In case of strongly correlated electron systems, the pressure will directly affect the electron-electron interactions through the change of lattice constants. Optical reflectivity experiment under high pressure can be carried out using a diamond anvil cell (DAC) because of not only the highest hardness on earth but also the high transparency in the wide energy region from terahertz (THz) to ultraviolet (UV) of the diamond. In addition the highest thermal conductivity on earth of the diamond also enables to get lower temperature in the sample space. On the other hand, there are some difficulties for this experiment. The sample space is as small as the culet of diamond which is less than several hundred μm in usual. At the same time, the maximum pressure is controlled by the size of culet. For example, DAC with 600 $\mu\text{m}\phi$ culet can achieve the maximum pressure up to 20 GPa, but it is risky that we go beyond 12 GPa with 800 $\mu\text{m}\phi$ one without spare. Here we should consider the diffraction limit at far-infrared (FIR) region. For example the photon energy of 10 meV is equal to the wavelength of 125 μm . Therefore the lowest photon energy and the highest pressure are exclusive for each other. A serious problem at the scene of experiment is that the pressure and temperature are hardly controlled individually because of the hysteresis procedure of them caused by finite friction of the moving part of apparatus at low temperatures. The sample position should be also adjusted at every pressure and temperature in the case of microscopy. On the basis of these experimental restrictions, we tried the reflectivity measurement at FIR region for metal-insulator change compound LiV_2O_4 under pressure at low temperature. Spinel oxide LiV_2O_4 has been found for the first time to show a heavy fermion state among 3d metal oxides. LiV_2O_4 has vanadium with half integer valence number of +3.5 ($d^{1.5}$) in a metallic state. In an insulating state it should exhibit the alternated valence numbers of $\text{V}^{3+}:\text{V}^{4+}=1:1$ or $\text{V}^{3+}:\text{V}^{5+}=3:1$ together with the constant states of Li^{1+} and O^{2-} . Under pressures, the low temperature metallic phase drastically changes to an insulating one [1]. The formation of charge ordering has been predicted in this insulating phase. A structural distortion involving the distribution of V-V

bond length is confirmed by a x-ray analysis and an EXAFS experiment. We have investigated the electronic states of LiV_2O_4 under pressures and low temperatures analyzed by optical study using an infrared microscope in SPring-8 [2-4]. There are three different phases showing the characteristic optical spectra. In the middle phase between the metallic and insulating ones, the spectra show a gradual change with pressure and temperature. The purpose of experiment in this beam time, we will observe this gradual change carefully inhibiting the pressure-shift as far as possible during temperature change.

Experimental

The optical reflectivities of single crystal LiV_2O_4 were measured at the microscope end station of UVSOR-II BL6B. The procedure of high pressure experiment was similar to the former studies. The observed wavenumber was between 80 and 700 cm^{-1} with the fixed pressure of 8 GPa. The temperature was changed between 20 and 300 K.

Results and Discussion

The tentative reflectivities obtained from the spectra of sample and Au film in DAC are shown in Fig. 1. Here we can confirm the gradual change from metallic spectrum at 300 K to the other ones of reduced intensities with decreasing temperature. The measurements were succeeded both in decay mode and Top-up mode.

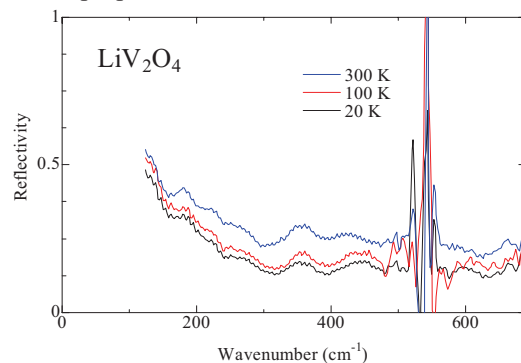


Fig. 1. Temperature change of reflectivity at FIR region under 8 GPa.

- [1] C. Urano, PhD thesis, University of Tokyo (2000).
 [2] K. Shimai, A. Irizawa *et al.*, *Infrared Physics & Technology* **51** (2008) 468.
 [3] A. Irizawa *et al.*, *Physica B*, **403** (2008) 948.
 [4] A. Irizawa *et al.*, *Journal of Phys: Conf. Ser.* **150** (2009) 042070.

Infrared Reflection Spectra of $\text{In}_x\text{Al}_{1-x}\text{N}$

K. Ozaki¹, R. Ueda¹, K. Fukui¹, A. Yamamoto¹

¹*Dept. Elec. Elec. Engi, Univ. Fukui, Fukui 910-8507, Japan*

The ternary $\text{In}_x\text{Al}_{1-x}\text{N}$ has great potential for applications in the solar cell with a wide variable bandgap range from 0.7 eV to 6.2 eV. However, many of its basic properties are still unknown, because it is difficult to obtain high quality thin films due to the huge differences of the growth conditions between InN and AlN. Our purpose in this report is to present the vibrational properties of the $\text{In}_x\text{Al}_{1-x}\text{N}$ over a wide In fraction range using the selected thin films whose infrared reflection spectra can be explained by the fitting calculations based on the dielectric function written by both LO and TO phonon contributions [1]

$$\varepsilon(\omega) = \varepsilon_\infty \prod_j \frac{\omega_{jL}^2 - \omega^2 + i\Gamma_{jL}\omega}{\omega_{jT}^2 - \omega^2 + i\Gamma_{jT}\omega} \quad (1)$$

where ε_∞ , ω_{jL} , ω_{jT} , γ_{jL} , γ_{jT} are high-frequency dielectric constant, j -th branch longitudinal and transverse optical phonon (LO, TO) frequencies and j -th branch LO and TO phonon damping.

Each $\text{In}_x\text{Al}_{1-x}\text{N}$ thin film was grown on the sapphire substrate with a GaN buffer layer by MOVPE at University of Fukui. The In fraction of the thin films were $x = 0.90, 0.70, 0.68, 0.60, 0.35,$ and 0.30 . The film thickness and the carrier density are $0.4 \sim 1.1 \mu\text{m}$ and $10^{18} \sim 10^{19} \text{cm}^{-3}$, respectively.

By using Eq. 1 and the transfer matrix method, the theoretical total reflectance with the consideration of the multiple reflection based on InAlN-sapphire two layers model can be described. Then, the fitting calculations between experimental and theoretical reflectance spectra have been carried out. The best fitting results suggest that the TO phonons consist of both InN-like and AlN-like TO phonons (two-mode behavior), and the LO phonon consists of one phonon (one-mode behavior). Similar one-mode LO – two-mode TO result was found in the ternary AlGaIn [2], and suggest that the TO phonon vibration is so localized and investigated theoretically [3].

The infrared reflection spectrum of $\text{In}_x\text{Al}_{1-x}\text{N}$ ($x = 0.6$) and the fitting result are shown in Figure 1. The dip at 480 cm^{-1} is attributed to the InN-like TO phonon. According to the fitting calculation, it is found that the shoulder like spectral feature at the lower wavenumber side of the 580 cm^{-1} peak is attributed to the AlN-like TO phonon, though it is not clearly seen in the spectrum. The rising edge at around 900 cm^{-1} from higher wavenumber side to lower is due to the beginning of the Reststrahlen band. Figure 2 shows the In fraction dependence of the fitted TO phonon and LO phonon wavenumber. It is clear that the In fraction dependences of both the InN-like TO phonon wavenumber and AlN-like TO

phonon wavenumber are relatively weak. On the other hand, the LO phonon wavenumber shows the clear In fraction dependence, and obvious softening above 0.7 In fraction. Such a strong softening is not predicted by Ref. 3 and further investigation is underway.

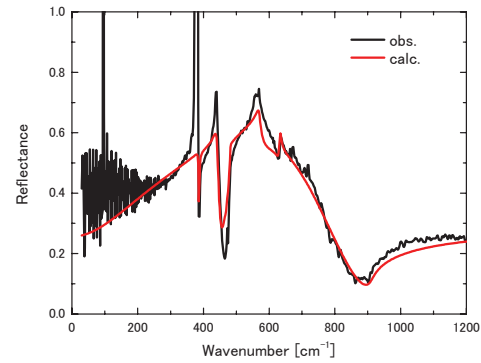


Fig. 1. Reflection spectrum of $\text{In}_x\text{Al}_{1-x}\text{N}$ ($x = 0.6$) and the fitting result.

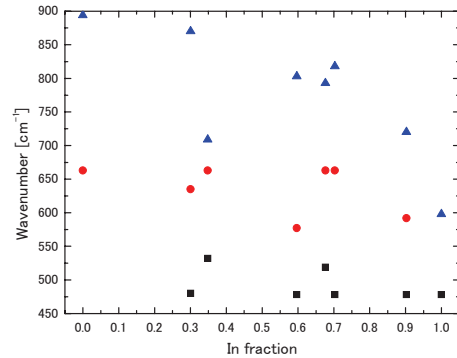


Fig. 2. Indium fraction dependence of the AlN-like TO phonon (circle), InN-like TO phonon (square), and LO phonon (triangle) wavenumber for $\text{In}_x\text{Al}_{1-x}\text{N}$.

[1] F. Gervais and B. Piriou, *J. Phys. C* **7** (1974) 2374.

[2] A. Cros, H. Angerer, R. Handschuh, O. Ambacher and M. Stutzmann, *Solid State Commun.* **104** (1997) 35.

[3] H. Grille, Ch. Schnittler and F. Bechstedt, *Phys. Rev. B* **61** (2000) 6091.

Temperature Dependent Angle-Resolved Photoemission Study on $\text{BaFe}_{1.8}\text{Co}_{0.2}\text{As}_2$

T. Hajiri¹, R. Niwa², S. Murakami², H. Miyazaki³, J. B. Hong⁴, Y. R. Jang⁴, S. Kimura^{3,5}, Y. S. Kwon⁴ and T. Ito^{1,6}

¹Graduated School of Engineering, Nagoya University, Nagoya 464-8603, Japan

²School of Engineering, Nagoya University, Nagoya 464-8603, Japan

³UVSOR Facility, Institute for Molecular Science, Okazaki 444-8585, Japan

⁴Department of Physics, Sungkyukwan University, Suwon 440-749, Korea

⁵School of Physical Sciences, the Graduate University for Advanced Studies (SOKENDAI), Okazaki 444-8585, Japan

⁶Nagoya University Synchrotron Radiation Research Center, Nagoya University, Nagoya 464-8603, Japan

Iron pnictides superconductor discovered recently has been intensively studied both from experiment and theory, however an essential mechanism of its anomalous superconductivity has not been clarified yet. To understand the mechanism of superconductivity, the superconducting gap information, i.e., the origin of superconducting pairing is one of the most important issues. For example, multiple isotropic gaps suggesting s-wave pairing have been reported on the optimally hole-doped $\text{Ba}_{0.6}\text{K}_{0.4}\text{Fe}_2\text{As}_2$ [1].

We have performed angle-resolved photoemission spectroscopy (ARPES) on electron-doped iron pnictides superconductor $\text{BaFe}_{1.8}\text{Co}_{0.2}\text{As}_2$ in the slightly underdoped regime ($T_c=25$ K), to elucidate the essential role of the doped carriers to the anomalous superconductivity [2].

Figure 1 shows the Fermi surface image of $\text{BaFe}_{1.8}\text{Co}_{0.2}\text{As}_2$ at 35 K (normal state) obtained by plotting the intensity of ARPES spectrum at $E_F \pm 10$ meV. Figures 2(a) and (b) show the ARPES spectra around the Γ and M point, respectively. From the present ARPES results, we have clearly found the hole- and the electron-pocket around the Γ and M point, respectively, which can be qualitatively reproduced by the band calculation on the '122' series [3]. It should be noted that the large electron-pocket expected in the calculation along cut2 disappears because of the matrix element effect with horizontal polarization of the present light source [4].

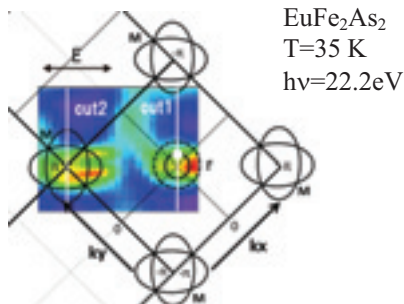


Fig. 1. Fermi surface image of $\text{BaFe}_{1.8}\text{Co}_{0.2}\text{As}_2$ compared with the expected Fermi surface topology from the band calculation on BaFe_2As_2 [3].

Figures 3(a) and (b) show the temperature dependence of ARPES spectra and their spectral DOS across T_c obtained at the hole-like FS (white circle in Fig. 1), respectively. We have observed superconducting gap opening below $T=22.5$ K. With decreasing temperature, DOS at E_F gradually decreases and the gap size increases. We have estimated the gap size is about 5~6 meV.

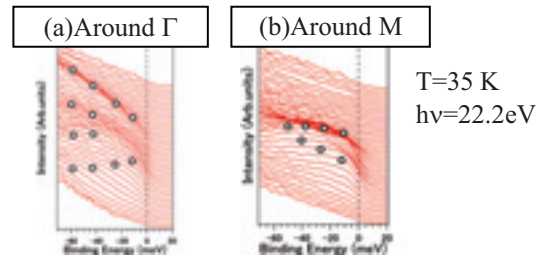


Fig. 2. ARPES spectra of $\text{BaFe}_{1.8}\text{Co}_{0.2}\text{As}_2$ at 35 K along cut 1 (a) and cut 2 (b) in Fig. 1.

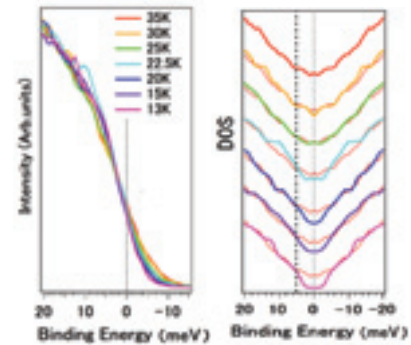


Fig. 3. (a) Temperature dependence of ARPES spectra at the hole-like Fermi surface (white circle in Fig. 1) of $\text{BaFe}_{1.8}\text{Co}_{0.2}\text{As}_2$. (b) Spectral DOS of Fig. 3(a) obtained by the symmetrization method [5]. Thin red lines correspond to one at 35 K.

- [1] H. Ding *et al.*, Euro Phys. Lett. **83** (2008) 47001.
 [2] Y. Kamihara *et al.*, J. Am. Chem. Soc. **130** (2008) 3296.
 [3] D. J. Singh *et al.*, Phys. Rev. B **78** (2008) 094511.
 [4] S. de Jong *et al.*, arXiv: **0912** (2009) 3434v1.
 [5] M. R. Norman *et al.*, Nature **392** (1998) 157-160.

Angle-Resolved Photoemission Study on Possible Kondo Insulator FeSb₂

S. Imada¹, K. Terashima¹, A. Sekiyama², S. Suga², A. Yamasaki³,
K. Mima¹, Y. Miyata¹, R. Yamaguchi¹, Y. Tachimori¹, Y. Yamanoi¹,
Y. Matsui³, J. Yamaguchi², S. Komori² and H. Nakamura⁴

¹ Faculty of Sci. and Eng., Ritsumeikan Univ., Shiga 525-8577, Japan

² Grad. School of Eng. and Sci., Osaka Univ., Osaka 560-8531, Japan

³ Faculty of Sci. and Eng., Konan Univ., Kobe 658-8501, Japan

⁴ Grad. School of Eng., Kyoto Univ., Kyoto 606-8501, Japan

Magnetic impurities in a metal trigger an upturn in the resistivity curve, so-called Kondo effect. This phenomenon has been reported in rare-earth compounds that contain localized *f*-electrons, as well as in transition metals with partial substitution of atoms. In a class of materials called Kondo insulators, Kondo effect induces an insulator-to-metal crossover under heating. Interestingly, even in some of the iron-based compounds, FeSi and FeSb₂, the temperature-dependence of the resistivity resembles that of Kondo insulator. A number of experimental techniques have indicated the existence of the energy gap at the low temperature in FeSb₂[1-3], while the mechanism for the formation of the energy gap remains highly controversial; whether FeSb₂ is a Kondo insulator[2] or a narrow-gap semiconductor[1, 3, 4]. To resolve this issue, a high-resolution angle-resolved photoemission (ARPES) study has been highly anticipated, since ARPES can directly observe the band structure and possible formation of the energy gap.

A single crystal of FeSb₂ has been synthesized by Sb-flux method. High-resolution photoemission study has been performed at BL7U in the UVSOR facility. Energy resolution was set at ~6 and ~15 meV for angle-integrated and angle-resolved measurement, respectively. We have obtained a clean surface of the sample by fracturing in an ultrahigh-vacuum of ~2x10⁻⁸ Pa.

Figure 1 shows a typical ARPES intensity plot of FeSb₂ at *T* = 15 K using 17-eV photons. Several dispersive bands are clearly seen in the figure, showing that we have succeeded in the ARPES measurement of FeSb₂. What is interesting is that there is a hole-like band crossing *E*_F (shown by arrow in the figure) although the bulk is insulating at this temperature[1]. Such an inconsistency between PES results and bulk property is also reported in FeSi[5], where the contribution of the surface state is discussed. In fig. 1, the hole-like band lies in a *k*-region where other bands are absent. Thus we attribute the origin of metallic band to the surface.

In Fig. 2, we show a temperature-dependence of angle-integrated photoemission spectra in FeSb₂ taken at *hν* = 6.5 eV. As we decrease the temperature, the spectral weight near *E*_F is gradually suppressed. However, a Fermi-edge cutoff remains in the spectra at *T* = 20 K, indicative of metallic state.

This metallic state may originate from the surface states shown in Fig. 1. Further study including the temperature dependence of bulk bands is necessary to clarify the origin of the energy gap in FeSb₂.

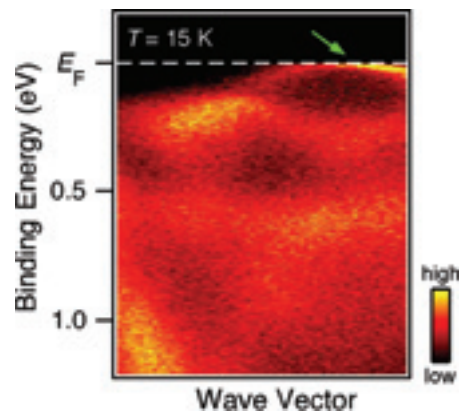


Fig. 1. ARPES intensity plot of FeSb₂ at *T* = 15 K (insulating phase). Green arrow points a hole-like band crossing *E*_F.

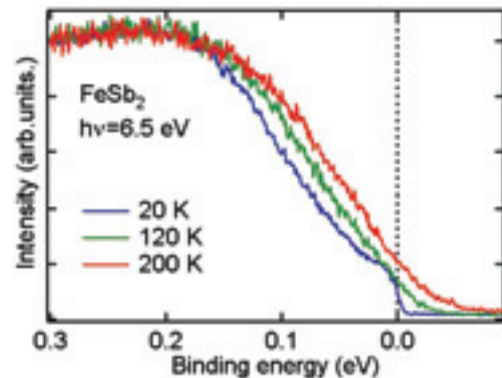


Fig. 2. Temperature-dependence of angle-integrated photoemission spectra in FeSb₂.

- [1] Z. Schlesinger *et al.*, Phys. Rev. Lett. **71** (1993) 11.
- [2] C. Petrovic *et al.*, Phys. Rev. B **72** (2005) 045103.
- [3] T. Koyama *et al.*, Phys. Rev. B **76** (2007) 073203.
- [4] A. V. Lukoyanov *et al.*, Euro. Phys. J. **53** (2006) 205.
- [5] K. Ishizaka *et al.*, Phys. Rev. **72** (2005) 233202.

High-Resolution Angle-Resolved Photoemission Study of Iron Pnictide Superconductor $\text{Ba}_{1-x}\text{K}_x\text{Fe}_2\text{As}_2$

K. Nakayama¹, T. Kawahara¹, T. Arakane¹, T. Qian¹, P. Richard², S. Souma², T. Sato¹ and T. Takahashi^{1,2}

¹Department of Physics, Tohoku University, Sendai 980-8578, Japan

²WPI Research Center, Advanced Institute for Material Research, Tohoku University, Sendai 980-8577, Japan

The discovery of superconductivity in $\text{LaFeAsO}_{1-x}\text{F}_x$ [1] has triggered intensive researches on the high-temperature (T_c) superconductivity of iron (Fe) pnictides. The T_c value has already exceeded 55 K by replacing La atom with other rare-earth atoms or by introducing oxygen vacancies, opening a new avenue for high- T_c material research beside cuprates. Remarkable aspects of the FeAs-based superconductors are (i) electrons in the Fe orbitals, generally believed to be the foe, indeed play an essential role in superconductivity, (ii) non-doped parent compounds commonly exhibit a collinear antiferromagnetic (AF) spin density wave (SDW), and (iii) superconductivity emerges either by the hole or electron doping into the parent compounds. Angle-resolved photoemission spectroscopy (ARPES) is a key experimental technique to elucidate electronic states responsible for the occurrence of superconductivity and the AF transition. Indeed, ARPES has revealed several essential features in cuprate superconductors, like the large Fermi surface, d -wave superconducting gap, and the pseudogap above T_c .

In this study, we have performed high-resolution ARPES study of iron-based superconductor $\text{Ba}_{1-x}\text{K}_x\text{Fe}_2\text{As}_2$ as a function of potassium concentration x . Figure 1 shows the comparison of ARPES intensity as a function of wave vector and binding energy for (a) optimally-doped superconducting $\text{Ba}_{0.6}\text{K}_{0.4}\text{Fe}_2\text{As}_2$ ($T_c = 37$ K) and (b) non-superconducting parent compound BaFe_2As_2 ($T_{\text{SDW}} = 138$ K) measured at $T = 17$ K and 25 K, respectively. Corresponding energy distribution curves (EDCs) are also displayed in (c) and (d), respectively. As clearly seen in Figs. 1(a) and (b), we find a highly dispersive holelike band centered at the Γ point. Leading-edge midpoint of this band around the Fermi vector is clearly shifted toward higher binding energy as shown in Fig. 1(c), indicating an opening of the superconducting gap, as in previous studies [2, 3]. In contrast, in the parent compound, the band structure seems to be apparently different. We clearly find two holelike branches centered at the Γ point. In addition, we also observe a weaker electronlike band showing an opposite dispersion from these two holelike bands. This dramatic difference of band structure between the superconducting and the AF compounds are ascribed to the absence (appearance) of magnetic order in the

superconducting (parent) compound. The complicated band structure in the AF sample would originate in the band folding which basically follows the periodicity of new magnetic Brillouin zone. All these experimental results indicate strong influence of magnetic order / fluctuations to the fine electronic structure in the vicinity of E_F of iron-based superconductors.

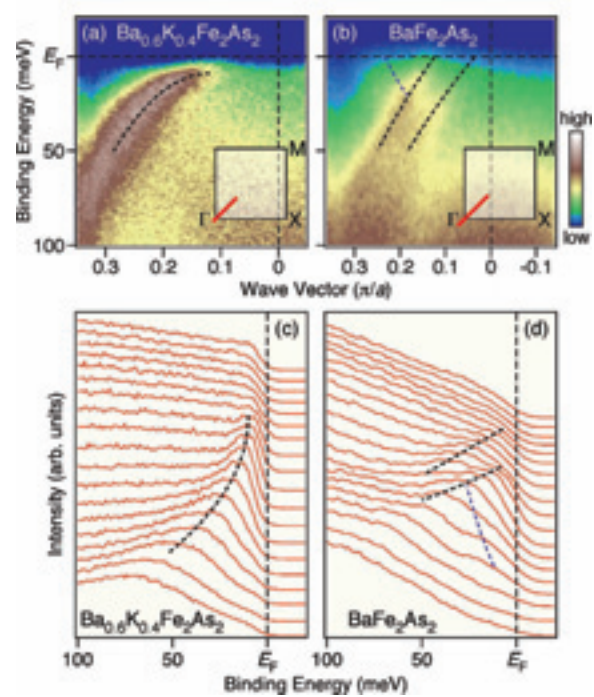


Fig. 1. ARPES intensity of (a) optimally-doped $\text{Ba}_{0.6}\text{K}_{0.4}\text{Fe}_2\text{As}_2$ ($T_c = 37$ K) at $T = 17$ K and (b) parent compound BaFe_2As_2 at $T = 25$ K plotted as a function of wave vector and binding energy, measured with the 21-eV photons. Corresponding energy distribution curves are plotted in (c) and (d), respectively. Dashed lines are guides for eyes to highlight the band dispersion.

[1] Y. Kamihara *et al.*, J. Am. Chem. Soc. **130** (2008) 3296.

[2] H. Ding *et al.*, Europhys. Lett. **83** (2008) 47001.

[3] K. Nakayama *et al.*, Europhys. Lett. **85** (2009) 67002.

Anisotropy of Electron Scattering and its Effect on Hall Coefficient of $(\text{Bi, Pb})_2(\text{Sr, La})_2\text{CuO}_{6+d}$ High- T_c Superconductor

T. Takeuchi^{1,2}, Y. Hamaya², K. Ogawa², T. Ito³ and S. Kimura⁴

¹*EcoTopia Science Institute, Nagoya University, Nagoya 464-8603, Japan*

²*Department of Crystalline Materials Science, Nagoya University, Nagoya 464-8603, Japan*

³*Department of Materials Science, Nagoya University, Nagoya 464-8603, Japan*

⁴*UVSOR, Institute for Molecular Science, Okazaki 444-8585, Japan*

Hall coefficient R_H of metals is generally accounted for with the well-known formula of $R_H = 1/(ne)$, where n and e represent carrier density and unit charge of carriers. This formula is valid only when the scattering of the electron near the Fermi level is isotropic. If we measure the Hall coefficient of the material that is characterized by the anisotropy in electron scattering, the measured Hall coefficient exceeds the value of $R_H = 1/(ne)$.

High- T_c superconductors are typical example that possesses anisotropy of electron scattering due to the strong electron correlation. The anisotropy of electron scattering is caused by the fluctuation of the anti-ferromagnetic spin ordering, and therefore electrons near the Fermi level are scattered only in the vicinity of the anti-ferromagnetic zone boundary (AFZB). These materials indeed possess a much larger magnitude of R_H than that expected from $R_H = 1/(ne)$. Since the strong scattering at AFZB is getting weakened with increasing temperature or increasing carrier concentration, the Hall coefficient increases with decreasing temperature or decreasing carrier concentration.

In this study, we try to quantitatively reproduce the behaviors of Hall coefficient observed for the high- T_c superconductors by using the information about both electronic structure and electron scatterings obtained by the angle resolved photoemission spectroscopy (ARPES). For this purpose, we employed the ARPES system located in BL7U of UVSOR, because it possesses an extremely good energy resolution. By using 9 eV photons as the incident beam of ARPES, we obtain the energy resolution better than a few meV.

We used the single crystal $(\text{Bi,Pb})_2(\text{Sr,La})_2\text{CuO}_{6+d}$ superconductors, in which Pb and La are partially substituted for Bi and Sr, respectively. The former substitution effectively weakens the superstructure in Bi-O layers, which generally prevents us from easily analyzing the ARPES spectra by creating the unfavorable umklapp-bands. The latter substitution is used to decrease the hole-concentration in the sample. By employing subsequent heat-treatment, we succeed in preparing variety of samples from heavily overdoped to underdoped ones.

In this study, we selected three samples, which are one overdoped sample possessing $T_c = 25$ K and two underdoped ones of $T_c = 31$ K and 28 K. The ARPES

measurement was performed at at 50 K, 100 K, and 150 K with incident energy of 9 eV.

The energy distribution curves (EDC's) were successfully extracted at each Fermi wave vector. By symmetrizing the EDC spectra at the Fermi level (ε_F), we confirmed that the consequently obtained spectra obviously possessed a peak at ε_F . The shape of the peak is well accounted for with the Lorentzian function and its FWHM is distributed over 30 ~ 50 meV. This fact indicates that the energy variation of imaginary part of self-energy, which represents the lifetime of coherent states, is roughly approximated to be constant over the narrow energy range of a few tenths of meV in width in the vicinity of ε_F .

By using the experimentally determined ε - \mathbf{k} dispersion, the group velocity, and the lifetime of coherent states, we calculated R_H of the samples using the Bloch-Boltzmann equation. The resulting value is plotted in Fig.1 together with the measured ones as a function of temperature. Although the temperature dependence and hole concentration dependence of R_H were qualitatively reproduced by the calculation, the absolute value was not completely reproduced. This fact unambiguously suggests that we have to consider some other special mechanism, such as the back flow current in vertex correction.

We are now in progress for quantitatively evaluating the effect of this back flow current on R_H of present samples using the present data.

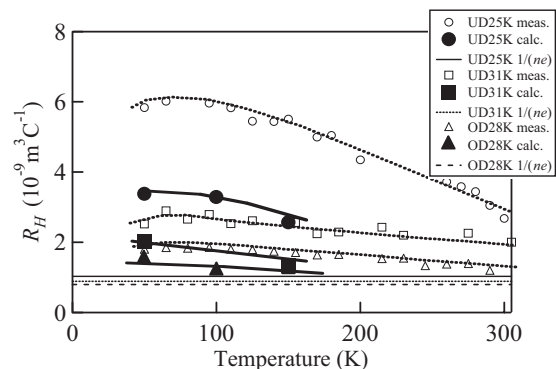


Fig. 1. The calculated and measured Hall coefficient (R_H) of $(\text{Bi,Pb})_2(\text{Sr,La})_2\text{CuO}_{6+d}$. The absolute value of R_H was not reproduced by the present calculation.

Study of VUV Reflection Spectroscopy of ZnO Thin Films Irradiated By Ar Plasma

N. Fujita, T. Yabumoto, H. Ito, T. Mizunuma, Y. Iwai,
S. Matsumoto and H. Matsumoto

School of Science & Technology, Meiji University, Kawasaki 214-8571, Japan

Transparent conductive oxide (TCO) films have been widely used in the field of optoelectronic devices, such as transparent electrodes for various kinds of flat panel displays (FPDs) or photovoltaic cell [1,2].

Recently, the demands for the large-area and high-quality FPDs, transparent conductive films including tin-doped In_2O_3 (ITO) films have attracted significant attention. However, due to rapid demand in recent years, the price of indium composing of ITO may raise even higher the future for a stable supply is concerned.

So, Instead of Indium as materials, ZnO is focused. ZnO is cheaper than ITO and, has the nature of the transparent conductive film by donor level is formed by oxygen vacancies or interstitial zinc in the film. As a means to lower resistance of ZnO, there is a way to include the addition of impurities and hydrogen plasma irradiation [3,4]. For Ar plasma irradiation method, no report of electrical characteristics has been made in details, and also optical properties are not reported [5].

In this study, ZnO thin films prepared by RF magnetron sputtering and fabricating by Ar plasma-irradiation. We report the optical properties of ZnO thin films for various irradiation times.

Experiment

ZnO thin films were deposited by RF magnetron sputtering on fused quartz substrate, and at room temperature. Sintered object of zinc oxide plate were used as the target, and the sputtering was carried out in argon gas with a base pressure 2.0×10^{-2} Pa. The film thickness is about 390 nm.

Thin films were irradiated with Ar plasma on various times up to 20 minutes. The RF power and Ar flow rate were 20 W and 3.0 sccm. Volume resistivities were measured for ZnO thin films irradiated Ar plasma.

Reflection spectra of the films were measured in the vacuum ultraviolet region up to 25 eV with the 3-m normal incident monochromator (grating: G1 and G2) at BL-7B of UVSOR-II. A silicon photodiode sensor was used as a detector of the reflection light.

Results and Discussion

XRD analysis showed that as deposited films were composed of polycrystalline of ZnO. Figure 1 shows the VUV reflection spectra between 5 and 25 eV of ZnO films by Ar plasma Irradiated at room temperature. The vertical axis indicates reflected

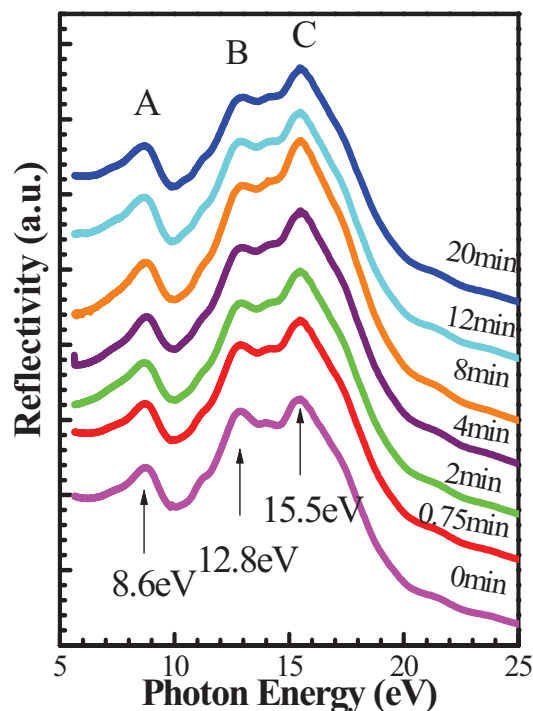


Fig. 1. VUV Reflection Spectra ZnO film by Ar plasma irradiation up to 20 min.

intensity. Three peaks A(8.6eV), B(12.8eV), C(15.5eV) appeared in all spectra. It was clearly observed that the intensity of peak increased with irradiation times of Ar plasma. Intensity of peak C is increased. However, A and B are not increased. These results are considered that the reflectivity increased with change of crystalline state with decreased irradiation times.

- [1] H. Koh, K. Sawada, M. Ohgawara, T. Kuwata, M. Akatsuka and M. Matsuhiro, SID Dig. Tech. Pap. **19** (1988) 53.
- [2] Y-M. LU *et al.*, Thin Solid Films **447- 448** (2004) 56.
- [3] P. F. Cai *et al.*, J Appl. Phys. **105** (2009) 083713.
- [4] H. Akazawa, Appl. Phys. Express **2** (2009) 081601.

Measurement of Reflectivity of Strongly Correlated Electron Systems between Infrared and VUV Regions at BL7B

A. Irizawa¹ and S. Kimura^{2,3}

¹Graduate School of Science and Technology, Kobe University, Kobe 657-8501, Japan

²School of Physical Sciences, The Graduate University for Advanced Studies (SOKENDAI), Okazaki 444-8585, Japan

³UVSOR Facility, Institute for Molecular Science, Okazaki 444-8585, Japan

Introduction

Studying optical conductivity is one of the most effective methods for understanding the electronic states of solids. In usual we measure the reflectivity between far-infrared (FIR) and near-infrared (NIR) regions using Fourier transfer type (FT) interferometer and at visible (VIS) region using the traditional grating type spectroscopy. The optical conductivity can be derived from the reflectivity through Kramers-Kronig (KK) transform where the accurate analysis can be achieved from the reflectivity in the wide energy range as far as possible. In that sense the reflectivity data from BL7B in the wide energy range between 1.2 and 40 eV (1000 nm – 30 nm) is one of the most important part for KK transform. Otherwise the reflectivity in the higher energy range should be extrapolated with a simple ω^{-4} function. In this machine time, we prepared several solid samples of strongly correlated electron systems for both *d* electron and *f* electrons. One of them ($\text{Ca}_{1-x}\text{Na}_x$) Co_2O_4 ($x=0-0.5$) is the newly synthesized system which shows metal-insulator change with increasing Na content *x* [1]. CaCo_2O_4 has been known to show a temperature-dependent large thermoelectric power with semiconductor-like resistivity [2-4]. The crystal structure is Ca-ferrite-type which belongs to one of the high pressure phases of spinel structure. It includes Co_2O_4 double chain component along *b* axis which consists t_{2g} orbital connection of Co 3*d* electrons. In that sense the success of carrier doping to this compound is interested in view of 1D conductor. Similar orbital network is also seen for the Na_xCoO_2 which has a 2-dimensional t_{2g} orbital connection. For substituting Ca^{2+} to Na^+ , doping of hole carriers can be expected into Co^{3+} t_{2g} low spin state. Actually the resistivity decreases drastically with increasing *x* and the insulating behavior transforms to a metallic one at $x=0.5$. The other samples are selected from the also newly synthesized compounds. $\text{CeT}_2\text{Al}_{10}$ (*T*=Fe,Ru, Os) is the series having cage-structure of *T*-Al in which Ce 4*f* electron acts an important role of electronic properties such as Kondo insulator and heavy fermion behavior [5]. In the beam time, we measured the reflectivities of all these compounds using 3-m normal incidence monochromator at BL7B.

Experimental

The optical reflectivities of ($\text{Ca}_{1-x}\text{Na}_x$) Co_2O_4 and $\text{CeT}_2\text{Al}_{10}$ were measured at UVSOR-II BL7B. The energy was changed from 1.2 to 40 eV with three gratings (1200, 600, and 300 lines/mm). There are several type of optical windows for avoiding the higher degree diffractions. In the former studies, the obtained spectra using 4 type optical windows with 3 gratings were hardly connected without complex process. This time we select 3 type windows with 2 gratings for simplifying.

Results and Discussion

As a result, the spectra can be connected without any compensation of raw data even in the case of small polycrystal samples. Figure 1 is one of the obtained results. The wide energy scan using G3 seems to be good agreement with the other results with 3 different pairs of optical windows and gratings. We are using these results of both series of compounds for getting optical conductivities with the experiments in the lower energy reflectivity measurements.

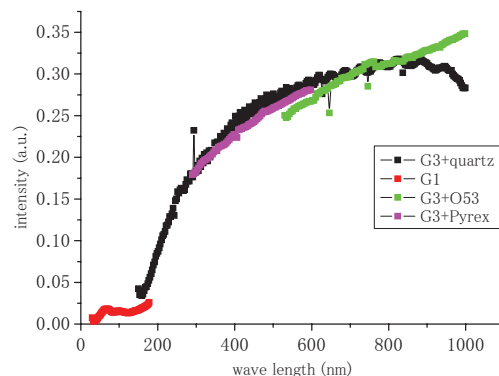


Fig. 1. Comparison of reflectivities with different optical windows and gratings.

- [1] M. Isobe *et al.*, the oral presentation in the conference of physical society of Japan (2009) 26aRG-5.
- [2] M. Shizuya, M. Isobe *et al.*, *J. Solid State Chem.*, **180** (2007) 2550.
- [3] M. Isobe *et al.*, *Physica C*, **469** (2009) 948.
- [4] M. Isobe *et al.*, *J. ELECTRONIC MATERIALS*, **38** (2009) 1166.
- [5] Y. Muro *et al.*, *JPSJ* **78** (2009) 083707; ICM 09 proceedings.

Photoluminescence and Photoluminescence Excitation Spectra of AlN

T. Ito, R. Ikematsu, S. Sawai and K. Fukui

Dept. Elec. Elec. Engi., Univ. Fukui, Fukui 910-8507, Japan

Aluminum nitride (AlN) has the widest direct band-gap in III-V nitride compound semiconductors. Therefore, the AlN is expected to utilize for deep UV light emitting diodes (LED) *etc.* It is known that the uppermost valence band (VB) of AlN splits into three bands (CH, HH and LH bands from bottom to top of the uppermost VB), and the transition between each level and the conduction band (CB) has the different polarization character, and knowledge of these transitions is important for fabricating the opt-electronic devices. These three transitions are usually labeled as A (from CH to CB), B (HH to CB), and C transition (LH to CB). Our purpose in this work is to present the uppermost VB structure of wurtzite AlN including A to C transition energies and their polarization characters. For this purpose, not only optical reflectance (OR) measurements but also photoluminescence (PL) and PL excitation (PLE) measurements are performed.

The AlN films were grown on the Al₂O₃ substrates by the MOVPE. The *c*-axis of the AlN is perpendicular to the sample surface, and the thickness is about 1 μm. Highly linear polarized incident light of BL7B were used to excite the samples with $\theta = 8^\circ$ and 60° in respect to the sample surface in the *p* configuration, where θ is an incident angle.

Figure 1 shows the PL spectra at $\theta = 8^\circ$ and 60° . The measurement temperature is 20K. There is no incidence angle dependence between two PL spectra. The emission bands at 5.94 eV and 5.84 eV are first and second LO phonon replicas, and the main emission band is at 6.05 eV. The inset of Fig. 1 shows the ratio between the 1-LO phonon replica band and the main band as a function of the photon energy.

Figure 2 shows that the PLE spectra at $\theta = 8^\circ$ and 60° . The PLE spectra are mainly monitored at the peak photon energy of main band (6.05 eV). However, the PLE spectra at the lower photon energy side are monitored at the peak photon energy of 1-LO band (5.94 eV). The measurement temperature is 20K. Since the *c*-axis of the sample is perpendicular to the sample surface, the PLE Intensity at $\theta = 8^\circ$ mostly consists of the $E \perp c$ component ($I_{E \perp c}$), where E is the electric field of the incident light. On the other hand, since that at $\theta = 60^\circ$ consists of both the $E \perp c$ and the $E // c$ components ($I_{E // c}$), the comparison between the spectra at $\theta = 8^\circ$ and 60° shows the contribution of the components. Therefore, using an expression,

$$I(\theta) = I_{E \perp c} \cos^2 \theta + I_{E // c} \sin^2 \theta,$$

we also show calculated $I_{E // c}$ in Fig. 2. The inset of Fig. 2 shows the normalized $I_{E \perp c}$ and $I_{E // c}$ for convenience. It is clear that only the $I_{E // c}$ component

is excited at the lower excitation photon energy. Comparison between these PLE spectra and the OR spectra, the peaks at 6.24 eV and 6.28 eV of the $I_{E \perp c}$ spectra in Fig. 2 are attributed to the B and C transition, respectively, and a 6.07 eV peak of the $I_{E // c}$ spectrum is to the A transition. These assignments are in good agreement with other work [1]. However, other peaks at 6.20 eV and 6.40 eV are also observed. The 6.20 eV transition is allowed under the $E // c$ condition, and the 6.40 eV transition is under both the $E // c$ and the $E \perp c$ conditions. It seems that the polarization characters of these two unknown transitions correspond to A and B (or C) transitions, respectively.

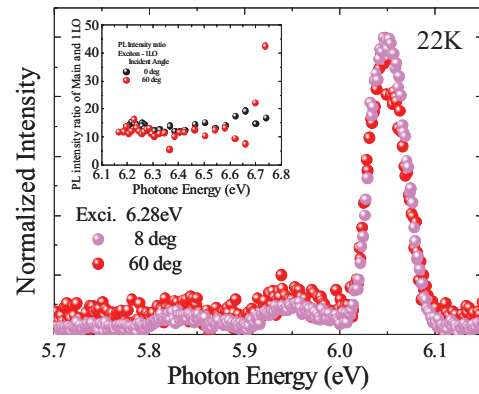


Fig 1. Incident angle dependence of PL spectra, and the PL intensity ratio of main and 1-LO bands as a function of the photon energy (inset).

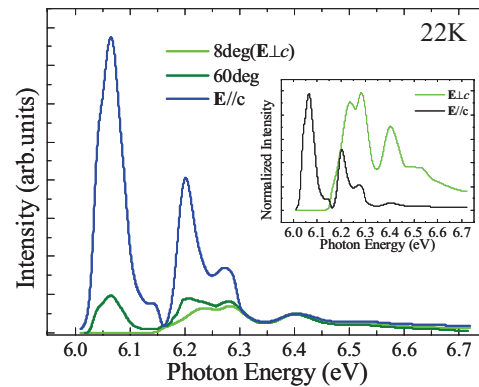


Fig 2. Incident angle dependence of PLE spectra, and normalized $E // c$ and $E \perp c$ components of PLE spectra (inset).

- [1] T. Onuma, T. Shibata, K. Kosaka, K. Asai, S. Sumiya, M. Tanaka, T. Sota, A. Uedono and S. F. Chichibu, *J. Appl. Phys.* **105** (2009) 023529.

Pressure Tuning of an Ionic Insulator into a Heavy Electron Metal: An Infrared Study of YbS

H. Okamura¹, M. Matsunami², A. Ochiai³ and T. Nanba¹

¹Graduate School of Science, Kobe University, Kobe 657-8501, Japan

²Institute of Solid State Physics, The University of Tokyo, Kashiwa 277-8581, Japan

³Center for Low Temperature Science, Tohoku University, Sendai 980-8578, Japan

YbS at ambient pressure is an ionic insulator ($\text{Yb}^{2+}\text{S}^{2-}$) with the NaCl crystal structure, and has a band gap of about 1.4 eV [1, 2]. A previous optical study [1] showed that the band gap of YbS decreased under increasing external pressure. The extrapolation of the shifts of the fundamental absorption edge with pressure suggested a gap closing at ~ 10 GPa. In addition, volume compression data and X-ray absorption data suggested that the Yb mean valence in YbS increased from 2 above 10 GPa, and reached ~ 2.4 at 20 GPa [2]. Namely, YbS above 10 GPa was in an intermediate-valence (IV) state, where the valence of each Yb ion is fluctuating between 2 and 3. However, since the previous optical study was performed at photon energies above 0.5 eV only, it was unclear whether or not the gap actually closed at ~ 10 GPa, and whether or not the IV state above 10 GPa was metallic. To answer these questions and to clarify the low-energy electronic structures of YbS under high pressure, we have carried out IR reflectivity studies of YbS [3]. The reflectivity spectra $R(\omega)$ under high pressure were measured at the IR beam line of SPring-8, while those at ambient pressure were measured using the apparatus at Kobe University below 2 eV, and using BL7B above 2 eV up to 30 eV. High pressure was generated with a diamond anvil cell (DAC). Optical conductivity spectra $\sigma(\omega)$ were derived from the measured $R(\omega)$ using Drude-Lorentz fitting technique.

Figure 1 shows the measured $\sigma(\omega)$ under pressure, together with that measured in the vacuum. The narrow peak below 0.1 eV, which are seen above 8 GPa, is a Drude peak due to free carriers. This result explicitly demonstrates that the high pressure phase in YbS has a metallic ground state. The energy gap is closed at 8 GPa, rather than at 10 GPa as previously conjectured [2]. In addition, two pronounced absorption peaks are seen to grow with pressure above 10 GPa. Namely, the high pressure phase above 10 GPa is not a simple metal, but it has some peculiar features in the electronic structures near the Fermi edge. The detailed analyses of the data show that the carriers giving rise to the Drude peak has a large effective mass of the order of $10 m_0$, where m_0 is the rest electron mass. [3] It can be shown that the observation of the Drude peak due to such heavy electrons, and that of the pronounced absorption peaks, can be understood together using a

model based on the hybridization of the f state with a conduction band, which is also consistent with the IV previously observed above 10 GPa.

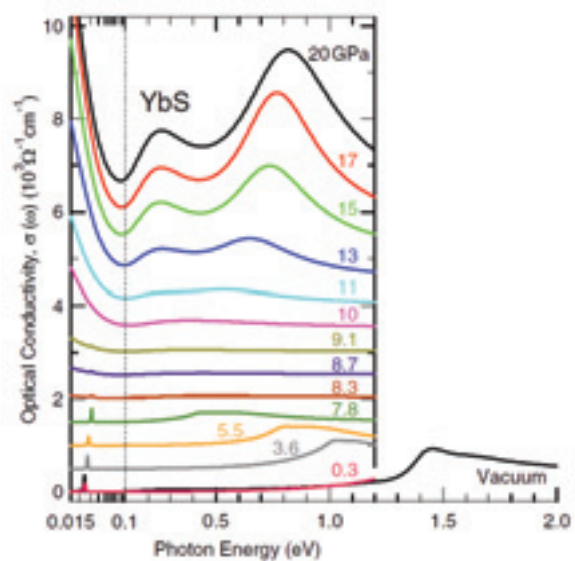


Fig. 1. Optical conductivity spectra $\sigma(\omega)$ of YbS at room temperature at different pressures, obtained with Drude-Lorentz fitting to the measured reflectivity spectra. The spectra are offset for clarity. Note the logarithmic scale below 0.1 eV.

- [1] K. Syassen, H. Winsen, H. G. Zimmer, H. Tups, and J. M. Leger, *Phys. Rev. B* **32** (1985) 8246.
 [2] K. Syassen, *Physica B+C* **139-140** (1985) 277.
 [3] M. Matsunami, H. Okamura, A. Ochiai and T. Nanba, *Phys. Rev. Lett.* **103** (2009) 237202.

Angular Dependence of Spectral Responsivity and Reflectance for UV Photodetectors

T. Saito¹, K. Ozaki², S. Sawai², K. Fukui² and I. Saito¹

¹National Metrology Institute of Japan, National Institute of Advanced Industrial Science and Technology, Tsukuba 305-8563, Japan,

²Faculty of Engineering, Univ. of Fukui, Fukui 910-8507, Japan

Introduction

Needs for quantitative measurements in the UV-VUV region are increasing in various fields like UV curing, disinfection, surface cleaning etc.. In these applications, UV irradiance meters are often used quite near the source, which means that the irradiance meters receive wide divergent beams. It is, therefore, very important to check if the meters satisfy the so-called cosine law, which is required as an ideal photodetector. In addition, internal quantum efficiency, η_{int} , that is a fundamental measure to evaluate detector performance, can be obtained by the two measurement results of the external quantum efficiency, η_{ext} , and the reflectance, R , from the equation,

$$\eta_{\text{int}} = \frac{\eta_{\text{ext}}}{1 - R}$$

Experimental

We have characterized various kinds of UV detectors (photoconductive diamond detectors, AlN, AlGaIn & GaAsP Schottky photodiodes, Si photodiodes), especially about their dependence on angle of incidence of spectral responsivity and of spectral reflectance by using p-polarization dominant radiation from the McPherson type monochromator beamline at BL7B.

Results and Summary

Figure 1 shows measurement results of spectral reflectance for a photoconductive HOD (Highly Oriented Diamond) detector at the angles of incident of 15, 30, 45 and 60 degrees. Also shown by a dashed line is a calculated spectrum at normal incidence. More detailed calculation results including s-polarization components are shown in Fig. 2. It has been confirmed that relative spectra agree well between the measurements and the calculations. Lower reflectance for the measurements can be attributed by its diffusive surface, which is easily visible.

The results also show that reflectance loss for p-polarization decreases as the angle of incidence increases at most of the wavelengths and hence it results in increase in detector responsivity, which was also experimentally confirmed.

In conclusion, angular measurements for reflectance and responsivity are powerful technique to characterize not only internal quantum efficiency

but also important polarization property and other optical property like a overlayer thickness and its absorption.

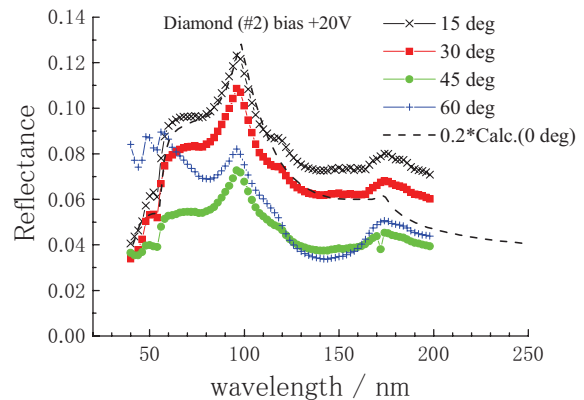


Fig. 1. Measured spectral reflectance spectra for a diamond detector (Calculated spectrum at normal incidence is also shown in dashed line).

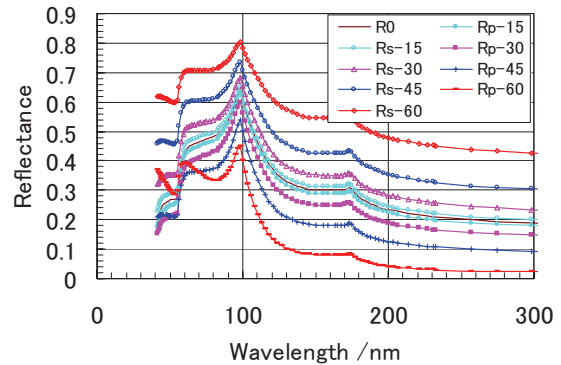


Fig. 2. Calculated spectral reflectance spectra for a diamond detector for both p- and s-components.

Acknowledgement

Authors are grateful to Dr. Kazushi Hayashi at Kobe Steel Ltd. for providing the diamond photodetectors.

- [1] T. Saito and K. Hayashi, Appl. Phys. Lett. **86** (2005) 122113.
- [2] T. Saito *et al.*, Diamond & Related Materials **14** (2005) 1984.
- [3] T. Saito *et al.*, Metrologia **43** (2006) S51.
- [4] T. Saito *et al.*, Phys Status Solidi C **6** (2009) S658.
- [5] T. Saito *et al.*, Metrologia **46** (2009) S272.

Photoluminescence and Photoluminescence Excitation Spectra from AlN Doped with Gd³⁺

S. Sawai¹, T. Ito¹, K. Fukui¹, S. Emura², T. Araki³ and A. Suzuki⁴

¹Dept. Elec. Elec. Engi., Univ. Fukui, Fukui 910-8507, Japan

²Inst. Sci. Indust. Res., Osaka Univ., Osaka 567-0047, Japan

³Dept. Photonics, Ritsumeikan Univ., Shiga 525-8577, Japan

⁴Res. Organi. Sci. Engi., Ritsumeikan Univ., Shiga 525-8577, Japan

III-V nitride compound semiconductor doped with rare elements are attractive systems because of the possibility of magnetic ordering coupled with a semiconducting nature and luminescence properties. In the ultraviolet region, a wide bandgap matrix semiconductor in combination with a Gd element is one of the target systems. In the case of Al_{1-x}Gd_xN there are several cathodeluminescence (CL) [1-4], electroluminescence [5], and photoluminescence (PL) [6] properties, in this case every result shows a sharp line at 3.90~3.94eV which is clearly observed and well assigned to the ⁶P_{7/2}→⁸S_{7/2} 4f intra transition of Gd³⁺. However, the electronic structure of Al_{1-x}Gd_xN is still not clear. In consequence, we have performed not only PL measurements but also PL excitation (PLE) measurements of Al_{0.98}Gd_{0.02}N and Al_{0.87}Gd_{0.13}N.

Al_{1-x}Gd_xN thin films were grown in a MBE system with a RF-plasma assisted radical cell on the Si-face of (0001)-oriented 6H-SiC substrates. The thicknesses of the samples are about 120 nm.

Figure 1 shows the PL spectra of (a) Al_{0.98}Gd_{0.02}N and (b) Al_{0.87}Gd_{0.13}N at 8K. The excitation photon energy is 6.27eV. The PL spectra mainly consist of two parts. The first part is the sharp lines seen at around 3.95 eV. These sharp lines are in agreement with previous research [1] and other results [2-6], as mentioned above. The second part is the broad emission bands observed in the lower energy side which may have been weakly observed in previous CL work [1]. Since the band width of the broad emission band in (b) is much wider than in (a), it is supposed that this band is correlated to the Gd concentration. The PLE spectra and the OR spectra from Al_{0.98}Gd_{0.02}N at 23 K are shown in Figs. 2(a) ($\theta = 8^\circ$) and 2(b) ($\theta = 60^\circ$). The emission photon energies are 3.95 eV and 2.76 eV which correspond to the peak energy positions of the sharp line and the broad band, respectively. Notable features in Fig. 2 are as follows: (i) PLE spectra monitored at 2.76 eV clearly show the band edge. (ii) PLE spectra monitored at 3.95 eV also show the band edge with a peak structure at 6.3 eV. (iii) Additional peaks and shoulders at 6.11 eV are obviously found in the PLE spectra at $\theta = 60^\circ$. These (i) ~ (iii) features suggest that the crystal structure of Al_{0.98}Gd_{0.02}N is basically

similar to that of AlN, and the uniaxial anisotropy character of AlN is still present.

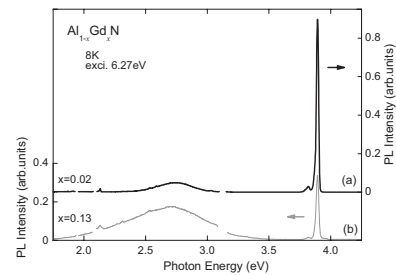


Fig. 1. Photoluminescence spectra from (a) Al_{0.98}Gd_{0.02}N and (b) Al_{0.87}Gd_{0.13}N at 8K.

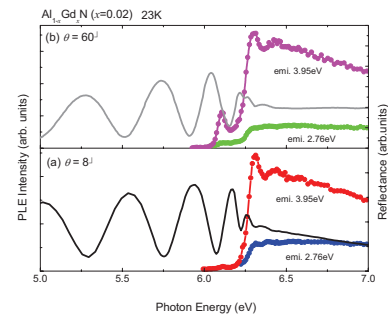


Fig. 2. Photoluminescence excitation spectra and optical reflectance spectra from Al_{0.98}Gd_{0.02}N at 23 K. The angles of incidence θ are (a) 8° and (b) 60° .

- [1] S. W. Choi, S. Emura, S. Kimura, M. S. Kim, Y. K. Zhou, N. Teraguchi, A. Suzuki, A. Yanase and H. Asahi, *J Alloys Compounds* **408-412** (2006) 717.
- [2] U. Vetter, J. Zenneck and H. Hofsäss, *Appl. Phys. Lett.* **83** (2003) 2145.
- [3] J. B. Gruber, U. Vetter, H. Hofsäss, *Phys. Rev. B* **69** (2004) 195202.
- [4] T. Kita, S. Kitayama, M. Kawamura, O. Wada, Y. Chigi, Y. Kasai, T. Nishimoto, H. Tanaka and M. Kobayashi, *Appl. Phys. Lett.* **93** (2008) 211901.
- [5] T. Toyama, J. Ota, D. Adachi, Y. Niioka, D. H. Lee and H. Okamoto, *J. Appl. Phys.* **105** (2009) 084512.
- [6] J. M. Zavada, N. Nepal, J. Y. Lin, H. X. Jiang, E. Brown, U. Hömmerich, J. Hite, G. T. Thaler, C. R. Abemathy, S. J. Pearton and R. Gwilliam, *Appl. Phys. Lett.* **89** (2006) 152107.

Electronic Structure of Yttrium and Carbon Atoms Encapsulated Metallofullerenes, $Y_2C_2@C_{82}$: Ultraviolet Photoelectron Spectroscopy and Theoretical Calculation

S. Hino¹, T. Miyazaki¹, Y. Aoki¹, N. Wanita², M. Kato², R. Sumii³, T. Akachi⁴, T. Inoue⁴,
Y. Ito⁴, T. Sugai⁴ and H. Shinohara⁴

¹ Graduate School of Science & Technology, Ehime University, Matsuyama 790-8577 Japan

² Graduate School of Science & Technology, Chiba University, Chiba 263-8522 Japan

³ Photon Factory, Institute for Materials Structure Science, Tsukuba 305-0801 Japan

⁴ Graduate School of Science, Nagoya University, Nagoya 464-8602 Japan

Extensive UPS study of metallofullerenes established an empirical rule that the cage structure is principally responsible for the electronic structure of mono-metal atom encapsulated metallofullerenes. That is, metallofullerenes of the same cage symmetry with an incorporated metal atom of the same oxidation state give essentially the same UPS. This empirical rule also holds in $Y_2C_2@C_{82}$ (III) and $Y_2@C_{82}$ (III), both of which have the same C_{2v} cage structure. However, it does not hold in $Ti_2C_2@C_{78}$ and $La_2@C_{78}$ although these endohedral fullerenes have the same D_{3h} (78:5) structure [11]. The case of $Ti_2C_2@C_{78}$ and $La_2@C_{78}$ is considered rather exceptional, since Ti atoms are fond of forming carbide and hybridization of orbitals derived from entrapped Ti and caged C atoms deforms the electronic structure of the fullerene cage so much. It is worthwhile to examine whether the empirical rule holds in three $Y_2C_2@C_{82}$ isomers.

Figures 1 and 2 show the valence band UPS of $Y_2C_2@C_{82}$ (I) and $Y_2C_2@C_{82}$ (II) obtained with $h\nu = 20 - 55$ eV photon energy. Their spectral onsets were 0.88 eV and 0.67 eV, respectively, and the previously reported value of $Y_2C_2@C_{82}$ (III) was 0.8eV [7]. The absorption spectral edge of these three isomers is 1400 nm (0.89 eV), longer than 2000 nm (0.62 eV) and 1100 nm (1.13 eV), respectively.

The UPS of $Y_2C_2@C_{82}$ (I) and $Y_2C_2@C_{82}$ (II) in 0 – 15 eV energy region show 10 explicit structures labeled by A – J in the figure. Their positions deviate slightly and their intensity changes when the incident photon energy is tuned, as has been observed in the UPS of other fullerenes [7-11, 15].

Theoretical calculation on $Y_2C_2@C_{82}$ (II) assuming D_{3h} cage structure reproduced the UPS very well. Optimized structure of entrapped Y_2C_2 was found to be distorted tetragonal form.

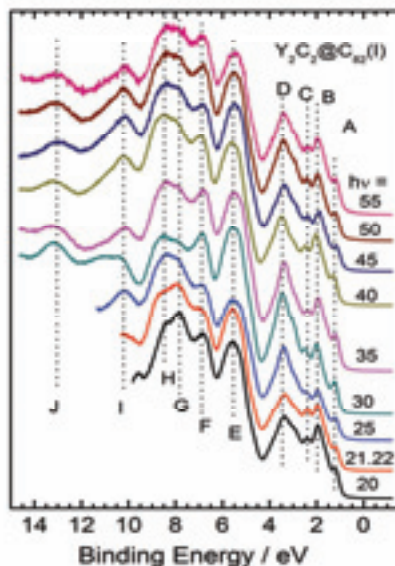


Fig. 1. UPS of $Y_2C_2@C_{82}$ (I)

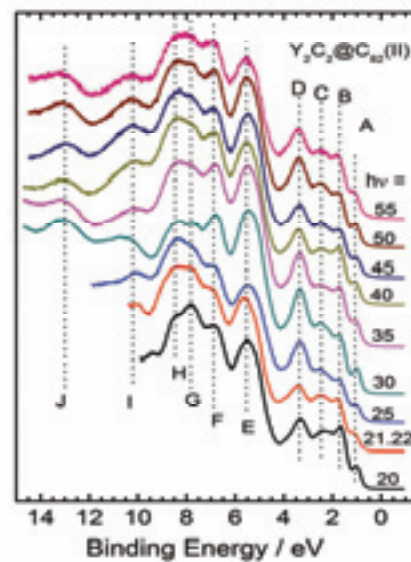


Fig. 2. UPS of $Y_2C_2@C_{82}$ (II)

[1] S. Hino *et al.*, Phys. Rev. B **75** (2005) 125418.

BL1A

Local Environment Analysis of Al Atoms in Proton-Conducting Amorphous Aluminum Phosphate Thin Films

Y. Aoki and H. Habazaki

Graduate School of Engineering, Hokkaido University, N13W8, Sapporo 060-8628, Japan

Inorganic phosphate compounds are attractive as an unhydrated proton conductor due to the presence of large number of native acid sites. Thin film of such materials has potential as an electrolyte membrane of next-generation intermediate temperature fuel cell. The conventional proton-conducting inorganic phosphate compounds are basically polycrystalline, and they have serious problem in forming the gas-tight membrane due to the difficulty in sintering. recently, we discovered that amorphous aluminum phosphate thin films exhibit the enhanced proton conductivity in nonhumidified atmosphere in the intermediate temperature range [1]. Amorphous metal oxides have intrinsic advantages for their application to thin film electrolyte, since they tend to be non-granular, dense layer without void formation at grain boundary due to the covalently-bonded M-O-M-O network. The study on the local environment of metal atoms are critical for identifying the protonic active sites in this film. Here, we study the local environment of Al atoms in amorphous zirconium phosphate thin films by Al K-edge XAS in order to identify the protonic active site.

Amorphous aluminum phosphate thin film, $a\text{-AlP}_m\text{O}_x$, was prepared on an ITO substrate (Aldrich) by multiple spin-coating of precursor solutions of phosphorous oxide (P_2O_5) (Kanto) and aluminum *sec*-butoxide ($\text{Al}(\text{O}^i\text{Bu})_3$) (Kanto) at the Al/Si atomic ratio of 3/2, 1/1, 1/2 and 1/3. The metal concentration (Al+P) in the precursor mixture sol was adjusted in 50 mM. A film with thickness of 100 nm was prepared from both of these sols. The precursor sols were spin-coated onto the ITO substrate at 3000 rpm for 40 sec by a Mikasa 1H-D7 spin coater. The deposited gel layer was hydrolyzed by blowing hot air for 30 sec (Iuchi hot gun), and the substrate was cooled to room temperature by blowing cold air for 20 sec. These cycles of spin-coating, hydrolysis and cooling were repeated 10-20 times and the gel film thus obtained was calcined at 400°C for 15 min. The combination of deposition and calcination was repeated more than 3 times, and the final calcination was performed at 450°C for 1 h.

Al K-edge XAS spectroscopy was carried out with $a\text{-AlP}_m\text{O}_x$ films of 100 nm-thickness (Figure 1). It is reported that Al K-edge spectra is very sensitive to the coordination number and geometry of AlO_x moieties in oxides.[1] Here, the Y-zeolite (Wako) was used as a reference material of tetrahedral AlO_4 configuration and $\alpha\text{-Al}_2\text{O}_3$ (Wako) as that of octahedral AlO_6 configuration, respectively. Y-zeolite shows a sharp

peaks at 1566 eV due to the transition from 1s to 3d unoccupied states and a broad peak at 1571 eV attributed to the six-coordinated Al atoms given by water adsorption [2]. These features are in agreement with the spectral features of tetrahedral AlO_4 compounds. $\alpha\text{-Al}_2\text{O}_3$ shows two sharp peaks at 1568 and 1572 eV, which are identical to the features of the compound given by the previous reports. The Al K-edge spectra of $a\text{-AlP}_m\text{O}_x$ films ($m = 0.67, 1.0, 2.0$ and 3.0) were drastically changed by Al/P atomic ratio. In $m = 0.67$ and 1.0, the film show a sharp peak at around 1566.5 eV, indicating that Al atoms inside film preferably take the tetrahedral AlO_4 configuration. However, the film with $m = 1.0$ and 2.0 apparently show an additional peak at higher-energy side of the main peak. This feature indicates that a part of Al atoms form octahedral AlO_6 configuration in these films. These results suggest that coordination environment of Al atoms in aluminophosphate films is changed from tetrahedral to octahedral with increasing phosphorous content m . The detail structure of phosphate groups will be investigated by P L-edge XAS.

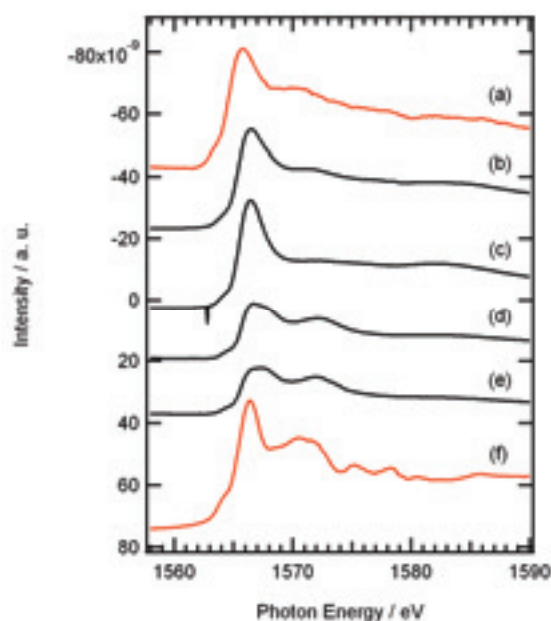


Fig. 1. Al K-edge XAS spectra of amorphous AlP_mO_x films of 100 nm-thickness and reference materials. (a) Y-zeolite powder, (b) $\text{AlP}_{0.67}\text{O}_x$, (c) AlPO_x , (d) AlP_2O_x , (e) AlP_3O_x and (f) $\alpha\text{-Al}_2\text{O}_3$ powder.

[1] Y. Kato *et al.*, PCCP **3** (2001) 1925.

[2] A. Omegna *et al.*, J. Phys. Chem. B **109** (2005) 9280.

Asymmetric Synthesis and Decomposition of Amino Acids by Using UVSOR-FEL

K. Kobayashi¹, S. Shima¹, T. Suzuki¹, T. Kaneko¹, H. Mita², J. Takahashi³, M. Hosaka⁴, M. Adachi⁵, H. Zen⁵ and M. Katoh⁵

¹Graduate School and Faculty of Engineering, Yokohama National University, Yokohama 240-8501, Japan

²Faculty of Engineering, Fukuoka Institute of Technology, Fukuoka 811-0295, Japan

³NTT Microsystem Integration Laboratories, Atsugi 243-0198, Japan

⁴Graduate School of Engineering, Nagoya University, Nagoya 464-8601, Japan

⁵Institute for Molecular Science, Okazaki 444-8585, Japan

Introduction

Terrestrial organisms basically use L-Amino acids and D-sugars. The origin of homochirality of biomolecules remains one of the largest riddles in the study of the origin of life. A number of hypotheses have been presented on the origin of biochemical homochirality. Finding of the enantiomeric excesses (*e. e.*'s) of certain amino acids in carbonaceous chondrites suggested that there were some physical sources to induce them in space. Recently Fukue *et al.* reported extended high circular polarization in the Orion massive star forming region [1]. It is of interest to examine possible generation of *e. e.*'s of amino acids by circularly polarized light. In order to examine this hypothesis, we irradiated amino acids or metal complexes of amino acids with circularly polarized ultraviolet light (CPL-UV) from a free-electron laser (FEL) of UVSOR. We chose two amino acids as targets: Isovaline (IVal), a non-proteinous amino acid which has α -methyl group in place of α -hydrogen atom, was selected since relatively large *e. e.* of IVal was found in Murchison meteorite [2]. A small *e. e.* formed by CPL-UV might have been enlarged by autocatalytic reactions in primordial ocean. From such a point of view, histidine (His), was used because it has catalytic activity. Aqueous solution of His, IVal, and metal complexes of them were irradiated with CPL-UV. Thin films of DL-His were also irradiated with CPL-UV.

Experimental

Aqueous solution of IVal, His, or copper complex of His (*pH* = 3, 7 or 11 in all cases) was irradiated with CPL-UV at 215 nm from an FEL of UVSOR II (IMS, Japan). DL-Amino acids were determined by HPLC.

Vacuum-evaporated thin films of DL-His were also irradiated with CPL-UV (Fig. 1). After the irradiation, optical anisotropy of the resulting thin films were observed with circular dichroism (CD) spectra.

Results and Discussion

After the irradiation with the CPL on DL-His film, no clear peaks appeared in the CD spectra from 170 to 300 nm region. This result suggests that photolysis of His film by the CPL-UV is more difficult than the cases of alanine (Ala) and IVal. In previous report, we reported that DL-Ala film after CPL-UV irradiation exhibited CD peaks with an opposite sign at 180 and 215 nm [3]. Theoretical investigation using *ab initio* quantum-chemistry calculations for alanine suggests that the emergence of CD peaks by CPL irradiation is derived from asymmetric dimerization of alanine molecular.

E. e.'s were not observed after CPL-UV irradiation to acidic / neutral amino acid solutions, but some *e. e.*'s were observed in the case of basic solutions. It was suggested that *pH* of the irradiated solution is an important parameter of chirogenesis by CPL-UV. In order to confirm the present results, further studies including more precise separation methods for DL-amino acids were required.

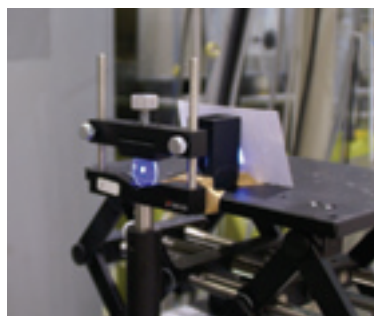


Fig. 1. Irradiation of amino acid film with CPL-UV from FEL.

[1] T. Fukue, *et al.*, *Origins Life Evol. Biosph.*, in press (2010).

[2] J. R. Cronin and S. Pizzarello, *Science* **275** (1997) 951.

[3] J. Takahashi *et al.*, *Int. J. Mol. Sci.* **10** (2009) 3044.

Local Environment Analysis of P Atoms in Proton-Conducting Amorphous Zirconium Phosphate Thin Films

Y. Aoki and H. Habazaki

Graduate School of Engineering, Hokkaido University, N13W8, Sapporo 060-8628, Japan

Inorganic phosphate compounds are attractive as an unhydrated proton conductor due to the presence of large number of native acid sites. Thin film of such materials has potential as an electrolyte membrane of next-generation intermediate temperature fuel cell. The conventional proton-conducting inorganic phosphate compounds are basically polycrystalline, and they have serious problem in forming the gas-tight membrane due to the difficulty in sintering. Previously, we reported that amorphous zirconium phosphate thin films exhibit the enhanced proton conductivity in nonhumidified atmosphere in the intermediate temperature range [1]. In addition, the films hydrated by heating in moisture at 400°C exhibit the increment of conductivity by two orders of magnitude. Amorphous metal oxides have intrinsic advantages for their application to thin film electrolyte, since they tend to be non-granular, dense layer without void formation at grain boundary due to the covalently-bonded M-O-M-O network. This superior conductivity is speculated to be related to the structure of phosphate groups. Here, we study the local environment of P atoms in amorphous zirconium phosphate thin films by P K-edge XANES in order to identify the protonic active site.

The amorphous zirconium phosphate, α -ZrP_{2.5}O_x, films were prepared on an ITO substrate (Aldrich) by multiple spin-coating of precursor solutions of tetrabutoxyzirconium (Zr(OⁿBu)₄) (Kanto) and phosphorous oxide (P₂O₅) (Kanto) at the Zr/P atomic ratio of 1/3. The details of the procedure were described elsewhere. [1] The metal concentration (Zr+P) in the precursor mixture sol was adjusted in 50 mM. The precursor sols were spin-coated onto the ITO substrate at 3000 rpm for 40 sec by a Mikasa 1H-D7 spin coater. The deposited gel layer was hydrolyzed by blowing hot air for 30 sec (luchi hot gun), and the substrate was cooled to room temperature by blowing cold air for 20 sec. These cycles of spin-coating, hydrolysis and cooling were repeated 10-20 times and the gel film thus obtained was calcined at 400°C for 30 min. The combination of deposition and calcination was repeated more than 3 times, and the final calcination was performed at 450°C for 2 h. The hydrated films were prepared by heating them at 450°C for 12 h in H₂O/air ($p_{\text{H}_2\text{O}} = 4.2$ kPa)

P K-edge XANES spectroscopy was carried out with α -ZrP_{2.5}O_x films of 40 nm, 100 nm and 300 nm-thickness (Figure 1). It is reported that P K-edge spectra of inorganic phosphate salts is very sensitive to the counter metal cation [2]. α -ZrP_{2.5}O_x films show a clear peak at 2154 eV and a lower-energy, pre-edge

peak at around 2151 eV in agreement with the spectral features of various phosphate salts [2]. These peaks correspond to the transition from P 1s P 3p-dominant unoccupied states which satisfy the dipole selection rule. The α -ZrP_{2.5}O_x films possess the same features of XANES in every thickness. Furthermore, the apparent change in spectra was not observed between the as-prepared and hydrated films. These results indicate the possibility that the polymerization degree, n , of phosphate group P_nO_{3n+1} does not change through the hydration. P L-edge XAS should be carried out in order to identify n in these thin films.

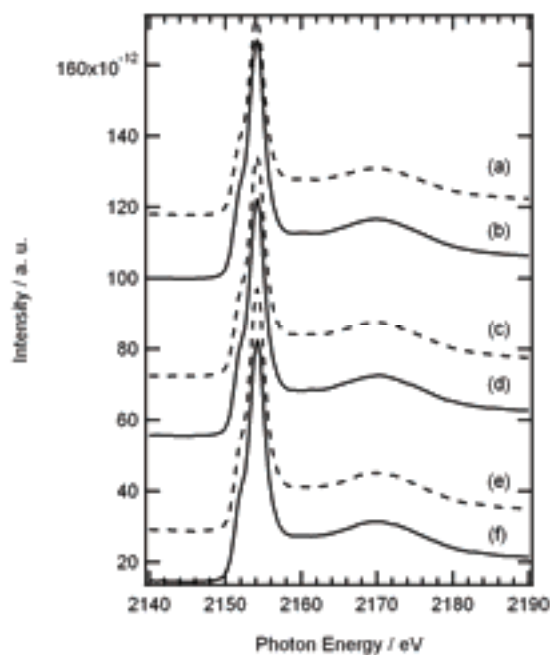


Fig. 1. P K-edge XANES spectra of amorphous ZrP_{2.5}O_x film with thickness of (a) and (b) 40 nm, (c) and (d) 100 nm and (e) and (f) 300 nm. Solid line indicates as-prepared film and dashed line hydrated film.

[1] Y. Li *et al.*, Adv. Mater. **20** (2008) 2398.

[2] N. Okude, J. Electron Spectrosc. Relat. Phenom. **101-103** (1999) 607.

Mo L_{III}-Edge XANES Study of Mo/H-MFI Catalysts for Methane Dehydroaromatization: Formation of Active Mo Carbide Species

H. Aritani¹, K. Nagashima¹, Y. Isozumi¹ and A. Nakahira²

¹Faculty of Engineering, Saitama Institute of Technology, Fukaya 369-0293, Japan

²Graduate School of Engineering, Osaka Prefecture University, Sakai 599-8531, Japan

A Mo/H-MFI catalyst shows high activity for methane dehydroaromatization in absence of oxygen. Because the catalytic system is of great value as a direct GTL (gas to liquid) process, noble catalysts with high and durable activity have been called for. Many workers have been revealed that reduction of Mo species is brought about in contact with methane in initial step. Reduced Mo ions tend to react methane to form carbide and/or oxycarbide species [1] in next step. The carbide species is active for methane dehydroaromatization, however, deactivation is brought about by carbon deposition on the catalyst surface at the same time. Ichikawa et al. [2] revealed that hydrogen co-feed gives a significant suppression effect for coking in methane conversion. On the other hand, excess hydrogen may affect a reduction of Mo species, and decrease of Mo-oxycarbide species² may give low reactivity. Thus the effect of hydrogen with methane is very important to give an effect on Mo state on H-MFI. This study addresses the effects of reaction temperature on methane dehydroaromatization over Mo/H-MFI catalysts. Mo L_{III}-edge XANES studies [3] were introduced to characterize the active Mo species on H-MFI after the methane dehydroaromatization.

Catalysts were prepared by impregnation of H-MFI support with MoO₂(acac)₂-CHCl₃ solution, and followed by drying overnight and calcination at 773 K for 3 h. Amount of MoO₃-loading is 5.0 wt% in this study. H-MFI supports with Si/Al₂ = 40–1880 were synthesized hydrothermally at 413 K for a week, and followed by ion-exchanging with NH₄Cl and calcination at 873 K. Crystallinity of Bulk phase on the whole catalysts before/after the catalytic reaction was evaluated by powdery X-ray diffraction (Rigaku, RINT2300). Amount of coking carbon was evaluated by means of thermogravimetry (Rigaku TG8120). Mo L_{III}-edge XANES spectra were measured in BL1A of UVSOR-IMS in a total-electron yield mode. Photon energy was calibrated by using Mo metal-foil at Mo L_{III}-edge, and normalized XANES spectra and their second derivatives are presented.

For Mo/H-MFI catalysts, high activity is shown in low Si/Al₂ ratio (less than 90) on H-MFI supports. In case of Mo/H-MFI in Si/Al₂=72, high and durable activity is shown at 973 K. In this case, Mo-oxycarbide species are formed during the reaction, as reported [4] previously. For the Mo/H-MFI catalysts, both high CH₄ conversion and rapid deactivation are brought about at 1023 K. At 1073 K, CH₄ conversion is scarcely seen because of sudden carbon deposition on Mo/H-MFI. Figure 1 shows the Mo L-edge XANES spectra of Mo/H-MFI

(after reaction at 973–1073 K) and reference Mo compounds. At 973 K, the Mo species consist of so-called oxycarbide species; *i.e.*, partly carbided Mo species are formed as the highly active species. At 1023 K, crystallized α -Mo₂C species are dominant. In addition, excess reduction (to form metallic/carbide species) is brought about at 1073 K. From these results, origin of the deactivation on Mo/H-MFI catalysts is not only carbon deposition but also excess reduction of Mo species to form carbide and/or metallic ones. At 973K, appropriate Mo species are formed by reduction with CH₄ to form amorphous Mo-carbide/oxycarbide species. It is concluded that the amorphous carbide/oxycarbide act as high and durable Mo species on H-MFI. Crystallization of Mo-carbide species affects the deactivation.

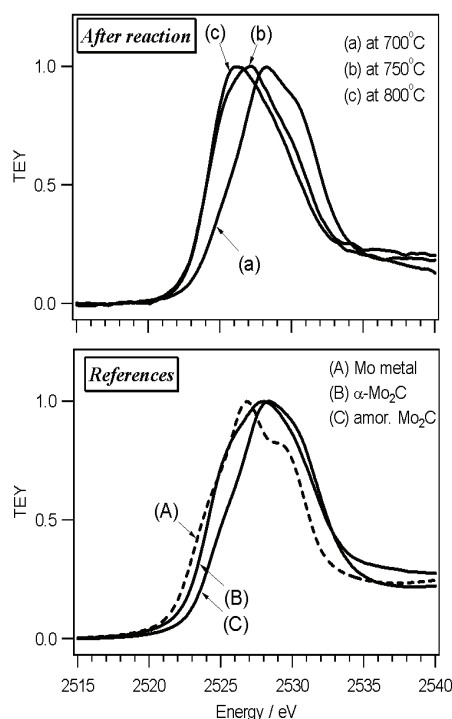


Fig. 1. Mo L_{III}-edge XANES spectra of MoO₃ (5wt%)/H-MFI(Si/Al₂=72) after CH₄ dehydroaromatization at various temperatures.

- [1] W. Li *et al.*, *J. Catal.* **191** (2000) 373.
- [2] H. Ma *et al.*, *Catal. Lett.* **89** (2003) 143.
- [3] H. Aritani *et al.*, *Chem. Lett.* **35** (2006) 416.
- [4] H. Aritani *et al.*, *UVSOR Activity Report*, **36** (2009) 113.

Study of Local Structures of Mg and Al in Hydrotalcite on Rehydration

A. Nakahira and T. Monden

Faculty of Engineering, Osaka Prefecture University, Sakai 599-8531, Japan

Layered double hydroxides (LDHs) is known as anionic clay, which is a class of lamellar compounds made up of positively charged hydroxide layers with charge balancing anions and water molecules between the layers. LDHs are expected to be useful for a large number of applications as catalyst, heavy metal ion removal, and bio-associated materials etc. Rehydration method is a one of conventional techniques of intercalation of specific anions for LDHs. It is important to clarify of local structure of LDHs on rehydration process. The investigation for the microstructures and Mg and Al local structure of LDHs in rehydration process were attempted with measurement of XANES of LDHs.

Mg/Al- CO_3 LDHs was synthesized by co-precipitation method and it was calcinated at 500°C . Rehydration process was carried out with aqueous solution of magnesium acetate. Obtained samples were identified by XRD and FT-IR. Mg K-edge XANES spectra were obtained in a total electron yield mode at room temperature using a KTP double-crystal monochromator at BL01A of the UVSOR. The spectra were collected in the photon energy range from 1300 to 1330 eV at intervals of 0.05 eV with a dwell time of 1 s.

LDH and rehydrated sample had LDH structure and calcined sample had MgO like structure by XRD and FT-IR.

Figure 1 shows the results of Mg K-edge XANES of various LDH samples: samples prepared by co-precipitation method (a), sample calcinated at 500°C (b), and samples rehydrated with aqueous solution of magnesium acetate (c). The spectrum of the samples was obviously different between each samples. From figure 1, the Mg local structures of LDH samples obtained after rehydration was similar to LDH before rehydration, suggesting that the local structure of Mg in LDHs was kept after rehydration process.

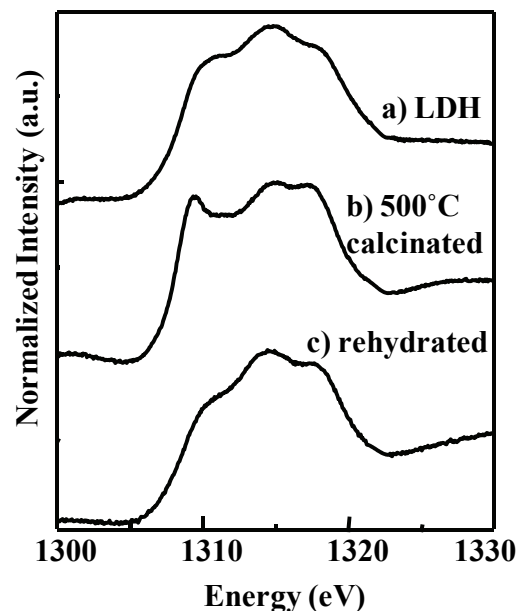


Fig. 1. Mg K-edge XANES spectra of LDHs; a) prepared by co-precipitation method, b) calcinated at 500°C , c) rehydrated with aqueous solution of magnesium acetate.

Investigation of Nanosheet in Mg/Al Type LDH Clay

A. Nakahira, T. Monden and S. Yamamoto

Faculty of Engineering, Osaka Prefecture University, Sakai 599-8531, Japan

Layered double hydroxides (LDHs) is one of important clay which is represented with the formula $[M^{2+}_{1-x}M^{3+}_x(OH)_2][A^{n-}_{x/n}mH_2O]$ (M^{2+} and M^{3+} are divalent and trivalent metals within the host layers of hydroxide sheets, and A^{n-} is an interlayer anion). Recently, the development of synthesis of hybrid LDH attracted much attention. In special, LDHs nanosheets are expected to be useful as a novel nanomaterial with various functionalities from their unique structures.

Here we synthesized LDH nanosheets by the rehydration of LDH materials heat-treated at 300 to 500 °C. In addition on the view point of the reduction of environmental load, it is important for development of a practical processing to synthesize LDHs nanosheets in aqueous system and investigate structures of LDHs nanosheets. XANES of LDHs nanosheets. was measured in order to investigate microstructures and Mg local structure.

LDH (DHT-6, Kyowa Chemical Industry Co.) was prepared as starting materials. It was calcined at 500 °C for 2 h. Calcined sample was rehydrated with aqueous solution of magnesium acetate. LDH and rehydrated LDH were calcined at 200 to- 400 °C in air atmosphere for 2h. Mg K-edge XANES spectra were obtained in a total electron yield mode at room temperature using a KTP double-crystal monochromator at BL01A of the UVSOR. The spectra were collected in the photon energy range from 1300 to 1330 eV at intervals of 0.05 eV with a dwell time of 1 s.

Water dispersions of rehydrated LDH showed tyndall phenomenon and gel formation. These features indicate that LDH nanosheets were the successfully synthesized. Figure 1 shows the results of Mg K-edge XANES spectra of LDHs and rehydrated LDHs calcined at 200 to 400 °C. These XANES spectrum of the samples were obviously different between LDHs and rehydrated LDHs. Therefore, it is estimated that Mg-local structure for rehydrated LDHs having nanosheet structure are different of ones for normal LDH.

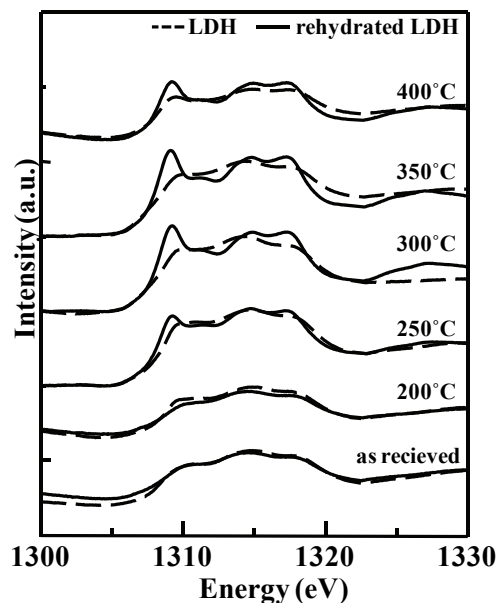


Fig. 1. Mg K-edge XANES spectra of LDH and rehydrated LDH.

Investigation of Local Structure of P K-Edge in Calcium Hydrogen Phosphate Dihydrates (DCPD) and Chitosan Composite

T. Onoki¹, S. Yamamoto¹, T. Moriguchi¹, Y. Kawabe¹, M. Sato² and A. Nakahira^{1,2}

¹Graduate School of Engineering, Osaka Prefecture University, Sakai 599-8531, Japan

²Osaka Center for Industrial Materials Research, Institute for Materials Research, Tohoku University, Sakai 599-8531, Japan

Human bone has an organic/inorganic composite structure. Bone replacing biomedical materials, for example hydroxyapatite (HA) ceramics, has been required more biocompatibility and optimal mechanical properties. Recently, bioceramics were fabricated by some hydrothermal techniques at low temperature [1, 2]. Calcium hydrogen phosphate dihydrate (DCPD) is one of starting materials for HA ceramics through a hydrothermal hot-pressing technique at around 100°C [2]. Chitosan was one of organic materials derived from crab shell. So we conducted for making an organic material composite HA ceramics for more biocompatibility and improving mechanical properties. As a first step, chitosan containing DCPD was prepared. In the present study, the structure evaluation of composite materials composed of (DCPD) and chitosan.

In this work, co-precipitation method was employed in order to prepare DCPD and chitosan composite materials. The DCPD was prepared by mixing 1.0M calcium nitrate solution (99.0%; $\text{Ca}(\text{NO}_3)_2 \cdot 4\text{H}_2\text{O}$, KANTO CHEMICAL, Japan) and 1.0M diammonium hydrogen phosphate solution (98.5%; $(\text{NH}_4)_2\text{HPO}_4$; KANTO CHEMICAL, Japan). Chitosan powder (LLWP Grade, KIMICA, Japan) was dissolved in water with a little acetic acid. The chitosan solution was added to $\text{Ca}(\text{NO}_3)_2 \cdot 4\text{H}_2\text{O}$ solution with various concentration before mixing to the $(\text{NH}_4)_2\text{HPO}_4$ solution. The mixing was carried out at a room temperature (approximately 20°C). In order to control the value of pH, acetic acid and ammonia solution were added. The precipitate from the mixture was filtered and washed with deionized water and acetone. The washed filter cake was oven-dried at 50°C for 24h, and then the dried cake was ground to a powder.

P K-edge XANES spectra for the DCPD powder were obtained in a total electron yield mode at room temperature using a InSb double-crystal monochromator at BL1A station of UVSOR. The spectra were collected in the photon energy range from 2120-2190 eV at intervals of 0.05eV with a dwell time of 1s. P-K edge XANES of the DCPD and chitosan composite powder with various concentration was shown in Figure 1. A change of the spectral patterns was not clearly observed within any preparative conditions of chitosan concentration. This result showed that the electronic structures of the phosphate ion in these composite materials are almost

same. It is needed that not only XANES but also EXAFS spectra analysis has been done.

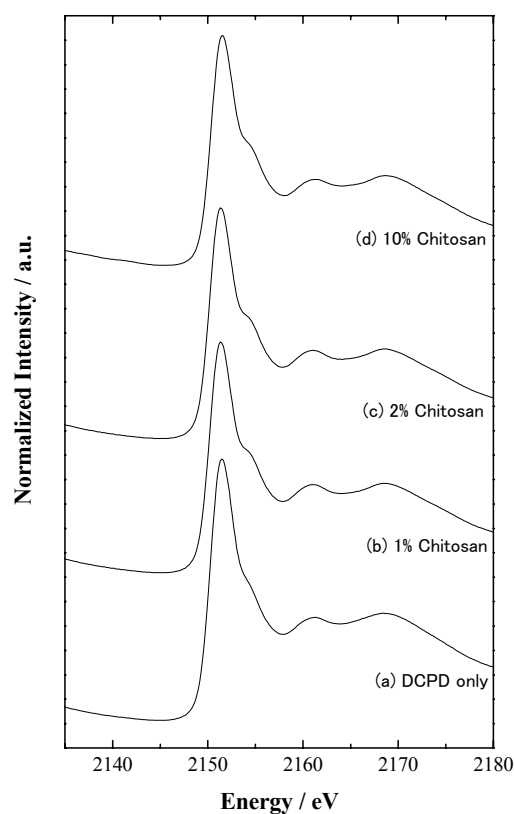


Fig. 1. XANES spectra of P K-edge of the DCPD powder with various concentration of chitosan.

[1] S. Ishihara, T. Matsumoto, T. Onoki, T. Sohmura and A. Nakahira, *Mater. Sci. Eng. C* **29** (2009) 1885-1888.

[2] T. Onoki, K. Hosoi and T. Hashida, *Ser. Mater.* **52** (2005) 767-770.

Total Photon Yield Measurement of Mg K-Edge XANES Spectrum

T. Yamamoto¹ and K. Kawabata²

¹Faculty of Science and Engineering, Waseda University, Shinjuku 169-8555, Japan

²Department of Holistic Sciences, Kwansei Gakuin University, Nishinomiya 662-8501, Japan

There are three types of popular methods to measure the X-ray absorption near-edge structure (XANES) spectrum, which are transmission, total electron yield (TEY) and total fluorescence or photon yield (TFY or TPY) methods. Among these methods, TEY is employed especially for the soft X-ray XANES, because it is difficult for such soft X-ray to pass through the sample and fluorescence yield of such energy region is quite low. However, TEY is surface sensitive detecting method like the X-ray photoelectron and Auger spectroscopy. This type of methods has disadvantages, when obtaining the electronic structure of bulk. For such purpose, TFY or TPY measurements are more suitable. Then we tried to measure Mg-K XANES of MgO before and after calcination by TEY and TPY methods to investigate the influence of surface hydration of the sample on the spectral profiles.

Mg-K XANES spectra of MgO and Mg(OH)₂ were observed at BL1A in UVSOR by TEY and TPY methods. Two types of MgO sample powders were prepared; 1) kept in air and 2) calcined just before the XANES measurements. The incident beam was monochromatized with a beryl (10 $\bar{1}$ 0) ($2d = 15.965 \text{ \AA}$) double crystal monochromator. For the TPY measurements, GaAsP photodiode (Hamamatsu Photonics) was used as a total photon yield detector.

Observed Mg-K XANES spectra of MgO before and after calcination by TEY method are shown in Fig. 1 together with that of Mg(OH)₂. From this comparison, slight difference between the spectra of MgO before and after calcination. Certain contribution of Mg(OH)₂ on peak C can be seen in the spectrum of MgO before calcination. TPY spectrum seems to contain no contribution of Mg(OH)₂ as shown in c).

We also performed the first-principles calculation for MgO by using the augmented plane wave plus local orbitals (APW+lo) package, WIEN2k [1]. Here the 3x3x3 supercell of rock-salt structured primitive cell is employed and core-hole effect is fully introduced. Calculated Mg-K XANES spectrum is also shown in Fig. 1. The calculated spectral profile has best reproduced the TPY spectrum.

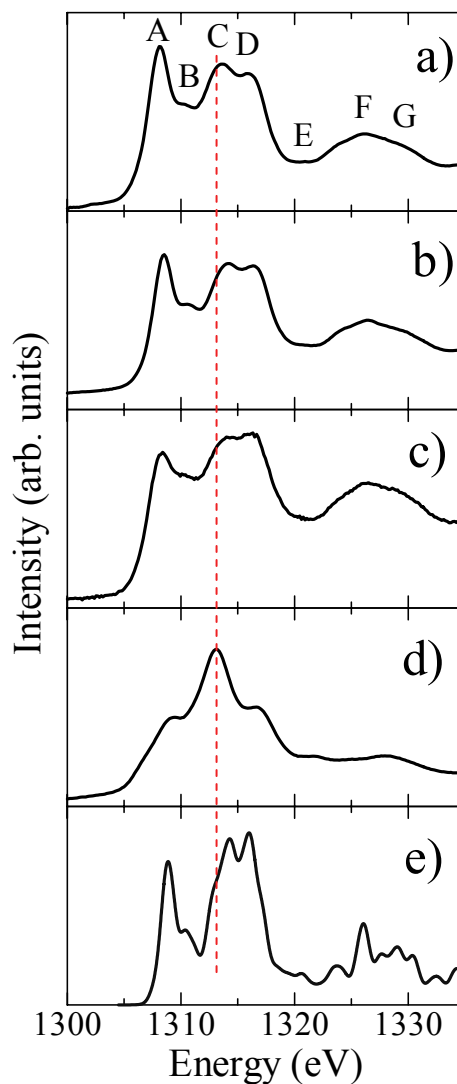


Fig. 1. Observed Mg-K XANES spectra of MgO a) before and b) after calcination by total electron yield method and by c) total photon yield method. That for d) Mg(OH)₂ and e) calculated spectrum are also shown.

[1] P. Blaha, K. Schwarz, G. Madsen, D. Kvasnicka and J. Luitz, WIEN2k, An Augmented Plane Wave + Local Orbital Program for Calculating Crystal Properties (Karlheinz Schwarz, Techn. Universitat Wien, Austria, 2001. ISBN 3-9501031-1-2)

Luminescence Properties of CsI:Ag⁻ and CsI:Au⁻ Crystals up to the Vacuum Ultraviolet Energy Region

T. Kawai¹ and T. Hirai²

¹Graduate School of Science, Osaka Prefecture University, Osaka 599-8531, Japan

²Graduate School of Science and Engineering, Ritsumeikan University, Kusatsu 525-8577, Japan

CsI:TI⁺ crystals have been well-known as the scintillator for γ -ray and their luminescence properties have been widely studied from the viewpoint of applications of this material as a phosphor. Recently, products containing toxicant heavy elements such as Tl and Pb are avoided from the viewpoint of environment. In this study, we have investigated the luminescence properties of CsI doped with Ag⁻ and Au⁻ ions without toxicity. The Au⁻ and Ag⁻ ions have the outermost s² electronic configuration in the ground state and belong to a family of TI⁺-type ions [1, 2]. Therefore, even at room temperature (RT), CsI crystals doped with the Au⁻ and Ag⁻ ions are expected to exhibit the intense luminescence from the relaxed excited-states of the sp electronic configuration.

The Ag⁻ and Au⁻ ions are not naturally present in CsI crystals. Therefore, a special treatment is needed in order to produce the negative ions. The detailed preparation of CsI:Au⁻ and CsI:Ag⁻ crystals was described elsewhere [1, 2]. The luminescence and excitation spectra up to the vacuum ultraviolet (VUV) energy region were measured at the BL-1B line of UVSOR.

Figure 1 (a) and (b) show the luminescence spectra of CsI:Ag⁻ and CsI:Au⁻ under the excitation on the energy below and above the band-gap of CsI bulk crystal. Under the excitation below the band-gap (red lines), the luminescence bands from the relaxed excited-states in impurities ions are observed at 2.46 and 2.64 eV for CsI:Ag⁻ and CsI:Au⁻, respectively. Under the excitation above the band-gap (blue lines), on the other hand, both the crystals exhibit the broader luminescence bands over the visible energy region.

In CsI:TI⁺ crystals, the broad luminescence band over the visible energy region has been attributed to the self-trapped exciton (STE) perturbed by the TI⁺ ions [3]. Since the excitation above the band-gap of CsI induces the STE, the broad luminescence spectra of CsI:Ag⁻ and CsI:Au⁻ might be attributed to the STE perturbed by the Ag⁻ and Au⁻ ions, respectively.

Figure 2 shows the excitation spectra for the visible luminescence of CsI:Au⁻ and CsI:Ag⁻ up to the VUV energy region. The remarkable response on the excitation spectra can be seen in the energy region below about 6.0 eV. The remarkable response is attributed to the intraionic transitions in the impurity ions. On the other hand, the response in the VUV energy region above the band-gap of CsI is weak.

However, the weak response in the VUV energy region indicates that photo-excited carriers and/or excitons migrate beside the impurity ions and transfer energy before self-trapping.

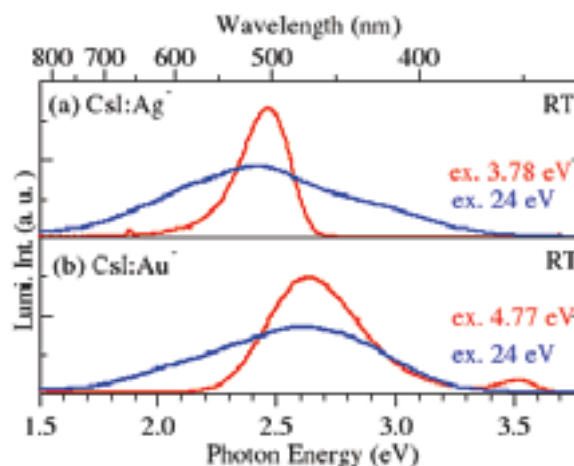


Fig. 1. Luminescence spectra of (a) CsI:Ag⁻ and (b) CsI:Au⁻ at the different excitation energies.

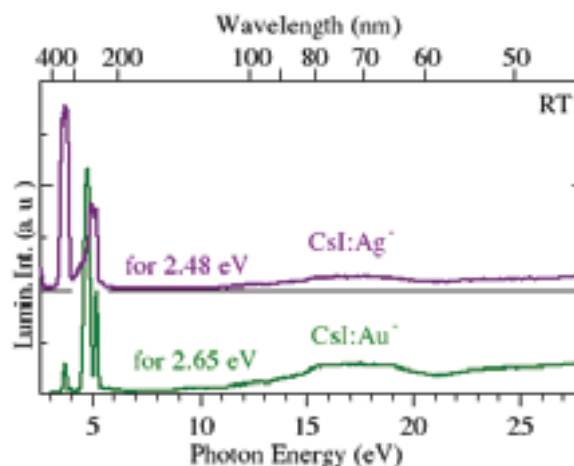


Fig. 2. Excitation spectra for the visible luminescence of CsI:Ag⁻ and CsI:Au⁻ at RT.

[1] S. Shimanuki and T. Kawai: *Phys. Stat. Sol. (b)* **168** (1991) 367.

[2] S. Shimanuki, M. Watanabe and T. Kawai, *Phys. Stat. Sol. (b)* **208** (1998) 105.

[3] V. Nagirnyi, S. Zazubovich, V. Zepelin, M. Nikl, and G. P. Pazzi, *Chem. Phys. Lett.* **227** (1994) 533.

Time-Resolved Luminescence of BaCl₂ under VUV Excitation

M. Koshimizu, K. Onodera and K. Asai

Department of Applied Chemistry, Graduate School of Engineering, Tohoku University, Sendai 980-8579, Japan

In recent years, the demand for fast scintillation materials has increased for applying in radiation detectors with an excellent timing property and the ability to operate at a high counting rate. BaCl₂ is a promising scintillation material having fast response. Thus far, we have revealed the scintillation properties of BaCl₂ [1]. Scintillation photons with wavelength ranging from 250–600 nm were observed with two luminescence bands at 310 and 410 nm. The scintillation time profiles consisted of two lifetime components. The shorter component had a lifetime of 1.6 ns, while the longer one had a lifetime of several tens of nanoseconds.

We have analyzed the luminescence properties of BaCl₂ under VUV excitation in order to reveal the origin of each scintillation component [2, 3]. A prominent band was observed at 410 nm under the excitation of almost the entire range of wavelengths region investigated, and it was revealed that this band is extrinsic, because this band was excited with sub-band-gap radiation. In addition, we observed a band at 310 nm under the excitation of only 170–190 nm, and this band was possibly a result of self-trapped excitons. Thus, the origins of two bands in scintillation spectrum were successfully analyzed. In this study, we analyzed the luminescence decay kinetics of BaCl₂ under VUV excitation in order to reveal the entire scintillation process in this material from the viewpoints of spectral and kinetic data.

A single crystal of BaCl₂ was grown by the Bridgman method. Luminescence time profile at each wavelength was measured with a monochromator and a photo-multiplier tube. The time profiles were measured at room temperature under the irradiation of synchrotron radiation having energies of 4–32 eV at the UVSOR facility (BL-1B) operating in single bunch mode.

Figure 1 shows the luminescence time profiles at various wavelengths under excitation at 158 nm. A weak subnanosecond decay component was observed at the entire wavelength region, and is possibly attributed to intraband luminescence. Unfortunately, we cannot observe the decay kinetics corresponding to the longer scintillation lifetime component, because the lifetime is expected to be comparable to the repetition interval of the excitation pulse of 176 ns.

Figure 2 shows the luminescence time profiles at 310 nm under VUV excitation at various wavelengths. In addition to the subnanosecond component, another component with a lifetime of 1.4 ns was observed only at the excitation wavelength of 170–190 nm.

This wavelength region coincides the peak in the excitation spectrum of the 310-nm luminescence band. Thus, the fast scintillation component corresponds to the luminescence band at 310 nm.

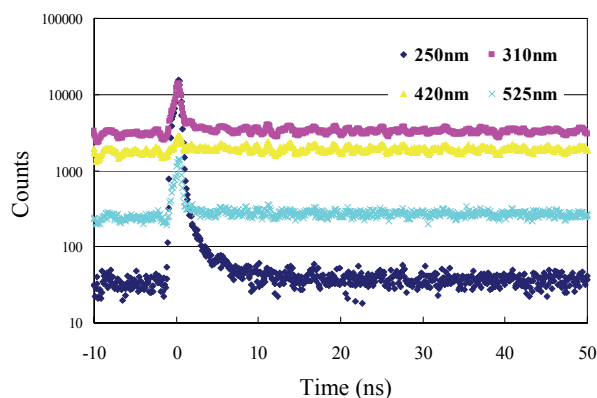


Fig. 1. Luminescence time profiles at various wavelengths under excitation at 158 nm.

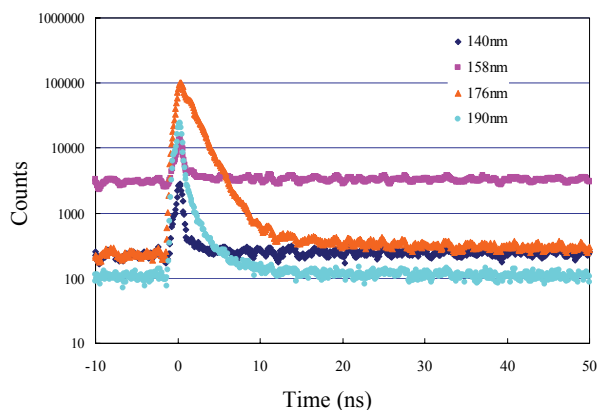


Fig. 2. Luminescence time profiles at 310 nm under VUV excitation at various wavelengths.

[1] M. Koshimizu, K. Onodera, K. Shibuya, H. Saito and K. Asai, *J. Appl. Phys.* **105** (2009) 114912.

[2] M. Koshimizu, K. Onodera and K. Asai, *UVSOR Activity Report* **36** (2009) 119.

[3] K. Onodera, M. Koshimizu and K. Asai, *Radiat. Phys. Chem.* **78** (2009) 1031.

Luminescence Properties of $\text{YBO}_3:\text{Tm}^{3+}$

N. Ohno, K. Tsugawa and K. Kohmoto

*Division of Electronics and Applied Physics, Graduate School of Engineering,
Osaka Electro-Communication University, Neyagawa, Osaka 572-8530, Japan*

Xe dimer (Xe_2) discharge fluorescent lamp is one of the candidates for alternative lighting sources to a conventional Hg discharge fluorescent lamp. New phosphors suitable for the conversion of vacuum ultraviolet (VUV) light into visible light are quite desired at present.

Under the Xe_2 discharge fluorescent excitation, phosphors are excited by VUV light of 7.2 and 8.4 eV. The Hg discharged blue-luminescence phosphor $\text{BAM}:\text{Eu}^{2+}$ ($\text{BaMgAl}_{10}\text{O}_{17}:\text{Eu}^{2+}$) becomes worse in a short time for excitation with VUV light [1]. Therefore, suitable alternative phosphors to $\text{BAM}:\text{Eu}^{2+}$ are necessary under the Xe_2 discharge light excitation. Most rare-earth metal borate hosts are transparent up to 7 - 8 eV, so that the VUV light can directly excite impurity activator in these hosts. The strong absorption due to the impurity ions would give efficient conversion of the VUV light of the Xe_2 discharge lamps [2, 3].

In the present study, luminescence properties of trivalent rare-earth metal ion center in yttrium borate have been studied in the UV and VUV region. The $\text{YBO}_3:\text{Tm}^{3+}$ phosphors were prepared by amounts of the appropriate starting compound powders of Y_2O_3 and H_3BO_3 adding Tm_2O_3 (1 mol %), mixing and firing in a porcelain crucible at 1100°C in the air atmosphere [4]. Impurity Tm^{3+} ions would be expected to be substituted for Y^{3+} ions in the host lattices.

Figure 1 shows luminescence (red curve) and photo-excitation (blue curve) spectra of $\text{YBO}_3:\text{Tm}^{3+}$ measured at room temperature. Luminescence peaks located at 2.3~4.2 eV are observed for the excitation of UV and VUV light. These luminescence lines are attributed to the $f-f$ transitions in Tm^{3+} impurity ions. The blue 2.69 eV line appears strong compared with the case of $\text{YPO}_4:\text{Tm}^{3+}$ phosphor [5]. The relative intensity of these lines would depend on the crystal field around Tm^{3+} ion.

The blue curve in the figure is the excitation spectrum for the 2.69 eV luminescence line. The luminescence of $\text{YBO}_3:\text{Tm}^{3+}$ is effectively excited with 6.1 and 7.2 eV light. These excitation peaks are located at the lower energy than the absorption edge of host YBO_3 (~7.7 eV). The excitation bands at around 6.1 and 6.9 -7.4 eV are ascribed to the $\text{Tm}^{3+} \rightarrow \text{O}^{2-}$ charge transfer transition in Tm^{3+} ions and the $f-d$ transition in Tm^{3+} ion split by the crystal field, respectively. The excitation band higher energy than 7.6 eV is due to the host lattice absorption. The $f-d$ transition energies in Tm^{3+} ions in YBO_3 are found to almost agree with the energy of Xe_2 discharge light.

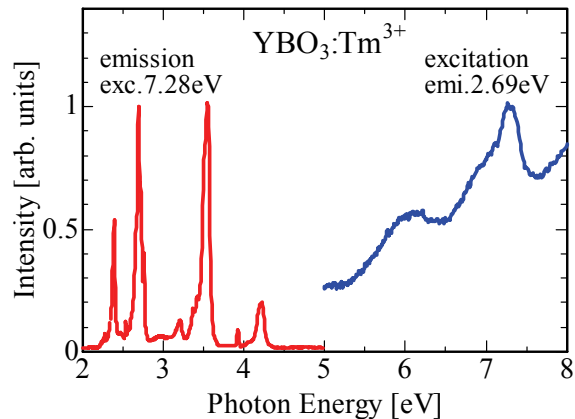


Fig. 1. Luminescence (red curve) and excitation (blue curve) spectra of $\text{YBO}_3:\text{Tm}^{3+}$ at room temperature.

- [1] W. B. Im, H. S. Yoo, S. Vaidyanathan, K. H. Kwon, H. J. Park, Y. I. Kim and D. Y. Jeon, *Mater. Chem. Phys.* **115** (2009) 161.
- [2] H. H. Lin, H. B. Liang, B. Han, J. P. Zhong, Q. Su, P. Dorenbos, M. D. Birowosuto, G. B. Zhang, Y. B. Fu, and W. Q. Wu, *Phys. Rev. B* **76** (2007) 035117.
- [3] N. Ohno and K. Kohmoto, *UVSOR Activity Report* **35** (2008) 82.
- [4] X. Z. Zeng, C. H. Yan, L. D. Sun, Z. G. Wei and C. S. Liao, *J. Lumin.* **121** (2006) 1.
- [5] W. Jia, Y. Zhou, D. A. Keszler, J.-Y. Jeong, K. W. Jang and R.S. Meltzer, *phys. stat. sol. (c)* **2** (2005) 48.

Optical Spectroscopy of Nd:Ce:YAG Ceramics and ZnO Thin Films

M. Yamaga, H. Uno, Y. Kubo and N. Kashiwagura

Department of Mathematical and Design Engineering, Gifu University, Gifu 501-1193, Japan

Ceramic lasers with high power density and high resistance to laser damage are very useful for energy conversion system from inexhaustible solar energy to other optical energy. The absorption spectrum of Ce^{3+} ions in $\text{Y}_3\text{Al}_5\text{O}_{12}$ (YAG) ceramics covers the UV and visible ranges (300-550 nm). On the other hand, ZnO thin films are one of transparent conductive oxides for use as electrodes of solar cell and liquid crystal display.

YAG ceramics codoped with 1 mol % Nd^{3+} and 0.05 mol % Ce^{3+} were sintered by Konoshima Chemical Company. ZnO thin films were deposited on a fused silica glass by the DC sputtering method. Optical absorption, luminescence and excitation spectra for these samples were measured using the BL1B beam in the temperature range of 8-300 K.

Figure 1 (a) shows the optical absorption spectrum in Nd:Ce:YAG ceramics. Fairly broad bands below 240 nm are due to the band-to-band transition and the 4f-5d transition of Nd^{3+} because the band-edge in pure YAG crystals is located around 180 nm. The broad absorption bands around 350 and 550 nm are due to the 4f-5f transitions of Ce^{3+} . Excitation below 240 nm in Nd:Ce:YAG ceramics produces several sharp luminescence lines in the visible (400-630 nm) and near-IR ranges, as shown in Fig. 1(b), being due to the transitions from the multiplet $^2F_{5/2}$ and $^4F_{3/2}$ metastable excited states to other multiplets of Nd^{3+} , respectively. The near-UV (354 nm) excitation of Ce^{3+} produces the visible and near-IR luminescence lines of Nd^{3+} , whereas the another 460 nm excitation of Ce^{3+} produces orange-colored broad band of the Ce^{3+} luminescence and only near-IR sharp Nd^{3+} lines with a lack of the visible lines. These results suggest that the energy transfer occurs from Ce^{3+} to Nd^{3+} in YAG ceramics.

Figure 2(a) shows the optical absorption spectrum and the excitation spectrum obtained by monitoring the 540-nm luminescence intensity in Fig. 2(b) for the ZnO thin films. The broad band below 360 nm is due to the band-to-band transition of ZnO. Figure 2(b) shows the luminescence spectra with various excitation wavelengths at 8 K. The band-to-band excitation below 400 nm produces two broad luminescence bands. In the case of the 450 nm excitation, the 440 nm luminescence band disappears and the 560 nm band remains. The form may be intrinsic luminescence (for example, self-trapped exciton), whereas the latter is the luminescence associated with defects (donor/acceptor recombination). The relation between the luminescence and electrical conductivity will be examined.

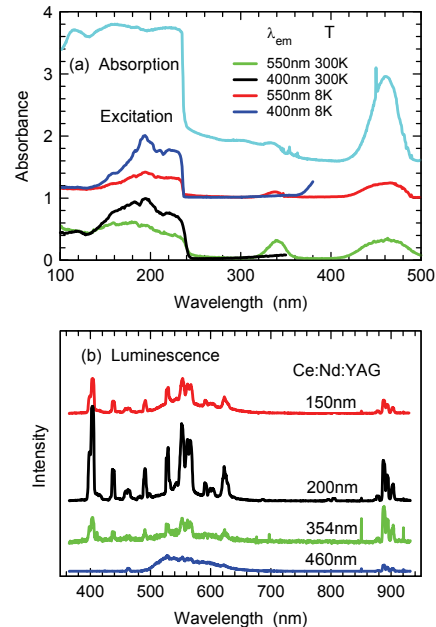


Fig. 1. (a) Absorption/excitation spectra and (b) luminescence spectra in Nd:Ce:YAG ceramics.

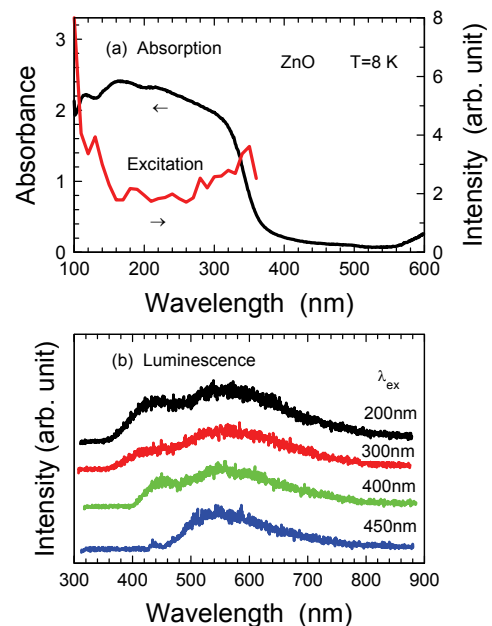


Fig. 2. (a) Absorption/excitation spectra and (b) luminescence spectra in ZnO thin films.

Excitation and Emission Spectra for Nd^{3+} in SrY_2O_4

M. Yoshino¹, Y. Ichikawa¹ and S. Watanabe²

¹ *Department of Materials, Physics and Energy Engineering, Nagoya University, Nagoya 464-8603, Japan*
² *Venture Business Laboratory, Nagoya University, Nagoya 464-8603, Japan*

The trivalent lanthanide ions (e.g. Er^{3+} , Ce^{3+} , Yb^{3+}) in oxide crystals have drawn attentions due to their application for luminescent materials in NIR to UV regions such as solid-state lasers or phosphors. And, Nd^{3+} has also attracted attentions as luminescence centers. In this work, the excitation spectra and emission spectra for Nd^{3+} in SrY_2O_4 crystal have been measured. The Nd doped SrY_2O_4 samples are produced by solid state reactions in 1373 K. The concentration of Nd^{3+} in the sample is 3 mol%. The emission spectrum for Nd^{3+} in SrY_2O_4 at 200 nm excitation is shown in Fig. 1. The broad peak appearing below 400 nm and the sharp peaks appearing around 400-600 nm are expected to relate to the emission of SrY_2O_4 host and Nd^{3+} 4f-4f

transition, respectively. The excitation spectrum monitored at 334 nm emission is shown in Fig. 2. The peak near 200 nm corresponds with that in the spectrum monitored at 423 nm in SrY_2O_4 host [1], and it relates to the absorption from the optical transition around the band edge in SrY_2O_4 . On the other hand, the peaks are measured around 230-250 nm in the excitation spectrum monitored at 555 nm emission (Fig. 3). These peaks are due to the Nd^{3+} 4f-5d transition. Then, in the excitation at 230 nm, Nd^{3+} ions are excited directly, the emission spectrum mainly shows the sharp peaks originated from Nd^{3+} 4f-4f transition (Fig. 4).

[1] M. Yoshino, S. Watanabe and Y. Ichikawa, UVSOR Activity Report 36 (2009) 122.

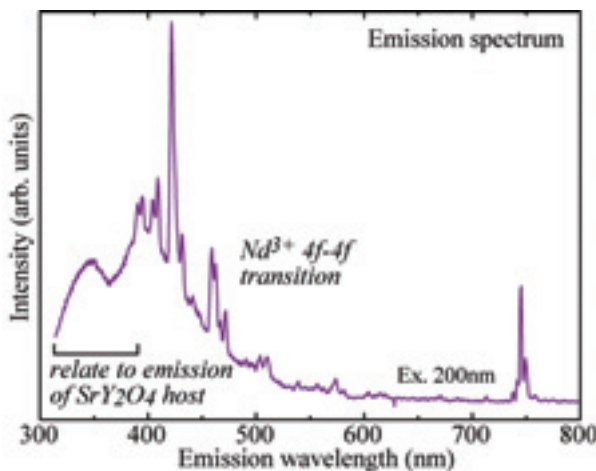


Fig. 1. Emission spectrum for Nd^{3+} in SrY_2O_4 .

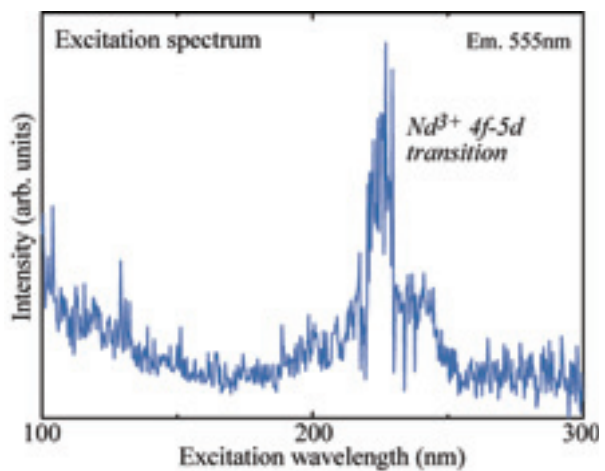


Fig. 3. Excitation spectrum for Nd^{3+} in SrY_2O_4 .

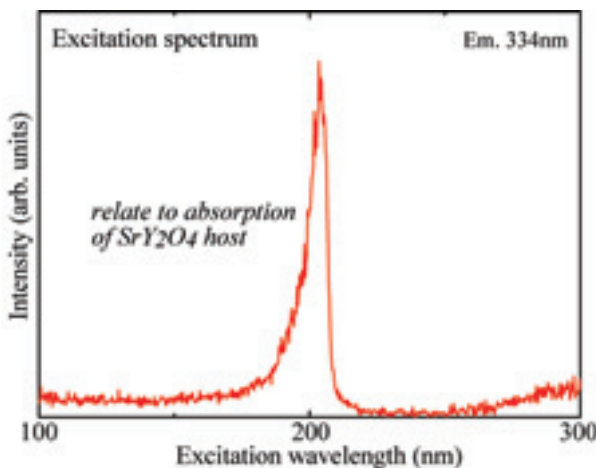


Fig. 2. Excitation spectrum for Nd^{3+} in SrY_2O_4 .

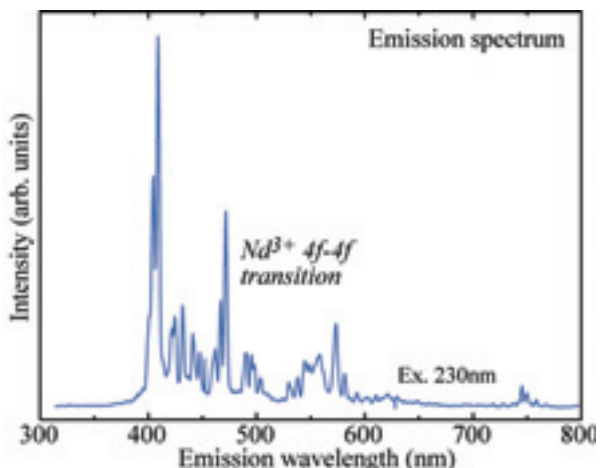


Fig. 4. Emission spectrum for Nd^{3+} in SrY_2O_4 .

Electronic Structural Changes of Electrochemically Oxidized $\text{Li}_{2-x}\text{CuO}_2$

Y. Arachi, K. Hinoshita and Y. Higuchi

Department of Chemistry, Materials Engineering, Kansai University, Osaka 564-8680, Japan

New potential cathode materials to replace LiCoO_2 are under extensive investigation. Among them, we focus on copper because of its abundant resources and the less toxicity. Additionally, higher cell potential can be expected in view of its electronic structure composed of trivalent Cu and O. Electrochemical study of Li_2CuO_2 was reported that a rechargeable capacity of 130 mAhg^{-1} was obtained with an average voltage of 2.5 V although it has 490 mAhg^{-1} of theoretical capacity[1]. In this study, using experimental and ab-initio calculation results we investigate the changes in electronic structure of Li_2CuO_2 caused by Li-de/intercalation electrochemically and discuss the possibility of cathode material with high energy density.

The conventional solid-state reaction was used. Starting materials were composed of chemical grade Li_2CO_3 and CuO . After mixing them properly, pellets were made by the pressing. Then, they were calcinated at 1023 K for 24 h and sintered at 1073 K for 24 h. De-lithiated samples were electrochemically prepared using coin-type cells with $\text{Li}/1\text{M LiClO}_4$ in $\text{PC}:\text{DMC}(1:1)$ /samples. X-ray absorption measurements of above samples at the Cu *L*- and O *K*-edges by the total electron yield were performed on BL4B and (UVSOR-II, Okazaki, Japan). The first principle calculations were carried out using the WIEN2k program package, which is based on the full potential augmented plane wave and local orbitals (APW+lo) method within the generalized gradient approximation (GGA). The maximum wavelength of APW, K_{max} , was determined to satisfy the condition of $R \times K_{\text{max}} = 7$, where R is the muffin-tin radius of the O atom. The warped electron density in the interstitial region was described by a finite Fourier series with maximum wave vector, G_{max} , where G_{max} satisfies 12. The maximum angular momentum l for partial spherical waves inside atomic spheres was 10. A mesh $10 \times 10 \times 10$ over the irreducible Brillouin zone was used, producing 224 inequivalent k -points.

Figure 1 shows that the results of a first principle calculation for Li_2CuO_2 and LiCuO_2 . It clearly indicates a difference between them, specifically in a valence band state distribution of oxygen. A considerable electron loss of oxygen was occurred by Li-extraction. Figure 2 shows XANES spectra of O *K*-edges for Li_2CuO_2 and electrochemically Li-deintercalated $\text{Li}_{2-x}\text{CuO}_2$ at various voltages. On the basis of these results, we will examine the role of oxygen during charging reaction at higher voltage region.

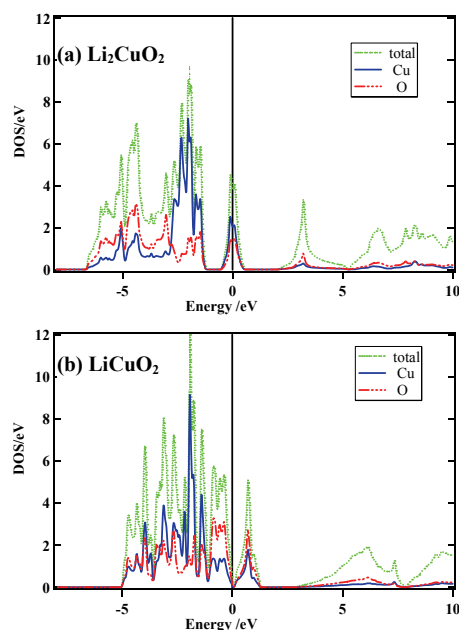


Fig. 1. Density of State for (a) Li_2CuO_2 and (b) LiCuO_2 .

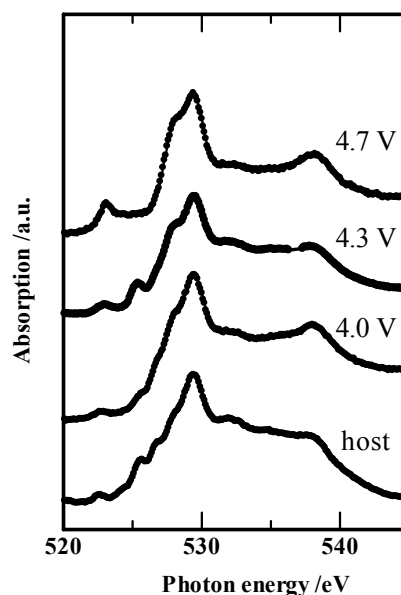


Fig. 2. O *K*-edge XANES of electrochemically oxidized $\text{Li}_{2-x}\text{CuO}_2$.

- [1] H. Arai *et al.*, *Solid State Ionics* **106** (1998) 45.
 [2] A. S. Prakash *et al.*, *Chem. Mater.* **17** (2005) 4406.

Effect of Periodicity Fluctuations on Mini-Band Structure in Strained Superlattice Semiconductor

T. Ujihara¹, K. Hashimoto¹, Y. Maeda¹, H. Miyazaki³, M. Kuwabara² and Y. Takeda¹

¹Graduate School of Engineering, Nagoya University, Nagoya 464-8603, Japan

²Graduate School of Science, Nagoya University, Nagoya 464-8602, Japan

³UVSOR Facility, Institute for Molecular Science, Okazaki 444-8585, Japan

Recently, a quantum dot solar cell is proposed to achieve a high conversion efficiency. The concept of the quantum dot solar cell is to utilize mini-bands in the periodic alignment of quantum dots, as middle band in the carrier excitation in order that the band structure is matched the solar light spectrum. The theoretical calculation indicates that the conversion efficiency can reach over 50% assuming "the perfectly periodic potential." However, it is presently impossible to produce quantum dots, of equal size, periodically.

In this study, the effect of periodicity fluctuation on the mini-band structure was investigated from the viewpoint of the followings: (1) the effect on energy and band width of the mini-band structure, (2) the effect on the conduction and lifetime of carriers in the mini-band. In place of quantum dot alignment, we examined the superlattice structure based on multiple quantum well of which the preparation method has been established.

We prepared the InGaAs/GaAs superlattice structures as shown in Fig. 1. On the structure with the periodicity fluctuation, the film thickness of one well layer of the superlattice structure was made thicker. On the evaluation of the mini-band structure, the synchrotron-radiation photoemission measurements at BL-5U of the UVSOR facility were scheduled. (However, we could measure only the GaAs bulk crystal as the preliminary experiment in the present study.) In addition, the quantum efficiency measurement was carried out as an evaluation of electronic conduction in the mini-band. In this study, the quantum efficiency was evaluated by measuring the current due to the electrons taken out from the conduction band to the vacuum via the NEA surface.

Figure 2 shows the angle-resolved photoemission mapping of GaAs bulk crystal. θ is the tilt angle from [001] to [110]. There are mainly three bands in this mapping profile. Since these band structures are symmetrical for the angle at around 1 deg, this symmetry center seems to be the Γ point of GaAs. Figure 2(b) is the spectrum mapping measured by changing the energy of incident beam. The symmetry around Γ point is also observed. From this mapping, the inner potential was determined to be around 50 eV. This value is useful for the measurement of superlattice mini-bands in future.

Figure 3 is the quantum efficiency spectrum as a

function of wavelength of excitation laser light. In the case of the sample without the periodicity fluctuation, the photocurrent was detected from 700 nm to over 1000 nm, and the spectrum was a step for the wavelength. The stepped spectrum reflects a density of state of superlattice structure. In the case of the sample with the periodicity fluctuation, the quantum efficiency decreases by 10^{-1} – 10^{-3} comparing that without the fluctuation. It is serious for the solar cell properties that the fluctuation of only one well layer thickness largely decreases the quantum efficiency.

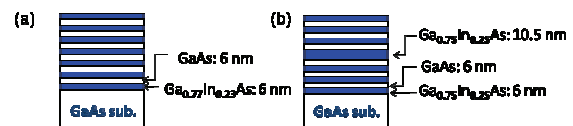


Fig. 1. Sample structures of (a) superlattice without periodicity fluctuation and (b) superlattice with periodicity fluctuation.

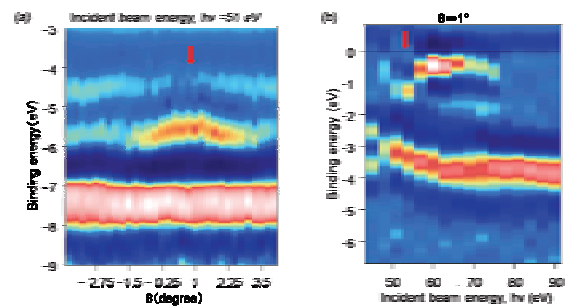


Fig. 2. Photoemission spectra mapping from GaAs bulk crystal: (a) Angle-resolved photoemission mapping and (b) Photoemission mapping as a function of incident beam energy.

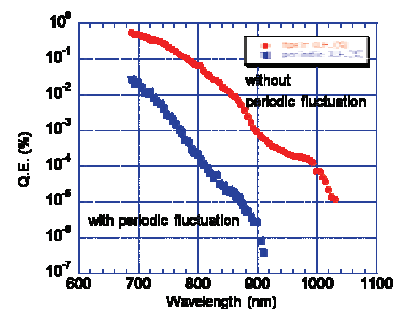


Fig. 3. Quantum efficiency as a function of wavelength of excitation light.

Observation of Photodegradation in Amorphous Semiconductors by Ultraviolet Synchrotron Orbital Radiation

K. Hayashi

Department of Electrical and Electronic Engineering, Gifu University, Gifu 501-1193, Japan

Introduction

The time-dependent change in photoconductivity during and after irradiation of bandgap (BG) light has been observed in many amorphous semiconductor materials. [1] This phenomenon usually called photodegradation and is explained in terms of the creation of photoinduced metastable defects. In device application of these materials, the creation of those defects is serious problem. The photodarkening is also a well-known phenomenon in amorphous chalcogenide materials. The photodarkening is a parallel shift to the optical absorption edge to lower energy side after irradiation of BG light. This darkened state is removed by annealing near the glass-transition temperature. The x-ray diffraction and the volume change of the films before and after irradiation of BG light suggest that photodarkening is due to a change of the local structure of the amorphous network.[2] Although many models are proposed for the creation of those defects and the photodarkening, details of the microscopic mechanism are still not clear. Understanding the physical mechanism metastability is one of the important fundamental problems associated with these materials.

The measurement of the total photoelectron yield (TPY) at the vacuum ultra-violet region is a powerful tool for the study of the energy structure. TPY will reflect the optical absorption and the photoconductivity of the material. In this report, we investigate photoinduced phenomena by measuring TPY of amorphous films.

Experimental

Thin films of amorphous materials (a-As₂S₃ and a-Si) were prepared onto quartz substrates which fabricated Au electrodes by conventional evaporation technique. The thickness of the amorphous films was from around 160nm to 300nm. The samples were annealed at appropriate temperature (443K for a-As₂S₃ and 473K for a-Si) for two hours in a vacuum. A xenon arc lamp with IR-cut-off filter was used as a BG light source. The measurements of TPY were performed at room temperature at the BL5B beam line. For a-As₂S₃, the VUV probe light to measure TPY was fixed to the wavelength that was able to excite 3d core level of As atom. For a-Si, the VUV probe light was fixed to the wavelength that was able to excite 2p core level of Si atom. A pinhole of 1.5mm in a diameter was inserted between the monochromator and sample to remove stray light. The intensity of the VUV probe light was monitored

by measuring TPY of two Au meshes.

Results and Discussion

Figure 1 shows examples of the time-dependent change in TPY of a-As₂S₃ and a-Si films by irradiation of BG light. This figure is obtained by TPY normalized by the initial value of the measurement. As shown in the figure, during irradiation of BG light, TPY of a-As₂S₃ is gradually increased and it seems to be finally saturated.[3] On the other hand, TPY of a-Si doesn't depend on the presence of irradiation of BG light, and decreased monotonously. It seems that the difference of the TPY change in both samples is related whether to cause the photodarkening. The photodarkening only is observed in amorphous chalcogenide materials, and not observed in a-Si. In a-Si film, since defects are also generated by irradiation of high energy photons [4], it is thought that TPY was decreased by the creation of defects dominantly induced by the VUV probe light. However, it doesn't understand that a decrease of TPY by the photodegradation is not observed in a-As₂S₃ at present. The relation among this TPY change, the photodegradation, and the photodarkening will be more clarified in the next step.

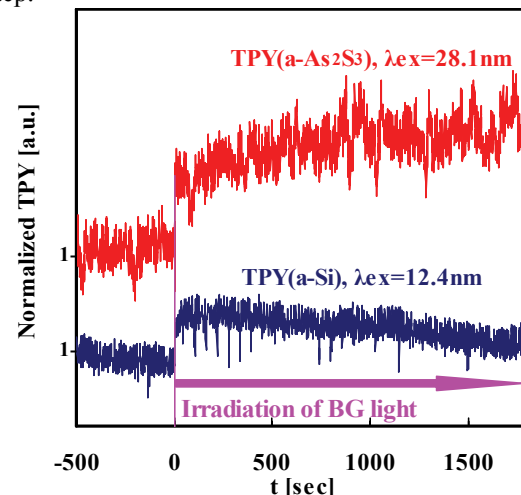


Fig. 1. The photoinduced change of TPY by irradiation of bandgap light in a-As₂S₃ and a-Si films.

References

- [1] D. L. Staebler and C. R. Wronski, *Appl. Phys. Lett.* **31** (1977) 292.
- [2] Ke. Tanaka, *Rev. Solid State Sci.* **4** (1990) 641.
- [3] K. Hayashi, *UVSOR Activity Report* **36** (2009)125.
- [4] Pontuschka *et al.*, *Phys. Rev. B.* **25** (1982) 4362.

Characterization of Novel TiO₂/ZnO Multilayer Mirrors at "Water-Window" Wavelengths

Y. H. Kumagai¹, Y. Tanaka¹, M. Murata¹, T. Shinagawa² and A. Kobayashi¹

¹Graduate School of Engineering, Osaka City University, Osaka 558-8585, Japan

²Inorganic Materials Lab., Osaka Municipal Technical Research Institute, Osaka 536-8553, Japan

Development of high-performance normal-incidence multilayer optics for the water-window wavelength region between the oxygen and carbon K absorption edges at 2.33 and 4.36 nm, respectively, where water is relatively transmissive and organic materials are absorptive, has been a technical challenge of great interest. The extremely small periods (1.2-2.2 nm) of soft-x-ray reflectors require very rigorous specifications to be met with respect to interface roughness and interlayer mixing, because interface roughness on an atomic scale has a substantial effect on soft-x-ray reflectance. Therefore, the highest reflectance achieved at water-window wavelengths ($\lambda=3.18$ nm) and near normal incidence ($\theta=9^\circ$) has been 3.3% at the first half of 1990's [1], in spite of the various efforts which have been made in this field. The reason that the reflectances achieved at these wavelengths are so low is that the Fresnel coefficients of materials are so small at these wavelengths that a large number of bilayers must be used, which means that the problems of interface roughness and imperfect interfaces due to interlayer mixing become serious.

The authors have proposed the use of a novel metal oxide multilayer for soft-x-ray reflectors at water-window wavelengths, because an oxide multilayer can prevent the formation of an alloy at the interface without any diffusion barrier, and the absorption of oxygen in oxides is negligible at the water-window wavelengths; moreover, the metal oxide multilayer can be fabricated by the atomic layer deposition or atomic layer epitaxy technique. These techniques can be used to control surfaces on an atomic scale by sequentially dosing the surface with appropriate chemical precursors and then promoting surface chemical reactions which are inherently self-limiting. We have found that the self-limiting adsorption mechanism works in the fabrication of oxide thin films such as aluminum oxide and titanium oxide [2]. And we reported that we have experimentally demonstrated high reflectance of over 30% at a wavelength of 2.734 nm and an incident angle of 71.8° from the normal incidence using novel metal oxide multilayers of titanium oxide and aluminum oxide fabricated by the atomic layer deposition method of controlled growth with sequential surface chemical reactions. For x-ray processing, crystalline multilayer mirrors might be rather useful than amorphous ones. Therefore, in this study, the authors demonstrated that novel oxide superlattice structures of crystalline TiO₂/ZnO on

sapphire substrates were fabricated for high-reflection multilayer mirrors at 2.734 nm. Theoretical calculations also indicated that these structures could give high reflectance over 50% at the wavelength. In the experimental study, both rutile TiO₂ (200) and wurtzite ZnO (0001) thin films were grown epitaxially on the same sapphire (0001) substrates by atomic layer epitaxy (ALE) at 450°C. We demonstrated for the first time that the novel oxide superlattice structure of 10-bilayer TiO₂/ZnO on a sapphire substrate gave high reflectance of 29.4% at a wavelength of 2.734 nm, as shown in Fig. 1.

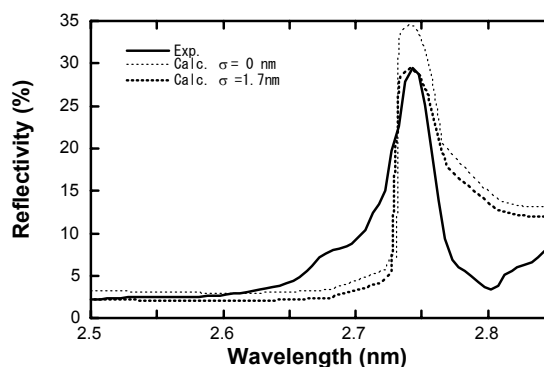


Fig. 1. Experimental reflectances of the ALE-grown 10-bilayer ZnO/ TiO₂ structure on a sapphire (0001) substrate. $\theta=85^\circ$.

[1] I. V. Kozhevnikov, A. I. Fedorenko, V. V. Kondratenko, Yu. P. Pershin, S. A. Yulin, E. N. Zubarev, H. A. Padmore, K. C. Cheung, G. E. van Dorssen, M. Roper, L. L. Balakireva, R. V. Serov and A. V. Vinogradov, Nucl. Instrum. Methods Phys. Res. A **345** (1994) 594.

[2] H. Kumagai, K. Toyoda, K. Kobayashi, M. Obara and Y. Iimura, Appl. Phys. Lett. **70** (1997) 2338.

Far-Infrared Reflective Study of Li-Doped Alkali Niobate System

H. Matsudo, Y. Shikai, S. Tachi, I. Kagomiya and K. Kakimoto

Graduate School of Engineering, Nagoya Institute of Technology, Nagoya 466-8555, Japan

Alkali niobate oxide is one of the lead-free piezoelectric materials. The electrical property varies with alkali component, especially with the density of Li ion. In our previous study at BL6B[1], the absorption of Na and K ion translational modes of $\text{Li}_{0.06}(\text{Na}_{0.5}\text{K}_{0.5})_{0.94}\text{NbO}_3$ (LNKN06) were not clear and the softening of the translational modes was not observed between the spectrum at 78 K and that at 300 K in spite that the phase transition from rhombohedral to orthorhombic crystal structure exists at 270 K. In this study, IR reflectivity of LNKN06 and NKN ceramics were measured to clarify the effect of Li incorporation against the lattice vibration around NbO_6 octahedral unit in perovskite structure.

Reflectivity far-infrared spectra of $\text{Na}_{0.5}\text{K}_{0.5}\text{NbO}_3$ (NKN) and LNKN6 ceramic samples were obtained at the range from 78 to 313 K at the BL6B beam line of UVSOR. The spectra were corrected by using Michelson interferometer (Bruker, IFS66v) and synchrotron radiation source.

Figure 1 shows far-infrared reflectivity spectra of NKN ceramics. Broad absorption was observed from 150 to 200 cm^{-1} that attributed by TO phonon of the vibration of Na and K ions against the NbO_6 octahedral unit. The spectra clearly show the phase transition from rhombohedral to orthorhombic crystal structure between 78 and 100 K on heating process. This reflects that the phase transition of NKN includes the softening of translational modes of Na and K ions.

On the other hand, the far-infrared reflectivity spectra of LNKN06 are not changed around at 273K, at which the LNKN06 ceramics shows orthorhombic to tetragonal phase transition. However, there is several absorption band ranging from 120 to 300 cm^{-1} .

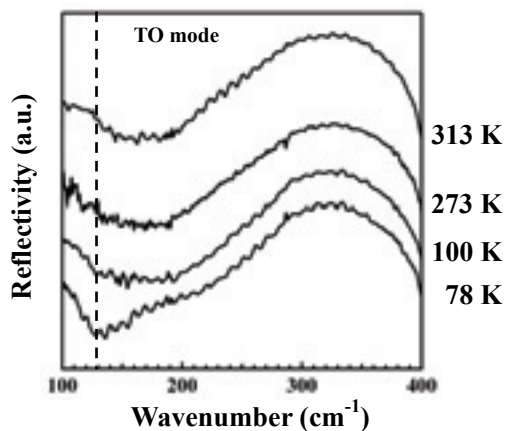


Fig. 1. Far-infrared reflectivity spectra of NKN ceramics at the range 78 to 313 K.

The real part of dielectric permittivity of NKN and LNKN ceramics at 273K, which were calculated from reflectivity by Kramers-Kronig relation, shows the difference around 200 cm^{-1} . This result indicates that the distortion of NbO_6 was induced by the small ion of Li in NKN perovskite structure, which corresponds to our previous study by Raman spectroscopy[2].

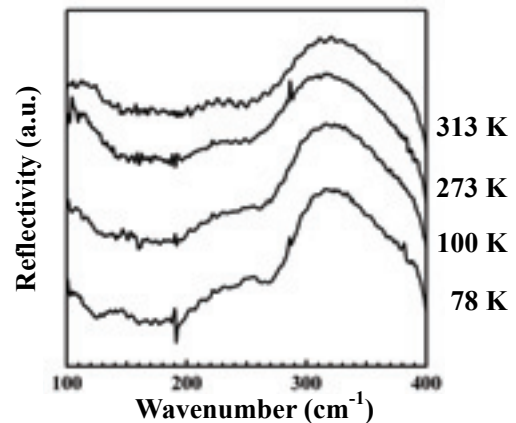


Fig. 2. Far-infrared reflectivity spectra of LNKN06 ceramics at the range 78 to 313 K.

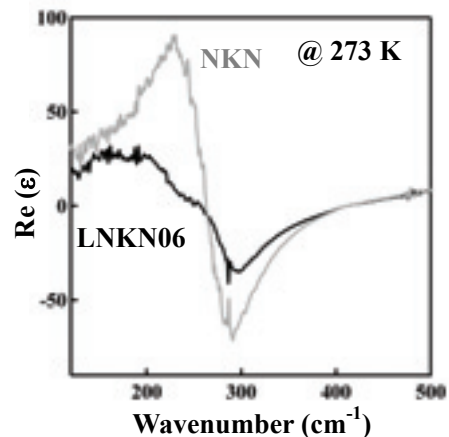


Fig. 3. The real part of dielectric permittivity of NKN and LNKN06 ceramics at 273K.

Acknowledgement

This research was supported by the Industrial Technology Research Grant Program in 2007 from the New Energy and Industrial Technology Development Organization (NEDO) of Japan

References

- [1] H. Matsudo, Y. Inagaki, T. Sumi, I. Kagomiya and K. Kakimoto, UVSOR Activity Report **36**(2009) 128.
- [2] T. Hotta, K. Kakimoto and H. Ohsato, Key Eng. Mater., **368-372** (2008) 1893.

Reflectivity Spectra of SrGa₂S₄ Crystals

M. Kitaura¹, A. Ohnishi¹, M. Sasaki¹ and M. Itoh²

¹Department of Physics, Yamagata University, Yamagata 990-8560, Japan

²Department of Electrical and Electronics Engineering, Shinshu University, Nagano 380-8553, Japan

Alkaline-earth thiogallates are known to be host materials of thin-film electroluminescence (EL) phosphors. The EL phenomena in inorganic phosphors originate from the creation of hot electrons by high electric field, but the excitation mechanism of luminescence centers still remains open in rare-earth doped alkaline-earth thiogallates. One of the reasons is that there are few studies on the electronic structures of them. Since the behavior of hot carriers reflects the valence and conduction bands, the electronic structure of host materials is of great importance in order to clarify the excitation mechanism of luminescence centers. In the present study, we have investigated the electronic structure of strontium thiogallate SrGa₂S₄ by the measurement of reflectivity and X-ray photoelectron spectroscopy (XPS) spectra and the cluster calculation based on the relativistic discrete variational X α (DV-X α) method [2].

The crystals of SrGa₂S₄ were grown by a chemical vapor transport method. A small amount of iodine was used as a transport agent. Our samples have high-quality surface for the crystalline *ac* plane, the average size of which was 3×0.5×2 mm³. From the X-ray diffraction measurement, it turns out that they have the structure of SrGa₂S₄. Reflectivity spectra of them were measured at the BL7B beam line of UVSOR. Optical constants were calculated by the Kramers-Kronig transformation of reflectivity.

Figure 1 shows the typical absorption spectrum of SrGa₂S₄ in the 3–30 eV energy range at 300 K. The first increase in absorption coefficient occurs at 4.34 eV, and a prominent peak appears at 5.36 eV. As the photon energy is increased, the second increase takes place around 9.5 eV, which is followed by a broad structure in the high-energy side.

The partial density of states (PDOS) curves for a number of atomic orbitals of Sr, Ga, S are shown in Fig. 2. The zero energy is set to the top of the valence band. The valence band (VB) is dominated by S 3p orbitals, the full base width of which is 6 eV in rough estimation. This value is in good agreement with the VB width estimated from XPS spectra. The conduction band (CB) is mainly composed of 4d orbitals of Sr in the lower part and p orbitals of Sr and Ga in the upper part.

From the PDOS curves of Fig. 2, the electronic transition from the VB of S 3p to the lower CB of Sr 4d is expected in the lowest energy position. Thus, we assign the 5.36 eV absorption peak to the VB → lower CB transition. In the high-energy position,

since the large joint density of states is expected for the transitions from the VB to the upper CB of Sr 5p + Ga 4p, the broad structure above 9.5 eV is assigned to the transition from the VB to the upper CB.

We found a number of fine structures in the absorption spectra at around 10 K. These structures showed remarkable dichroism. An analysis for the polarization dependence of absorption spectra is now in progress.

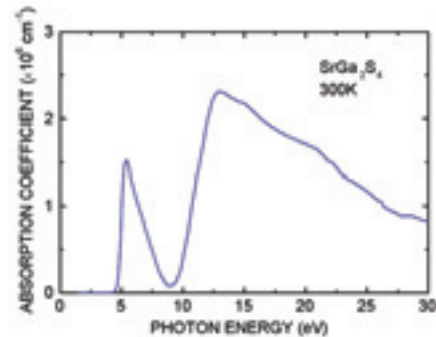


Fig. 1. Absorption spectrum of SrGa₂S₄ crystal at 300 K calculated by the Kramers-Kronig analysis.

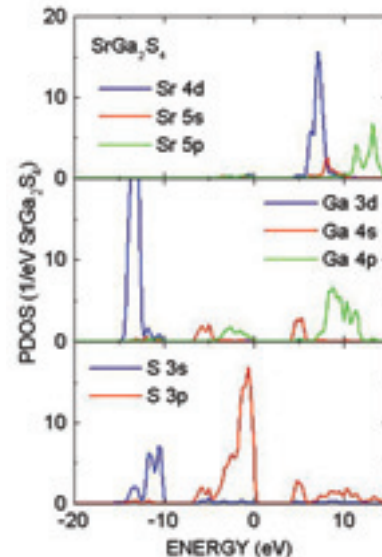


Fig. 2. Partial density of states curves of SrGa₂S₄. The zero energy was set to the top of the valence band.

[1] M. Yoshida, A. Mikami and T. Inoguchi: in *Phosphor Handbook*, ed. S. Shionoya and W. M. Yen (CRC Press, Boca Raton, FL, 1999) p. 581.

[2] H. Adachi, M. Tsukada and C. Satoko, *J. Phys. Soc. Jpn.* **45** (1978) 875.

Azo Dyes as Photosensitizers for Organic Solar Cells

K. Nakajima^{1,2}, K. Ohta¹, H. Katayanagi^{2,3} and K. Mitsuke^{2,3}

¹Science Research Center, Hosei University, Tokyo 102-8160, Japan

²Institute for Molecular Science, Okazaki 444-8585, Japan

³Graduate University for Advanced Studies, Okazaki 444-8585, Japan

The dye sensitized solar cell (DSC) has attracted universal attention because of its high-solar-energy-to-electricity conversion efficiency and relatively low cost of its manufacturing [1]. Panchromatic sensitizers which can efficiently absorb the sunlight are in the stage of research and development. So far the best photovoltaic performance has been achieved with ruthenium complex dyes, but organic dyes have also stimulated intensive research efforts [2]. In the present study, we focused our attention on azo compounds which have been widely used for dyes and pigments with excellent lightfastness. The main advantage of azo dyes is their facile introduction of various substituents onto the main structure R-N=N-R', permitting us to easily modify their electronic and spectroscopic properties.

We designed various azo dyes having carboxylate and hydroxy groups whose positions and numbers differ from one dye to another. We synthesized 25 azo dyes and compared their performance among nine azo dyes that have the same basic structure (naphthyl-azo-benzene). Titanium dioxide paste (PST-18NR: Shokubaikasei kogyo) was applied on the FTO glass (Asahi glass) by screen printing, and sintered at 450°C for 30 min. After adsorption of an azo dye, electrolyte solution (AN-50: Solaronix Inc) was dropped on the titania electrode which was combined with a counter electrode glass covered with Pt.

Photovoltaic measurements of the DSCs thus fabricated were performed using a solar simulator

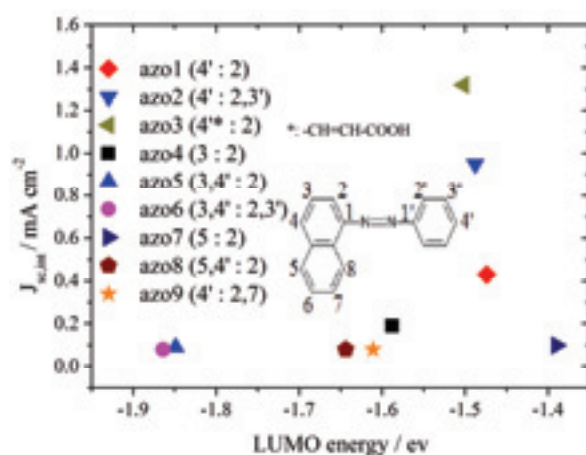


Fig. 1. Correlation between the experimental data of the short current density of DSCs and the theoretical LUMO energy levels of the solitary azo dyes. The positions of carboxylate and hydroxy groups are shown using the numbers before and after the semicolon in the parentheses, respectively.

equipped with a xenon lamp (Peccell Technologies, PEC-L11). Figure 1 shows a plot of the short current density $J_{SC,int}$ vs LUMO energy among 9 DSCs. The LUMO energies were estimated by using MOPAC7 for the semiempirical quantum chemistry program. There is a salient correlation between $J_{SC,int}$ and the LUMO energies, that is, the three dyes with the LUMO energies of ca. -1.5eV give higher $J_{SC,int}$ than the other dyes having the energies of < -1.5 eV. This observation suggests that the performance of the present DSCs is dominated crucially by the quantum yield of the electron injection from the excited dyes. An only exception is DSC made of azo7 whose calculated LUMO level is as high as -1.390 eV. Explanation for the low-performance of the DSC with azo7 might be its possible incompatibility with AN-50. When homemade redox electrolyte solution was employed in place of AN-50, $J_{SC,int}$ for azo7 was found to be improved and become almost comparable with that for azo2.

The optical densities of dye molecules adsorbed on TiO₂ can be evaluated from $\log_{10}(I_{blank}/I_{cell})$, where I_{blank} and I_{cell} are the intensities of the transmitted BL7B synchrotron radiation through a blank cell and a DSC, respectively, in addition to the measurement of J_{sc} . The quantum yield Y_{inj} for electron injection from the excited dye to TiO₂ can be evaluated by using these data [3], and are shown in Fig. 2.

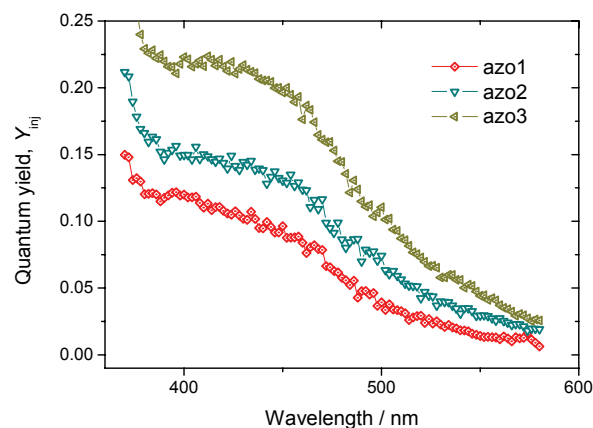


Fig. 2. Approximate quantum yields for electron injection from the excited level of the dyes.

[1] B. O'Regan and M. Grätzel, *Nature* **353** (1991) 737.

[2] Y. Ooyama and Y. Harima, *Eur. J. Org. Chem.* **2009** (2009) 2903.

[3] K. Nakajima, *et al.*, in the Proceedings of Pure and Applied Chemistry International Conference 2010 (PACCON 2010), Thailand, PTC-PO-19.

Local Environment Analysis of P Atoms in Proton-Conducting Amorphous Zirconium Phosphate Thin Films

Y. Aoki, K. Ogawa and H. Habazaki

Graduate School of Engineering, Hokkaido University, N13W8, Sapporo 060-8628, Japan

Previously, we reported that amorphous zirconium phosphate thin films exhibit the enhanced proton conductivity in nonhumidified atmosphere in the intermediate temperature range [1]. This superior conductivity is speculated to be related to the structure of phosphate groups. Here, we identify the phosphate species in amorphous zirconium phosphate thin film by P L-edge XAS.

The amorphous zirconium phosphate, α -ZrP_{2.5}O_x, films were prepared on an ITO substrate (Aldrich) by multiple spin-coating of precursor solutions of tetrabutoxyzirconium (Zr(O^tBu)₄) (Kanto) and phosphorous oxide (P₂O₅) (Kanto) at the Zr/P atomic ratio of 1/3. The details of the procedure were described elsewhere [1]. The metal concentration (Zr+P) in the precursor mixture sol was adjusted in 50 mM. The precursor sols were spin-coated onto the ITO substrate at 3000 rpm for 40 sec by a Mikasa 1H-D7 spin coater. The deposited gel layer was hydrolyzed by blowing hot air for 30 sec (Iuchi hot gun), and the substrate was cooled to room temperature by blowing cold air for 20 sec. These cycles of spin-coating, hydrolysis and cooling were repeated 10-20 times and the gel film thus obtained was calcined at 400°C for 30 min. The combination of deposition and calcination was repeated more than 3 times, and the final calcination was performed at 450°C for 2 h. The hydrated films were prepared by heating them at 450°C for 12 h in H₂O/air ($p_{\text{H}_2\text{O}} = 4.2$ kPa).

P L-edge XAS spectroscopy was carried out with α -ZrP_{2.5}O_x films of 40 nm, 55 nm, 100 nm and 300 nm-thickness (Figure 1). It is reported that P L-edge spectra of inorganic phosphate salts is very sensitive to the polymerization degree, n , of phosphate group P_nO_{3n+1}[2]. Here, the Zr(HPO₄)₂ was used as a reference material of orthophosphate configuration and ZrP₂O₇ as that of pyrophosphate configuration, respectively. The P L-edge spectra of zirconium phosphates was composed of the several peaks in agreement with those of the other phosphate compounds, which are assigned largely to the transition from P core level to unoccupied states. Peaks C and C' appear at around 139 eV and 141 eV, respectively, and are assigned to the transition of P 2p electron to 3p-like t₂ states. Peak D at around 148 eV is attributed to the transition 3d-like e states. Peak A is assigned to the transition of P 2p electron to 3s-like a₁ states and splits into two peaks of A' and A by spin-orbit interaction of P 2p orbitals. Yin et al reported that the peaks A and A' in P L-edge spectra rapidly shift to high energy from orthophosphate to pyrophosphate to metaphosphate and peak A of

Na₃PO₄, Na₄P₂O₇ and Na₅P₃O₁₀ appears at 135.35, 135.85 and 135.96 eV, respectively [2]. Peak A' in zirconium phosphates is very weak to appear as a shoulder. Peak A appears at 136.3 eV for ZrH₂(PO₄)₂ and at 136.7 eV for ZrP₂O₇. P L-edge spectra of dry α -ZrP_{2.5}O_x films are very similar for all thicknesses and the peak A appears at 136.8 ± 0.07 eV. This value is very close to the peak A of ZrP₂O₇. Furthermore, the spectral features of hydrated α -ZrP_{2.5}O_x films are almost same as those of the dry films. These results indicate that the pyrophosphate is predominant form of phosphate group in the films even though they are as-prepared or hydrated at elevated temperatures.

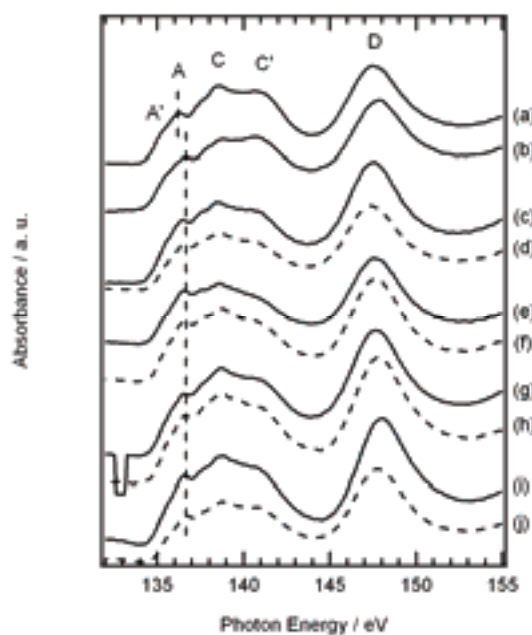


Fig. 1. P L-edge XANES spectra of (a) Zr(HPO₄)₂ and (b) ZrP₂O₇, and amorphous ZrP_{2.5}O_x films with thickness of (c), (d) 40 nm, (e), (f) 55 nm, (g), (h) 100 nm and (i), (j) 300 nm. Solid line indicates as-prepared film and dashed line hydrated film.

[1] Y. Li *et al.*, Adv. Mater. **20** (2008) 2398.

[2] Z. Yin *et al.*, Phys. Rev. B **51** (1995) 742.

N K-Edge XANES Analysis of Nitrogen Doped TiO₂ Photocatalyst

T. Yoshida¹, S. Muto¹ and E. Kuda²

¹*EcoTopia Science Institute, Nagoya University, Nagoya 464-8603, Japan*

²*Department of Materials, Physics and Energy Engineering, Nagoya University, Nagoya 464-8603, Japan*

Introduction

In the field of catalytic chemistry, a specific function in a solid catalyst crucially depends on the chemical state of a specific active component (active site). In this context X-ray absorption fine structure (XAFS) and electron energy loss spectroscopy (EELS) are expected as one of the most powerful techniques for chemical state analysis of the active site, because they provide information on the local structure and electronic states around the specific element of interest. The purpose of the present study is to examine the local chemical states of nitrogen injected into TiO₂ photocatalysis by means of a sophisticated combination of XAFS and EELS. The nitrogen doped TiO₂ has been attracting much attention due to its visible-light response to natural solar light.

Experimental

The samples used in this study were TiO₂ (1 0 0) single crystals (5 × 5 × 0.5 mm³), supplied by Furuuchi Kagaku, Japan. Mass analyzed 100 keV N₂⁺ ions (50 keV/N⁺ ion) were injected into the samples at room temperature, perpendicular to the sample surface. The N⁺ fluence ranged from 1 to 5 × 10²¹ m⁻². After the ion implantation, parts of the samples were heat-treated at 573 K for 2 hours in air.

N K-edge XANES spectra of the N⁺-implanted TiO₂ samples were measured at the BL-8B1 station of UVSOR-II at the Institute for Molecular Science, Okazaki, Japan. Data were recorded at room temperature in total electron yield mode, and the X-ray energy dependence of the N Auger electron yield was monitored.

EEL spectra were recorded with a Gatan ENFINA 1000 spectrometer attached to a JEM200CX TEM operated at 200 kV. The detecting system consists of a fiber-coupled YAG scintillator combined with a CCD of 1340 × 100 pixels.

Results and Discussion

The photocatalytic activity reached its maximum at a fluence of 3 × 10²¹ m⁻² and then decreased with the fluence. The sample implanted at a fluence of 5 × 10²¹ m⁻² followed by heat-treatment at 573 K was almost photocatalytically- inactive under visible-light irradiation.

Figure 1 (left) shows N K-edge XANES spectra of the N⁺-implanted TiO₂ samples and a TiN powder for reference. Common XANES features in (a) and (b) suggest that N in the sample implanted by 3 × 10²¹ m⁻² (highest active photocatalyst) is in a chemical environment similar to that in TiN. More thorough observation suggested that double-peak around 400

eV in (b) shifted to the lower energy side compared with that of TiN, which was well reproduced by the theoretical prediction using FEFF code when N occupies one of the O sites of TiO₂. On the other hand, the XANES spectrum of the sample implanted with the N⁺ fluence of 5 × 10²¹ m⁻² followed by heat-treatment (almost inactive to visible-light) shows a distinct single peak around 401 eV (Fig. 1c). This peak could be empirically attributed to formation of molecular species such as N–O bonds near the surface.

Figure 1 (right) shows extracted depth-resolved profiles of the N K-edge ELNES of the samples implanted with the N⁺ fluence of 3 × 10²¹ m⁻². The double-peak structure around 398–401 eV was again observed near the surface region, and the distinct single peak around 401 eV gradually grows with increasing the depth, which reflects the different chemical states of nitrogen, presumably depending on the local N concentration. The double-peak structure near the surface region is in good agreement with the XANES spectrum of the same sample, indicating that N atoms replacing the O sites in TiO₂ dominate up to about 25 nm from the surface. On the other hand the single peak around 401 eV for the deeper regions was observed both in XANES (Fig. 1, c) and ELNES over the entire implanted region of the catalytically inactive sample (the sample implanted at the fluence of 5 × 10²¹ m⁻², followed by heat-treated at 573 K). Considering that the photocatalytic reactions predominate near the surface, the visible-light responsive property should be closely related to the double-peak structure in the XANES/ELNES. Thus, we confirmed that substitutional N at O sites is essential for visible-light responsive photocatalytic activity.

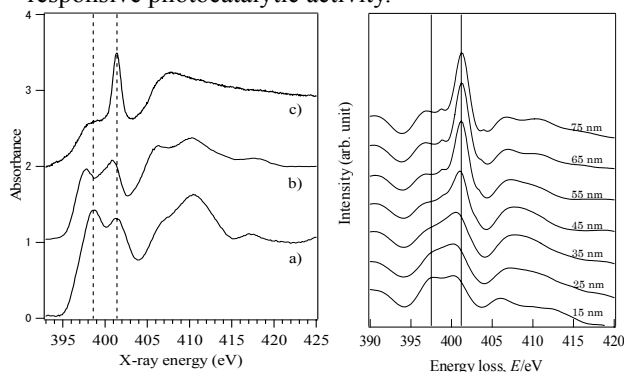


Fig. 1. (left) N K-edge XANES spectra of a TiN(a), N⁺-implanted at 3 × 10²¹ m⁻²(b) and 5 × 10²¹ m⁻² followed by heating at 573 K for 2 h(c), (right) Depth-resolved N K-edge ELNES of photocatalytic active sample, N⁺-implanted with fluence of 3 × 10²¹ m⁻². The numbers inset indicate the depths from the surface.

Photoemission Studies on a Neutral Radical Molecular Crystal of a Tetrathiafulvalene-Based Nitronyl Nitroxide

Y. Nakayama¹, S. Machida², Y. Noguchi^{1,2}, H. Ishii^{1,2},
H. Komatsu³, M. M. Matsushita^{3†} and T. Sugawara³

¹Center for Frontier Science, Chiba University, Chiba 263-8522, Japan

²Graduate School of Advanced Integration Science, Chiba University, Chiba 263-8522, Japan

³Graduate School of Arts and Sciences, The University of Tokyo, Tokyo 153-8902, Japan

Spintronics is a key issue for the next-generation device applications also in the organic electronics field. Requisite materials as a building block of organic spintronics devices are neutral radicals that manifest interactive conductivity and magnetism upon carrier injection. Recently, a neutral radical crystal of 2-[2-(4,5-dibromo-[1,3]dithiol-2-ylidene)-1,3-benzodithiol-5-yl]-4,4,5,5-tetramethylimidazoline-3-oxide-1-oxyl [BTBN; Fig. 1(a)] was synthesized, and the magnetoresistance and narrow-gap semiconducting behavior were discovered on it [1].

In the present study, we conducted the photoelectron spectroscopy (PES) measurements on the BTBN crystals to elucidate the electronic structure of this novel candidate for organic spintronics application.

Needle-like BTBN crystals were produced by electrocrystallization and aligned onto a conductive carbon tape pasted on a polycrystalline Au substrate [Fig. 1(b)]. The both ends of the needles were then bounded by silver paste to ensure good electrical contact. PES measurements were carried out at BL8B2 in UVSOR. During PES measurements, the crystals were illuminated by a violet (405 nm) laser and were biased at +5 V to cancel sample charging that has prevented one from obtaining reliable PES spectra on organic semiconducting crystals [2, 3]. In order to verify the PES results, photoelectron yield spectroscopy (PYS) [4] was also conducted to determine the ionization energy of the BTBN crystal.

Figure 1(d) shows a PES spectrum of the BTBN crystals. The spectral shape looks consistent to the quantum chemical calculation results [Fig. 1(c)], which suggests successful relief of sample charging. The lowest binding energy (BE) component can be assigned to the highest occupied and singly occupied molecular orbitals (HOMO and SOMO). As shown in Fig. 2(a), the carbon tape did not contribute on the PES spectra near the Fermi level. The edge of the lowest BE component is estimated to be 0.5 eV beneath the Fermi level from a line fitting of the peak onset. It corresponds to the ionization energy of 4.85 eV, which is in good accordance to the PYS result. However, by a close look around the Fermi level, one can find a slight tailing further above the HOMO edge [Fig. 2(b)]. This feature also appeared on the PYS spectra. The onset of the tail reached BE \sim 0.1 eV, and it may be an origin of reported sufficient hole

injection even at low temperature [1].

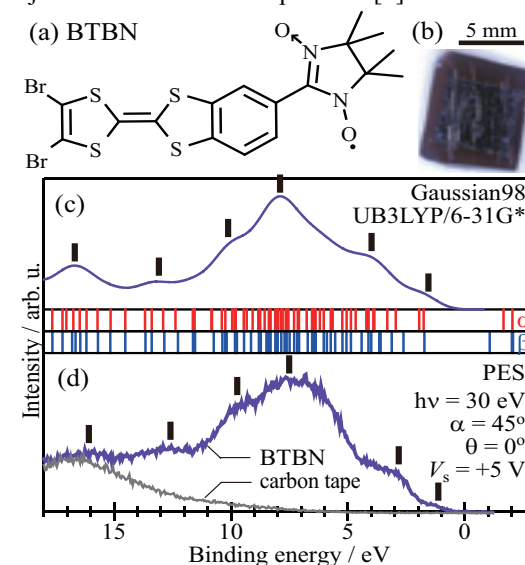


Fig. 1. (a) The chemical structure of BTBN. (b) A photograph of the sample. (c) The “density of states (DOS)” curve obtained by convoluting the molecular orbital energies (vertical bars) with a Gaussian function (FWHM of 1.5 eV). (d) PES spectra of the BTBN crystals and the carbon tape.

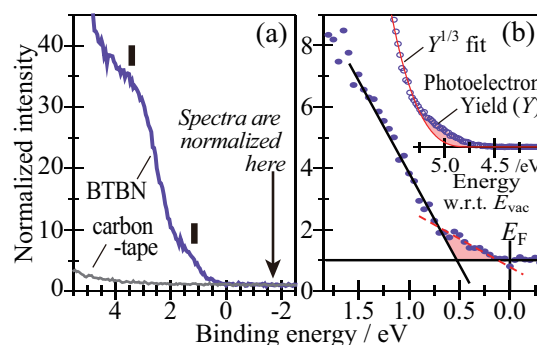


Fig. 2. (a) Magnified PES spectra. (b) PES and PYS spectra of the BTBN crystals.

[†] Present address: Dept. of Chemistry and Research Center for Materials Science, Nagoya University.

[1] H. Komatsu, *et al.*, *J. Am. Chem. Soc.* in press.

[2] Y. Nakayama, *et al.*, *UVSOR Activity Report 2008 (2009) 70.*

[3] S. Machida, *et al.*, *Phys. Rev. Lett.* in press.

[4] Y. Nakayama, *et al.*, *Appl. Phys. Lett.* 92 (2008) 153306.

Hole Injection Barriers at Organic Hetero-Interfaces in Organic Light-Emitting Diodes

Y. Miyazaki¹, S. Machida¹, Y. Nakayama², Y. Noguchi^{1,2} and H. Ishii^{1,2}

¹Graduate School of Advanced Integration Science, Chiba University, Chiba 263-8522, Japan

²Center for Frontier Science, Chiba University, Chiba 263-8522, Japan

Organic light-emitting diodes (OLEDs) usually have two or more organic layers sandwiched by metal electrodes. At organic hetero-interfaces, carrier accumulation properties play an important role in the device performance, such as the confinement of charge recombination region, providing balanced carriers, and device degradation processes [1-3]. To reveal carrier accumulation mechanisms, we have been investigated this process at various interfaces by using displacement current measurement(DCM) [4, 5].

Carrier injection barriers are a key factor for the carrier accumulation mechanisms. Therefore, it is essential to investigate energy level alignments at interfaces and to know carrier injection barriers. In this study, we investigated energy level alignments by ultraviolet photoelectron spectroscopy (UPS) at 1,3,5-tri(phenyl-2-benzimidazole)-benzene (TPBi), 1,3-Bis[2-(4-tert-butylphenyl)-1,3,4-oxadiazole-5-yl]benzene(OXD-7) and *p*-bis (triphenylsilyl) benzene (UGH2) on 4,4'-bis[*N*-(1-naphthyl)-*N*-phenylamino]-biphenyl(α -NPD) interfaces. Figure 1 shows chemical structures of these materials.

UPS measurement was performed at BL8B2 in UVSOR. Au covered SiO₂ wafers were used as substrates. At first, an α -NPD thin film(10nm) was formed by vacuum deposition on the substrate. Then TPBi, OXD-7 or UGH2 layer was deposited gradually onto the α -NPD film.

Figure 2 shows UPS spectra of TPBi on a α -NPD film. When 6 nm-TPBi was deposited, HOMO peak derived from α -NPD was completely disappeared. Further increase of the TPBi thickness did not change the spectral shape. From the offset of the HOMO edges between 20 nm TPBi and bare α -NPD film, the hole injection barrier is estimated as 1.3 eV. The hole injection barriers at α -NPD/OXD-7 and α -NPD/UGH2 interfaces were estimated as 1.3 eV and 2.0 eV, respectively, in the same manner as the α -NPD/TPBi system. Together with the DCM results, we are now trying to figure out how the observed injection barriers affect electrical behaviors in the actual devices.

[1] J. C. Scott *et al.*, J. Appl. Phys. **89** (2001) 4575.

[2] H. Aziz *et al.*, Science. **283** (1999) 1900.

[3] D. Y. Kondakov *et al.*, J. Appl. Phys. **93** (2003) 1108.

[4] S. Egusa *et al.*, J. Jpn. Appl. Phys. **33** (1994) 2741.

[5] Y. Noguchi *et al.*, Appl. Phys. Lett. **92** (2008) 203306.

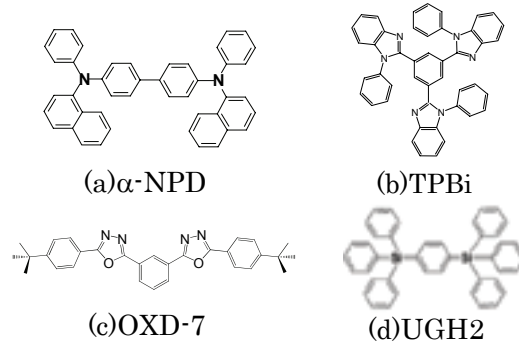


Fig. 1. Molecular structures of materials used in this study.

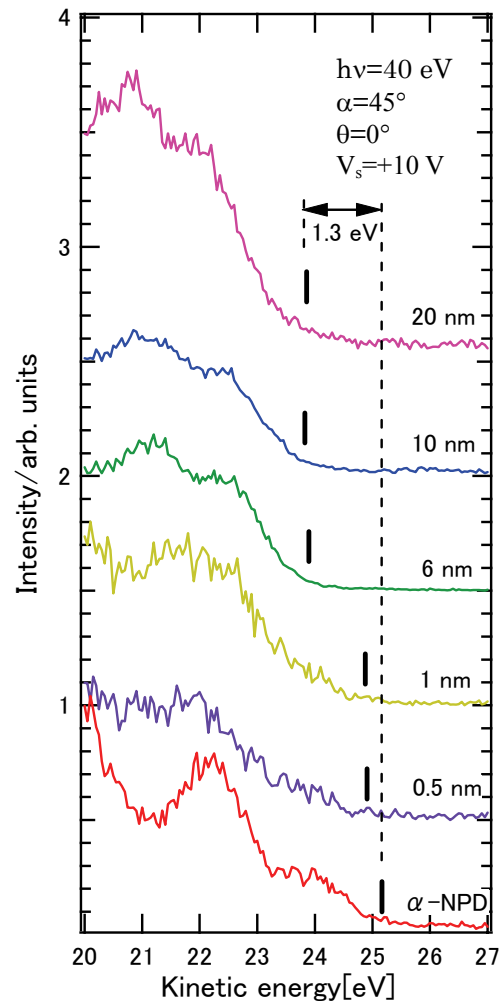


Fig. 2. UPS spectra of TPBi on α -NPD.

List of Publications

- Y. Aoki, H. Habazaki and T. Kunitake, “**Size-Scaling of Proton Conductivity in Amorphous Aluminosilicate Acid Thin Films**”, *J. Am. Chem. Soc.* **131** (2009) 14399.
- H. Aritani, H. Shibasaki, H. Orihara and A. Nakahira, “**Methane Dehydroaromatization over Mo-Modified H-MFI for Gas to Liquid Catalysts**”, *J. Environ. Sci.* **21** (2009) 736.
- T. Awano and T. Takahashi, “**Far-Infrared and Millimeter Wave Spectroscopy of Halides-Doped Silver Phosphate Glasses**”, *J. Phys. Soc. Jpn.* **79**, Suppl. A (2010) 118.
- C. Evain, C. Szwaj, S. Bielawski, M. Hosaka, A. Mochihashi, M. Katoh and M.-E. Couprie, “**Shifted Feedback Suppression of Turbulent Behavior in Advection-Diffusion Systems**”, *Phys. Rev. Lett.* **102** (2009) 134501.
- M. Fujita, M. Itoh, H. Mitani, Sangeeta and M. Tyagi, “**Exciton Transition and Electronic Structure of PbMoO₄ Crystals Studied by Polarized Light**”, *Phys. Status Solidi B* **247** (2010) 405.
- S. Hino, T. Miyazaki, Y. Aoki, N. Wanita, M. Kato, R. Sumii, T. Akachi, T. Inoue, Y. Ito, T. Sugai and H. Shinoh, “**Electronic Structure of Yttrium and Carbon Atoms Encapsulated Metallofullerenes, Y₂C₂@C₈₂: Ultraviolet Photoelectron Spectroscopy and Theoretical Calculation**”, *Bull. Chem. Soc. Jpn.* **82** (2009) 963.
- H. J. Im, T. Ito, S. Kimura, H.-D. Kim, J. B. Hong and Y. S. Kwon, “**Crystalline Electric Field Effects in Ce 3d Core-Level Spectra of Heavy-Fermion Systems: Hard X-Ray Photoemission Spectroscopy on CeNi_{1-x}Co_xGe₂**”, *Phys. Rev. B* **79** (2009) 193105.
- K. Kanai, H. Yoshida, Y. Noda, A. Iwasaki, R. Suizu, J. Tsutumi, H. Imabayashi, Y. Ouchi, N. Sato, K. Seki and K. Awaga, “**Electronic Structure of Disjoint Diradical 4,4'-bis(1,2,3,5-Dithiadiazolyl) Thin Films**”, *Phys. Chem. Chem. Phys.* **11** (2009) 11432.
- H. Katayanagi, B. P. Kafle, C. Huang, Md. S. I. Prodhon, H. Yagi and K. Mitsuke, “**Feasibility Study on the Mass-Selected Velocity Map Imaging of Polyatomic Molecules and Fullerenes**”, *PACCON* (2010) 0.
- H. S. Kato, R. Hirakawa, F. Yamauchi, M. Kawai, T. Hatsui and N. Kosugi, “**Electronic State Observation of Inner Organic Thin Films beneath Electrodes: Fluorescence-Yield X-Ray Absorption Spectra of Pentacene Derivative Films**”, *J. Electron Spectrosc. Relat. Phenom.* **174** (2009) 93.
- J. H. Kim, S. J. Kim, C. I. Lee, M. A. Jung, H. J. Oh, J.-S. Rhyee, Y. Jo, H. Mitani, H. Miyazaki, S. Kimura and Y. S. Kwon, “**Kondo-Like Behavior in Magnetic and Thermal Properties of Single-Crystal Tm₅Si₂Ge₂**”, *Phys. Rev. B* **81** (2010) 104401.
- S. Kimura, “**Origin of Infrared Peaks in the Optical Conductivity of Ytterbium Compounds**”, *Phys. Rev. B* **80** (2009) 073103.
- S. Kimura, T. Mizuno and T. Iizuka, “**Synchrotron Terahertz Spectroscopy of Solids under Extreme Conditions**”, *AIP Conf. Proc.* **1214** (2010) 71.
- M. Kitaura, N. Fujita, M. Itoh and H. Nakagawa, “**Origin of Photocarrier Traps in Photorefractive α -LiIO₃ Crystals by Optical Measurement and Cluster Calculation**”, *Phys. Rev. B* **73** (2006) 115110.
- M. Matsunami, H. Okamura, A. Ochiai and T. Nanba, “**Pressure Tuning of an Ionic Insulator into a Heavy Electron Metal: An Infrared Study**”, *Phys. Rev. Lett.* **103** (2009) 237202.
- H. Miyazaki, T. Ito, H. J. Im, K. Terashima, T. Iizuka, S. Yagi, M. Kato, K. Soda and S. Kimura, “**Change of Lattice Constant due to Hybridization Effect of a Ferromagnetic Semiconductor EuO**”, *J. Phys.: Conference Series* **200** (2010) 012124.
- H. Miyazaki, T. Ito, H. J. Im, S. Yagi, M. Kato, K. Soda and S. Kimura, “**Direct Observation of Momentum-Dependent Exchange Interaction in a Heisenberg Ferromagnet**”, *Phys. Rev. Lett.* **102** (2009) 227203.
- H. Miyazaki, T. Ito, H. Im, K. Terashima, S. Yagi, M. Kato, K. Soda and S. Kimura, “**Single Crystal Growth and Magnetic, Optical, and Photoelectrical Properties of EuO Thin Film**”, *Jpn. J. Appl. Phys.* **48** (2009) 055504.
- M. Nagasaka, T. Hatsui, T. Horigome, Y. Hamamura and N. Kosugi, “**Development of a Liquid Flow Cell to Measure Soft X-Ray Absorption in Transmission Mode: A Test for Liquid Water**”, *J. Electron Spectrosc. Relat. Phenom.* **177** (2010) 130.

- K. Nagashima, S. Nakamura, K. Okada, A. Nakahira and H. Aritani, **“Gallosilicate-Based Catalysts for NO_x-SCR with CH₄”**, Bull. Chem. Soc. Jpn. **82** (2009) 1203.
- K. Onodera, M. Koshimizu and K. Asai, **“Luminescent Properties of BaCl₂ under VUV Excitation”**, Radiat. Phys. Chem. **78** (2009) 1031.
- S. R. Park, W. S. Jung, Chul Kim, D. J. Song, C. Kim, S. Kimura, K. D. Lee and N. Hur, **“Quasiparticle Scattering and the Protected Nature of the Topological States in a Parent Topological Insulator Bi₂Se₃”**, Phys. Rev. B **81** (2010) 041405(R).
- M. Shimada, M. Katoh, M. Adachi, T. Tanikawa, S. Kimura, M. Hosaka, N. Yamamoto, Y. Takashima and T. Takahashi, **“Transverse-Longitudinal Coupling Effect in Laser Bunch Slicing”**, Phys. Rev. Lett. **103** (2009) 144802.
- T. Shishido, H. Asakura, S. Yamazoe, K. Teramura and T. Tanaka, **“Structural Analysis of Group V, VI, VII Metal Compounds by XAFS and DFT Calculation”**, J. Phys.: Conference Series **190** (2009) 012073.
- K. Soda, H. Miyazaki, K. Yamamoto, T. Mochizuki, M. Inukai, M. Kato and S. Yagi, **“Synchrotron Radiation Photoelectron Study of Heusler-Type Fe₂Va1-Based Alloys”**, Advances in Synchrotron Radiation **1** (2008) 235.
- M. Suzuki, S. Sawai, K. Fukui, K. Nagamatsu and H. Amano, **“Photoluminescence and Excitation Spectrum of Mg-Doped p-Type Al_xGa_{1-x}N”**, Phys. Stat. Sol. C **6** (2009) S759.
- Y. Takagi, K. Isami, I. Yamamoto, T. Nakagawa and T. Yokoyama, **“Structure and Magnetic Properties of Iron Nitride Thin Films on Cu(001)”**, Phys. Rev. B **81** (2010) 035422.
- J. Takahashi, H. Shinojima, M. Seyama, Y. Ueno, T. Kaneko, K. Kobayashi, H. Mita, M. Adachi, M. Hosaka and M. Katoh, **“Chirality Emergence in Thin Solid Films of Amino Acids by Polarized Light from Synchrotron Radiation and Free Electron Laser”**, Int. J. Mol. Sci. **10** (2009) 3044.
- H. Yagi, K. Nakajima, K. R. Koswattage, K. Nakagawa, H. Katayanagi and K. Mitsuke, **“Photoabsorption Cross Section of C₇₀ Thin Films from Visible to Vacuum Ultraviolet”**, J. Chem. Phys. **130** (2009) 234510.
- H. Yamane, K. Kanai, Y. Ouchi, N. Ueno and K. Seki, **“Impact of Interface Geometric Structure on Organic-Metal Interface Energetics and Subsequent Films Electronic Structure”**, J. Electron Spectrosc. Relat. Phenom. **174** (2009) 28.
- (in Japanese)
- Y. Iwai, K. Nakagawa, N. Miura, S. Matsumoto, R. Nakano and H. Matsumoto, **“Effect of Electrical Properties of Platinum Palladium Oxide Thin Films on the Optical Properties”**, J. Vac. Soc. Jpn. **52** (2009) 53.
- M. Kitaura, **“Improvement of Photoluminescence Properties in YPO₄:Mn²⁺ Phosphor Codoped with Tetravalent Cations”**, Journal of the Institute of Image Information and Television Engineers **63** (2009) 1418.
- H. Miyazaki and S. Kimura, **“Future Perspective on Rare-Earth Oxide Thin Films”**, KINOZAIRYOU **30** (2010) 55.
- K. Nakagawa, **“Role of Radiation on Chemical Evolution at the Universe”**, Viva Origino **37** (2009) 24.
- K. Nakagawa, N. Miura, S. Matsumoto, R. Nakano and H. Matsumoto, **“Preparation and Evaluation of WO₃-Bi₂O₃ Composite Thin Films”**, J. Vac. Soc. Jpn. **52** (2009) 49.
- H. Yamane, N. Ueno and K. Seki, **“Elucidation and Control of Electronic Properties Related to Organic Electronics”**, J. Jpn. Soc. Synchrotron Radiat. Res. **22** (2009) 192.

2nd International UVSOR Workshop on Low-Energy Photoemission of Solids using Synchrotron Radiation (LEPES09)

October 3rd - 4th, 2009 [A Satellite Meeting of ICES 11, Nara, Japan]

INVITED SPEAKERS

Donglai FENG

Hojun IM

Akihiro INO

Chengyoung KIM

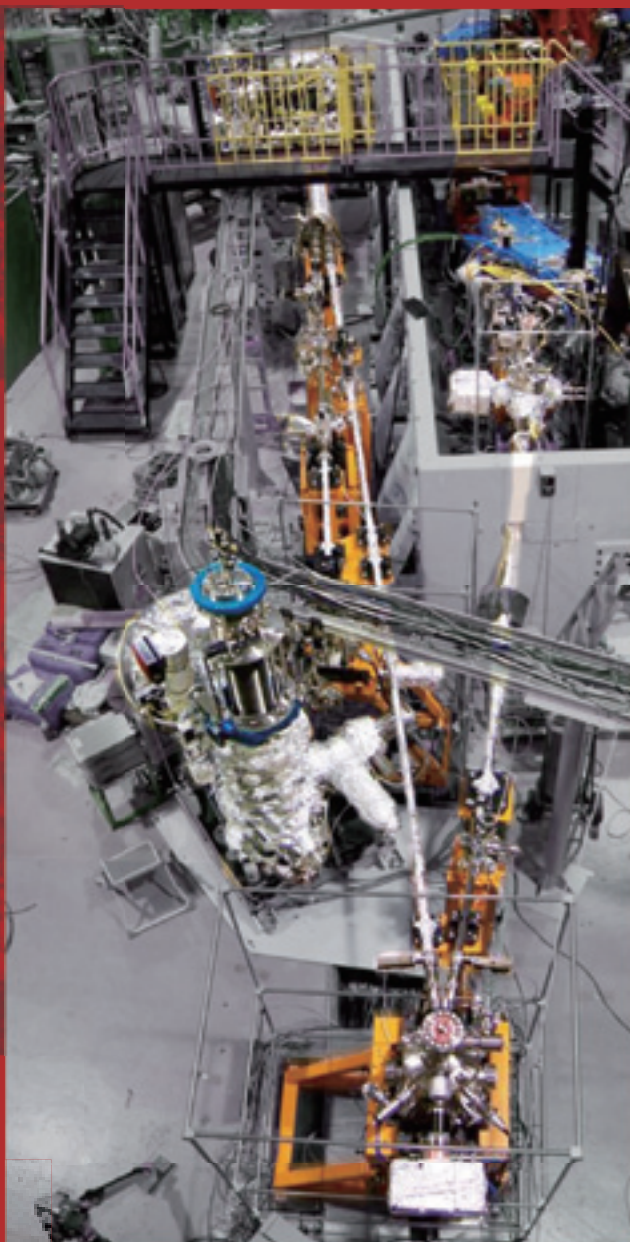
Takayuki KISS

Luca PETACCIA

Seigo SOUMA

Tsunehiro TAKEUCHI

Teppei YOSHIDA



UVSOR II
since 2003

PHOTOEMISSION SPECTROSCOPY OF SOLIDS
USING SYNCHROTRON RADIATION
RELATED SPECTROSCOPIC RESEARCH
OF LOW ENERGY ELECTRONIC STRUCTURE AND FERMILOGY
NEW INSTRUMENTS FOR PHOTOEMISSION SPECTROSCOPY
OF SOLIDS USING SYNCHROTRON RADIATION



Place:

Okazaki Conference Center, and UVSOR Facility,
Institute for Molecular Science

Contact Person:

Shin-ichi KIMURA [kimura@ims.ac.jp]

Program

October 3rd (Sat.)		
Place: Middle conference room (1st floor), Okazaki Conference Center, Okazaki, Japan		
15:00-	Registration.	
18:00-(20:00)	Get together party	
October 4th (Sun.)		
Place: Small conference room (2nd floor), Okazaki Conference Center		
9:00-9:10	S. Kimura (UVSOR)	Opening remark
1. Superconductors (Chair; T. Ito)		
9:10-9:35	D. Feng (Fudan Univ.)	Electronic structure of iron-based superconductors
9:35-10:00	T. Yoshida (Univ. Tokyo)	Two-gap behaviors of the high-T _c cuprate superconductors: Universal versus material-dependent properties
10:00-10:25	A. Ino (Hiroshima Univ.)	Low-energy ARPES study of novel multi-band superconductors at HiSOR
10:25-11:00	Coffee break + Group photo	
2. Oxides and theory (Chair; S. Suga)		
11:00-11:25	C. Kim (Yonsei Univ.)	Temperature dependent ARPES studies of Sr ₄ RuO ₄
11:25-11:50	L. Petaccia (Elettra)	Quasiparticles at the Mott transition in V ₂ O ₃ studied by bulk-sensitive VUV angle-resolved photoemission spectroscopy
11:50-12:15	K. Ji (KEK)	Quasiparticle dynamics and electron-phonon coupling in graphene
12:15-15:00	Lunch + Poster session + UVSOR site tour	
3. Functional materials (Chair; K. Soda)		
15:00-15:25	T. Takeuchi (Nagoya Univ.)	Role of coherent part and incoherent part in the electron transport properties of the materials characterized by strong electron correlation
15:25-15:50	H. J. Im (Hirosaki Univ.)	Systematic angle-resolved photoemission study of Ce-based heavy-fermion systems
15:50-16:15	T. V. Kuznetsova (Russian Academy of Science)	Electronic structure of CuIn ₅ Se ₈ studied by angle-resolved photoemission spectroscopy
16:15-16:45	Coffee break	
4. Low-energy PES using other sources (Chair; S. Kimura)		
16:45-17:10	T. Kiss (Univ. Tokyo)	Ultrahigh resolution laser-angle-resolved photoemission spectroscopy
17:10-17:35	S. Souma (Tohoku Univ.)	Development of bulk-sensitive spin-resolved ultrahigh-resolution photoemission spectrometer
17:35-	T. Ito (Nagoya Univ.)	Closing remark
18:30-(20:30)	Banquet at an Izakaya restaurant (Japanese pub)	
October 5th (Mon.)		
Move to Nara by public transportations.		

Poster presentation

01	K. Iwano (KEK)	Direct Domain Excitation by Photoemission and Its Dynamical Features Manifesting in ARPES spectra
02	Y. Takeichi (Univ. Tokyo)	Valence-band Electronic Structure of FeSi studied by high-resolution Angle-Resolved Photoelectron Spectroscopy (ARPES)
03	T. Hirahara (Univ. Tokyo)	A topological metal at the surface of an ultrathin BiSb alloy film
04	K. Soda (Nagoya Univ.)	Electronic Structure of Pseudo-one Dimensional $\text{Ba}_3\text{Co}_2\text{O}_6(\text{CO}_3)_{0.7}$
05	M. Imamura (Kobe Univ.)	Surface Chemistry of Butyl-Passivated Silicon Nanoparticles Studied by Synchrotron-Radiation Photoelectron Spectroscopy
06	K. Nakayama (Tohoku Univ.)	Low-energy angle-resolved photoemission spectroscopy of Fe-based high-Tc superconductor $\text{Ba}_{1-x}\text{K}_x\text{Fe}_2\text{As}_2$
07	T. Nakagawa (IMS)	Magnetic Circular Dichroism in Valence Band using Laser Excitation
08	J. Onoe (Tokyo Inst. Tech.)	In situ photoelectron spectra of an electron-beam irradiated C_{60} film
09	Y. Miyata (Ritsumeikan Univ.)	Electronic structure of $\text{Mn}_3\text{Cu}_{1-x}\text{Ga}_x\text{N}$ studied by soft X-ray photoelectron spectroscopy
10	V. I. Grebennikov (Russian Academy of Science)	"L+1 rule" for continuous electron-hole excitations in photoemission spectra
11	A. Sekiyama (Osaka Univ.)	Temperature and substitution dependence of extremely low-energy photoemission spectra on $\text{Sm}_{1-x}\text{Eu}_x\text{B}_6$
12	A. Taleb-Ibrahimi (SOLEIL)	ARPES and spin resolved Investigations on the 8-1500 eV high resolution Cassiopee beamline at SOLEIL
13	H. Miyazaki (UVSOR)	Temperature Dependent Angle-Resolved Photoemission Spectroscopy on Ferromagnetic EuO Thin Films
14	T. Ito (Nagoya Univ.)	Present status of VUV angle-resolved photoemission beamline BL7U at UVSOR-II
15	T. Ito (Nagoya Univ.)	Improvement of the SGM-TRAIN monochromator at UVSOR-II BL5U for low excitation-energy photoemission
16	M. Sakai (UVSOR)	Development of Integrated Software for Beamline Control for Photoemission Beamlines at UVSOR-II

Electronic structure of iron-based superconductors

Donglai Feng

Department of Physics, Fudan University, Shanghai, 200433, China

Iron based superconductors have ignited another round of intensive research on high temperature superconductivity. The electronic structure measured by angle resolved photoemission spectroscopy provides crucial information on the microscopic nature of this new class of superconductors.

In this talk I will discuss some of our recent works in this area.

(1) Multiple orbitals are considered a key feature of this new class of superconductors. With polarization-dependent photoemission and matrix element analysis, we were able to identify the orbital nature of various bands in the superconducting $\text{BaFe}_{2-x}\text{Co}_x\text{As}_2$ and $\text{FeTe}_x\text{Se}_{1-x}$ systems. Our results are rather different from the LDA calculations, indicative strong correlation effects.

(2) Anomalous band splittings in the spin density wave (SDW) state of the parent compounds have been observed, which leads to a novel SDW mechanism that does not require Fermi surface nesting in these materials.

(3) The isotropic superconducting gap around individual Fermi surfaces of $\text{Ba}_{1-x}\text{K}_x\text{Fe}_2\text{As}_2$ has been examined with various photon energies that sample different k_z 's.

[1] L. X. Yang et al. Phys. Rev. Lett. **102**, 107002 (2009).

[2] Y. Zhang et al. Phys. Rev. Lett. **102**, 127003 (2009).

[3] Y. Zhang et al. arXiv: cond-mat/0904.4022 (2009)

Two-gap behaviors of the high- T_c cuprate superconductors: Universal versus material-dependent properties

T. Yoshida¹, M. Hashimoto¹, K. Tanaka², N. Mannella², Z. Hussain³, Z.-X. Shen²,
A. Fujimori¹, M. Kubota⁴, K. Ono⁴, S. Komiya⁵, Y. Ando⁶, H. Eisaki⁷, S. Uchida¹

¹ *Department of Physics, University of Tokyo, Bunkyo-ku, Tokyo 113-0033, Japan*

² *Department of Applied Physics and Stanford Synchrotron Radiation Laboratory, Stanford University, Stanford, CA94305*

³ *Advanced Light Source, Lawrence Berkeley National Lab, Berkeley, CA 94720, USA*

⁴ *Photon Factory, Institute of Materials Structure Science, KEK, Tsukuba, Ibaraki 305-0801, Japan*

⁵ *Central Research Institute of Electric Power Industry, Komae, Tokyo 201-8511, Japan*

⁶ *The Institute of Scientific and Industrial Research, Osaka University, Ibaraki, Osaka 567-0047, Japan*

⁷ *National Institute of Advanced Industrial Science and Technology, Tsukuba 305-8568, Japan*

One of the central issues in the research of the high- T_c cuprates superconductors is whether the pseudogap is a distinct phenomenon from superconductivity or a gap due to local pairing or incoherent superconducting fluctuations above T_c . In the former scenario, a possible origin of the pseudogap is preformed Cooper pairs lacking phase coherence. In the latter scenario, the pseudogap is due to a competing order such as spin density wave, charge density wave, d-density wave, etc. It has been well known that the pseudogap in the anti-nodal ($\pi, 0$) region increases with underdoping as observed by angle-resolved photoemission spectroscopy (ARPES). However, the energy gap measured by other experimental methods such as Andreev reflection, which is more directly associated with superconductivity, exhibits opposite trend, that is, the gap decreases with underdoping, suggesting a different origin of the superconducting gap from the antinodal gap.

A recent ARPES study of $\text{Bi}_2\text{Sr}_2\text{Ca}_{1-x}\text{Y}_x\text{Cu}_2\text{O}_8$ (Bi2212) has revealed the presence of two distinct energy gaps in different regions of momentum space [1,2]. One is the antinodal region as mentioned above, and increases with underdoping. The other opens in the near-nodal region showing a coherent peak, and does not increase with underdoping. On the other hand, attempts have been made to understand the pseudogap within a single d -wave energy gap [3]. In such a single gap picture, preformed Cooper pairs are the most likely origin of the pseudogap.

Since the doping and temperature dependences of the energy gap would reveal the entangled two-gap behavior, we have investigated the energy gap of lightly- to optimally-doped LSCO by ARPES as a function of doping and temperature. In the present work, the momentum dependence of the gap clearly exhibits two-gap behavior as in the case of heavily underdoped Bi2212: the pseudogap Δ^* in the antinodal region and the d -wave like gap Δ_0 around

the node (Fig. 1). The doping dependence of the obtained parameter Δ_0 qualitatively explains the reduction of the T_c with underdoping. Furthermore, from comparison of the present results with those on Bi2212 and other cuprates with higher T_c 's, we have found that the magnitude of the Δ^* and the pseudogap temperature T^* is not appreciably material-dependent, suggesting that the pseudogap is properties of a single CuO_2 plane. On the other hand, the magnitude of the Δ_0 , which is proportional to the superconducting gap, is strongly material-dependent (CuO_2 layer number dependent) like T_c , suggesting that they are influenced by the effect of neighboring CuO_2 planes and block layers.

References

- [1] K. Tanaka *et al.*, *Science* **314**, 1910 (2006).
- [2] W. S. Lee *et al.*, *Nature* **450**, 81 (2007).
- [3] A. Kanigel *et al.*, *Nature Physics* **2**, 447 (2006)

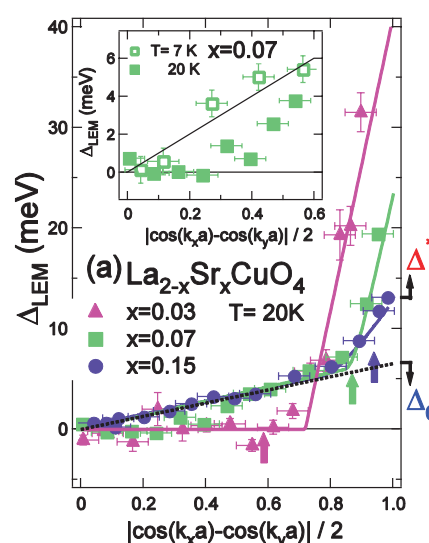


Fig. 1. Angular dependence of the gap of LSCO observed by ARPES. The definition of Δ^* and Δ_0 is shown for $x=0.15$.

Low-energy ARPES study of novel multi-band superconductors at HiSOR

A. Ino¹¹Graduate School of Science, Hiroshima University, Higashi-Hiroshima 739-8526, Japan

For understanding the mechanism of novel high-T_c superconductivity, the resolution of multiple sheets of Fermi surfaces is important issue. In bilayer cuprates, which are empirically known to have higher T_c than single-layered systems, two sheets of Fermi surfaces are present in close proximity due to small hybridization between two adjacent CuO₂ layers. In iron-based superconductors, all of five Fe 3d orbitals are responsible for low-energy electronic states, and more than three sheets of Fermi surfaces have been observed so far.

Using low-energy synchrotron radiation as the excitation photons of angle-resolved photoemission (ARPES), in general, the momentum- and energy-resolution become higher, the probing depth increases, and the perpendicular-momentum selectivity increases.

Bilayer cuprate, Bi₂Sr₂CaCu₂O_{8+δ} (Bi2212), has been studied by low-energy ARPES. We have found that the spectral-intensity ratio of a bonding band to an antibonding band drastically changes from 0% to 70% as a function of excitation photon energy due to the effect of transition matrix elements, and thus resolved the quasiparticle properties of two bilayer states. The nodal scattering rate is higher for antibonding band than for the bonding band in superconducting phase, indicating that the quasiparticles are scattered by the inhomogeneity of the potential from out-of-plane dopant oxygens. The magnitude of the superconducting gap is almost identical between the bonding and antibonding bands as shown in Fig. 1. With decreasing hole concentration, near-nodal superconducting gap region shrinks in momentum space for both of the bilayer bands. The width of bilayer splitting is narrower for the underdoped sample, showing the increase in two-dimensionality of electronic structure. This result is consistent with transport experiments.

Iron-based system, BaFe₂As₂ has been studied by a combination of low-energy ARPES at BL9A and polarization-dependent ARPES at BL1 in HiSOR. The orbital characters of low-energy bands have been determined from perpendicular-momentum dependence and polarization dependence. As shown in Fig. 2, the inner Fermi surface around Γ -Z axis shows strong dispersion in k_z direction, so that the Fermi-surface nesting is weak for the undoped material. Our results show that the top of this hole pocket comes down below the Fermi level at $k_z=0$, and that even- and odd-parity bands are degenerate at Γ point. Therefore, the inner Fermi surface is attributed to d_{xz} and d_{yz} orbitals.

This work was done in collaboration with H. Anzai, T. Fujita, Y. Nakashima, G. Hara, M. Arita, H. Namatame, M. Taniguchi, A. Fujimori, Z.-X. Shen, M. Ishikado, K. Fujita, S. Uchida, K. Kihou, C. H. Lee, H. Eisaki, A. Iyo, H. Kito, I. Hase, Y. Aiura.

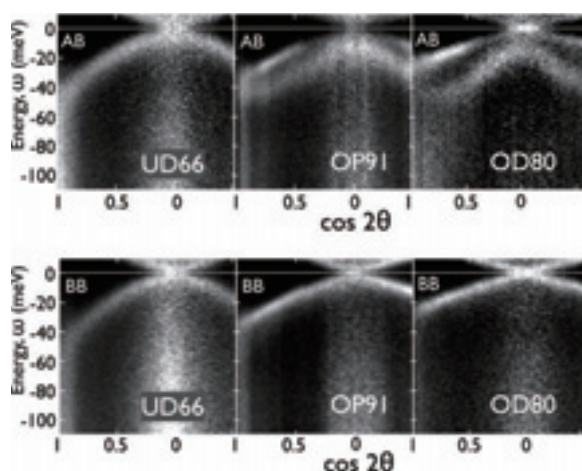


Fig. 1. ARPES spectral image taken along the antibonding-band (AB) and bonding-band (BB) Fermi surfaces of Bi₂Sr₂CaCu₂O_{8+δ} in superconducting phase (T = 10 K).

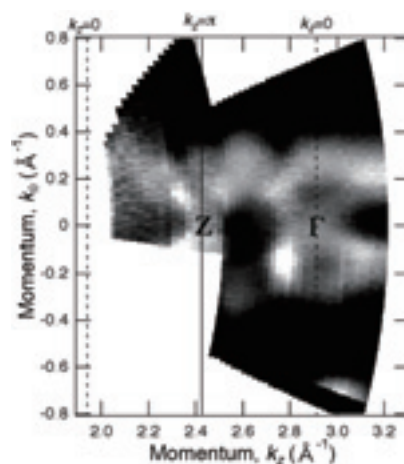


Fig. 2. ARPES spectral image taken along Γ -Z axis, a direction perpendicular to surface, for BaFe₂As₂.

Temperature dependent ARPES studies of Sr₂RuO₄

Chul Kim^{1*}, S. R. Park¹, C. S. Leem¹, D. J. Song¹, Y. K. Kim¹, S. K. Choi¹, W. S. Jung¹, Y. Y. Ko¹, H. Y. Choi¹, W. S. Kyung¹, G. R. Han¹, Y. Yoshida², R. G. Moore³, C. Kim¹

¹ Institute of Physics and Applied Physics, Yonsei University, Korea

² Nanoelectronics Research Institute, National Institute of Advanced Industrial Science and Technology, Japan

³ Stanford Synchrotron Radiation Lightsource, SLAC National Accelerator Laboratory, USA

Discovery of spin triplet superconductivity in Sr₂RuO₄ brought attention to the electronic structure studies on the system, especially by using angle resolved photoemission (ARPES). There are three bands that cross the Fermi level. The system is particularly interesting because these bands have different orbitals with different characters such as dimensionality. Along the way, it was found that there are surface states due to RuO₆ octahedral rotation on the surface layer, which results in a dramatic change in the electronic structure.

So far, only static properties of Sr₂RuO₄ have been studied by ARPES. To investigate the dynamic properties of Sr₂RuO₄ in the electronic structure, we have performed temperature dependent ARPES studies on Sr₂RuO₄ as well as LEED IV experiments. We found that there is very strong temperature dependence in the surface electronic structures. While 10K data show very strong surface states, raising temperature practically kills the surface state signal (figure 1). Surprisingly, the states are recovered when the samples are cooled back down to lower temperature.

To investigate the possible role of the structural change, we performed temperature dependent LEED IV experiment. The indication is that there is not much structural change in the surface atomic structure. This suggest that disappearance of the surface ARPES signal comes from dynamic fluctuation in the octahedral rotation. We will discuss the result in terms of possible quantum critical point.

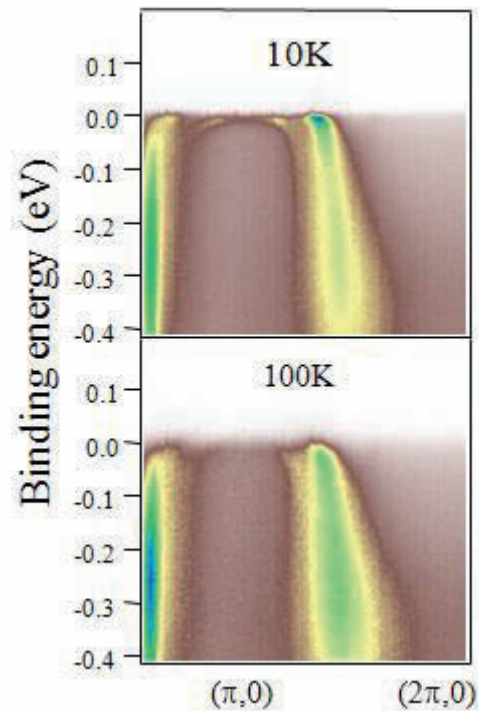


Fig. 1. Temperature dependent ARPES data from Sr₂RuO₄. The flat band near ($\pi,0$) is from the surface states.

Quasiparticles at the Mott transition in V_2O_3 studied by bulk-sensitive VUV angle-resolved photoemission spectroscopy

L. Petaccia¹, F. Rodolakis^{2,3}, B. Mansart², E. Papalazarou⁴, S. Gorovikov¹, P. Vilmercati¹, A. Goldoni¹, J. P. Rueff³, S. Lupi⁵, P. Metcalf⁶ and M. Marsi²

¹*Sincrotrone Trieste S.C.p.A., Strada Statale 14 Km 163.5, I-34149 Trieste, Italy*

²*Laboratoire de Physique des Solides, CNRS-UMR 8502, Université Paris-Sud, F-91405 Orsay, France*

³*Synchrotron SOLEIL, L'Orme des merisiers, Saint-Aubin BP 48, F-91192 Gif-sur-Yvette, France*

⁴*Laboratoire d'Optique Appliquée, ENSTA–Ecole Polytechnique, F-91761 Palaiseau, France*

⁵*CNR-INFN COHERENTIA and Dipartimento di Fisica, Università di Roma “La Sapienza”, Piazzale Aldo Moro 2, I-00185 Roma, Italy*

⁶*Department of Chemistry, Purdue University, West Lafayette, Indiana 47907, USA*

Understanding the electronic properties of quasiparticles in strongly correlated materials is the key to answer many important open questions in condensed matter physics. Angle resolved photoemission spectroscopy (ARPES) is one of the main experimental techniques to study this problem, but its intrinsic surface sensitivity often turns out to be a problem for the fermiology of coherent electronic states.

The BaD EIPh beamline at the Elettra synchrotron light source was constructed to perform ARPES at low photon energy, thus in a more bulk sensitive way, in conditions of high flux and high energy resolution [1]. These characteristics were exploited to explore the electronic properties of the prototype Mott compound V_2O_3 .

We found that spectral features corresponding to the quasiparticle peak in the metallic phase present a marked wave vector dependence, with a stronger intensity along the ΓZ direction. The analysis of their intensity for different probing depths shows the existence of a characteristic length scale for the attenuation of coherent electronic excitations at the surface. This length scale, which is larger than the thickness of the surface region as normally defined for noncorrelated electronic states, is found to increase when approaching the Mott transition [2]. These results are in agreement with the behavior of quasiparticles at surfaces as predicted by a very recent theoretical work [3], and appear to be of general interest also for other strongly correlated materials [4].

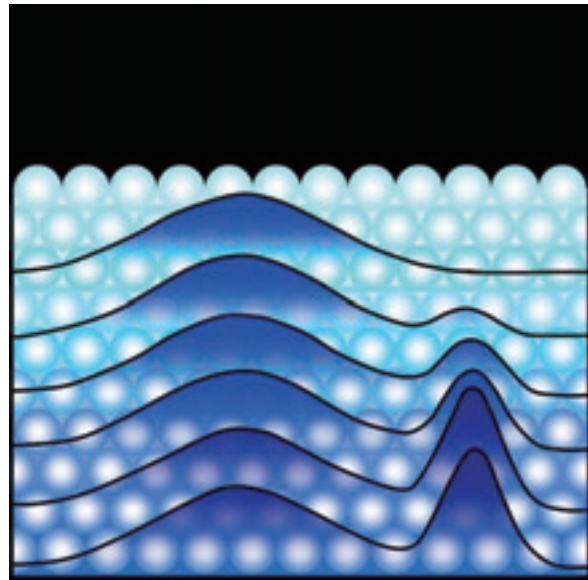


Fig. 1. In the V_2O_3 prototype Mott compound an insulating layer is present in a region near the surface even when the bulk is still a metal [4].

- [1] L. Petaccia, P. Vilmercati, S. Gorovikov, M. Barnaba, A. Bianco, D. Cocco, C. Masciovecchio and A. Goldoni, Nucl. Instr. and Meth. A **606** (2009) 780.
 [2] F. Rodolakis, B. Mansart, E. Papalazarou, S. Gorovikov, P. Vilmercati, L. Petaccia, A. Goldoni, J. P. Rueff, S. Lupi, P. Metcalf and M. Marsi, Phys. Rev. Lett. **102** (2009) 066805.
 [3] G. Borghi, M. Fabrizio and E. Tosatti, Phys. Rev. Lett. **102** (2009) 066806.
 [4] Synopsis in “Physics”:
<http://physics.aps.org/synopsis-for/10.1103/PhysRevLett.102.066805>

Quasiparticle dynamics and electron-phonon coupling in graphene

K. Ji, K. Iwano and K. Nasu

*Solid State Theory Division, Institute of Materials Structure Science, KEK
Graduate University for Advanced Studies, Oho 1-1, Tsukuba, Ibaraki 305-0801, Japan*

Graphene and graphite are important mother systems for carbon-based materials such as carbon nanotube and fullerene. Insight into these materials to understand the role of electron-phonon (e-ph) interaction has been attracting considerable research interests. Recently, experiments of high resolution angle-resolved photoemission spectroscopy (ARPES) are performed on graphite, and a sharp quasiparticle (QP) peak is observed at the Fermi surface (E_F). However, up to now, it is still puzzling and controversial that whether this sharp QP peak is due to a strong e-ph interaction or not [1,2].

In order to reveal the nature of this QP peak, we theoretically study the ARPES of a monolayer graphene by using quantum Monte Carlo simulation method. Our calculation confirms that a well-defined sharp QP peak arises at E_F , as shown in Fig. 1(c). But intensity of this peak decreases dramatically with the increase of e-ph coupling strength S . Furthermore, an energy gap may open at E_F provided large coupling S , justifying that the e-ph interaction in graphene cannot be very strong. In connection with ARPES, we have also intensively investigated the relation between QP dynamics and e-ph interaction, electronic states and doping level in graphene.

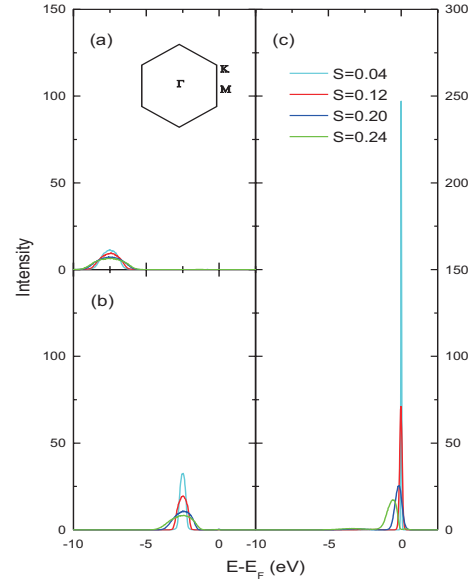


Fig. 1. Calculated ARPES intensity for graphene at (a) Γ , (b) M , and (c) K points under given e-ph coupling constants S . Inset of (a) shows Brillouin zone.

- [1] K. Sugawara, T. Sato, S. Souma, T. Takahashi, and H. Suematsu, *Phys. Rev. Lett.* **98** (2007) 036801.
- [2] C. S. Leem, B. J. Kim, Chul Kim, S. R. Park, T. Ohta, A. Bostwick, E. Rotenberg, H.-D. Kim, M. K. Kim, H. J. Choi, and C. Kim, *Phys. Rev. Lett.* **100** (2008) 016802.

Role of coherent part and incoherent part in the electron transport properties of the materials characterized by strong electron correlation

Tsunehiro Takeuchi

¹*EcoTopia Science Institute, Nagoya University, Nagoya 464-8603, Japan*

Recent progress in angle resolved photoemission spectroscopy (ARPES) allows us to gain deep insight into the momentum dependent electronic structure of the materials. The self-energy of quasiparticles can be also investigated by ARPES as a function of energy and momentum, in which information about the variety of many body effects including the electron correlations is involved. The real part of the self-energy indicates the energy shift from that of the bare electrons free from the many body effects, while the imaginary part represents the lifetime of the quasiparticles. A large number of groups including us have employed this highly sophisticated experimental technique to investigate the electronic structure and the many body effects of materials, such as the high- T_c superconductors.

We realized by using ARPES measurements that the electron transport properties could be quantitatively analyzed, because all factors, the number of electrons at a given energy, momentum dependent group velocity, and momentum dependent relaxation time, are obtainable from the ARPES measurements, provided that the lifetime of the quasiparticles is considered as the relaxation time of conducting wave packets. For the high- T_c superconductors, in which almost of all quasiparticles behave as a coherent wave, this method worked well and the electrical resistivity, thermoelectric power, and Hall coefficient were quantitatively reproduced by calculation using the information obtained from the ARPES measurement. [1]

The layered cobalt oxide Na_xCoO_2 is widely known to possess variety of unusual properties, such as superconductivity, the large magnitude of thermoelectric power, the Curie-Weiss magnetic susceptibility behavior coexisting together with the metallic electrical conduction, the charge density wave oriented insulating phase, and the spin density wave behaviors. Those characteristics are presumably caused by the strong electron correlation. Recently, we have intensively investigated the effect of strong electron correlation upon the electronic structure and the electron transport properties of Na_xCoO_2 by using high-resolution ARPES measurements, and found that the incoherent part as well as the coherent part, strongly affects the electron transport properties.

The electronic structure of layered cobalt oxides, including the present material Na_xCoO_2 , is characterized by the simultaneous possession of coherent part and incoherent part shown as Fig.1. Generally speaking, the incoherent part is caused by the strong electron correlation, and this strong

electron correlation drastically reduces the energy-width of the “coherent band”. Indeed, the observed energy-width of the “coherent band” is reduced to 1/3 of that of the band calculated by the FLAPW-LDA method. Note here that these characteristics in electronic structure cannot be predicted by the first principle calculation using the mean field theory. The use of the high-resolution ARPES, therefore, is of great importance in order to reveal the electronic structure of materials under the strong many body effects.

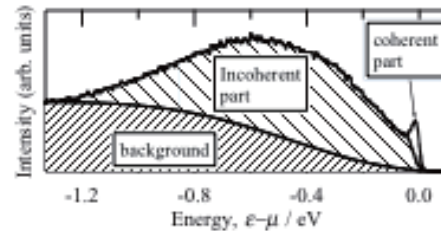


Fig. 1. An energy distribution curve of the $\text{Na}_{0.7}\text{CoO}_2$ at a Fermi wave vector. The spectrum is definitely characterized by the coherent and incoherent parts.

The temperature dependence of the thermoelectric power and the electrical resistivity was well accounted for with the Boltzmann transport theory provided that the contributions of coherent and incoherent part are properly taken into account. Both properties are dominantly determined by the coherent part at low temperature below 150 K and by the incoherent part at high temperature above 300K, respectively. The measured and calculated thermoelectric power of $\text{Na}_{0.7}\text{CoO}_2$ is shown in Fig.2 as one of the typical examples.

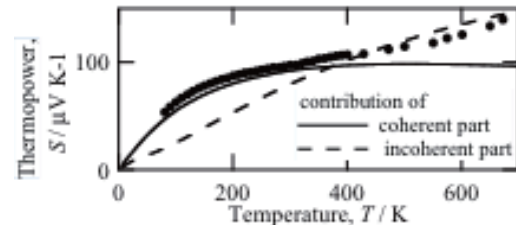


Fig. 2. Measured (markers) and calculated (lines) thermoelectric power of $\text{Na}_{0.7}\text{CoO}_2$.

[1] T. Kondo *et al.*, Phys. Rev. B **72** (2005) 024533., T. Kondo *et al.*, Phys. Rev. B **74** (2006) 225411., T. Kondo *et al.*, J. Elec. Spec. Relat. Phenom. **144-147** (2005) 1249-1252., T. Takeuchi *et al.*, J. Elec. Spec. Relat. Phenom. **156-158** (2007) 452-456., H. Komoto and T. Takeuchi, J. Elec. Mater. **38** (2009) 1365-1370.

Systematic angle-resolved photoemission study of Ce-based heavy-fermion systems

H. J. Im,¹ H. Miyazaki,² T. Ito,³ S. Kimura,^{2,4} K. E. Lee,⁵ Y. S. Kwon,⁵
A. Yasui,⁶ and H. Yamagami^{6,7}

¹ *Department of Advanced Physics, Hirosaki University, Hirosaki 036-8561, Japan*

² *UVSOR Facility, Institute for Molecular Science, Okazaki 444-8585, Japan*

³ *Graduate School of Engineering, Nagoya University, Nagoya 464-8603, Japan*

⁴ *School of Physical Sciences, The Graduate University for Advanced Studies, Okazaki 444-8585, Japan*

⁵ *Department of Physics, Sungkyunkwan University, Suwon 440-746, Korea*

⁶ *Synchrotron Radiation Research Center, Japan Atomic Energy Agency, SPring-8, Sayo, Hyogo 679-5148, Japan*

⁷ *Department of Physics, Kyoto Sangyo University, Kyoto 603-8555, Japan*

We present the systematic angle-resolved photoemission (ARPES) studies of Ce-based heavy fermion compounds, $\text{CeNi}_{1-x}\text{Co}_x\text{Ge}_2$, whose ground states are change from antiferromagnetic to non-magnetic heavy fermion via quantum critical point (QCP). Recently, it was clearly observed that the Kondo resonance (KR) peaks (Ce $4f^1$ state) are dispersed from above the Fermi-level (E_F) and cross E_F forming the diamond-shaped Fermi-surface (FS) in non-magnetic heavy-fermion system, $\text{CeCoGe}_{0.8}\text{Si}_{1.2}$ [1]. The systematic Ce $4d$ - $4f$ resonant ARPES studies of $\text{CeNi}_{1-x}\text{Co}_x\text{Ge}_2$ reveal that such momentum-dependence of KR peaks exists across QCP, indicating the itinerant character of f -electrons in agreement with the results of angle-integrated photoelectron spectroscopy [2].

References:

- [1] H. J. Im et al., Phys. Rev. Lett. **100**, 176402 (2008).
[2] H. J. Im et al., Phys. Rev. B **72**, 220405 (2005).

Electronic structure of CuIn_5Se_8 studied by angle-resolved photoemission spectroscopy

T.V. Kuznetsova¹, V.I. Grebennikov¹, C. Taubitz², M. Neumann²,
M.V. Yakushev³, M.V. Kuznetsov⁴

¹ *Institute of Metal Physics, UB RAS, 620041 Ekaterinburg, Russia*

² *Dortmund, DELTA, University of Osnabrück, D-49069 Osnabrück, Germany*

³ *Strathclyde University, G4 0NG Glasgow, United Kingdom*

⁴ *Institute of Solid State Chemistry, UB RAS, 620990 Ekaterinburg, Russia*

CuInSe_2 and related chalcopyrite compounds are recently attracting much attention due to potential applications for thin-film solar cells. Conversion efficiencies up to 19% for solar cells based on polycrystalline CuInSe_2 layers have been reached despite a lack of detailed information on material properties. Indium-rich compounds such as ordered defect compound CuIn_5Se_8 and CuIn_3Se_5 on surface of CuInSe_2 in the typical $\text{CdS}/\text{CuInSe}_2$ heterojunction play an important role for photovoltaic application due to their outstanding photoelectric characteristics [1]. However, the electronic structure of the compound CuIn_5Se_8 and the mechanism of strong localization of the states with the energies close to the Fermi level remained obscure. Knowledge on the stable surface structures of Cu chalcopyrites is very limited due to the difficulties in preparing clean well defined surfaces [2]. The electronic structure of the single crystal CuIn_5Se_8 surface has been investigated by angle-resolved photoelectron spectroscopy (ARPES) and x-ray photoemission spectroscopy (XPS). The samples were cleaved in ultrahigh vacuum of the analyzer chamber. Data have been collected for three different values of the incoming photon energy $h\nu = 20, 25,$ and 30 eV. We found that ARPES spectra along two different high symmetry directions in reciprocal space show existence of four bands. They are situated from 0 to 8 eV below the Fermi energy and have flat dispersions indicating a considerable localization of the electron states. In order to determine the chemical state of the surface and binding energy of the each core-level CuIn_5Se_8 the x-ray photoemission spectroscopy was performed using Al K_α radiation. The shape of valence-band spectra strongly depends on the exciting photon energies.

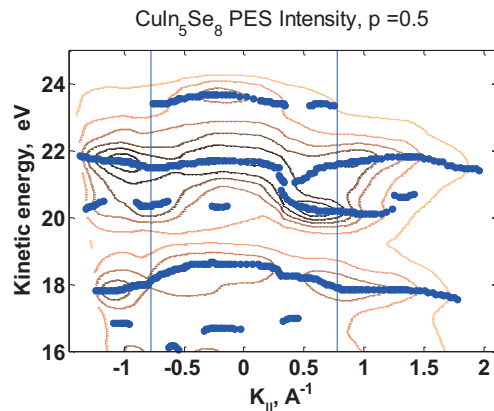


Fig. 1. The diagram of photoemission intensity as functions two variable: a wave vector (parallel a surface, along ΓM direction) and kinetic energy. Greasy curve - the coordinates of maxima of intensity on variable \AA , correspond to the law of dispersion of strips. The vertical lines show borders of the first Brillouin zone.

References:

- [1] S. Lany and A. Zunger, Phys. Rev. Lett., 100, 016401 (2008)
- [2] Th. Deniozou, N. Esser, Th. Schulmeyer, R. Hunger, Applied Phys. Lett., 88, 052102 (2006)

Ultrahigh resolution laser-angle-resolved photoemission spectroscopy

T. Kiss¹, K. Ishizaka^{1,2} and S. Shin^{1,2}

¹*Institute for Solid State Physics (ISSP), University of Tokyo, Kashiwa, Chiba 277-8581, Japan*

²*CREST, Japan Science and Technology Corporation (JST), Kashiwa, Chiba 277-8581, Japan*

It is well known that the variety of properties that conducting materials display stems from the electronic structure at and near the Fermi level (E_F). One of the most fascinating examples is superconductivity, in which pairing of two electrons makes a tiny energy gap at E_F , leading to unexpected physical properties. Angle-resolved photoemission spectroscopy (ARPES) is a very powerful method to measure electronic structure at and below E_F as it can provide the energy (ω) and momentum (k) resolved spectral function $A(k, \omega)$ of a solid. ARPES can thus measure band dispersions and Fermi surface topology as a function of temperature (T). [1] It has contributed significantly to our understanding of the electronic structure of solids. In the angle-integrated version also, PES has given us valuable results allowing comparisons with other techniques which probe the one-electron removal function, such as tunneling spectroscopy. Since the discovery of high- T_c superconductors, ARPES studies have followed a remarkable progress in energy and momentum resolution, driven by the purpose of determining the superconducting gap symmetry. These studies have usually employed synchrotron radiation or gas discharge lamps as a photon source coupled to a photoemission spectrometer, and for high energy resolution achieved using a He discharge lamp (He I : 21.218 eV). PES is also usually considered to be very surface sensitive as tunneling spectroscopy, it is well-known that the escape depth of photoelectrons show strong kinetic-energy dependence : it is highly surface sensitive for kinetic energies between 20- 50 eV, but can be made more bulk sensitive by changing the kinetic energy to very low and very high energies. [2] This can be done by simply changing the incident photon energy. Consequently, the increase of escape depth using soft-x rays ($h\nu \sim 1000$ eV) has been demonstrated with a resolution of ~ 100 meV. [3] This energy resolution is good enough to study the overall electronic structure but is about 100 times larger than, for example, the SC gap energy scale of a low- T_c superconductor, typically less than 1 meV. The energy resolution using synchrotron radiation with 20-30 eV photon energy is ~ 5 meV (recently ~ 2 meV below 10eV photon energy) for solid-state studies, which is again not enough for studying very low energy scale low temperature electronic structures. While PES using a He I resonance line (21.2 eV) can produce a ~ 1 -2 meV resolution, the escape depths using a photon energy of ~ 20 eV are less than 10 Å. This may not be suitable for studying materials having a surface electronic structure

completely different from the bulk, as is known for some correlated-electron systems.

To achieve the ultrahigh energy-momentum resolution and high bulk sensitivity, we have developed a low-temperature ultrahigh resolution system for polarization dependent ARPES using a vacuum ultra-violet (VUV) laser ($h\nu = 6.994$ eV) as a photon source. With the aim of addressing low energy physics, we show the system performance with angle-integrated PES at the highest energy resolution of 360 μeV and the lowest temperature of 2.9 K. [4] At present, we have been achieved 150 meV of energy resolution and 1.8 K of lowest temperature in advanced 7 eV laser ARPES system. These new photoemission systems demonstrate that the ultrahigh resolution ARPES is quite important to understand electronic property of materials.

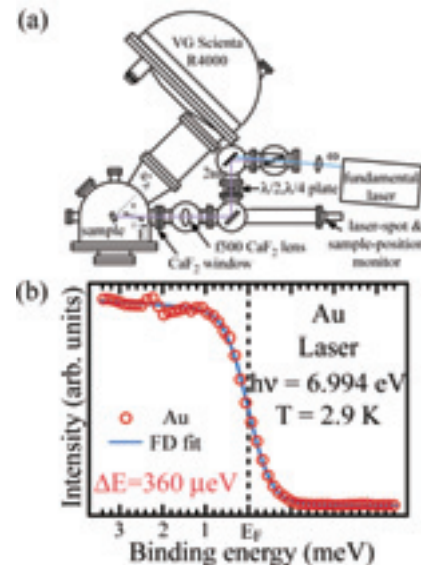


Fig. 1. (a) Schematic diagram of the LPES system. (b) Ultrahigh-resolution PES spectrum of an evaporated gold film measured at 2.9 K (red circles), together with the FD function at 2.9 K convolved by a Gaussian with full width at half maximum of 360 μeV (a blue line).

[1] A. Kaminski *et al.*, Nature **416**, 610 (2002).

[2] M.P. Seah and W.A. Dench, Surface. Interface. Anal. **1**, 2 (1979).

[3] A. Sekiyama *et al.*, Nature **403**, 396 (2000).

[4] T. Kiss *et al.*, Rev. Sci. Instrum. **79**, 023106 (2008).

Development of bulk-sensitive spin-resolved ultrahigh-resolution photoemission spectrometer

S. Souma¹, A. Takayama², K. Sugawara², T. Sato² and T. Takahashi^{1,2,3}

¹WPI-AIMR, Tohoku University, Sendai 980-8578, Japan

²Department of Physics, Tohoku University, Sendai 980-8578, Japan

³Japan Science and Technology Agency, CREST, Kawaguchi 332-0012, Japan

Angle-resolved photoemission spectroscopy (ARPES) is known as a powerful technique to investigate the fine electronic structure relevant to the intriguing physical phenomena in solids such as superconductivity, heavy fermions, metal-insulator transition, and so on. This technique, yet, has suffered from two inherent problems originating in the principle of PES itself, namely, (1) the high surface sensitivity, and (2) the difficulty in resolving the spin polarization of electrons. To overcome those problems, we have constructed an ultrahigh resolution photoemission spectrometer equipped with a newly developed xenon-plasma discharge lamp and a mini-Mott detector.

Figure 1 shows the xenon plasma discharge lamp that provides several intense resonance lines from xenon plasma in the energy range of 8-11 eV, which is enough to achieve high bulk-sensitivity.[1] The energy width of radiation from the lamp is intrinsically very narrow owing to small Doppler broadening due to the high mass of the xenon atom, and low pressure operation of the discharging plasma reducing the self absorption effect. Combined with a large hemispherical energy analyzer and a spherical concaved grating, we achieved high energy resolution less than 1 meV as a total system in the spin-integrated mode. The photoelectron intensity excited by the xenon lamp is bigger than that of the ordinary helium lamps by 1-2 order of magnitude. This is quite useful to compensate the low efficiency in the case of spin-resolved photoemission.

We have developed a compact Mott spin detector operating at 25 kV and adapted it to the large hemispherical electron energy analyzer through an electron deflector lens. We have redesigned the analyzer and mounted the entrance of the deflector lens at a location close to the $\phi 40\text{mm}$ microchannel plate (MCP). This enables the observation of electron energy and momentum by the MCP with comparable quality to modern electron analyzers, simultaneously to the electron spin measurement by the Mott detector.

Figure 2 shows spin-resolved ARPES spectra of the Shockley state of the Sb(111) surface, which is known as a typical case where the spin of the electron band is polarized along the plane due to the surface Rashba effect.[2] The spectra are recorded by four channeltrons in the Mott detector to measure the electron spin polarization of two orthogonal

directions, that is, in-plane and out-of plane to the (111) surface. As clearly seen, a pronounced peak at 0.1 eV in the up-spin spectrum of the in-plane direction is considerably reduced in the down-spin spectrum, in sharp contrast to the perfect superimposing of the up- and down-spin spectra of the out-of-plane direction. This result is in good agreement with the surface Rashba effect and unambiguously shows the spin-resolving performance of the developed photoemission system.



Fig. 1. Xenon-plasma discharge lamp

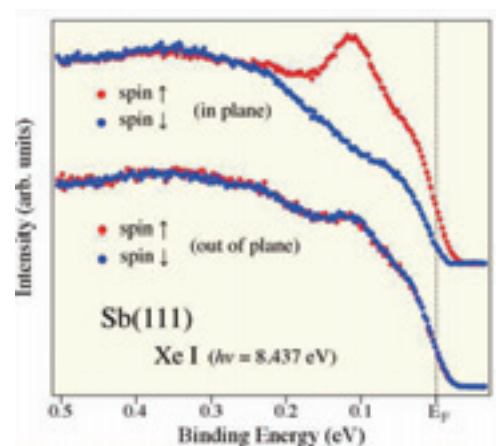


Fig. 2. Spin-resolved ARPES spectra of Sb(111)

[1] S. Souma *et al.*, RSI, **78** (2007) 123104.

[2] K. Sugawara *et al.*, PRL, **96** (2006) 046411.

Direct Domain Excitation by Photoemission and Its Dynamical Features Manifesting in ARPES spectra

K. Iwano

Photon Factory, Institute of Materials Structure Science, KEK, Tsukuba 305-0801, Japan

The theoretical and experimental studies of angle-resolved photoemission (ARPES) have focused on quasi-particle properties in various kinds of materials. Among them, heavily renormalized nature of quasi-particles typically seen in strongly-correlated electron systems have collected much attention, since the nature can provide important information on the many-body properties of those systems. However, even in such cases the quasi-particle basically consists of one hole; the strong renormalization only increases the particle mass and the lifetime. In this sense, what we observe in ARPES is inevitably of one-hole nature, however it is modified by interactions.

In this paper, we report on a completely different type of excitation that can be detected in the ARPES. In Fig. 1, we show a schematic picture in which a system that is located close to a phase boundary absorbed one high-energy photon. Assuming a valence photoemission, we are left with one hole in the valence band. In ordinary insulators, the process stops at this point. However, in this system, it does not stop but proceeds to form a domain [1]. We here think of a one-dimensional system whose ground state is expressed as in Fig. 1(a). TTF-CA, an organic molecular solid, is a system appropriate for this situation, having nearly degenerate neutral (N) and ionic (I) phases. In the process shown in Fig. 1(b), we expect that a domain of the I phase is created in the background of the N phase. It is emphasized that the driving force is the proximity to the N-I phase boundary combined with inherent electron itineracy, and that the detection of this process requires no pump-probe experiment but only an ordinary type of photoemission measurement.

In Fig. 2, we show calculated ARPES spectra (black lines) at two momenta, which are obtained very close to the phase boundary [2]. What is quite unique is that each spectrum exhibits a special spectral shape; the spectrum at $k=0$ takes a cusp-like shape, while the left-hand side of the spectrum at $k=\pi/2$ is almost fitted to a straight line. We also tried deriving an effective model that retains the two basic degrees of freedom of a single domain, namely, its center of gravity and its spatial size, plus spin degrees of freedom inside the domain. As a result of its analysis, we find that the effective model reproduces the spectral features, as shown by the red lines. In particular, the above-mentioned spectra shapes are

governed by the spin degrees of freedom, in a way that domain states with various spin configurations form a Hilbert space that can be accessed via the ARPES measurement.

This type of domain excitation is new in the ARPES studies, in the sense that it has never been observed so far. In addition to this, it also has important meaning in the context of photoinduced phase transitions. We hope for future experimental attempts that try to identify them in actual materials.

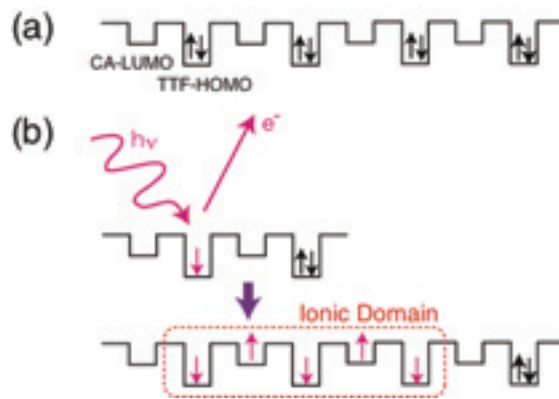


Fig. 1. (a) Neutral ground state and (b) schematic picture of an I-domain formation process.

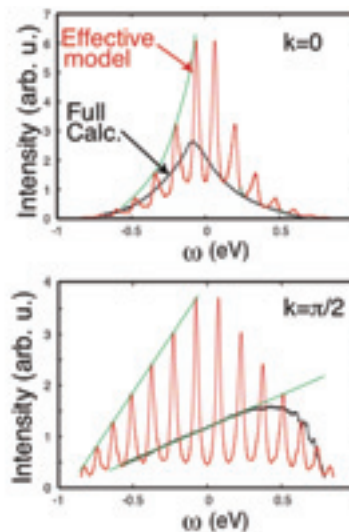


Fig. 2. Calculated ARPES spectra.

[1] K. Iwano, Phys. Rev. Lett., 97, 226404 (2006).
[2] K. Iwano, Phys. Rev. Lett. 102, 106405 (2009).

Valence-band Electronic Structure of FeSi studied by high-resolution Angle-Resolved Photoelectron Spectroscopy (ARPES)

Y. Takeichi¹, A. Nishide¹, K. Nakatsuji¹, T. Okuda¹, F. Komori¹, J. Yoshinobu¹, H. Kondoh², I. Matsuda¹, F. Bertran³, P. Le Fevre³, A. Taleb-Ibrahimi³, H. Yamagami⁴, A. Kakizaki¹

¹ISSP, the Univ. of Tokyo, Kashiwanoha, Kashiwa 277-8581, Japan

²Department of Chemistry, Keio University, Yokohama 223-8522, Japan

³SOLEIL / LURE, Saint-Aubin, BP 48, 91192 Gif-sur-Yvette Cedex, France

⁴Department of Physics, Kyoto Sangyo Univ., Kamigamo, Kita-ku, Kyoto 603-8555, Japan

Among transition metal mono-silicides: MSi (M=Cr, Mn, Fe, Co, Ni), FeSi has been intensively studied as one of the possible candidates for the d-electron Kondo insulators. While FeSi has an insulating ground state, electric conductivity shows a semiconductor to insulator crossover at 300K. Another interesting feature is the temperature dependence of its magnetic susceptibility, which rises nearly exponentially up to 500K making a broad maximum followed by a Curie-Weiss law at even high temperatures. To explain these unusual electric and magnetic properties, many theoretical models have been discussed so far. They are for example, thermally excited spin-fluctuation theory, phenomenological models assuming two narrow *d* bands in the vicinity of the band gap. Such a model density of states is quite similar to those for Kondo insulator description, and due to this similarity, it was often claimed that FeSi is the first Kondo insulator containing no *f*-electrons.

A number of valence band photoemission spectroscopy studies have been performed to elucidate the electronic structures near the Fermi level (E_F) [2]. In spite of careful measurement with sufficiently high-energy resolution smaller than the expected semiconductor band gap, results are not conclusive about the existence of the band gap [3]. Recently, Klein *et al.* made an effort to cleave a single crystal at (001) plane and observed ARPES spectra [4]. Though the sample surface consists of several faces, they observed that the spectral features are almost consistent with calculated band structure along the $\Gamma X\Gamma$ plane in the Brillouin zone showing a sharp peak feature at 300meV below E_F . In the following, we present the valence band structures of FeSi(001) single crystal surface observed by ARPES and discuss on the electronic structures of this material.

Experiments were carried out at CASSIOPEE beamline of SOLEIL. The ARPES apparatus consists of a sample preparation chamber equipped with an Auger electron spectrometer (AES) and a low energy electron diffraction (LEED) apparatus and an analysis chamber with a hemispherical electron energy analyzer (SCIENTA R4000). Clean FeSi(001) single crystal surface was obtained by the procedure described elsewhere [5].

Figure 1 shows the valence band structure of FeSi(001) single crystal surface observed along the Γ -X direction in the Brillouin zone, where the Fe 3*d* originated valence band shows a very small energy dispersion. The results are basically consistent with the calculated valence band structure with an energy gap very close to the E_F . The obtained band dispersion well reproduces the theoretical calculation, except the reduction of the bandwidth of about 30% due to the renormalization effect.

This work resolves the controversial evidences, which have been provided for the arguments of the Kondo-like interaction in this material.

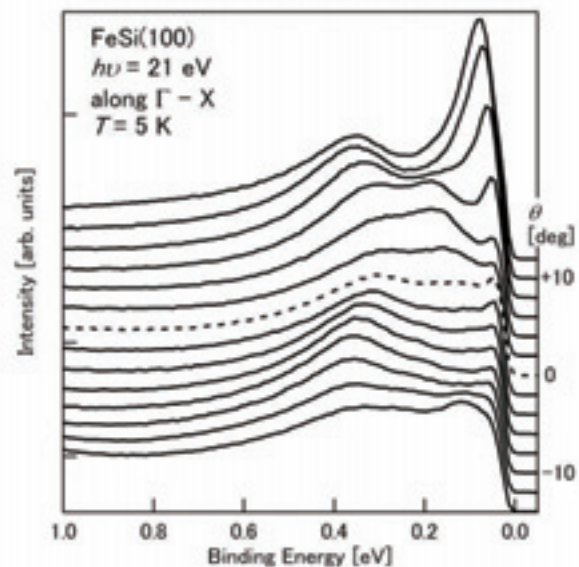


Fig. 1. ARPES spectra of FeSi(100).

- [1] C. Fu and S. Doniach, Phys. Rev. B **51**, 17439 (1995).
- [2] A. Kakizaki, *et al.*, J. Phys. Soc. Jpn., **51**, 2597 (1982).
- [3] K. Breuer, *et al.*, Phys. Rev. B **56**, R7061 (1995).
- [4] M. Klein, *et al.*, Phys. Rev. Lett., **101**, 046406 (2008).
- [5] K. Kura, *et al.* J. Phys. Soc. Jpn., **77**, 024709 (2008).

A topological metal at the surface of an ultrathin BiSb alloy film

T. Hirahara¹, Y. Sakamoto¹, Y. Saisyu¹, H. Miyazaki², S. Kimura²,
T. Okuda^{3,4}, I. Matsuda⁴, S. Murakami⁵, and S. Hasegawa¹

¹*Department of Physics, University of Tokyo, 7-3-1 Hongo, Bunkyo-ku, Tokyo 113-0033, Japan*

²*UVSOR Facility, Institute for Molecular Science, Okazaki 444-8585, Japan*

³*Hiroshima Synchrotron Radiation Center, Hiroshima University,
Higashi-Hiroshima 739-0046, Japan*

⁴*Synchrotron Radiation Laboratory, ISSP University of Tokyo, Kashiwa 277-8581, Japan*

⁵*Department of Physics, Tokyo Institute of Technology, Tokyo 152-8551, Japan*

Recently there has been growing interest in *topological insulators* or the *quantum spin Hall (QSH) phase*, which are insulating materials with bulk band gaps but have metallic edge states that are formed topologically and robust against any non-magnetic impurity [1]. In a three-dimensional material, the two-dimensional surface states correspond to the edge states (topological metal) and their intriguing nature in terms of electronic and spin structures have been experimentally observed in bulk $\text{Bi}_{1-x}\text{Sb}_x$ single crystals [2,3,4]. However, if we want to know the transport properties of these topological metals, high purity samples as well as very low temperature will be needed because of the contribution from bulk states or impurity effects. In a recent report, it was also shown that an intriguing coupling between the surface and bulk states will occur [5]. A simple solution to this bothersome problem is to prepare a topological metal on an ultrathin film, in which the surface-to-bulk ratio is drastically increased.

Therefore in the present study, we have investigated if there is a method to make an ultrathin $\text{Bi}_{1-x}\text{Sb}_x$ film on a semiconductor substrate. From reflection high-energy electron diffraction observation, it was found that single crystal $\text{Bi}_{1-x}\text{Sb}_x$ films ($0 < x < 0.25$) as thin as ~ 30 Å can be prepared on Si(111)-7x7. The transport properties of such films were characterized by *in situ* monolithic micro four-point probes [6]. The temperature dependence of the resistivity for the $x=0.1$ samples was insulating when the film thickness was 240 Å. However, it became metallic as the thickness was reduced down to 30 Å, indicating surface-state dominant electrical conduction. Figure 1 shows the Fermi surface of 40 Å thick $\text{Bi}_{0.92}\text{Sb}_{0.08}$ (a) and $\text{Bi}_{0.84}\text{Sb}_{0.16}$ (b) films mapped by angle-resolved photoemission spectroscopy. The basic features of the electronic structure of these surface states were shown to be the same as those found on bulk surfaces, meaning that topological metals can be prepared at the surface of an ultrathin film. The details will be given in the presentation.

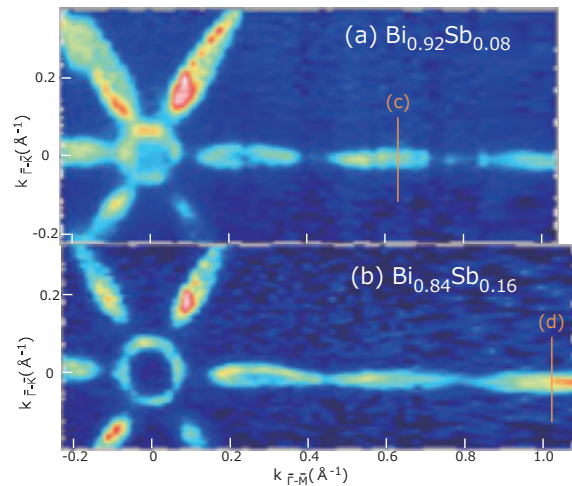


Fig. 1. The Fermi surface mapped by ARPES at 10 K for 40 Å thick $\text{Bi}_{0.92}\text{Sb}_{0.08}$ (a) and $\text{Bi}_{0.84}\text{Sb}_{0.16}$ (b) films, respectively. A circularly polarized light was used at the photon energy of 28 eV.

References:

- [1] L. Fu and C. L. Kane, *Phys. Rev. B* **76**, 045302 (2007).
- [2] D. Hsieh *et al.*, *Nature* **452**, 970 (2008).
- [3] D. Hsieh *et al.*, *Science* **323**, 919 (2009).
- [4] A. Nishide *et al.*, cond-mat/09022251, submitted to *Phys. Rev. Lett.* (2009)
- [5] A. A. Taskin and Y. Ando, *Phys. Rev. B* **80**, 085303 (2009).
- [6] T. Tanikawa *et al.*, *e-Journal of Surface Science and Nanotechnology*, **1**, 50 (2003).

Electronic Structure of Pseudo-one Dimensional $\text{Ba}_3\text{Co}_2\text{O}_6(\text{CO}_3)_{0.7}$

K. Soda¹, M. Kikuchi², S. Ogawa¹, H. Miyazaki^{1,3}, M. Inukai^{1,4}, M. Kato¹, S. Yagi¹,
K. Iwasaki^{1,5} and T. Matsui^{1,6},

¹Graduate School of Engineering, Nagoya University, Nagoya 464-8603 Japan

²School of Engineering, Nagoya University, Nagoya 464-8603 Japan

³UVSOR Facility, Institute for Molecular Science, Okazaki 444-8585, Japan

⁴Venture Business Laboratory, Nagoya University, Nagoya 464-8603 Japan

⁵Toyota Boshoku Coporation, Kariya 448-8651, Japan

⁶EcoTopia Science Institute, Nagoya University, Nagoya 464-8603 Japan

Cobalt oxides such as Na_xCoO_2 have attracted much attention because of their fascinating transport and magnetic properties. Recently it has been found that a barium cobalt oxycarbonate $\text{Ba}_3\text{Co}_2\text{O}_6(\text{CO}_3)_{0.7}$, which has pseudo-one dimensional structure with Co-O chains consisting of face-sharing CoO_6 octahedra along the c axis, shows a fairly large thermoelectric power factor of $0.9 \text{ mWm}^{-1}\text{K}^{-2}$ at 300 K with the thermoelectric power of about $+120 \mu\text{V K}^{-1}$ and metallic behavior of its electric conductivity above 300 K [1]. In this report, we have investigated its valence-band electronic structure by photoelectron spectroscopy to understand the physical properties.

Photoelectron measurements were carried out at the beamline BL-5U of UVSOR-II. Single crystalline specimens of $\text{Ba}_3\text{Co}_2\text{O}_6(\text{CO}_3)_{0.7}$ was prepared in size of $5 \times 0.5 \times 0.5 \text{ mm}^3$ by a flux method [1], and their clean surfaces was obtained by *in situ* fracturing the specimens in perpendicular to the c axis.

Figure 1 shows typical photoelectron spectra recorded at 20 K with the excitation photon energies $h\nu$ of 60 and 75 eV as well as their difference spectrum. Each spectrum is normalized with the integrated intensity and subtracted the background by an iteration method [2]. There are features A to H observed in the spectra; the features A to C are ascribed to the hybridized bands of the Co $3d$ and O $2p$ states, while the features D, F, G and H are assigned to the CO_3 -derived states, Ba $5p$ spin-orbit doublets and O $2s$ state, respectively. The feature E is attributed to the surface components. The remarkable suppression of the features A and B at $h\nu = 60 \text{ eV}$ is due to the Co $3p$ - $3d$ resonance, which indicates the relatively large Co $3d$ contribution to the features A and B while the O $2p$ one to the feature C.

Figure 2 shows detailed spectra near the Fermi level E_F measured at $h\nu = 40 \text{ eV}$ and several temperatures T in comparison with reference Au spectra. $\text{Ba}_3\text{Co}_2\text{O}_6(\text{CO}_3)_{0.7}$ reveals large reduction in intensity towards E_F but clear finite intensity at E_F . This may suggest the electron doping into the low-spin bands of $\text{Co}^{4+}(t_{2g}3d^5)$, which causes the positive thermoelectric power of 81 or $141 \mu\text{V K}^{-1}$ at high temperatures for the Co^{4+} concentration x of 0.7 [3], consistent with the observed value. Although a $1/8$ -power-law dependence of the intensity on the binding energy E_B

might be expected in one-dimensional fermion system [4], the anomalous exponents from 0.5 at 20 K to 0.8 at 200 K are obtained for $E_B = 0.01\text{--}0.1 \text{ eV}$, suggesting the larger short-range interaction at the lower temperature. A small hump at $E_B \sim 0.02 \text{ eV}$ observed at $T = 20 \text{ K}$ might also imply opening of a pseudogap or a magnetic ordering, which causes the recently observed reduction in the electric conductivity at low temperatures [5].

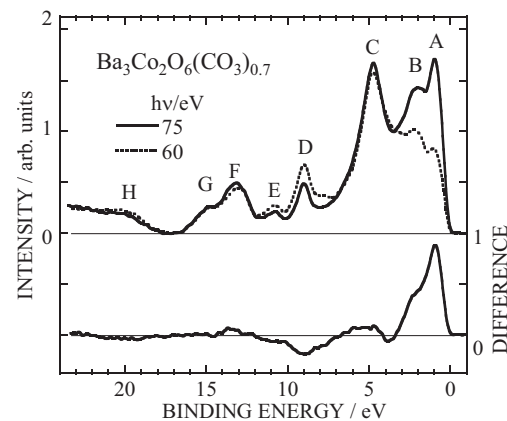


Fig.1. Valence-band spectra of $\text{Ba}_3\text{Co}_2\text{O}_6(\text{CO}_3)_{0.7}$.

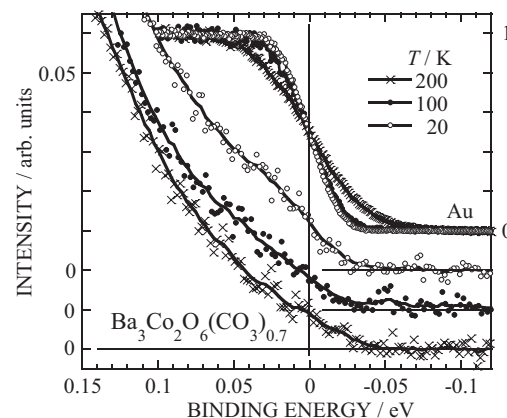


Fig.2. Valence-band spectra near the Fermi level.

- [1] T. Yamamoto *et al.*, Proc. Int. Symp. on EcoTopia Science 2007, p.145.
- [2] K. Soda *et al.*, J. Phys. Soc.Jpn. **60** (1991) 3059.
- [3] W. Koshibae *et al.*, Phys. Rev. B **62** (2000) 6869.
- [4] J. Voit, Pep. Prog. Phys. **57** (1994) 977.
- [5] K. Iwasaki, *private communication*.

Surface Chemistry of Butyl-Passivated Silicon Nanoparticles Studied by Synchrotron-Radiation Photoelectron Spectroscopy

M. Imamura, N. Takashima, J. Nakamura, S. Fujimasa, and H. Yasuda

Department of Mechanical Engineering, Kobe University, Kobe 657-8501, Japan

Various Si-based nanostructures have a great interest, since it has been reported that they show a strong photoluminescence, and therefore there is a possibility of future integrating electronic devices with optical sensing technique. Numerous works focused on the optical properties of Si nanoparticles prepared by various methods have been reported to date. However, data in the literatures are no universally accepted, and depend on various factors in the individual samples. Especially, the physical and chemical properties of nanoparticles are greatly influenced by surface chemical states due to the large surface to volume ratio with decreasing the size to the nanometer scale. In this work, we have synthesized n-butyl-passivated Si nanoparticles with well crystalline nature and well surface-passivated surface by the solution routes, and have directly characterized their electronic structures in the vicinity of Fermi level using synchrotron-radiation photo-electron spectroscopy. Furthermore, we have compared the valence-band photoemission spectra of fully n-butyl-passivated Si nanoparticles and those with oxygen contaminants in order to directly investigate the effect of surface chemical nature on their electronic structures.

Figure 1 shows the synchrotron-radiation valence-band photoemission spectra of as-prepared n-butyl-passivated Si nanoparticles with $d_c = 1.1$ nm and those exposed to ambient air for 10 min, on the HOPG substrate at room temperature with photon energy of 195 eV. The spectral features around 7 and 5.5 eV binding energies in the photoemission spectrum of as-prepared n-butyl-passivated Si nanoparticles originate from the C 2p derived states. The spectral feature around 7 eV binding energy originates from the C–H bonds in the butyl surface-passivants, and that around 5.5 eV binding energy originates from the Si–C bonds between the Si nanoparticle and butyl surface-passivants. This spectral feature around 5.5 eV in binding energy indicates that the present Si nanoparticles are well surface-passivated by butyl molecules. The spectral feature around 13.5 eV binding energy originates from the C 2s-derived states. The other spectral features around 3.5, 9, and 11 eV in binding energies originate from Si 3s- and 3p-derived electronic states. On the other hand, the valence-band photoemission spectrum of n-butyl-passivated Si nanoparticles with $d_c = 1.1$ nm after exposure to ambient air for 10 min is similar to that of as-prepared n-butyl-passivated Si nanoparticle. However, the spectral intensity derived from Si–C bonds around 5.5 eV binding energy

decreases with oxygen contaminants. This clearly indicates the removal of the surface-passivants of butyl molecules and subsequent contamination of oxygen. It should be noted that the valence-band photoemission spectrum of n-butyl-passivated Si nanoparticles with oxygen contaminants exhibits an additional feature centered around 2.6 eV binding energy (shown by the arrow). Puzder *et al.* have previously reported the Density of State (DOS) of hydrogen-passivated Si nanoparticles with various contaminants by means of local density approximation (LDA) in order to see physical origin of the effect of oxygen on the gap. [1] When a double bonded contaminant such as oxygen and sulfur is added to Si nanoparticles, the Si sp_3 network is considerably distorted and the HOMO and LUMO change their nature significantly. As a result, HOMO and LUMO states localized in the vicinity of the Si=O double bond, and the modified DOS originated from the HOMO and LUMO appears near the Fermi level as the additional features. From the comparison with this LDA theoretical DOS, it is concluded that this additional feature is ascribed to oxygen-contaminants-induced states, and this result provides a direct evidence of the effect of oxygen contaminants on the electronic structure that the previous calculation has predicted.

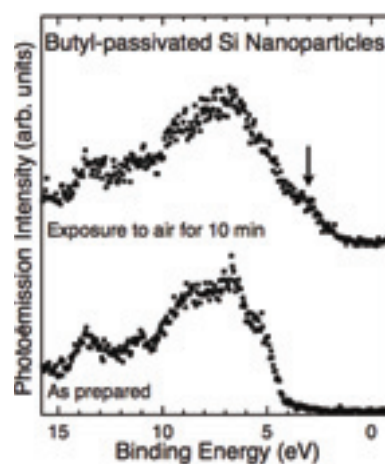


Figure. 1 Valence-band photoemission spectrum of as-synthesized n-butyl-passivated Si nanoparticles with $d_c = 1.1$ nm and those exposed to air for 10 min. The arrow indicates the additional feature originated from the oxygen-contaminant-induced states.

[1] A. Puzder, A. J. Williamson, J. C. Grossman, and G. Galli, *Phys. Rev. Lett.*, **88**, 097401 (2002).

Low-energy angle-resolved photoemission spectroscopy of Fe-based high- T_c superconductor $\text{Ba}_{1-x}\text{K}_x\text{Fe}_2\text{As}_2$

K. Nakayama¹, K. Terashima², T. Sato^{1,3}, T. Kawahara¹, Y. Sekiba¹, T. Qian¹, P. Richard⁴, S. Souma⁴, T. Ito², S. Kimura², G. F. Chen⁵, J. L. Luo⁵, N. L. Wang⁵, H. Ding⁵ and T. Takahashi^{1,4}

¹Department of Physics, Tohoku University, Sendai 980-8578, Japan

²UVSOR Facility, Institute for Molecular Science, Okazaki 444-8585, Japan

³TRiP, Japan Science and Technology Agency (JST), Kawaguchi 332-0012, Japan

⁴WPI Research Center, Advanced Institute for Materials Research, Tohoku University, Sendai 980-8577, Japan

⁵Beijing National Laboratory for Condensed Matter Physics, and Institute of Physics, Chinese Academy of Sciences, Beijing 100190, China

The recent discovery of high- T_c superconductivity in iron pnictide compounds has generated fierce debates on the high- T_c mechanism. The parent compounds of iron pnictide superconductors exhibit long-range antiferromagnetic order below T_N accompanied by the structural phase transition. By doping hole or electron carriers, the magnetic and structural phase transitions are suppressed and eventually the superconductivity emerges. To clarify the superconducting mechanism, it is essentially important to understand the doping-induced evolution of the low-energy band structures responsible for the emergence of the superconductivity. The understanding of the superconducting gap character is also critically important, since it is intimately related to the superconducting pairing interactions. To elucidate these points, we have performed high-resolution angle-resolved photoemission spectroscopy (ARPES) on $\text{Ba}_{1-x}\text{K}_x\text{Fe}_2\text{As}_2$.

ARPES measurements were performed using MB Scientific A1 spectrometer at the beamline 7U of UVSOL-II. We used low-energy photons ($h\nu = 6\text{-}25$ eV) to excite photoelectrons. The energy resolution was set to 8-14 meV.

Figure 1 (a) shows the ARPES spectral intensity of optimally hole-doped $\text{Ba}_{0.6}\text{K}_{0.4}\text{Fe}_2\text{As}_2$ ($T_c = 37$ K) measured at 17 K along the red line in the Brillouin zone shown in the inset. We clearly observed a hole-like band centered at the Γ point. In Fig. 1(b), we show the ARPES spectrum measured at the Fermi wave vector of this band. A sharp quasiparticle peak together with a leading-edge shift toward higher binding energy is clearly seen, indicating a superconducting gap opening. The superconducting gap size (Δ) estimated from the peak position is about 10 meV. This is significantly larger than the value (~ 5.5 meV) expected from the weak-coupling theory, suggesting an anomalously strong-coupling nature of the superconductivity in this compound. In this presentation, we also discuss the doping dependence of the electronic structures in relation to the occurrence of the superconductivity.

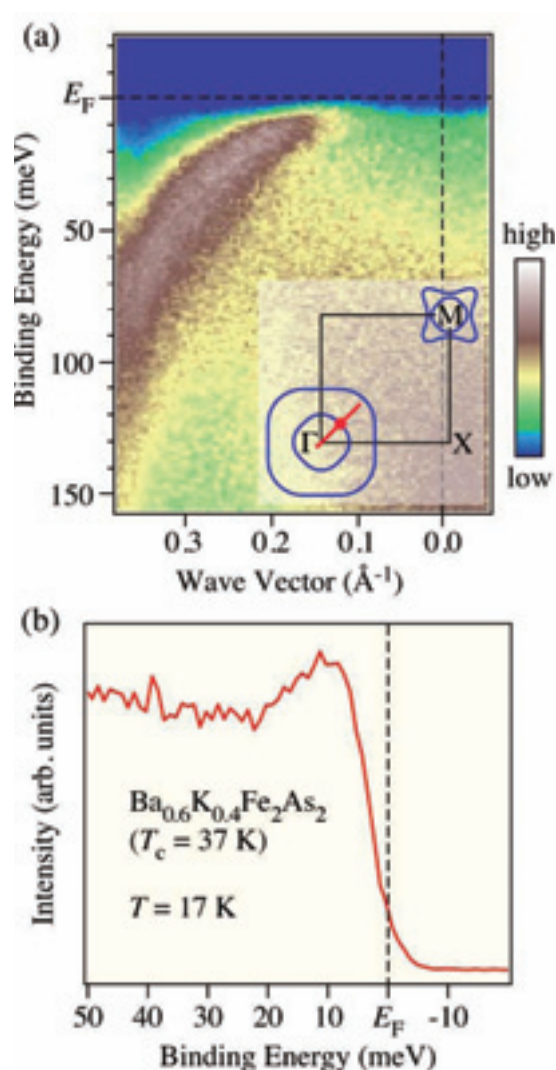


Fig. 1. (a) ARPES intensity plot near the Γ point of $\text{Ba}_{0.6}\text{K}_{0.4}\text{Fe}_2\text{As}_2$ ($T_c = 37$ K) as a function of binding energy and wave vector measured at 17 K with 21 eV photons. The inset indicates schematic Fermi surfaces (blue curves) and the measurement location (red line). (b) High-resolution ARPES spectrum near E_F at 17 K measured at the Fermi vector of the hole-like band (red circle).

Magnetic Circular Dichroism in Valence Band using Laser Excitation

T. Nakagawa, I. Yamamoto, Y. Takagi and T. Yokoyama

Department of Electronic Structure, Institute for Molecular Science, Okazaki 444-8585, Japan

Recently the magnetic circular dichroism has been a widely used method since it can detect the magnetic properties of thin films without spin detector, namely the measurement is simple and efficient. However valence band magnetic circular dichroism is generally known to be tiny due to the weak spin orbit coupling in valence band. Together with angle and energy resolved photoemission, it has been revealed that the MCD asymmetry is large enough to be measured ($\sim 10\%$).^[1] Enhanced MCD also can be obtained in threshold photoemission with total electron yield method,^[2,3] but away from the threshold the MCD asymmetry is drastically reduced. Since the valence band electron excitation is achieved by pulse lasers, it is expected that MCD in valence band would be investigated by multiphoton process.^[4] Although in principal the multiphoton MCD process is possible, it is completely unclear how much asymmetry is achieved.

We report an observation of two photon photoemission (2PPE) magnetic circular dichroism (MCD) on Ni(15 ML)/Cu(001) near the Fermi level using short pulse laser.^[1, 2] Figures 1(a) and (b) show ARPES spectra and the MCD asymmetry for 2PPE. The spectra are taken along the surface normal using circularly polarized light. Ni 3d peak are observed near the Fermi level, and the 3d peak shows slight shift by inverting the direction of the magnetization, which is the manifestation of MCD. The derived MCD spectra show $\sim 20\%$ asymmetry

The reduction of Ni MCD asymmetry by the overlayer metal capping is examined. It is believed that the electron escape depth for low kinetic energy is large, ~ 10 nm. However the estimation of the escape depth usually neglects the diffraction effect of electrons by overlayers, which is significantly important for the angle resolved photoemission experiments. Fig.1 (c) plots the variation of the MCD asymmetry by increasing the Cu overlayer onto the Ni film and it is found that for the electron kinetic energy of ~ 1 eV the attenuation depth is only ~ 2 ML (0.32 nm) for Cu deposition, which is much smaller than the escape depth by universal curves (~ 10 nm). This reduced electron escape depth is explained by electron diffraction effects when the photoelectrons pass through the capping layer.

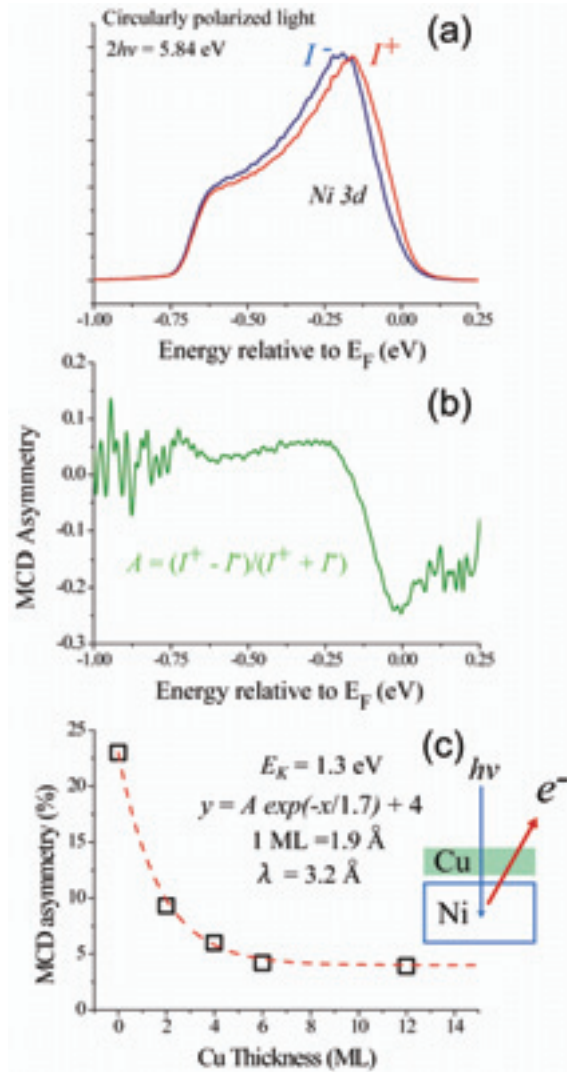


Fig. 1 (a) Two photon ARPES spectra for Ni(15 ML)/Cu(001) sample. The sample magnetization is inverted by pulse coil and the helicity of the circularly polarization is fixed. (b) MCD asymmetry derived from the spectra in (a). (c) The variation of the MCD asymmetry by increasing the thickness of Cu overlayer.

[1] T. Nakagawa, and T. Yokoyama, *Phys. Rev. Lett.* **96**, 237402(2006).

[2] T. Nakagawa *et al.*, *Phys. Rev. B.* **79**, 172404 (2009).

In situ photoelectron spectra of an electron-beam irradiated C₆₀ film

J. Onoe^{1*}, T. Ito², S. Kimura³, H. Shima⁴ and H. Yoshioka⁵

¹Research Laboratory for Nuclear Reactors and Department of Nuclear Engineering, Tokyo Institute of Technology, Tokyo 152-8550, Japan

²Department of Materials, Physics and Energy Engineering, Nagoya University, Nagoya 464-8601, Japan

³UVSOR Facility, Institute for Molecular Science, and School of Physical Sciences, The Graduate University for Advanced Studies (SOKENDAI), Okazaki 444-8585, Japan

⁴Department of Applied Physics, Hokkaido University, Sapporo 060-8628, Japan

⁵Department of Physics, Nara Women's University, Nara 630-8506, Japan

We have found that electron-beam (EB) irradiation of a C₆₀ film gives rise to formation of a peanut-shaped C₆₀ polymer with metallic electron-transport properties in air at room temperature [1]. The temperature dependence of the photo-excited carriers lifetime for the peanut-shaped polymer indicated the energy gap formation at below 50 K in a similar manner to the Peierls instability for quasi-one-dimensional (1D) metallic materials such as K_{0.3}MO₃ [2], thus suggesting that the polymer is a 1D metal as illustrated in Fig. 1.

The 1D peanut-shaped polymer is fascinating from a viewpoint of topology, because it has both positive and negative Gaussian curvatures (κ) lined alternatively and periodically. As shown in Table 1, this nanocarbon can be classified into a new π -electron conjugated carbon allotrope that is different from graphite ($\kappa = 0$), fullerenes ($\kappa > 0$), nanotubes ($\kappa = 0$ at body, $\kappa > 0$ at cap edge), and hypothetical Mackay crystal ($\kappa < 0$). Accordingly, the 1D peanut-shaped polymer is expected to exhibit physical and chemical properties different from those of the conventional π -electron conjugated carbon materials.

We have recently examined the valence photoelectron spectra of the polymer, using *in situ* high-resolution ultraviolet photoelectron spectroscopy [3, 4], and observed the Tomonaga-Luttinger liquids (TLL) behavior as the direct evidence for 1D metal and obtained the TLL exponent (α) to be ca. 0.6 [5], which is somewhat larger than that of ca. 0.5 for 1D metallic single-walled carbon nanotubes [6]. Using the Schrodinger equation dealing with the motion of free particles on a curved surface modulated by positive and negative Gaussian curvatures periodically and alternatively, we have first demonstrated that the increase in the exponent value is caused by a curvature-induced effective potential that works for electrons conducting along the curved surface [7].

To our best knowledge, the peanut-shaped C₆₀ polymer is only an existed material with a negative Gaussian curvature, whose electronic and optical properties are revealed. Thus we believe that the present system will open a new field of “quantum

science of condensed matters in Liemannian space”.

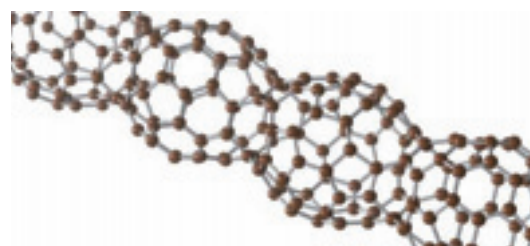


Fig. 1. Schematic illustration of one-dimensional peanut-shaped C₆₀ polymer.

Table 1. Classification of π -electron conjugated carbon materials using Gaussian curvature.

Material	Gaussian curvature (K)
Graphite	0
Fullerenes	> 0
Nanotubes	0 (body), > 0 (capped edge)
Mackay crystal	< 0
Peanut-shaped polymer	> 0, < 0

*E-mail: jonoe@nr.titech.ac.jp

[1] J. Onoe, T. Nakayama, M Aono, and T. Hara, Appl. Phys. Letters **82** (2003) 595.

[2] Y. Toda, S. Ryuzaki, and J. Onoe, Appl. Phys. Letters **92** (2008) 094102.

[3] J. Onoe *et al.*, Phys. Rev. B **75** (2007) 233410.

[4] J. Onoe, T. Ito, and S. Kimura, J. Appl. Phys. **104** (2008) 103706.

[5] T. Ito, J. Onoe, H. Shima, H. Yoshioka, and S. Kimura, in preparation for submission.

[6] H. Ishii *et al.*, Nature **426** (2003) 540.

[7] H. Shima, H. Yoshioka, and J. Onoe, Phys. Rev. B **79** (2009) 201401 (R).

Electronic structure of $\text{Mn}_3\text{Cu}_{1-x}\text{Ga}_x\text{N}$ studied by soft X-ray photoelectron spectroscopy

Y. Miyata¹, K. Mima¹, R. Yamaguchi¹, A. Yamasaki², A. Higashiya³, T. Muro⁴,
K. Terashima¹, K. Takenaka⁵, A. Ozawa⁵, T. Inagaki⁵, S. Imada¹

¹ Department of Physics, Ritsumeikan University, Kusatsu, Shiga 525-8577, Japan.

² Department of Physics, Faculty of Science and Engineering, Konan University, Kobe
658-8501, Japan

³ SPring-8 / RIKEN, Hyogo 679-5148, Japan

⁴ JASRI, SPring-8, Hyogo 679-5198, Japan

⁵ Department of Crystalline Materials Science, Nagoya University, Nagoya 464-8603, Japan

Antiperovskite manganese nitrides Mn_3XN (A=Zn, Ga, etc) are potential candidates for large negative thermal expansion (NTE) materials. These nitrides are well known for their large magnetovolume effect (MVE) [1]. Unlike other Mn_3XN , Mn_3CuN does not show MVE. Instead, Mn_3CuN undergoes a first-order transition from the high-temperature paramagnetic to the low-temperature ferromagnetic phase at $T_C=143\text{K}$, accompanied by cubic-to-tetragonal structural deformation [2].

In order to clarify the relationship between crystal structure and magnetic structure in this system, we studied the electronic states of $\text{Mn}_3\text{Cu}_{1-x}\text{Ga}_x\text{N}$ by soft X-ray photoelectron spectroscopy (SXPES). We have also carried out band structure calculation, and compared the obtained electronic structures with the experimental results. Figure 1 shows the valence band SXPES spectra of Mn_3CuN and $\text{Mn}_3\text{Cu}_{0.5}\text{Ga}_{0.5}\text{N}$, the latter showing MVE, measured with the incident photon energy of 700 eV. Both spectra consists of three characteristic structures; a peak in the vicinity of Fermi level, a peak at 3.5 eV, and a hump at ~ 8 eV. From the comparison between the SXPES result and band calculation, we identify each as mainly N 2p, Cu 3d, and Mn 3d bands, respectively. Next we compared the electronic states of $\text{Mn}_3\text{Cu}_{0.5}\text{Ga}_{0.5}\text{N}$ with Mn_3CuN . Through the substitution of Ga for Cu, the photoelectron intensity peak at 3.5 eV decreases, whereas the peak in the vicinity of Fermi level becomes sharper. These changes are consistent with the results of the band calculation.

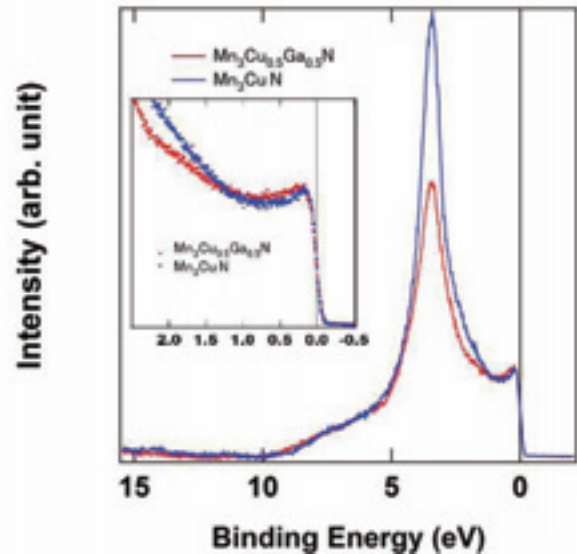


Fig. 1. SXPES spectra of Mn_3CuN and $\text{Mn}_3\text{Cu}_{0.5}\text{Ga}_{0.5}\text{N}$. In the main panel, the lines represent the spectra measured at 170K (paramagnetic phase), respectively. These spectra are normalized by the integrated intensity. The inset shows the magnified view of the spectra near the Fermi level where the red filled circles and the blue filled circles represent the spectra in Mn_3CuN and $\text{Mn}_3\text{Cu}_{0.5}\text{Ga}_{0.5}\text{N}$ respectively.

[1] K. Takenaka *et al.*, Appl. Phys. Lett. **87** 261902 (2008)

[2] K. Takenaka *et al.*, Appl. Phys. Lett. **92** 161909 (2008)

“L+1 rule” for continuous electron-hole excitations in photoemission spectra

V. I. Grebennikov, T.V. Kuznetsova.

Institute of Metal Physics, UD RAS, Ekaterinburg 620041, Russia

Low-energy excitations in valence bands are studied by means of XPS spectroscopy. The analysis of a form of core levels spectra gives the size of effects of electron-hole interactions on atoms of different chemical elements in the compound $\text{Ni}_{0.5}\text{TiTe}_2$. The rule for many-electron excitations in solids under action of core-level photo holes is offered.

$\text{Ti}2p$ and $\text{Te}3d$ XPS spectra in the intercalated compound $\text{Ni}_{0.5}\text{TiTe}_2$ are shown in fig. 1. The lines of the $\text{Ti}2p$ spin-orbital doublet are broadened asymmetrically due to many-body excitations of valence-band electrons generated by sudden creation of the $2p$ photo holes [1]. At the same time such effects on the $\text{Te}3d$ lines are much smaller. To extract the quantitative information the experimental spectra were approximated by a sum of two spin-orbital lines and an inelastic background I_{bg} : $I(E) = I_1(E) + I_2(E) + I_{bg}(E)$. The form of each line $I_j(E) = A_j \text{Im}g(E - E_j - i\Gamma_j)$ is determined by an imaginary part of the power function [2]

$$g(z) = \frac{1}{(1-\alpha)b} [1 - (1-b/z)^{1-\alpha}] \quad (1)$$

Here A_j is line weights; α is the asymmetry coefficient, shown intensity of the valence electron excitations accompanying creation of the photo hole; b is their maximal energy; E_j and Γ_j stand for binding energy and decay of the lines. The power of electron-hole interaction for different XPS lines in $\text{Ni}_{0.5}\text{TiTe}_2$ has the following magnitudes:

Line	Ti2p	Te3d	Ti 3s	Te4d
α	0.33	0.06	0.23	0.08

The asymmetry of a spectrum (dynamic screening of the photo hole) in titanium is much more, than in other components of compound. It is characterized by $\alpha = 0.33$ (the values of α in nickel and tellurium are small, see table and spectra). The important conclusion follows. Despite of a collective character of the valence band electrons in solids, their reactions on photo holes, arising on core levels of various elements, are completely different. Exaggerating, it is possible to tell, that in this case there is no common band excitations, each atom in itself.

Analyses of XPS spectra of $\text{Ni}_{0.5}\text{TiTe}_2$ and other compounds allow us to conclude that the many-body excitations in solids are followed by the “ $l + 1$ rule”: photo-hole with the moment l shakes up the band electrons of $l + 1$ states, mainly. So, for example, $3d$ -electrons react basically on $2p$ -hole, therefore the many-electron effects are strongest on titanium atoms.

These effects are smaller on nickel atoms because of the almost filled Ni $3d$ -shell does not respond on external perturbations. The Te $3d$ - and $4d$ -spectra are narrow symmetric lines like in an isolated atom because of f -electrons absence.

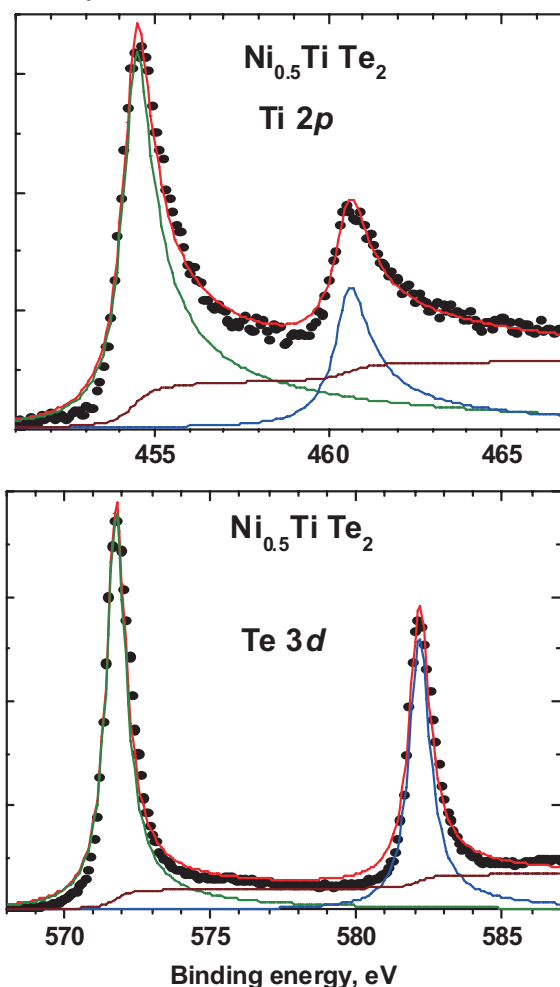


Fig. 1. $\text{Ti}2p$ and $\text{Te}3d$ XPS spectra in the compound $\text{Ni}_{0.5}\text{TiTe}_2$ and their decomposition on sum of two standard lines (1) and a background.

The origin of the rule is connected to prevalence of the dipole matrix elements in coulomb interaction $l' = l \pm 1$. However the probability of a transition with reduction of the orbital moment in solids is much less than that in free atoms because of strong delocalization of electron states with the moment $l - 1$. In result the $l + 1$ transition dominate, as it is clearly visible in experimental spectra.

[1] S. Doniach, M. Sundjic, J. Phys. C **3** (1970) 285.

[2] V. I. Grebennikov, J. Electr. Spectr. Rel. Phenom. **137-140** (2004) 741.

Temperature and substitution dependence of extremely low-energy photoemission spectra on $\text{Sm}_{1-x}\text{Eu}_x\text{B}_6$

J. Yamaguchi¹, A. Sekiyama¹, M. Y. Kimura¹, H. Sugiyama¹, S. Komori¹, Y. Tomida¹, G. Kuwahara,¹ T. Ito², S. Kimura², S. Yeo³, S.-I. Lee⁴, H.-D. Kim⁵, and S. Suga¹
¹Graduate school of Engineering Science, Osaka University, Toyonaka, Osaka 560-8531, Japan
²UVSOR Facility, Institute for Molecular Science, Okazaki 444-8585, Japan
³Korea Atomic Energy Research Institute, Daejeon 305-6000, Korea
⁴Department of Physics, Sogang University, Seoul 121-742, Korea
⁵Pohang Accelerator Laboratory, Pohang 790-784, Korea

SmB_6 and YbB_{12} have been well known as valence fluctuating (VF) Kondo semiconductors (insulators) and intensively studied because of their physical properties. The Kondo semiconductors behave as metals with localized f magnetic moments at high temperatures (T), whereas they develop a narrow hybridization gap (~ 10 meV) at the Fermi level (E_F) at low T . It is thought that the gap formation originates from the hybridization of the narrow f band with broad itinerant valence-bands, but the mechanism of the gap is still controversial.

In our previous hard x-ray photoemission (HAXPES) studies for the Lu substitution Kondo semiconductor alloys $\text{Yb}_{1-x}\text{Lu}_x\text{B}_{12}$ [1], we have found from the T dependence of the Yb $4f$ spectral analyses that the $4f$ lattice coherence plays important roles for developing the gap. The gap for YbB_{12} is suggested to be rapidly closed by the Lu substitution of $x = 0.125$ due to the collapse of the $4f$ lattice coherence. On the other hand, our HAXPES study for the Eu substitution alloys $\text{Sm}_{1-x}\text{Eu}_x\text{B}_6$ shows that the T dependence of the Sm^{2+} $4f$ spectra for $x = 0.15$ is qualitatively similar to that for pure YbB_{12} . Thus, it is expected from our HAXPES results that a finite gap is still open for $\text{Sm}_{0.85}\text{Eu}_{0.15}\text{B}_6$, although the $4f$ lattice coherence could be broken by the Eu substitution. In order to directly investigate the existence of the gap, we have performed the extremely low-energy photoemission (ELEPES) study on $\text{Sm}_{1-x}\text{Eu}_x\text{B}_6$ ($x = 0, 0.15, \text{ and } 0.5$). The ELEPES spectra for $x = 0.15$ and 0.5 were measured by use of synchrotron radiation ($h\nu = 7$ eV) at UVSOR-II BL7U and those for $x = 0$ and 0.5 were measured with the Xe I ($h\nu = 8.4$ eV) resonance line. The energy resolution was set to ~ 6 meV in all measurements.

Figure 1 shows the T dependence of the ELEPES spectra near E_F for $x = 0, 0.15, \text{ and } 0.5$. According to the photoionization cross section [2], the observed spectra are dominated by the non- $4f$ (Sm and/or Eu $5d$ and B $2sp$) states. For $x = 0$, we find that a so-called leading-edge of the spectra is on the occupied side, which indicates the existence of the finite gap. In addition, the prominent peak is observed at ~ 15 meV, which is comparable to that due to the magnetic excitation observed by neutron scattering

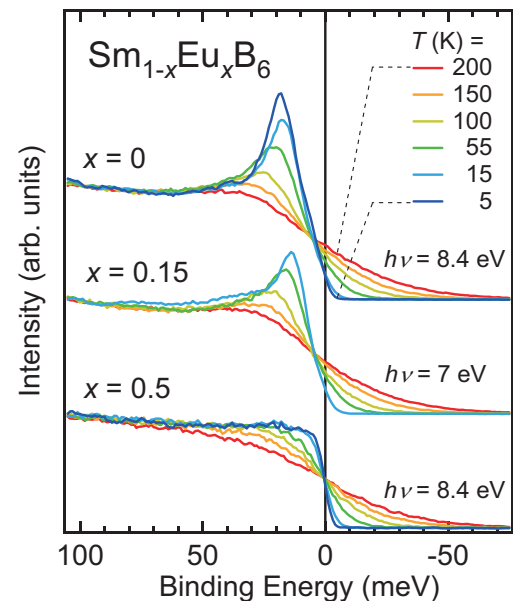


Fig. 1. Temperature dependence of the ELEPES spectra near E_F for $\text{Sm}_{1-x}\text{Eu}_x\text{B}_6$.

measurements for SmB_6 [3]. With increasing T from 5 to 200 K, the spectral weight on E_F increases and the peak shifts toward the higher binding energy side. It should be noted that the spectra for $x = 0.15$ show the essentially equivalent T dependence for $x = 0$, which indicates that $\text{Sm}_{0.85}\text{Eu}_{0.15}\text{B}_6$ is still a Kondo semiconductor against the collapse of the $4f$ lattice coherence. In contrast, the spectra for $x = 0.5$ show no prominent peak and thus a typical metallic thermal behavior. These ELEPES results indicate that SmB_6 is a “robust” Kondo semiconductor against a rare-earth substitution, which is significantly different from YbB_{12} .

[1] J. Yamaguchi *et al.*, Phys. Rev. B **79**, 125121 (2009).

[2] J. J. Yeh and I. Lindau, At. Data Nucl. Data Tables **32**, 1 (1985).

[3] P. A. Alekseev *et al.*, J. Solid State Chem. **133**, 230-236 (1995).

SOLEIL, Cassiopée

ARPES and spin resolved Investigations on the 8-1500 eV high resolution Cassiopée beamline at SOLEIL

Alessandro Nicolaou^{1,2}, François Bertran, Patrick Lefevre¹, Antonio Tejada¹, Julien Pinon, Daniel Ragonnet and Amina Taleb-Ibrahimi*

¹*Synchrotron SOLEIL, GIF-sur-YVETTE, France*

²*Lab. Physique des Solides, Université Paris-Sud XI, Orsay, France*

In this poster an overview of the performances of the high resolution Photoemission Beamline Cassiopée at SOLEIL will be shown.

This beamline is divided in two branches dedicated to High energy resolution ARPES and spin –resolved photoemission.

We will present an angle-resolved photoemission (ARPES) study of the low energy electronic structure of “misfit” cobaltates. Misfits are lamellar compounds, where metallic CoO₂ layers are separated by an “insulating” rock-salt structure, which acts as charge reservoir. The two sub-structures are generally incommensurate, this is why they are called misfit. In 2003, Takada et al. observed superconductivity along the same CoO₂ in Na_{0.3}CoO₂:2H₂O . Since then, the family of Na_xCoO₂, are heavily studied and showed a rich phase diagram in function of electron doping, from the Mott insulator limit (CoO₂) to the band insulator NaCoO₂ . The “misfits” are located near the band insulator limit (X=0.7-1) and show coexistence of high thermoelectric power, good metallicity and Curie-Weiss susceptibility as Na cobaltates of the same doping. However, the transport properties suggest an evolution toward an insulating phase before the band insulator limit, not observed in Na cobaltates. We are interested in the comparison between the two systems to understand what is intrinsic of the metallic CoO₂ layers.

In addition, spin polarized photoemission data on Cassiopée allowing the determination of the polarization at the Fermi level in epitaxial FeV alloys, a step toward the understanding of the tunnel transport in MgO epitaxial junctions using these alloys as electrodes, will be shown.

* amina.taleb@synchrotron-soleil.fr

Temperature Dependent Angle-Resolved Photoemission Spectroscopy on Ferromagnetic EuO Thin Films

H. Miyazaki¹, T. Ito², H. J. Im³, S. Yagi², M. Kato², K. Soda² and S. Kimura^{1,4}

¹UVSOR Facility, Institute for Molecular Science, Okazaki 444-8585, Japan

²Graduate School of Engineering, Nagoya University, Nagoya 464-8603, Japan

Department of Advanced Physics, Hirosaki University, Hirosaki 036-8560, Japan

⁴School of Physical Sciences, The Graduate University for Advanced Studies, Okazaki 444-8585, Japan

Europium monoxide (EuO) is a ferromagnetic semiconductor with the Curie temperature (T_C) at around 70 K [1, 2]. In the electron doping case by the Eu excess or substitute Gd^{3+} or La^{3+} from Eu^{2+} ion, the T_C increases up to 150 K and the electrical resistivity drops twelve-order of magnitude below the T_C originating in a metal-insulator transition (MIT) [2, 3]. To reveal the origin of these physical properties of EuO, it is important to clarify the electronic structure. Three dimensional angle-resolved photoemission spectroscopy (3D-ARPES) using a synchrotron radiation source is the most powerful technique to directly determine the electronic band structure. Using this technique we observed the change in the Eu 4f and O 2p states across T_C .

Single-crystalline EuO thin films with a thickness of about 50 nm were fabricated by the molecular beam epitaxy (MBE) [4]. Epitaxial growth of the single-crystalline EuO thin films with the 1 x 1 EuO (100) patterns was confirmed with low energy electron diffraction (LEED) and reflection high energy electron diffraction (RHEED) methods. The T_C measured with a superconducting quantum interference device (SQUID) magnetometer was 71 K. The 3D-ARPES measurements were performed at the beam line 5U of UVSOR-II combined with the MBE system.

Figures 1(g1) [1(g2)] and 1(x1) [1(x2)] show the temperature dependence of the Eu 4f [O 2p] band at the Γ and X points, respectively. The circles and bright area correspond to the peak positions of the second-derivative energy distribution curves (EDCs). With decreasing temperature across T_C , all of the bands shift by 0.2–0.3 eV to the lower binding energy side. The overall energy shift is in good agreement with the magnetic red shift estimated from the optical absorption spectra [5]. This indicates that the overall energy shift originates from the changing of the bottom energy of the Eu 5d conduction band at the X point due to the energy gain of the Eu 5d majority-spin state after band splitting caused by ferromagnetic ordering. In addition, the top of the Eu 4f states is shifted away from the main 4f states at the Γ and X points. In contrast, the O 2p state is splitted into two bands below T_C . The bands at the higher and lower binding energies are attributed to the majority and minority spin states, respectively. Since the Eu 4f state is fully polarized, the 4f state mainly hybridizes

with the majority spin state of O 2p and Eu 5d. Therefore, the band shifts can be attributed to the hybridization effect between the Eu 4f and O 2p states (superexchange interaction) and between the Eu 4f and 5d states (indirect exchange interaction). The observed temperature dependent energy shift of the 4f state is the essential origin of the ferromagnetic phase transition of EuO.

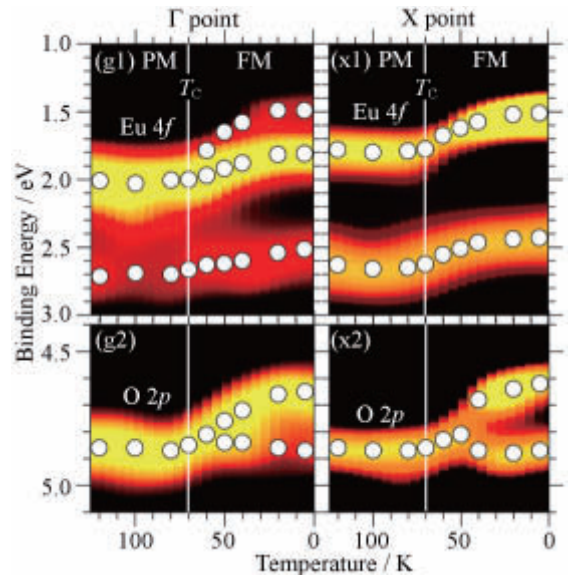


Fig. 1 Temperature dependence of the photoemission peak energies derived from the second-derivative EDCs of the Eu 4f [(g1), (x1)] and O 2p [(g2), (x2)] states at the Γ and X points. The open circles indicate the peaks of the second derivative EDCs.

- [1] N. Tsuda *et al.*, *Electronic Conduction in Oxides* (Springers College) (1976).
- [2] A. Mauger *et al.*, *J. Phys. (paris)* **39**, 1125 (1978).
- [3] Y. Shapira, S. Foner, and T. B. Reed, *Phys. Rev. B* **8**, 2299(1973); **8**, 2316 (1973).
- [4] H. Miyazaki *et al.*, *Jpn. J. Appl. Phys.* **48**, 055504 (2009).
- [5] S. Kimura *et al.*, *Phys. Rev. B* **78**, 052409 (2008).

Present status of VUV angle-resolved photoemission beamline BL7U at UVSOR-II

T. Ito^{1,2}, M. Sakai¹, E. Nakamura¹, N. Kondo¹, and S. Kimura^{1,2}

¹UVSOR Facility, Institute for Molecular Science, Okazaki 444-8585, Japan

²School of Physical Sciences, the Graduate University for Advanced Studies (SOKENDAI), Okazaki 444-8585, Japan

BL7U, the VUV angle-resolved photoemission (ARPES) beamline for advanced studies of strongly correlated electron systems, has been constructed in FY2006 and opened for users in FY2007 [1]. To satisfy the needs from users, especially (1) higher photon-flux, (2) reduction of higher-order light and (3) better base pressure of the photoemission chamber, we have improved the beamline in FY2008. As a result, we successfully achieved the sufficient throughput for ARPES experiments.

To improve the photon-flux especially at the bulk-sensitive low photon-energy ($h\nu < 15$ eV), we updated the lowest photon-energy grating G3 from Au-coating to SiC-coating one. After the update of G3, we realign the beamline to be optimized with the center of the undulator light. As a result, the photon flux as well as the focusing at the sample position has intensively been improved than that in FY2007. Figures 1(a), (b) and (c) show the improved throughput spectra obtained at low (red line)-, medium (red line)-, and high (red, yellow, green, blue lines)-photon energy regions compared with the previous one (black lines), respectively. At each energy region, the spectrum becomes sharper and shifts to the higher energy side in the same condition, indicating successful alignment with the optimum parameter of the undulator light. Clear vibration sub-bands observed higher and lower energy side of the main peak of the throughput spectrum (Fig. 2), which is consistent with a calculation, ensures the correct alignment getting the center of the undulator light.

To reduce the intensity of higher order light at the low photon-energy region, we equipped a VUV filter of MgF_2 just after the exit slit. As a result, we successfully reduced the higher-order light above $h\nu = 11$ eV (see Fig. 3). Typical loss of efficiency by the filter is less than 10%, which ensures sufficient throughput for VUV ARPES experiments with bulk-sensitive low-photon energies.

Finally, to improve the base pressure at the sample, we added a cryopump (ULVAC Cryogenic Inc., U8H) and an ion pump (ULVAC, PST-200CX2) to the photoemission chamber. As a result, we achieved the base pressure of 5×10^{-9} Pa better than before (2×10^{-8} Pa). For further improvement of base pressure, we plan to equip a thermal radiation shield around the sample in FY2009.

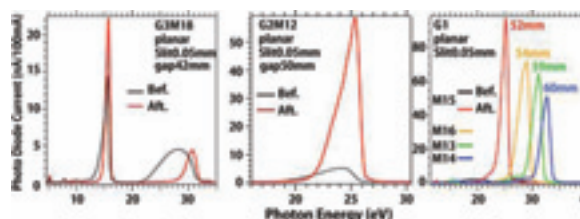


Fig. 1. Improvements of throughput spectra before and after the realignment of optics at BL7U.

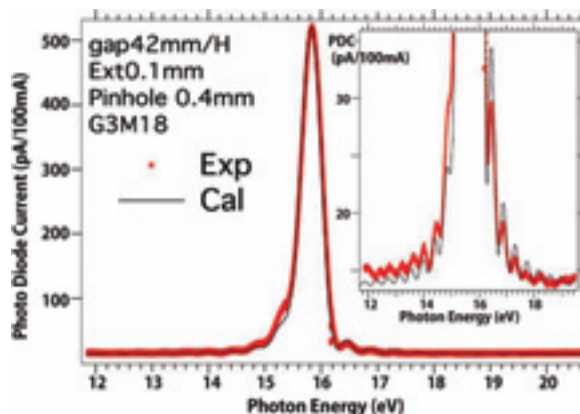


Fig. 2. Throughput spectrum at low photon-energy region in comparison with the calculation.

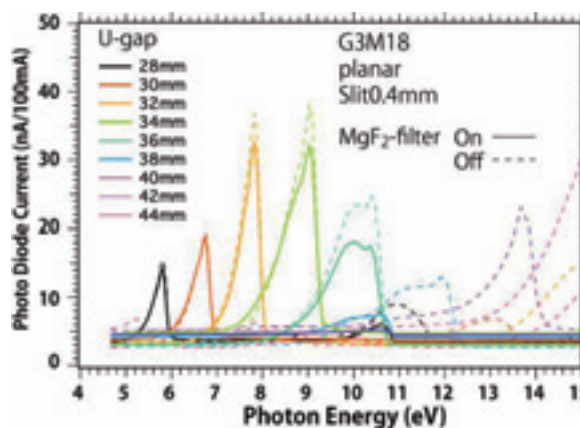


Fig. 3. Throughput spectra with some undulator gap size with and without a VUV filter, MgF_2 , in the low photon-energy region.

[1] S. Kimura *et al.*, AIP Conf. Proc. **879** (2007) 527.

Improvement of the SGM-TRAIN monochromator at UVSOR-II BL5U for low excitation-energy photoemission

T. Ito, H.J. Im*, S. Kimura, E. Nakamura

UVSOR Facility, Institute for Molecular Science, Okazaki 444-8585, Japan

*School of Physical Science, The Graduate University for Advanced Studies, Okazaki 444-8585, Japan

BL5U at UVSOR-II storage ring has been reconstructed in 2004's for high-resolution photoemission (HRPES) study for solids and surfaces [1]. The energy and angular resolutions of the photoemission apparatus constructed at the end-station of BL5U have been improved to $\Delta E \sim 1.2$ meV and $\Delta\theta \sim \pm 0.1^\circ$, which is sufficient to study the anomalous physical properties such as the metal-insulator transition, superconductivity, magnetic phase transition, *etc.* However, it has been hard to study the above properties at BL5U because of the old-type beamline designed in 1995's, in spite of the extensive improvement of the end-station and the storage ring [1,2]. Main problems interrupting a high-resolution study were as follows. (1) Mechanism for optimizing the front mirror was too rough to operate the focus position of the undulator light. (2) Entrance slit has no cooling system. (3) The grating G3 with normal incident mount for the low energy region ($h\nu = 5 - 25$ eV) has been optimized to the bending magnet radiation [3]. The above has caused the extremely low throughput at the low-energy region and restricted the HRPES experiment.

Taking account of the problems listed above, we have reconstructed the beamline in the following way to improve the efficiency in the PES experiment with using the low-energy photons at BL5U. (1) The mechanics at the front mirror was updated to the high-precision system controlled by the pulse-motors. (2) The water-cooling system was attached at the holder of the entrance slit. (3) The monochromator (SGM-TRAIN) was re-arranged to the optimum condition to the undulator light.

Figure 2 shows the improved throughput from the SGM-TRAIN monochromator after the present reconstruction. Comparing with the previous throughput spectra (Fig. 1), we can clearly find that the mesh current increases about 30 times higher, and the energy resolution becomes better because of the sharper interference from the optical klystron-type undulator as shown in Fig. 2. Due to the high-throughput of the photocurrent at the low-energy region, the HRPES measurement at BL5U becomes available. For example, HRPES spectrum at the Fermi-level of gold (Fig. 3) has been corrected within 1 hour with the resolution of $h\nu/\Delta E \sim 1000$. We believe that the present reconstruction makes it

possible to explore the origin of the anomalous physical properties by using the high-resolution bulk-sensitive angle-resolved photoemission apparatus at UVSOR-II BL5U.

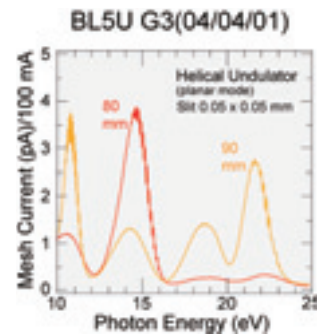


Fig. 1. Throughput spectra from the SGM-TRAIN monochromator with the normal incident grating G3 measured before the present reconstruction [1].

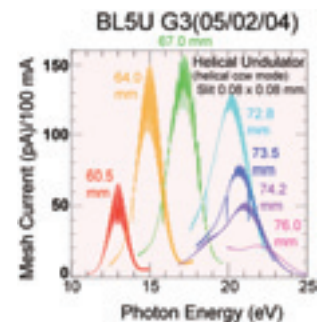


Fig. 2. Same as Fig. 1, but measured after the present reconstruction.

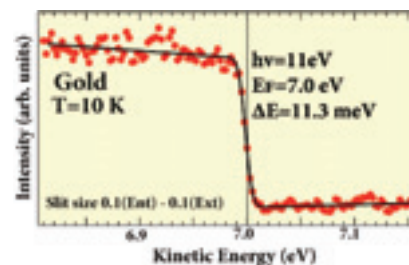


Fig. 3. HRPES spectrum at the Fermi level of gold measured after the present reconstruction.

- [1] T. Ito *et al.*, UVSOR Activity Report 2003, 40.
- [2] M. Katoh *et al.*, UVSOR Activity Report 2003, 5.
- [3] M. Kamada *et al.*, Rev. Sci. Instrum. **66**, 1537 (1995)

Development of Integrated Software for Beamline Control for Photoemission Beamlines at UVSOR-II

Masahiro Sakai,¹ Takahiro Ito,² Shin-ichi Kimura^{1,3}

¹*UVSOR Facility, Institute for Molecular Science, Okazaki 444-8585, Japan*

²*Graduate School of Engineering, Nagoya University, Nagoya 464-8603, Japan*

³*School of Physical Sciences, The Graduate University for Advanced Studies, Okazaki 444-8585, Japan*

We developed integrated software for synchronized motion of a beamline from the undulator light source to the photoemission end station. UVSOR-II, Institute for Molecular Science, has two photoemission beamlines with undulator light sources. One of the beamlines, BL7B, is dedicated for a high-resolution angle-resolved photoemission and equips an APPLE-II-type undulator (NEOMAX Co.), a Wadsworth-type 10-m normal-incidence monochromator (TOYAMA Co.), a 200-mm radius hemispherical photoelectron analyzer (MB Scientific AB, A-1), and a 6-axes manipulator with liquid-helium-cooled cryostat (R-dec Co., i-GONIO). [1] Another beamline, BL5U, also equips the same photoelectron analyzer. [2] In both beamlines, since the control PCs are spatially separated, the operability of the beamline has not satisfied. Then we developed a new multi-client server/client system using the TCP/IP protocol by the LabVIEW software. At present, absorption measurements where the undulator and the monochromator are controlled can be performed. Since the photoelectron analyzer and the manipulator are also controlled by the LabVIEW software, a constant initial state (CIS) measurement and a Fermi surface mapping will be automatically realized in the near future. In this paper, we report the present progress in the development.

[1] S. Kimura, T. Ito, E. Nakamura, M. Hosaka, M. Katoh, AIP Conf. Proc. **879**, 527 (2007).

[2] T. Ito, S. Kimura, H.J. Im, E. Nakamura, M. Sakai, T. Horigome, K. Soda, T. Takeuchi, AIP Conf. Proc. **879**, 587 (2007).

UVSOR Users Meeting

Place: Okazaki Conference Center

November 13, 2009

13:30-14:30

Opening Remarks

Preface

Present Status and Upgrade Plan of UVSOR Accelerators

Electronic Structure and Structure of Endohedral

Metallofullerenes by Photoelectron Spectroscopy

14:40 - 16:30

Photoluminescence and Photoluminescence Excitation Spectra
from AlN doped with Gd³⁺

Dependence of Reflectance and Responsivity of UV Detectors on
Angle of Incidence

Multiproduction by Hot Photocarriers Created in Inorganic EL
Phosphors

Luminescence of Rare Earth Ion doped Hydroxyapatites Excited
by UVSOR

Design for VIS-VUV Spectroscopic Beam Line BL3B

K. Fukui (Fukui Univ.)

N. Kosugi (UVSOR)

M. Katoh (UVSOR)

T. Miyazaki (Ehime Univ.)

S. Sawai (Fukui Univ.)

T. Saito (NMIJ, AIST)

M. Kitaura
(Yamagata Univ.)

M. Ohota (Niigata Univ.)

R. Ikematsu (Fukui Univ.)

16:30-18:00

Poster Session

18:15-

Banquet

November 14, 2009

9:00-10:20

Current Status of BL6U

Present Status of BL7U

Electronic Structure of Organic Thin Films and

Interfaces: Present Understanding and Future Prospects

10:30 - 12:00

Fragmentation of Fullerenes Induced by Extreme UV
Photoirradiation

Crystal Quality Evaluation of Superconducting InN by
Phonon-Polariton

Origin of the Valence Transition of SmS Revealed by Infrared
and Terahertz Spectroscopy at High Pressure and Low
Temperature

Effect of Temperature Dependent Chemical Potential on
Thermoelectric Power

Ferromagnetic Phase Transition and Electronic Structure of
EuO Thin Films

E. Shigemasa (UVSOR)

T. Ito (Nagoya Univ.)

H. Yamane (IMS)

K. Mitsuke (IMS)

T. Inushima (Tokai Univ.)

S. Kimura (UVSOR)

T. Takeuchi (Nagoya Univ.)

H. Miyazaki (UVSOR)

Poster Session

1. Luminescence Properties of CsI Crystals Activated with Ag⁻ and Au⁻ Ions
 2. XANES Spectra of Sulfur K-edge of Cystine
 3. Vacuum Ultraviolet Absorption Spectrum of DNA Bases and Examination of the Thomas-Reiche-Kuhn Sum Rule
 4. Absorption Cross Section of L-Methionine in Sulfur K-Edge Region
 5. Optical Oscillator Strength Distribution of Amino Acids in Ultra Vacuum Violet
 6. Photoelectron Spectroscopy of Pseudo-one Dimensional Ba₃Co₂O₆(CO₃)_{0.7}
 7. Optical Properties of YAG Ceramics Doped with Impurity Ions
 8. Strong Coupling Superconductivity in Iron-Based Superconductor Ba_{1-x}K_xFe₂As₂ Studied by High-Resolution ARPES
 9. Study of Local Structure of SiO₂-Hydroxyapatite by Hydrothermal Process
 10. In Situ Observation of Photostructural Changes in Amorphous Semiconductor by Total Photoyield
 11. Local Structure of Mg in ZrO₂ for Alternative Joints with High Biocompatibility
 12. Electronic Structure of Mn₃Cu_{1-x}Ga_xN Studied by Ultraviolet and Soft X-Ray Photoemission
 13. Design for VIS-VUV Spectroscopic Beam Line BL3B
 14. Electronic Structure of Mn₃Cu_{1-x}Ga_xN Studied by Ultraviolet and Soft X-Ray Photoemission
 15. Polarization Properties of Optical Reflectance, Photoluminescence and Photoluminescence Excitation Spectra from AlN
 16. Photoluminescence and Photoluminescence Excitation Spectra from AlN Doped with Gd³⁺
 17. Reflection Measurement on Si/W/Co and Si/W/C Multilayers for Use in 50–110 nm Region
 18. Study of the Magnetic Film Formed on the Si Substrate with Passivation Layer
 19. Electronic Structure Analysis of Mn and Fe Ions in In₂O₃
 20. XANES Analysis of Electronic Structure of Mn in Pr_{1-x}A_xMnO_{3-δ} (A=Ca, Sr)
 21. Amounts of Electron Transfer in Tm-Entrapped Metallofullerens
 22. Electronic Structure of Sulfur-Containing Organic Solid with High Mobility
 23. UVSOR Accelerators Upgrade Plan in Spring of 2010
 24. Generation of Ultra-Short Gamma-ray Pulses by Laser Compton Scattering in an Electron Storage Ring
 25. Status of Top-Up Operation at UVSOR-II
 26. Present Status of UVSOR-II Free-Electron Laser
 27. Pressure-Dependent IR/THz Reflectivity Spectra of CeIn₃
 28. Current Status of Coherent Harmonics Light Source in UVSOR-II
 29. Three-Dimensional Angle-Resolved Photoemission Spectroscopy of EuO Thin Films
 30. Present Status of THz Coherent Light Source Development
 31. Ce 4d-4f Resonant Angle-Resolved Photoemission Study of Heavy-Fermion Systems in Weakly Hybridized Regime
 32. Decomposition and Chirality Formation of Amino Acids by CP-UVL Irradiation
- T. Kawai (Osaka Pref. Univ.) et al.
M. Tabe (Kobe Univ.) et al.
A. Mimoto (Kobe Univ.) et al.
Y. Izumi (Kobe Univ.) et al.
A. Imazu (Kobe Univ.) et al.
K. Soda (Nagoya Univ.) et al.
H. Uno (Gifu Univ.) et al.
K. Nakayama (Tohoku Univ.) et al.
K. Nakata (Osaka Pref. Univ.) et al.
K. Hayashi (Gifu Univ.)
T. Monden (Osaka Pref. Univ.) et al.
Y. Miyata (Ritsumeikan Univ.) et al.
R. Ikematsu (Fukui Univ.) et al.
K. Ozaki (Fukui Univ.) et al.
T. Ito (Fukui Univ.) et al.
S. Sawai (Fukui Univ.) et al.
M. Watanabe (Shanghai Dianji Univ.) et al.
Y. Takagi (IMS) et al.
T. Okazaki (Waseda Univ.) et al.
H. Kanamori (Waseda Univ.) et al.
Y. Tokumoto (Ehime Univ.) et al.
T. Zaima (Ehime Univ.) et al.
J. Yamazaki (UVSOR) et al.
Y. Taira (Nagoya Univ., UVSOR) et al.
K. Hayashi (UVSOR) et al.
H. Zen (UVSOR) et al.
T. Iizuka (SOKENDAI, UVSOR) et al.
T. Tanikawa (SOKENDAI, UVSOR) et al.
H. Mitani (Shinshu Univ., UVSOR) et al.
M. Adachi (UVSOR) et al.
H. J. Im (Hirosaki Univ.) et al.
S. Shima (Yokohama National Univ.) et al.

Status and Prospects of Synchrotron Light Source Technologies

Feb. 19, 2010

Room 301, IMS Research Facilities Building

12:55	Opening Remark	M. Katoh (UVSOR)
13:00	Status of UVSOR-II	M. Katoh (UVSOR)
13:30	Status of HiSOR	K. Gotoh (HiSOR)
14:00	Status of PF/PF-AR	T. Honda (KEK)
14:30	Status of KEK-ERL Project	M. Shimada (KEK)
15:00	Coffee Break	
15:15	Top-up Operation at PF	K. Harada (KEK)
15:45	Top-up Operation at UVSOR-II	H. Zen (UVSOR)
16:15	Top-up Operation at New SUBARU	Y. Shoji (New SUBARU)
16:45	Coffee Break	
17:00	Beam Injection with Pulsed Multi-Pole Magnet at PF	H. Takagi (Tokyo Univ.)
17:30	Status and Prospects of Beam Feedback Technologies	M. Tobishima (KEK)
18:00	Dust-Trapping at PF-AR	Y. Tanimoto (KEK)
18:30	UVSOR Facility Tour	
19:00	Banquet at UVSOR	

Feb. 20, 2010

9:00	Beam Diagnostics at PF	T. Obina (KEK)
9:30	Status of Visible Light Beam Line and Beam Diagnostic Beam Line at SPring-8	K. Tamura (SP8/JASRI)
10:00	Performance Characteristics Measurements of X-Ray Streak Camera at SPring-8	A. Mochihashi (SP8/JASRI)
10:30	Beam Diagnostics with Electronic Scheme at SPring-8	T. Fujita (SP8/JASRI)
11:00	Coffee Break	
11:15	Status of Light Source Developments at UVSOR-II	M. Adachi (UVSOR)
11:45	Status and Prospects of SAGA-LS	S. Koda (SAGA-LS)
12:15	Status of Central Japan Synchrotron Radiation Research Facility and Light Source Accelerator	N. Yamamoto (Nagoya Univ.)
12:45	Closing Remark	T. Kasuga (KEK)



Editorial Board

M. Adachi

H. Hagiwara

M. Masuda

H. Zen